Approximate basis and a priori closure models for energy-conserving reduced order modeling of fluid flows

Gustaw Cegielski

Master Thesis

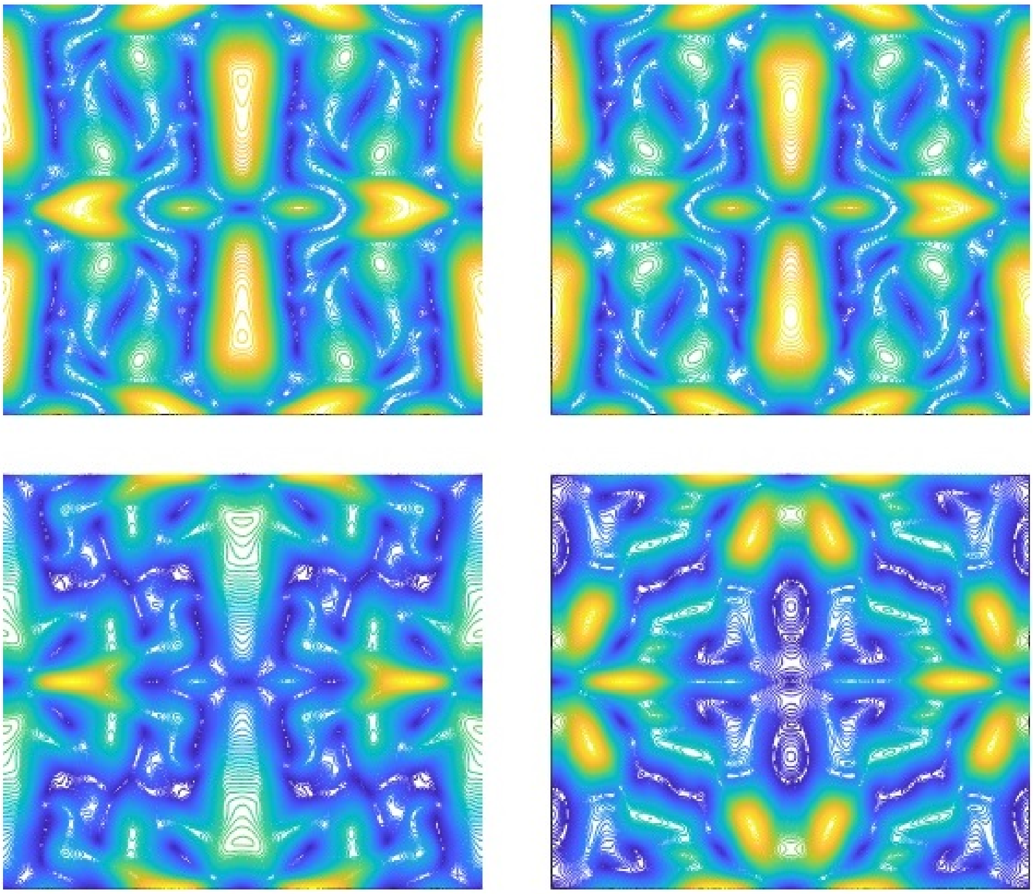

Approximate basis and a priori closure models for energy-conserving reduced order modeling of fluid flows

by

Gustaw Cegielski

to obtain the degree of Master of Science
at the Delft University of Technology,
to be defended publicly on Tuesday October 25, 2021 at 15:00 AM.

Student number:	4621670	
Project duration:	September 24, 2019 – October 25, 2021	
Thesis committee:	Dr. Richard P. Dwight,	TU Delft, supervisor
	Dr. Benjamin Sanderse,	CWI Amsterdam, supervisor
	Dr. Sergio R. Turteltaub,	TU Delft
	Dr. Giovanni Stabile,	SISSA Trieste

Cover: Taylor-Green Vortex

TU Delft

Abstract

Model order reduction (MOR) has been a field of active research in the past twenty years, more recently also in fluid dynamics. The main advantage of MOR is computational cost reduction, which, along with equally important accuracy, constitute main objective in the MOR community. A main ongoing issue is that data volumes in fluid flow simulations (such as turbulent flows) are usually very large, hence processing is costly. An example of a high-cost operation in MOR is the construction of reduced basis (RB) via singular value decomposition (SVD) of snapshot data of turbulent flows. The present research, in its first objective, aims at tackling this problem by applying and adapting an incremental SVD algorithm (iSVD). The procedure does not require simultaneous access to the entire snapshot matrix, but the price to pay is that accurate approximations of RB via iSVD are obtained only for low-index. ROMs require exactly those, therefore application of iSVD is plausible. The algorithm is tested on high-fidelity data representing transitional and turbulent flow solutions, obtained with an energy-conserving code (INS3D). Important iSVD paramters are identified and their influence on key properties of RB: orthogonality, zero-divergence and fidelity w.r.t. conventional SVD basis is examined.

The second objective concerns closure modeling. MOR by definition neglects a part of information. Hence inaccuracies and/or instabilities often develop in the reduced order model (ROM) solution. The applied ROM framework is energy-conserving (EC-ROM), thereby ensuring non-linear stability. Accuracy is not guaranteed, therefore a correction is desirable. In ROM context several strategies exist. In the present research one such strategy, dissipation via a closure term, is examined in an 'a priori' test. Based on the full order model (FOM) data and projection of it onto the reduced space, exact expression for missing information (exact closure term) is derived. Subsequently, an eddy viscosity (EV) ansatz is applied, whereby also high-fidelity data is used to compute EV. The turbulence model is of mixing-length type. The related turbulent diffusive term with variable EV is regressed on the exact closure term.

It is concluded that iSVD is a feasible algorithm in MOR applications, particularly in combination with EC-ROM, provided that parameters of iSVD: increment size, maximum dimension of RB and threshold are far from their lower bounds. EV mixing length model is considered inadequate as a means of improving accuracy of EC-ROM in periodic shear-layer.

Preface

This thesis crowns two-year studies of reduced order modeling of fluid flows, that I had undertaken. It was originally intended as a forward leap into the common area that machine learning and fluid-flow model order reduction share. It is self-evident that computational time and memory efficiency are key factors in contemporary engineering and computational science, hence the field itself has enjoyed a high rate of development in the last years.

My primordial ambition was to delve into artificial neural networks in order to tackle the problem of closure modeling in three-dimensional turbulent flows with reduced order representation. Complexity of such phenomena and sheer volumes of involved data sets, necessitated the use of special techniques, which inexorably introduced complexity of its own. The research objectives had to be adjusted multiple times. Eventually, to achieve interpretable results within a reasonable time scale, I needed to settle for simple regression techniques. The significance of this thesis lies in the use of energy-conserving model framework combined with a special approximate basis construction algorithm as well as in the study of turbulence modeling in this context.

When I came to TU Delft as an aerodynamics master student five years ago, I was not prepared for what was coming. I took a long (6-month) internship at Airbus, which was poorly synchronized with my academic year plan. On top of that, when the thesis project had begun, COVID-19 was not even heard of. Inherent complexity of the topics, my own shortcomings and the pandemic, which separated me from the academic community, had all affected the time span of the project and my studies at TU Delft in general.

This entire enterprise would have never succeeded had I not received support from people, whom I would now like to thank. I owe the most to my parents, who have had enough patience to withstand my chronic stress, remaining sane at the same time. Without their love and understanding I would not have even dreamt of starting this project, let alone accomplishing it. I owe special thanks to my promoters: Richard Dwight and Benjamin Sanderse. Their professionalism and can-do attitude had shown me, that endeavours such as this project are not close to impossible, as I had primordially thought. I am particularly grateful to Ben, who had the resilience and sheer good will to go through my thesis in detail, at a time when it was far from ready. Further, the one person, who stood by me whenever possible, was my girlfriend Ewa, whom I also want to thank with all my heart. Thank you for enduring my state of mind and letting me finish this. Moreover, I wish everyone during their thesis projects had so supportive friends as I was lucky to have: Michał, Tosia, Wojtek - I cannot express how much this meant to me. Lastly, even though we only had one short scientific discussion on differential equations and Galerking methods, I would like to acknowledge the inspiration provided by dr. Anna Karczewska and prof. Piotr Rozmej.

Gustaw Cegielski
Zielona Góra, September 2021

Contents

List of Figures 7

1 Introduction 9
- 1.1 Background . . . 9
- 1.2 Research objective and questions . . . 11
- 1.3 Overview . . . 13

2 Literature Review and ROM preliminaries 15
- 2.1 Basic notions and equations . . . 15
- 2.2 ROM literature overview . . . 16
- 2.3 Eddy viscosity ansatz . . . 19
- 2.4 Reduced basis . . . 20
- 2.5 Closure in ROM context . . . 25

3 Methodology 27
- 3.1 Energy-Conserving ROM . . . 27
- 3.2 Closure modeling . . . 30
- 3.3 Error estimators . . . 35
- 3.4 Other investigated quantities . . . 36

4 Setup of numerical experiments 39
- 4.1 Test cases . . . 39
- 4.2 Experiments . . . 40
- 4.3 Estimation of some grid parameters . . . 42
- 4.4 Software . . . 43

5 Basis computation 45
- 5.1 Basis quality . . . 45
- 5.2 Comparison of modes: shapes . . . 54
- 5.3 Comparison of modes: spectra . . . 57
- 5.4 Comparison of bases: singular values . . . 60
- 5.5 Summary . . . 60

6 ROM simulation 63
- 6.1 Shear layer: main results . . . 63
- 6.2 Shear layer: additional results . . . 71
- 6.3 Taylor-Green vortex . . . 79

7 A priori analysis 83

8 Conclusion and recommendations 91
- 8.1 Answers to research questions . . . 91
- 8.2 Conclusion . . . 94
- 8.3 Recommendations . . . 95

A Appendix 97
- A.1 SV decay comparison . . . 97
- A.2 Selected fields . . . 97
- A.3 A priori eddy viscosity plots . . . 100
- A.4 A priori absolute errors . . . 103
- A.5 A priori relative errors . . . 104
- A.6 Pressure Poisson equation . . . 107
- A.7 Optimal snapshot selection . . . 107

A.8 LS regression - derivation of formulas . . . 108
A.9 Proposition of LS regression (more sophisticated) . . . 109
A.10 Performed computations . . . 109
Bibliography 113

Nomenclature

Acronyms

AD-ROM	Approximate-Deconvolution Reduced Order Model
BC	Boundary Condition(s)
CFD	Computational Fluid Dynamics
CFL	Courant-Friedrichs-Levy
cSVD	conventional Singular Value Decomposition
DEIM	Discrete Empirical Interpolation Method
DMD	Dynamic Mode Decomposition
DNS	Direct Numerical Simulation
DoF	Degree of Freedom
EC-ROM	Energy-Conserving Reduced Order Model
EV	Eddy Viscosity
EV-ROM	Eddy Viscosity Reduced Order Model
FE	Finite Element
FFT	Fast Fourier Transform
FOM	Full Order Model
FV	Finite Volume
GS	Gram-Schmidt (orthogonalization)
HDD	Hard Disk Drive
IC	Initial Condition(s)
iSVD	incremental Singular Value Decomposition
LES	Large Eddy Simulation
LHS	Left-Hand Side
LS	Least Squares
ML	Mixing Length or Machine Learning
MOR	Model Order Reduction
MoS	Method of Snapshots
NS	Navier-Stokes (equations)
ODE	Ordinary Differential Equation
PCA	Principle Component Analysis

PDE	Partial Differential Equation(s)
POD	Proper Orthogonal Decomposition
RANS	Reynolds-Averaged Navier-Stokes (equations)
RB	Reduced Basis
RHS	Right-Hand Side
RK	Runge-Kutta
ROM	Reduced Order Model
RST	Reynolds Stress Tensor
SL	Shear Layer
SV	Singular Value
SVD	Singular Value Decomposition
TG	Taylor-Green (vortex)
TKE	Turbulence Kinetic Energy
VMS	Variational Multi-Scale

Symbols: Latin letters

$\boldsymbol{u}'$	unresolved velocity (continuous)
$\boldsymbol{u}$	velocity (continuous)
$\hat{X}, \tilde{X}$	modified snapshot matrix
$\mathbb{I}$	Identity matrix
$\mathbb{I}$	identity matrix
$\mathbb{R}$	set of real numbers
$\mathscr{P}$	general projection operator
$\overline{\boldsymbol{u}}$	resolved velocity (continuous)
$\overline{p}$	resolved pressure (continuous)
A	averaging operator
A	generic matrix
a	ROM POD coefficient, generic matrix element
C	convective operator
c	Courant number
D	diffusion operator
d	Kolmogorov n-width
e	error, vector of 0 and 1 with 1 corr. to a particular direction
F	right-hand side of ROM equation
f	generic function

G	gradient operator, orthogonal transformation
g	POD coefficients for eddy viscosity basis
H	Eddy-viscosity ROM diffusion operator
h	filter kernel, cell width
I	interpolation operator, imaginary unit
K	subset in a Hilbert space, differencing operator
k	total kinetic energy, increment size, generic function
k'	fine scale (turbulence) kinetic energy
L	Hilbert space, divergence operator, domain length
M	dimension of reduced space, divergence operator
M	divergence operator
M'	difference btw. M used in ROM and largest possible M
N	no. of cells / no.of time steps/ dimension (context-dependent)
NS	Navier-Stokes operator
P	linear momentum
p	pressure, percentage
p'	unresolved pressure (continuous)
Pe	Peclet number
Q	product element in diffusion operator decomposition, matrix Q of QR-decomposition, Q-criterion
q	velocity magnitude
R	target function in a priori analysis, matrix R of QR-decomposition, rotation matrix
Re	Reynolds number
S	sub-matrix of orthogonal matrix corr. to subordinate subspace, symmetricized gradient
T	period of interest
T	sub-matrix of orthogonal matrix corr. to dominant subspace
t	time
u	generic discretized velocity
V	velocity (discretized)
W	regressor in a priori analysis
X	snapshot matrix
x, y, z	system coordinates
Y	random variable

Symbols: Greek letters

α	coeff. of regression, coeff. in Robbin BC, rotation angle

β	coeff. in Robbin BC
$\boldsymbol{\varphi}$	ROM POD basis function (continuous)
$\boldsymbol{\xi}, \xi$	wavenumber vector, wavenumber
δ	a constant in BCs
ϵ	error, machine epsilon, a constant in BCs
η	POD basis of eddy viscosity field
γ	filter parameter
λ	eigenvalue
μ	parameter vector
ν	viscosity
ω	an element of Ω_h matrix
Ω, Ω_h	computational domain (continuous,discrete)
$\overline{\Delta}$	filter width
$\overline{\Phi}$	reduced basis vector
$\partial\Omega$	domain boundary
Φ	ROM POD basis function (discrete)
Φ'	unresolved-scales basis vector
Ψ	right singular vectors (of snapshot matrix)
Σ	diagonal matrix of singular values
σ	singular value

Subscripts

$>$	corresponding to unresolved scales
$\hat{}$	corresponding to Fourier space
Ω	measured in L_2, Ω-weighted norm
add	additive, added in increment
$ansatz$	with a form assumed in advanced
avg	averaged
div	divergence
dom	dominant
end	in last instant
F	Frobenius
h	spatially discrete, corresponding to FOM
i,j,k	context-appropriate indices
n	index of time instant, dimensionality, integer

p	pressure
r	corresponding to reduced space
start	in first instant
true	derived from FOM, reference
trunc	truncated
t	temporal, turbulent
u,v,w	in u, v, w direction
V	velocity
x,y,z	corresponding to x, y, z coordinates

List of Figures

2.1 Kolmogorov n-width, orientation of subspace $\mathbb{W}_n$ w.r.t. to K 17
2.2 Energy cascade [24]. Here: κ-wavenumber, $E(\kappa)$-energy density spectrum 18

3.1 Possible ways of obtaining projection-ROM [31]. PDE, ODE, DDE - partial/ordinary/discretized differential equation. 27

4.1 Shear layer: Initial conditions for u, v, w-velocities. 39
4.2 Taylor-Green Vortex: Initial condition for u-velocity, sections in 3 midplanes. 40
4.3 Stability regions of Runge-Kutta methods [15]. Here abscissa and ordinates are real and imaginary axes respectively, $Re(\lambda), Im(\lambda)$ 43

5.1 Frobenius L_2 orthogonality error, $\|\mathbb{I} - \Phi^T \Omega_h \Phi\|^F_{\Omega_h}$. Influence of threshold, k_{add} and M_{dom} 46
5.2 Frobenius L_2 orthogonality error, $\|\mathbb{I} - \Phi^T \Omega_h \Phi\|^F_{\Omega_h}$. Influence of k_{add} and downsampling. 46
5.3 L_2 orthogonality error, $\|\mathbb{I} - \Phi^T \Omega_h \Phi\|_{\Omega_h}$. Influence of Gram-Schmidt and Helmholtz procedures. 47
5.4 Frobenius L_2 divergence error, $\|M_h \Phi\|^F_{\Omega_h}$. 48
5.5 Frobenius L_2 divergence error, $\|M_h \Phi\|^F_{\Omega_h}$. Influence of downsampling. 48
5.6 L_2 Divergence error $\|M_h \Phi_i\|_{\Omega_h}$ of individual modes. Full and downsampled sets, threshold 10^{-6} $M_{dom} = 100$, varying k_{add} 49
5.7 L_2 Divergence error $\|M_h \Phi_i\|_{\Omega_h}$ of individual modes. 49
5.8 L_2 Divergence error $\|M_h \Phi_i\|_{\Omega_h}$ of individual modes. Influence of Gram-Schmidt and Helmholtz procedures. Threshold 10^{-6}, $k_{add} = 100$, $M_{dom} = 100$ 50
5.9 L_2 mode-to-mode error $\|\Phi_{i,\text{cSVD}} - \Phi_{i,\text{iSVD}}\|_{\Omega_h}$. 51
5.10 L_2 mode-to-mode error $\|\Phi_{i,\text{cSVD}} - \Phi_{i,\text{iSVD}}\|_{\Omega_h}$. 51
5.11 L_2 mode-to-mode error $\|\Phi_{i,\text{cSVD}} - \Phi_{i,\text{iSVD}}\|_{\Omega_h}$ with $M_{dom} = 100$, $k_{add} = 100$, threshold 10^{-6}. Influence of GS and Helmholtz procedures. 52
5.12 Singular value decay, $M_{dom} = 100$, threshold 10^{-6}. 53
5.13 Singular value decay 53
5.14 L_2 orthogonality error, $\|\mathbb{I} - \Phi^T \Omega_h \Phi\|_{\Omega_h}$, for various distortions of the reference basis. 54
5.15 L_2 divergence and mode-to-mode errors , for various distortions of the reference basis. 54
5.16 Isosurfaces of Φ^u_1, $N_p = 150^3$ for various settings 55
5.17 Isosurfaces of Φ^u_2, $N_p = 150^3$ for various settings 55
5.18 Isosurfaces of Φ^u_8, $N_p = 150^3$ for various settings 55
5.19 Isosurfaces of Φ^u_1, $N_p = 250^3$ for FOMs with various end times, $t_{end} = 10, 15, 20$ 56
5.20 Isosurfaces of Φ^u_2, $N_p = 250^3$ for FOMs with various end times, $t_{end} = 10, 15, 20$ 56
5.21 Isosurfaces of Φ^u_8, $N_p = 250^3$ for FOMs with various end times, $t_{end} = 10, 15, 20$ 56
5.22 Isosurfaces of Φ^u_1,Φ^v_1 on grid $N_p = 250^3$ 57
5.23 Isosurfaces of Φ^u_2,Φ^u_{16} on grid $N_p = 250^3$ 57
5.24 Energy spectra of **mode 100**, threshold 10^{-6}, $M_{dom} = 100$, varying k_{add}. Full and 50% downsampled set of snasphots used. 58
5.25 Energy spectra of **mode 100** varying threshold, $k_{add} = 100$. Full set of snasphots used. 58
5.26 Energy spectra of **mode 100** threshold 10^{-6} , $k_{add} = 100$. GS and Helmholtz procedures applied. 59
5.27 Energy spectra of randomly distorted/rotated basis 59
5.28 Comparison of singular value decay. 60

6.1 L_2 velocity error: basis w/o treatment. 64
6.2 Total kinetic energy K and u-momentum temporal evolution, basis w/o treatment. 65
6.3 Error in total kinetic energy K and u-momentum, basis w/o treatment. 65
6.4 Divergence error $\|\nabla \cdot \boldsymbol{u}(t)\| \approx \|M_h V_h(t)\|_\infty$ in maximum norm. 65

6.5 L_2 velocity error. Full and downsampled snapshot sets used to obtain basis - comparison. 66
6.6 Total kinetic energy K and u-momentum. Full and downsampled snapshot sets used to obtain basis - comparison. 66
6.7 Divergence error $\|\nabla \cdot \boldsymbol{u}(t)\| \approx \|M_h V_h(t)\|_\infty$ in maximum norm. 67
6.8 Divergence error $\|\nabla \cdot \boldsymbol{u}(t)\| \approx \|M_h V_h(t)\|_\infty$ in maximum norm. 67
6.9 Velocity magnitude at $t = 5$: FOM and ROMs. Contours in xy plane. 68
6.10 Velocity magnitude at $t = 20$: FOM and ROMs. Contours in xy plane. 69
6.11 Instantaneous energy spectra of FOM and ROMs with $M = 8, 16, 32, 48$. 70
6.12 L_2 velocity error, cSVD-basis with 5% distortion 71
6.13 Error in kinetic energy (to FOM at time t): cSVD basis with 5,10% distortion 72
6.14 L_2 velocity error, cSVD-basis with 10% distortion 72
6.15 Error in u-momentum (to FOM IC) : cSVD basis with distortion. 73
6.16 Max divergence error $\|M_h V_h(t)\|_\infty$ temporal evolution: cSVD basis with 5- and 10% distortion . 73
6.17 Velocity magnitude at $t = 10$: ROM $M = 16$, $t_{end} = 10$, cSVD reference basis and distorted bases. Contours in xy-plane. 73
6.18 ROM trajectories for clean, distorted and rotated ROM. Variables in primary and rotated space. 74
6.19 L_2 velocity error, enforced momentum conservation. 74
6.20 L_2 velocity error, enforced momentum conservation and iSVD reference simulation. 75
6.21 Error in kinetic energy (to FOM at time t) temporal evolution, with and w/o enforced momentum conservation. 75
6.22 Error in u-momentum (to FOM IC) temporal evolution, with and w/o enforced momentum conservation. 76
6.23 Divergence error $\|M_h V_h(t)\|_\infty$ in maximum norm. 76
6.24 L_2 velocity error for $t_{end} = 10, 15, 20$ and fixed $M = 32$. 77
6.25 Error in total kinetic energy and momentum with $M = 32$ and $t_{end} = 10, 15, 20$. 77
6.26 Divergence error $\|M_h V_h(t)\|_\infty$. Comparison of $t_{end} = 10, 15, 20$ cases. 78
6.27 L_2 velocity error, time-extrapolated case. 78
6.28 Energy and error (to FOM at time t). Time-extrapolated cases. 79
6.29 Divergence error $\|M_h V_h(t)\|_\infty$ and u-momentum error (to FOM IC). Time-extrapolated cases. . 79
6.30 L_2 velocity error, $t_{end} = 10$. 80
6.31 Velocity magnitude at $t = 5$: FOM and ROM with $M = 8, 16, 32$, $t_{end} = 10$, . Contours in xy-plane. 80
6.32 Total kinetic energy k and error (to FOM at time t) temporal evolution: GS-orthogonalized and Helmholtz-decomposed basis. 81
6.33 u-momentum and error (to FOM IC) temporal evolution: GS orthogonalized and Helmholtz-decomposed basis. 81
6.34 $\|M_h V_h(t)\|_\infty$ temporal evolution 82
6.35 Spectra at three selected instants. On the first figure excessive accumulation of energy in FOM on highest resolved wave numbers is clearly noticable. 82

7.1 Coefficients of regression for $M = 8, 16, 32, 48$ and $t \in [0, 20]$ 85
7.2 Relative error for $M = 8, 16$ and $t \in [0, 20]$ in averaged terms. 86
7.3 Relative error for $M = 32, 48$ and $t \in [0, 20]$ in averaged terms. 87
7.4 Regressor and target function for $M = 8, 16, 32, 48$ at $t = 5$, with and without EV-POD 88
7.5 Regressor and target function for $M = 8, 16, 32, 48$ at $t = 20$, with and without EV-POD 89

A.1 Comparison of singular value decay for all tested cases: full range. 97
A.2 Shear layer. Fine grid. Velocity magnitude at $t = 10$: FOM and ROMs. Contours in xy plane. . . . 98
A.3 Shear Layer. Fine grid. Velocity magnitude at $t = 15$: FOM and ROMs. Contours in xy plane. . . 99
A.4 Talor-Green vortex. Fine grid. Velocity magnitude at $t = 10$: FOM and ROM with $M = 8, 16, 32$, $t_{end} = 10$, . Contours in xy-plane. 100
A.5 Eddy viscosity at $t = 5$ 101
A.6 Eddy viscosity at $t = 20$ 102
A.7 Absolute error for $M = 8, 16$ and $t \in [0, 20]$ in averaged terms. 103
A.8 Absolute error for $M = 32, 48$ and $t \in [0, 20]$ in averaged terms. 104
A.9 Relative error for $M = 8, 16$ and $t \in [0, 20]$ in global terms. 105
A.10 Relative error for $M = 32, 48$ and $t \in [0, 20]$ in global terms. 106

1

Introduction

Some define engineering as the art of negligence. If there is one feature that all engineering disciplines have in common, it is this. The surrounding reality is governed by inherently complex laws of physics. It cannot be entirely and accurately described, at least the state-of-the-art does not allow that as of yet. Consequently, the true art of engineering lies in the accurate choice of retained information.

In terms of physics involved, the present project concerns merely a small part of real phenomena: incompressible single-phase flows of Newtonian fluids. As it turns out, even this small piece is incredibly complex, to the point of eluding being understood by a single person. The underlying reason is the multi-scale phenomenon of turbulence.

Engineering by definition aims at solving practical problems. Usually this requires finding the right balance between the accuracy of results and time needed to obtain them. Most often there is no need to precisely describe the whole complexity of the involved physics, as long as the problem-relevant parts are considered. For example, the model required to solve the problem of finding instantaneous aerodynamic loads on an aircraft wing during take-off, would become computationally expensive, were it to include phenomena that occur on all scales. This would render such model useless in solving the problem online, i.e. during the maneuver. Similar examples of operations where fast computation constitutes an important factor may be easily imagined.

Extraction of features of physics that are relevant to a particular problem is one of the main ideas of model order reduction (MOR). In the fluid mechanics context, as will be described in section 1.1, a system of partial differential equations (PDE) governs the evolution of the flow. As discussed, a computational model, the full order model (FOM), is formed from the equations, that is typically of high dimensionality. A common way to reduce order of FOM is by projection onto lower-dimensional subspace. The resultant model is called projection reduced order model (projection ROM or simply ROM). Part of the information is lost in the process, which causes inaccuracies of such models. It so turns out that, when a particularly convenient subspace is selected, a special structural relation between the retained and truncated information emerges. This allows to draw some analogies with more conventional turbulence modeling techniques .

In the first part this thesis studies a particular method of finding subspaces. In the second part, the investigated method from previous part is applied in ROM simulation. The third part is focused on turbulence modeling aspects. The remainder of this chapter draws a brief background of MOR (section 1.1), research objective and questions are posed (section 1.2) and an overview of the further chapters (section 1.3) is given, once some initial notions are introduced.

1.1. Background

This section will present a broader background but will not discuss ROM literature and ROMs in detail. The following concepts and particular forms of the equations below will be expanded in further chapters. Incompressible flows of Newtonian fluids are most accurately described by Navier-Stokes (NS) equations, written in short as:

$$NS\left(\boldsymbol{u}, p\right) = 0, \tag{1.1}$$

where $\boldsymbol{u}(\boldsymbol{x}, t)$ is a time-dependent vector field defined on a regular domain $\Omega \subset \mathbb{R}^3$, $\boldsymbol{u} : \Omega \times [0, T] \to \mathbb{R}^3$ and p a scalar field, $p : \Omega \times [0, T] \to \mathbb{R}$ and NS is an operator defined on a function space. The full form will be given in latter chapters. It is a system of partial differential equations (PDE) for variables: $\boldsymbol{u}$ (velocity - 3 spatial time-dependent components) and p (pressure - 1 component). Laminar and turbulent flows, along with all possible intermittent states, are all described by the same system. To an extent, turbulence exhibits self-similar structure [25], which is to say that quantitatively similar phenomena appear on different scales. As Richardson explains it in his famous energy cascade hypothesis [28], large-scale vortices transfer their kinetic energy to progressively smaller scales. In this way, the majority of the small scale vortices are not interdependent, but all do depend on the larger scales of motion, which they drain energy from.

Since there exists no closed-form solution, a way is needed to enable approximation numerically. On the other hand, the PDE is defined at every point of continuous domain Ω and only a finite number of data points may be represented. Discretization of equations in space and time is thus necessary, so as to consider only a finite subset of the degrees of freedom (DoFs) of the continuous PDE. As Kolmogorov discovered, in every turbulent flow there exist smallest possible (finite) scales of motion. A model with resolution sufficient to capture those scales would provide an approximate solution conforming to the exact one. In the context of fluid mechanics, this could mean a considerable number of DoFs, enough to capture the smallest (Kolmogorov) scales of turbulent motion [25]. This brute-force method is called Direct Numerical Simulation (DNS).

The cost of DNS scales with at least Re^3, see [33] by various authors. This poses significant demands on computational power for high-Re flows typical of aerospace engineering. To circumvent this, researchers have attempted to approximate variables in NS equations with $\left(\overline{\boldsymbol{u}},\overline{p}\right)$, where the bars indicate scale separation operator [24], neglecting some information. With these variables, NS equations in general do not hold (notation and reasoning based on [37] by Wilcox) :

$$NS\left(\overline{\boldsymbol{u}},\overline{p}\right) \neq 0. \tag{1.2}$$

There exist two main strategies of obtaining $\left(\overline{\boldsymbol{u}},\overline{p}\right)$ and finding the term that would balance (non)-equality eq. (1.2): Reynolds-Averaged Navier-Stokes (RANS) and Large Eddy Simulation (LES). They both use the coarse-fine scale (or 'Reynolds-') decomposition:

$$\boldsymbol{u} = \overline{\boldsymbol{u}} + \boldsymbol{u}', \tag{1.3}$$

where $\overline{\boldsymbol{u}}$ is the part of the velocity field that is being resolved, so structures up to a certain wavenumber (or just ensemble-averaged in case of RANS). Inserting eq. (1.3) into NS operator and acting on it with the scale-separation operator yields:

$$\overline{NS\left(\overline{\boldsymbol{u}} + \boldsymbol{u}', \overline{p} + p'\right)} = 0.$$

Simplifying this reveals the shape of a so called *closure term* , leading to equality:

$$NS\left(\overline{\boldsymbol{u}},\overline{p}\right) + f\left(\overline{\boldsymbol{u}},\boldsymbol{u}',\overline{p},p'\right) = 0, \tag{1.4}$$

here denoted by f and required to balance eq. (1.2). In RANS the scale separation operator is an idempotent operator, $\overline{\overline{\boldsymbol{u}}} = \overline{\boldsymbol{u}}$, while in LES in general it is not idempotent, $\overline{\overline{\boldsymbol{u}}} \neq \overline{\boldsymbol{u}}$, (see [24] by Sagaut et al.). Rich, well-grounded literature is available on RANS ([37] by Wilcox, [18] by Leschziner).

Both of the popular approaches require a closure term to balance the equations, which is the task of a fine-scale model. Even though RANS is cheaper than LES and LES is cheaper than DNS, depending on a particular application of the CFD code (purposes of design, optimization, uncertainty quantification, requiring multiple runs), the need to save on computational cost persists.

Hence an idea of Model Order Reduction (MOR) emerged. First attempts of representing flow structures by means of a reduced basis (RB) are attributed to Aubry et al. [4], who have used Proper Orthogonal Decomposition (POD) to extract dominant structures from wall region in an incompressible wall-bounded flow. Although in the mentioned article no ROMs were constructed, the POD reduced basis that was considered is currently frequently used in one of the most popular ROM types, projection ROM:

$$\mathscr{P} NS\left(\overline{\boldsymbol{u}},\overline{p}\right) = \mathscr{P} g\left(\overline{\boldsymbol{u}},\boldsymbol{u}',\overline{p},p'\right). \tag{1.5}$$

Here, the bar denotes Galerkin truncation, $\mathscr{P}$ a Galerkin projection and the (projected) closure term g on the right-hand is not the same as the one from RANS or LES, unless FOM is RANS- or LES-based.

It is imperative that NS equations are discretized, though in the very general eq. (1.4)-(1.5) this is omitted, for the sake of giving an overview. In fact however, there have been ROM attempts, in which a continuous Full Order Model (FOM) equations have been used directly to construct ROM (albeit for Burgers Equation [30] by

San and Maulik). In more detailed terms, let $\{\boldsymbol{\varphi}_i(\boldsymbol{x})\}$, $i = 1, ...M$, be functions forming a basis in some function space $\mathbb{W} \subset (L_2(\Omega))^3$, used for approximation $\boldsymbol{u} \approx \overline{\boldsymbol{u}} = \sum_{i=1}^{M} a_j \boldsymbol{\varphi}_j$. If the same space is used for projection, then left hand side of eq. (1.5) is expressed as a collection of inner products (summation convention applied):

$$\left(\boldsymbol{\varphi}_i, NS\left(a_j \boldsymbol{\varphi}_j, \overline{p}\right)\right)_{L_2(\Omega)}, \tag{1.6}$$

where $a_j(t)$ are time-dependent coefficients and where similar expansions/projections in general need also be performed for $\overline{p}$. The aforementioned discretization may be applied to such equations at ROM or FOM level. The sequence, as will be explained in chapter 3, is of crucial importance.

The particular ROM/FOM framework used in the present research is non-linearly stable energy-conserving ROM (EC-ROM) developed by Sanderse in [31]. It uses POD to obtain $\{\Phi_i\} \in \mathbb{R}^N$, discrete counterpart of $\{\boldsymbol{\varphi}_i\}$, i.e. a certain basis. Semi-discrete FOM equations (and ODE system) are projected onto this basis. To achieve ROM energy-conservation, the author firstly uses a discrete FOM that has this property, which is achieved by retaining certain symmetries of the operators present in NS equations. Incidentally, one of those symmetries renders ROM velocity-only, but puts stringent conditions on the basis, namely that all Φ_i are divergence-free.

A brief view of what is missing in literature and what is to be improved now follows. Singular Value Decomposition (SVD) happens to be equivalent to performing POD on FOM solution (which is the technique used in EC-ROM to obtain ROM basis). Because in conventional version SVD requires input of the whole discrete FOM solution $\{V_h(t_1), ..., V_h(t_{N_t})\}$ into operational memory (in form of snapshots at various instants), it becomes imperative to approximate SVD when large data sets are considered. In EC-ROM papers published so far (e.g.[31] by Sanderse) only 2D flow cases are considered and conventional SVD (cSVD) suffices. Since true[1] turbulence only occurs in 3D and at high Reynolds numbers, the involved data sets inevitably become large (for DNS-based FOM). To alleviate this issue, an incremental algorithm of finding dominant singular subspaces (iSVD), developed by Baker in [5], will be merged into EC-ROM. To the knowledge of the author, the present thesis is the first time when EC-ROM (from [31]) is applied in 3D setting and also the first, in which iSVD is applied.

Even though EC-ROM is non-linearly stable, it might still be inaccurate due to truncation of some information in projection onto lower-dimensional subspace. This imbalance is expressed by right-hand side of eq. (1.5), i.e. a closure term. The closure term depends on unresolved scales. Therefore, in an attempt to improve accuracy, it could be modeled, s.t. $g\left(\overline{\boldsymbol{u}}, \boldsymbol{u}', \overline{p}, p'\right) \approx \overline{g}\left(\overline{\boldsymbol{u}}, \overline{p}\right)$. One of such modeling techniques, of eddy-viscosity (EV) type, will be investigated in an a priori test. In this technique, an additional diffusion term is introduced.

1.2. Research objective and questions

The first objective is to investigate the effects of applying approximate method of obtaining reduced basis (iSVD) on the accuracy of RB and ROM solution through error and spectral analysis. To achieve this, first INS2D-EC-ROM[2] implementation will be generalized to 3D. The present research will officially be the first application of INS3D-EC-ROM. Subsequently Baker's iSVD library [5] is to be incorporated into INS3D-EC-ROM). To the author's knowledge, so far Baker's incremental SVD had not been applied to compute POD-ROM basis in turbulent flow problems. RB obtained by means of iSVD will be tested before being used in ROM simulation. The test will examine properties of the basis that are essential for the main equations to hold (i.e. orthogonality, zero-divergence). It will also aim at establishing a source of possible deviations from these sought properties of RB, using conventional SVD basis as reference. Furthermore, in simulations, velocity error will be computed, along with energy spectrum. Iso-surfaces of modes will be presented. Global energy and momentum evolution in time will also be plotted. Aiming at obtaining turbulent state of the flow, ROM simulations will be performed mainly on a fine grid, where no reference SVD basis is available.

Additional tests include the following. It may be expected that iSVD will introduce errors or noise to RB. It is prudent to examine the susceptibility of INS3D-EC-ROM accuracy to distortions of basis. Therefore, regular POD basis will be randomly distorted and/or rotated to find the effects on basis quality (section 5.1.5) and ROM solution (section 6.2.1). Moreover, an additional EC-ROM capability: constrained SVD, invented by Sanderse in [31], will be tested in the new 3D setting. This technique yields enforced momentum conservation, which will be an object of a comparative test (section 6.2.2). Next, ROMs with bases from three different FOM integration periods will be compared (section 6.2.3). Finally, time extrapolation will be attempted to

---

[1] one to which energy cascade hypothesis refers

[2] ROM solver implemented by Sanderse in [31]

find out the behavior of velocity error and other quantities past FOM integration time (section 6.2.4). The second objective is to implement a mixing-length eddy viscosity (EV) closure model for ROM and perform an *a priori* analysis to verify the validity of the modeling. This is different than a ROM simulation with an added corrective term. Bases of different dimensions will be obtained via iSVD. FOM solution snapshots will be projected onto the respectable subspaces. Projected FOM solutions will be used to compute EV. An exact formula for discrete closure term will be derived (section 3.2.1). Finally, this term will be compared with the term of EV closure term (chapter 7). The latter will be fit by basic least squares regression. Error to actual FOM exact term will be measured and plotted. This is aimed at determining whether this paradigm of modeling is feasible at all in the present context. Additionally, precomputation of EV term will be attempted, whereby POD of EV will be used to achieve simplified form of the involved operator.

The following list contains research questions with references to corresponding chapters with results. The main questions correspond to chapters, however the sections do not necessarily reflect sub-questions. When a sub-question has no referred section, then the chapter/section of the main question is to be referred to. This is organized in such manner due to maintain balance between order and 'story line'. The research questions, with numbers of corresponding chapters with results, are the following:

1. Is it possible and to what extent, to use Baker's incremental SVD algorithm as an approximate, memory-efficient method of computing ROM basis? (chapter 5)
    (a) What influences the accuracy of basis computation and in what way?
    (b) How useful are Gram-Schmidt (GS) orthonormalization and Helmholtz decomposition as means of counteracting possible non-divergence-free or non-orthogonal output bases?
    (c) What is the effect of downsampling on the basis accuracy?
    (d) How susceptible is the 3D EC-ROM basis to distortions or rotations, in terms of basis quality?
2. How well does INS3D-EC-ROM code perform, in particular with iSVD-basis? (chapter 6)
    (a) What is the accuracy in terms of errors in velocity, energy, momentum and divergence? (chapter 6 throughout)
    (b) How do the ROM energy spectra compare to FOM? (section 6.1.3)
    (c) How susceptible is 3D EC-ROM solution to distortions or rotations of basis in terms of the mentioned errors? (section 6.2.1)
    (d) Is constrained SVD compatible with incremental algorithm? (section 6.2.2)
    (e) How does the model behave when different FOM integration times are applied to construct basis of the same dimension? (section 6.2.3)
    (f) How does the model behave when computed past FOM integration time? (section 6.2.4)
3. Is EV modeling of mixing length type an appropriate technique to model unresolved scale terms in the EC-ROM setting? (section 3.2, chapter 7)
    (a) What is the exact form of the discrete closure term, i.e. what exactly is missing in ROM? (section 3.2.1)
    (b) What are the errors of closure term w.r. to the exact closure term?
    (c) What is the behavior of regression coefficients for various dimensions of RB?
    (d) Is POD a viable choice for EV field approximation in this type of modeling?
    (e) Is precomputation of the EV diffusion operator in closure term possible?

RQ1 and RQ3 correspond to the first and second objective respectively. RQ2 has no corresponding self-standing objective, but it is closely related to the first objective. 3D capability of EC-ROM was enabled in the course of present research. RQ2 is merely a 'sanity check' of how the (approximate) basis performs in actual 3D-EC-ROM simulations.

1.3. Overview

The following will give an overview of each chapter.

A literature review with a brief introduction to MOR is contained in chapter 2. Firstly, basic notions and equations are stated to lay ground for the first glimpse of ROM literature in section 2.2 The concept of eddy viscosity ansatz will be presented in section 2.3. Reduced basis (RB) will be introduced in section 2.4, with particular focus on POD and SVD. The final section section 2.5 is a brief review of how the closure problem is tackled in literature, with pressure put on eddy-viscosity ROM closure.

In chapter 3 a thorough description of the proposed research is given. Details of EC-ROM are provided in section 3.1, where it shown how the ROM is conceived from PDEs by discretization and SVD. In section 3.2 the exact closure term is derived, eddy viscosity ansatz is proposed along with a precomputation procedure of closure term. Finally, section 3.3 focuses on error measures, that will be used in the later chapters to quantify errors in reduced basis and in ROM solution. In section 3.4 definitions of miscellaneous investigated quantities are given.

Chapter 4 outlines the setup of numerical experiments that are performed in the research. Section 4.4 presents the software used and discusses some settings of the runs. Section 4.1 describes the two test cases used: periodic shear layer and Taylor-Green vortex. Section 4.3 is an attempt to assess the stability of the used discretization and time march combination. An estimate of Courant and Peclet numbers for either test case is made. This allows to assess whether the method is operating within the limits of its stability region.

Reduced bases are analyzed in chapter 5. The quality of basis is investigated in section 5.1 in terms of orthogonality, zero-divergence, fidelity to conventional SVD and SV decay. Iso-surfaces of selected components of several modes are examined in section 5.2 for either test case (SL and TG). Spectra of individual modes are compared section 5.3. The singular value spectrum for selected test cases is presented and discussed in section 5.4. Practical conclusions of iSVD investigations for further chapters are summarized in section 5.5.

ROM simulation results are reported in chapter 6. The main shear layer results are discussed in section 6.1, while section 6.2 contains additional shear layer results. Finally Taylor-Green vortex results are presented in section 6.3.

The capstone of the thesis lies in chapter 7. There, an a priori analysis of turbulence modeling is performed, which includes computation of eddy viscosity, finding a least squares fit of the model constant and computation of error w.r. to exact closure term derived in an earlier chapter.

The thesis is finalized with chapter 8, where answers to research questions are provided, conclusions are made and recommendations for future research proposed.

2

Literature Review and ROM preliminaries

The purpose of this chapter is to lay out the basics of MOR. Governing equations and some basic notions are first introduced. This is followed by a general review of related literature. Further part of the review is focused on reduced basis and closure modeling.

2.1. Basic notions and equations

As a more detailed, but still introductory step, since all the discussed (and present) research concerns incompressible flows, it makes sense to invoke the full form of the governing PDE system. This will be followed by a general explanation of how to obtain projection ROM. By first writing discretized PDE with RB-approximation of variables and then projecting the equations onto reduced basis, ROM is obtained. The details of RB will later become relevant.

Let $\left(\boldsymbol{u}, p\right)$ be time- and space-dependent vector and scalar fields on the domain $\Omega \subset \mathbb{R}^3$. Let $L_2\left(\Omega\right)$ denote the space of square-integrable functions on Ω. Let the scalar product of two elements $\boldsymbol{u}, \boldsymbol{v} \in L_2\left(\Omega\right)$ be defined by $\left(\boldsymbol{u}, \boldsymbol{v}\right)_\Omega := \int_\Omega \boldsymbol{u} \cdot \boldsymbol{v} d\Omega$, i.e. standard (real) Hilbert space inner product is used. The Navier-Stokes equations read:

$$\nabla \cdot \boldsymbol{u} = 0 \quad \text{in } \Omega, \tag{2.1}$$

$$\frac{\partial \boldsymbol{u}}{\partial t} + \nabla \cdot \left(\boldsymbol{u} \otimes \boldsymbol{u}\right) = -\nabla p + \nabla \cdot \nu \left(\nabla \boldsymbol{u} + \left(\nabla \boldsymbol{u}\right)^T\right) \quad \text{in } \Omega, \tag{2.2}$$

and are to be appended with proper boundary and initial conditions:

$$B\left(\boldsymbol{u}, \nabla \boldsymbol{u}, p, \nabla p\right) = 0 \quad \text{on } \partial\Omega, \tag{2.3}$$

$$\boldsymbol{u}\left(0, \boldsymbol{x}\right) = \boldsymbol{u}_0\left(\boldsymbol{x}\right) \quad \text{in } \Omega. \tag{2.4}$$

Equation 2.1 expresses mass conservation. Linear momentum balance is represented by eq. (2.2). Let $V_h\left(t\right) \in \mathbb{R}^{N_V}, p_h\left(t\right) \in \mathbb{R}^{N_p}$ denote spatially discretized velocity and pressure fields, where N_V is the number of velocity DoFs and N_p is the number of pressure DoFs. Details of discretization will later become relevant, the present considerations are valid for finite volume (FV) method. However, the ROM equation, that will now be derived, is very similar to ones obtained via finite element (FE) method, e.g. in [39] by Xie et al. Also, in the present case, only periodic boundary conditions will be considered from now on. This is to keep considerations simple because the present research is also focused on other aspects of MOR. Discretized NS equations may be written:

$$M_h V_h = 0, \tag{2.5}$$

$$\Omega_h \dot{V}_h = \underbrace{-G_h p_h - C_h\left(V_h\right) V_h + \nu D_h V_h}_{F_h\left(V_h, p_h\right)}. \tag{2.6}$$

These equations comprise an ODE system for V_h, p_h. Since FV method is applied, the variables appear as cell-integrated values, with $\int_{\Omega_i} \boldsymbol{u} d\Omega \approx [\Omega_h V_h]_i$, where $\Omega_h \in \mathbb{R}^{N_V \times N_V}$ is a diagonal matrix with volumes of V_h-cells and Ω_i is the volume of i-th cell. On the right-hand side of eq. (2.6) no Ω_h term appears, because the integration is encoded in the operators C_h, D_h, G_h (discrete counterparts of convective, diffusive and gradient operators respectively).

Now if an expansion of those variables in a certain basis is considered, e.g. $V_h \approx \sum_{i=1}^{M} a_i(t)\Phi_i$, with $a_i \in \mathbb{R}, \Phi_i \in \mathbb{R}^{N_V}$ the coefficients of this expansion may be found. A discrete scalar product needs to be defined first. FV method is best accommodated with a product that is weighted with the positive-definite matrix Ω_h: $(U_h, W_h)_{\Omega_h} := V_h^T \Omega_h U_h$ for $U_h, W_h \in R^{N_V}$. By solving the following system, expansion coefficients are found, finalizing the widely known Galerkin procedure:

$$\Phi^T \Omega_h \Phi \dot{a} = \Phi^T F_h\left(\Phi a, p_h\right), \tag{2.7}$$

where $\Phi \in \mathbb{R}^{N_V \times M}$ is a matrix whose M columns are collected Φ_i basis vectors. In some circumstances, when pressure-velocity compatibility condition is respected by FOM and basis vectors are discretely divergence-free ($M_h \Phi_i = 0$ for $i = 1, \ldots M$), the pressure term cancels. Further, some rearrangements allow to write projected convective operator as a third order tensor and when the basis Φ is orthogonal, i.e. $\Phi^T \Omega \Phi = \mathbb{I}_M$, eq. (2.7) becomes velocity-only:

$$\dot{a} = a^T B a + A a, \tag{2.8}$$

where $A \in \mathbb{R}^{M \times M}, B \in \mathbb{R}^{M \times M \times M}$ are diffusive and convective ROM operators. The gain in computational efficiency is immediately noticeable, as the number of equations reduces from $N_V + N_p$ (sum of velocity and pressure DoFs) to M.

2.2. ROM literature overview

Model Order Reduction (MOR) is a field of intensive research globally, combining many disciplines. For the sake of conciseness the considerations will be limited to projection-ROMs, i.e. where ROM operators are obtained by projecting FOM operators onto a certain subspace with a certain basis called Reduced Basis (RB).

Historically, one of the earliest papers on RB applied in incompressible flow computations was the paper by Peterson [23]. As mentioned, POD-RB was earlier used by Aubry et al. [4], but only to describe the flow in a particular part of the domain. In [23] full solutions to NS equations are being approximated.

Before POD was an RB technique, it was used [1] by statisticians in the early 20th century, as described by Quarteroni et al. [27]. The mathematical foundations can be traced back to the beginning of 20th century.

As described in [11] by Fick et al., there are essentially two main types of ROM problems: reproduction and parametric problem. In either case, FOM solution is required, $\left\{V_h\left(t^i, \mu\right)\right\}_{i=1}^{N_t}$ which is conceived as a set of N_t snapshots. These are obtained for a single parameter vector $\mu \in \mathbb{R}^p$, where p is the number of parameters in the analysis. Snapshots are samples of solutions at time instants $\left\{t^i\right\}_{i=1}^{N_t}$, $0 \le t_i \le t_{end}$. Solution reproduction problem is to find a reduced order solution that approximates FOM solution (for a single μ) at all t_i. This requires construction of a reduced basis $\{\Phi_i\}$. An implicit assumption here is that FOM evolves within or in a sense close to the subspace spanned by the basis vectors. It is to say that $V_h(t) \approx \sum_{i=1}^{M} \Phi_i a_i(t)$, as mentioned in the introduction to this chapter. There are two kinds of reproduction in the solution reproduction problem. One is that in which the FOM solution data is simply compressed by projection onto RB. The other is actually solving a new ODE system in the reduced space (ROM simulation), derived from projection of FOM equation terms. Both kinds of solution reproduction will be investigated in this study. Parametric problem comprises finding approximation to FOM solution for any parameter μ value in a certain range. The parameter values may in general vary in range different from the training data. The scope of the present thesis is limited to the former: solution reproduction problem, which is also crucial in parametric analysis.

Projection Galerkin-POD-ROMs for turbulent flows based on L_2 inner product notoriously suffer from stability issues (see e.g. [36] by Wells et al.) connected to the convective character of the flow, whereby spurious oscillations occur. It is widely believed that the underlying reasons are similar to the case of RANS/LES: insufficient dissipation of turbulent kinetic energy (TKE) of fine scales present in the model. Fick et al. in [11] provide a wide overview of strategies applied to stabilize ROM, which include: using different scalar products, enriching POD basis, using Dynamic Mode Decomposition (DMD) to compute the basis, and finally providing dissipation via a closure term. The last approach will be investigated in the present project.

---

[1] In other fields POD is called Karhunen–Loève expansion or Principle Component Analysis (PCA)

All of these aim at overcoming stability issues, which is necessary for accuracy but in general does not guarantee it. As will be further explained, the code INS3D-EC-ROM (a 3D version of INS2D-EC-ROM by Sanderse [31]) used in the present thesis is by construct non-linearly stable, in the sense that there exists an upper bound on kinetic energy. This guarantees that $L_2(\Omega)$-norm of the solution is bounded at all times, but not that the solution conforms to that of FOM.

2.2.1. Mathematical perspective

The purpose of this section is to outline some fundamental aspects of MOR, and to relate the present and existing research to those fundamentals.

There are several perspectives to look at ROM. Works of Benner et al. [7] or Lasilla et al. [26] are examples of papers focused entirely on mathematics of MOR. Such context is needed to solve the more general parametric problem. In those articles the physical aspects of numerical modeling are rarely mentioned. The complexity of parametric problem necessitates the choice of more primitive RB construction procedure via so called greedy algorithms, rather than POD. Although parametric problem is outside the scope of the current study, the above publications also put ROM in a broader context of dynamical systems and applied functional analysis. The authors discuss constructing basis more generally, applying Petrov-Galerkin method. In the present context however, only (Bubnov-)Galerkin projection is considered, i.e. the FOM solution is expanded in a set of functions and the same set serves as basis to project onto. Strictly speaking, if the FOM approximation V_h evolves in time in an N-dimensional manifold, then ROM approximation V_r (or rather the reconstructed solution) evolves in an M-dimensional *submanifold.* Quarteroni in [27] writes that the approximation is accurate when the two manifolds lie in a sense close together.

As formulated by e.g. Grimberg in [13], the problem of MOR in turbulent flows lies in Kolmogorov n-width of the FOM manifold, which is large and slowly-decaying. This results in there being a high number of modes required to accurately capture the dynamics of FOM. Due to already existing nomenclature, in the present section n is identified with M. Kolmogorov n-width, in [27] denoted by $d_n(\cdot,\cdot)$, determines limits of accuracy of projection-based approximation. It is a meaningful quantity, as it takes into account all possible n-dimensional approximation spaces and all possible functions to be represented in those spaces. It is essentially a *particular* distance between the solution and its possible approximation for a given dimensionality n.

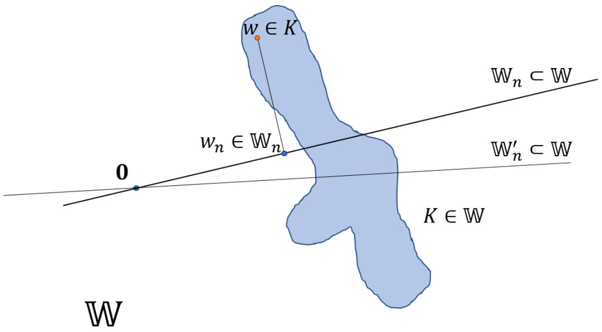

Figure 2.1: Kolmogorov n-width, orientation of subspace $\mathbb{W}_n$ w.r.t. to K

It is useful to refer to the definition, as given by Quarteroni [27]. Let $\mathbb{W}$ denote a Hilbert space and K a set within the space. Let $\mathbb{W}_n$ be an n-dimensional linear subspace of $\mathbb{W}$. The quantity

$$d_n(K;\mathbb{W}) = \inf_{\mathbb{W}_n \subset \mathbb{W}} \sup_{w \in K} \inf_{w_n \in \mathbb{W}_n} \|w - w_n\|_{\mathbb{W}}, \tag{2.9}$$

is called Kolmogorov n-width. Note that since $\mathbb{W}_n$ is not allowed to be an *affine* subspace (only linear), it may be more complicated to find a plausible approximation space, as the offset influences the inf and sup in eq. (2.9), see fig. 2.1. In this situation the generated linear subspace, even of arbitrarily high dimension might not lie close to the actual solution space. This arises when K does not contain the zero-element. In several articles, when snapshot-based POD is concerned, e.g. [38] by Xie et al.,[30] by San and Maulik, a *centering trajectory,* $\underline{V_h} = \frac{1}{N_t}\sum_{i=1}^{N_t} V_h(t_i)$, is first subtracted from all snapshots (solution field instants), to eliminate the offset.

Kolmogorov length decays slowly with n in convection-dominated problems (see e.g. [11] by Fick et al.), so that in general a high dimensionality of basis is required to solve long-term turbulent flow integration accurately. This shows that ROM accuracy is a fundamental mathematical problem of dimensionality of solution set (see section 5.4 of [27]). Many authors from the projection-ROM field (e.g.Lasilla et al. [26]) observed that ROMs tend to deviate from FOM trajectory, especially past the FOM integration time. The well known problem of time-extrapolation is not directly connected to the property of slowly decaying d_n. It is the result of using a particular type of basis, which captures dynamics of the system only within the time period where high-fidelity data is available.

The core message is that in convection-dominated problems dimensionality of the solution set is high, which inevitably leads to either large computational burden or inaccuracy, and that framework outlined here is limited to approximations of known spaces. Therefore time extrapolation is bound to fail when no additional information about the solution set is taken into account, e.g. through physics-informed corrections.

2.2.2. Phenomenological perspective

One could say that turbulent flow is not really random, only chaotic in a deterministic sense. That is, the underlying dynamical system is sensitive to small perturbations in initial and boundary conditions. There is also empirical evidence confirming that turbulence is not random: there exist spatial correlations of flow variables. The solution varies erratically with IC and BC, always remaining deterministic for a particular IC and BC. This happens due to non-linearity of convective term in NS equations. Examining the term in detail, as done in e.g. [25] by Pope, reveals that in turbulent flows there may appear interactions between scales from different ranges.

Typically, at high Reynolds number, the number of DoFs is very high, rendering DNS unsuitable. In classical approaches to limiting this complexity, RANS and LES, there appears a fundamental problem of *closure.* In eq. (1.4) there is an unknown term $f\left(\overline{\boldsymbol{u}}, \boldsymbol{u}', \overline{p}, p'\right)$, which requires modeling. Derivations may be found in classic textbooks, e.g. by Pope [25], Wilcox [37] or Sagaut [29]. The reasoning is based on energy cascade hypothesis, see fig. 2.2.

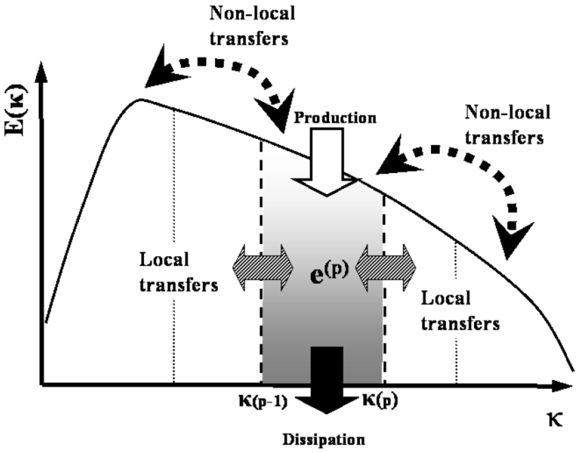

Figure 2.2: Energy cascade [24]. Here: κ-wavenumber, $E(\kappa)$-energy density spectrum

In essence, kinetic energy is carried mostly by large scales of motion. Most of energy dissipation occurs on fine scales. There exists an intermediate range, according to famous Kolmogorov hypotheses [17], exhibiting universal characteristics. Within this range energy is mostly being transferred from coarser to finer scales at an approximately constant rate (w.r. to wavenumber). Truncation of fine scales could potentially lead to a situation where energy is transferred from universal, inertial range, but is not destroyed in the viscous range. Instead, it piles up right below the cut-off wavenumber. This in turn could lead to instabilities and/or inaccuracy. This reasoning, according to Couplet et al. [10], is valid in the POD setting, as later explained.

As shown e.g. in [39], projection onto POD basis in ROM is filtering. It is therefore widely believed that there is analogy to LES, i.e. that truncation of higher modes is bound to destabilize the solution. Grimberg et al. however, in a recent paper [13] notice that supporters of the physics-argued explanation do not consider numerical aspects of Galerkin projection framework, focusing only on Reduced Basis (RB) resolution. The authors successfully apply a Petrov-Galerkin framework to stabilize the ROMs. This challenges the popular claims that the absence of fine scales is the sole cause of instability.

The problem of instability of numerical schemes is frequently tackled through adding artificial dissipation thus changing the eigenvalue spectrum of the underlying ODE system, as described e.g. in [15]. This is not exactly the same as adding eddy viscosity, which is derived through physics-based reasoning (assumption of proportionality between Reynolds stress tensor and deviator of mean shear strain, see next section). In section 3.2, a derivation of the exact shape of discrete closure term is presented.

2.3. Eddy viscosity ansatz

The concept of turbulent (eddy) viscosity, originally invented by Boussinesq, lies close to the foundation of RANS methodology (see e.g. [37] by Wilcox or [33] by various authors). Maybe the most helpful explanation, with listed limitations of models of this kind was given by Leschziner in [18]. Hence it is along the lines of this textbook, that EV concept will be presented. In Reynolds decomposition $\boldsymbol{u} = \overline{\boldsymbol{u}} + \boldsymbol{u}'$ the bar denotes ensemble averaging operator:

$$\overline{\boldsymbol{u}}(\boldsymbol{x}, t) = \lim_{N\to\infty} \frac{1}{N} \sum_{i=1}^{N} \boldsymbol{u}_i(\boldsymbol{x}, t),$$

where $\boldsymbol{u}_i$ are realizations of the process. Inserting Reynolds decomposition into eq. (2.2) and applying averaging to the entire equation yields Reynolds-Averaged Navier-Stokes (RANS) equations:

$$\nabla \cdot \overline{\boldsymbol{u}} = 0 \quad \text{in } \Omega, \tag{2.10}$$

$$\frac{\partial \overline{\boldsymbol{u}}}{\partial t} + \overline{\boldsymbol{u}} \cdot \nabla \overline{\boldsymbol{u}} + \overline{\boldsymbol{u}' \cdot \nabla \boldsymbol{u}'} = -\nabla p + \nu \Delta \overline{\boldsymbol{u}} \quad \text{in } \Omega, \tag{2.11}$$

where mass conservation of fine scales $\nabla \cdot \boldsymbol{u}' = 0$, and some basic properties of Reynolds averaging were used to simplify multiple terms (see e.g.[37] by Wilcox for details).

Equations (2.1)-(2.2) for variables $\{\boldsymbol{u}, p\}$ are identical in form with equations (2.10)-(2.11) for variables $\{\overline{\boldsymbol{u}}, \overline{p}\}$ except for the term $\overline{\boldsymbol{u}' \cdot \nabla \boldsymbol{u}'}$. The term represents a *Reynolds stress tensor* (RST), which is a surplus unknown. Therefore the problem of closure arises.

As Leschziner (see [18]) recalls, Boussinesq in 19th century argued that action turbulence is the same as action of viscous diffusion on the micro-level, i.e. transverse transmission of longitudinal momentum. Simplification of this hypothesis lies in the assumption, that turbulence has no spatial coherence, as is the case for viscous diffusion.

Mass conservation of fine scales permits rewriting RST as $\overline{\boldsymbol{u}' \cdot \nabla \boldsymbol{u}'} = \nabla \cdot \overline{\left(\boldsymbol{u}' \otimes \boldsymbol{u}'\right)}$. Writing diffusion term as $\nu \Delta \overline{\boldsymbol{u}} = \nabla \cdot \left(\nu \left(\nabla \overline{\boldsymbol{u}} + \left(\nabla \overline{\boldsymbol{u}}\right)^T\right)\right)$ enables to include (by linearity of divergence operator) to write diffusion under common $\nabla\cdot$ with RST moved from the left side of eq. (2.11) and state the approximation as:

$$\nabla \cdot \left(\nu \left(\nabla \overline{\boldsymbol{u}} + \left(\nabla \overline{\boldsymbol{u}}\right)^T\right) - \overline{\boldsymbol{u}' \otimes \boldsymbol{u}'}\right) \approx \nabla \cdot \left((\nu + \nu_t) \nabla \overline{\boldsymbol{u}}\right). \tag{2.12}$$

So in fact RST is approximated as:

$$-\overline{\boldsymbol{u}' \otimes \boldsymbol{u}'} \approx \nu_t \left(\nabla \overline{\boldsymbol{u}} + \left(\nabla \overline{\boldsymbol{u}}\right)^T\right). \tag{2.13}$$

Eddy viscosity in general is a function of $\overline{\boldsymbol{u}}$ - the mean field: $\nu_t = \nu_t\left(\overline{\boldsymbol{u}}(\boldsymbol{x}, t)\right)$. Upon inspection of eq. (2.12), it can be clearly noticed, that an unknown 6-component tensor $-\overline{\boldsymbol{u}' \otimes \boldsymbol{u}'}$ is being substituted with a product of an unknown *scalar* field (ν_t) and a known[2] 6-component tensor $\left(\nabla \overline{\boldsymbol{u}} + \left(\nabla \overline{\boldsymbol{u}}\right)^T\right)$. This substitution essentially introduces an approximation on the level of complexity of continuous operators. Namely, following Leschziner [18], a single scalar field cannot possibly be selected such that the approximation eq. (2.12) is accurate for all components of RST simultaneously in general case. The tensor $\left(\nabla \overline{\boldsymbol{u}} + \left(\nabla \overline{\boldsymbol{u}}\right)^T\right)$ is sometimes written $\nabla^s \overline{\boldsymbol{u}}$ with ∇^s denoting symmetrical gradient.

Boussinesq hypothesis in its primordial form requires a correction to account for non-zero turbulent stress states in the absence of mean straining, a situation which may frequently occur in real-life situations. By making the following modification to eq. (2.13) an augmented version of the hypothesis is obtained:

$$-\overline{\boldsymbol{u}' \otimes \boldsymbol{u}'} \approx \nu_t \left(\nabla \overline{\boldsymbol{u}} + \left(\nabla \overline{\boldsymbol{u}}\right)^T\right) - \frac{2}{3} \boldsymbol{I} k, \tag{2.14}$$

---

[2] The tensor is mean strain rate tensor and it is only known so long as the equations for mean flow are solved

where $\boldsymbol{I}$ is an identity element in the space of tensors to which RST belongs and $k = \frac{1}{2}\left({u'_1}^2 + {u'_2}^2 + {u'_3}^2\right)$ is the turbulence kinetic energy, defined as half the trace of RST. One might say (see e.g. [33]), that instead of RST, the traceless part of RST is modeled now.

EV modeling has clear advantages of conceptual and simplicity and fairly low computational cost. However, they are also known to exhibit the following shortcomings:

1. Fail to compute normal stress in shear flow etc.
2. May produce unphysical, negative normal stresses in strong shear strain
3. Returns state of normal stress anisotropy in pure shear strain

2.4. Reduced basis

In this section the POD reduced basis concept are outlined. After some basic notions are introduced (section 2.4.1), five methods of obtaining basis reduction are briefly presented (section 2.4.2). Two of them (cSVD and iSVD) are given more attention (section 2.4.3-section 2.4.4), since those methods are used in this thesis.

2.4.1. Basic notions

Let Ω_h be an positive-definite matrix, that induces a scalar product $(\cdot,\cdot)_{\Omega_h}$ in $\mathbb{R}^N$:

$$(V,W)_{\Omega_h} := V^T \Omega_h W, \tag{2.15}$$

and thus a norm $\|\cdot\|_{\Omega_h}$:

$$\|V\|_{\Omega_h} := \sqrt{(V,V)_{\Omega_h}}. \tag{2.16}$$

In the further part of the thesis Ω_h is not only positive-definite, but also diagonal. Let $\{\Phi_i\}$ be a system of M orthogonal vectors, where $\Phi_i \in \mathbb{R}^N$. Orthogonality condition reads $\Phi^T \Omega_h \Phi = \mathbb{I}_M$. The vectors form a basis of an M-dimensional subspace of $\mathbb{R}^N$.

Let $u \in \mathbb{R}^N$ and $a \in \mathbb{R}^M$. An orthogonal projection of u onto span(Φ) (the linear subspace spanned by all the Φ_i) is the solution to the minimization problem:

$$\min_{a\in\mathbb{R}^M} f(a) = \frac{1}{2}\left\| u - \Phi a \right\|^2_{\Omega_h}, \tag{2.17}$$

i.e. find coefficients of linear combination of vectors Φ_i such that it lies as close as possible (in the $\|\cdot\|_{\Omega_h}$-norm) to the original vector u. The factor $\frac{1}{2}$ is to simplify computations, while the squared norm is used to cast the problem into convex differentiable form. For such a problem, a^* is the solution if and only if $\nabla f(a^*) = 0$. Writing $f(a)$ as:

$$f(a) = \frac{1}{2}(u - \Phi a)^T \Omega_h (u - \Phi a), \tag{2.18}$$

allows to write:

$$\nabla f\left(a^*\right) = \Phi^T \Omega_h \Phi a^* - \Phi^T \Omega_h u = 0, \tag{2.19}$$

where Ω_h-induced scalar product was used. The (only) solution is:

$$a^* = \Phi^T \Omega_h u. \tag{2.20}$$

Hence the projection of u onto span(Φ) is:

$$\mathscr{P}_{\text{span}\Phi}(u) = \Phi\Phi^T \Omega_h u. \tag{2.21}$$

2.4.2. Proper Orthogonal Decomposition

The textbook by Quarteroni et al. [27] or the paper by Sanderse [31] discuss what follows in more detail.

POD aims at finding dominant structures in a data set. The set may be of any kind, as long as it can be cast into a matrix form. The problem is that of finding an orthonormal basis $\Phi \in \mathbb{R}^{N\times M}$, such that the snapshots (columns) can be well approximated with combinations of these basis vectors. In other words, that the distance between snapshots and their projections onto the space spanned by POD modes must be minimized in a certain norm. The problem is formulated as:

$$\Phi = \arg \min_{\Phi \in \mathbb{R}^{N\times M}} \left\| X - \Phi\Phi^T \Omega_h X \right\|_F \quad \text{under constraint:} \quad \Phi^T \Omega \Phi = \mathbb{I}_M, \tag{2.22}$$

where X is the matrix of snapshots $X := \left[X_1, ..., X_{N_t}\right]$ and $\|\cdot\|_F$ stands for Frobenius norm, which for an $N \times M$ matrix A with entries a_{ij} is $\|A\|_F = \sqrt{\sum_{i=1}^N \sum_{j=1}^M |a_{ij}|^2}$. Using this particular norm means that Φ is sought, such that it minimizes the difference between snapshots and their projections *globally*, i.e. for *all* the snapshots. In comparison to Fourier modes, which are of fixed form, the POD basis is dependent on the data set (snapshots). An important observation may be made at this point, also following [7] by Benner et al. or [27] by Quarteroni et al., that Φ is built based on available snapshots. Hence problems may arise when the actual flow solution exemplifies structures that are not available in the snapshots used to construct reduced basis - when time extrapolation is attempted. As succinctly formulated in [7]: *If it's not in the snapshots, it's not in the ROM.*

The problem eq. (2.22) may be cast into a simpler form:

$$\hat{\Phi} = \arg \min_{\hat{\Phi} \in \mathbb{R}^{N\times M}} \left\| \hat{X} - \hat{\Phi}\hat{\Phi}^T \hat{X} \right\|_F \quad \text{under constraint:} \quad \hat{\Phi}^T \hat{\Phi} = \mathbb{I}_M, \tag{2.23}$$

where $\hat{X} = \Omega_h^{\frac{1}{2}} X$, which requires only minor treatment of the snapshots. The Frobenius norm in the two problems is not the same, in the former it is in fact a weighted Frobenius norm, i.e. $\|A\|_{F,\Omega_h} = \sqrt{\sum_{i=1}^N \sum_{j=1}^M \omega_i |a_{ij}|^2}$. Note that $\|\Omega_h^{\frac{1}{2}} A\|_F^2 = \sum_{i=1}^N \sum_{j=1}^M \left(\omega_i^{\frac{1}{2}} a_{ij}\right)^2 = \sum_{i=1}^N \omega_i^{\frac{1}{2}} \sum_{j=1}^M \left(a_{ij}\right)^2 = \|A\|_{F,\Omega_h}^2$. The relation between the solutions to eq. (2.22) and eq. (2.23) is $\Phi = \Omega_h^{-\frac{1}{2}} \hat{\Phi}$. Clearly $\Omega_h^{\frac{1}{2}}$ and $\Omega_h^{-\frac{1}{2}}$ are positive definite when Ω_h is positive definite.

Furthermore, from eq. (2.23) or its weighted version, it is not obvious that for bases with M_1, M_2 elements, where $M_1 < M_2$ the first M_1 vectors of both bases are the same. This is a feature of POD and it is implied by the Schmidt-Eckart-Young theorem (see e.g. [27] by Quarteroni et al.).

The following methods of obtaining Φ, related to the present research, will be briefly described:

1. Direct method: solution of eq. (2.23). This necessitates high-dimensional optimization with equality constraints. Typically this is very expensive. Obtaining RB for a high-dimensional solution in this way is inefficient in the present context of turbulent flows.

2. Singular value decomposition (SVD, see [27] by Quarteroni): finding a special decomposition of snapshot matrix $X = \Phi\Sigma\Psi$ (to be described in section 2.4.3) in which one of the resultant matrices comprises the basis vectors as columns. In principle the method provides an accurate POD basis. However, it is not well suited for high $N \times N_t$, such as are typical in turbulent flows.

3. Method of snapshots (MoS, see [32] by Sirovich): finding right-singular vectors Ψ of SVD by solving a cheaper eigenvalue problem $X^T X \Psi = \Psi \Sigma^T \Sigma$, which is obtained with the use of Moore-Penrose inverse $\Sigma^\dagger$. It is suitable only for $N_t \ll N$. In the present case where N_t is of the order 10^3, it would require solution of a large eigenvalue problem and access to all the snapshots at once. Hence MoS is not used, although there is an additional insight that the framework of the method provides. Namely, that POD modes Φ_i are all linear combinations of snapshots X_i. To summarize, the method is cheap but requires $N_t \ll N$ and N_t small.

4. By solving an eigenvalue problem with snapshot-correlation matrix XX^T (see e.g. [16] by Holmes et al.) : similar to MoS in that there is also an eigenvalue problem to be solved. Here the solution directly yields Φ, but the size of the problem matrix is as high as $N \times N$. This is an even larger eigenvalue problem than in MoS and additionally it is a dense matrix typically. This renders the method impractical for most applications in turbulent flows, although Baker in [5] mentions that an iterative eigensolver could be used to compute the largest eigenvalues of interest without the need to compute the full spectrum of XX^T.

5. Low-rank approximation of SVD: using an algorithm that approximates singular value decomposition up to a specified number of singular values (and vectors). The advantage is that it is memory-efficient. The drawback is the error w.r. to classical SVD, whose behaviour is not well known. A particular algorithm (Baker's iSVD from [5]) will be discussed in section 2.4.4.

2.4.3. Singular Value Decomposition

Considering eq. (2.22) and eq. (2.23), mostly Ω_h-weighted norm (and the related orthogonality condition) will be used, as it better suits the finite volume method used in INS3D code. For simplicity however, the hat sign will be omitted, unless confusion could arise. It must be kept in mind that it is actually the *weighted* problem that is being solved though. Thus whenever Φ is obtained it must be scaled by $\Omega_h^{-\frac{1}{2}}$, as it was explained in section 2.4.2.

As shown by Quarteroni et al. in [27], the solution of the problem eq. (2.23) for $M = N$ (best possible RB) is equivalent to obtaining the left-singular vectors of the SVD of the (real) snapshot matrix $X \in \mathbb{R}^{N \times N_t}$:

$$X = \Phi \Sigma \Psi^T, \tag{2.24}$$

where columns of $\Phi \in \mathbb{R}^{N \times N}$ are the left-singular vectors, $\Sigma \in \mathbb{R}^{N \times N_t}$ is a rectangular diagonal matrix and $\Psi \in \mathbb{R}^{N_t \times N_t}$ are the right singular vectors. Both Φ and Ψ are orthogonal matrices.

The full form SVD, in case $N > N_t$, reads:

$$X = \begin{bmatrix} \Phi_1 & \cdots & \Phi_N \end{bmatrix} \begin{bmatrix} \sigma_1 & 0 & \cdots & 0 \\ 0 & \sigma_2 & \cdots & 0 \\ \vdots & \vdots & \ddots & \vdots \\ 0 & 0 & \cdots & \sigma_{N_t} \\ \vdots & \vdots & \vdots & \vdots \\ 0 & 0 & \cdots & 0 \end{bmatrix} \begin{bmatrix} \Psi_1^T \\ \Psi_2^T \\ \vdots \\ \Psi_{N_t}^T \end{bmatrix}, \tag{2.25}$$

where $\sigma_1 \geq \sigma_2 \geq ... \geq \sigma_{N_t} \geq 0$. Any real matrix may be decomposed in this fashion (see [12] by Golub et al.). In many cases, as in the present project, the cost of full SVD is prohibitive, because the combined number of spatial and temporal DoFs, $N + N_t$, usually exceeds operational memory limitations. However, SVD theoretical framework lays ground to other methods.

When $N > N_t$, Φ_i with $i > N_t$ are redundant, as they are multiplied by zeroes of the Σ matrix, below row N_t. So called *thin* SVD may then be computed, instead of full SVD, cost of which might still be prohibitive.

The properties of data set X might be such that for a certain M all σ_i with $i > M$ are negligibly small. When the purpose of this decomposition allows treating these as zeroes, one might speak of *truncated* SVD, which at that point ceases to be exact (multiplying the matrices Φ, Σ, Ψ^T does not yield the primordial matrix X). All of these variations of SVD will be called conventional/classical SVD (cSVD).

A POD feature of key importance for this research is the way the basis is ordered. Namely, that the lowest-index modes carry the most energy. Examining eq. (2.25) provides information, that singular values $\sigma_i, i = 1, ..., N_t$ are somehow governing the magnitudes of snapshots X_i (Φ_i and Ψ_i are normalized). As may be found in e.g. [10] by Couplet et al., POD basis has similarities with Fourier basis. The intermodal energy transfer is local, as in case of Fourier modes. Low-index Fourier modes also carry the most energy (when turbulent flow data is considered). What is different is that diffusion term in POD case participates in intermodal energy transfer, which does not occur when Fourier basis is considered [10]. It is concluded that the concept of energy cascade is therefore valid in POD setting. Implications of this for individual modes energies will be discussed in section 3.1.3.

An important conceptual analogy has been shown between LES and ROM by Xie et al. [39], such that POD projection is also a type of spatial filter. Other comparison studies were made between Fourier and POD basis, e.g. by San and Maulik [30] where Burgers equation analytical solution serves as FOM. Similarities have also been found there between and Fourier- and POD-ROM basis results.

2.4.4. Incremental SVD

When σ_n for some $n < M$ drops below machine precision, then there is practically no need to include it in SVD. Sometimes even higher values of σ_i are of little interest, depending on the problem, and could be neglected, set to 0, similarly as in truncated SVD. The POD-modes corresponding to those small singular values are then also neglected, as multiplied by very small numbers. This threshold could be manually set and then one could speak of *dominant* singular values. This is called *low-rank approximation.*

In the present research the point of interest is to obtain an accurate reduced basis and to make it efficiently (memory- and time wise). Methods of SVD approximation that require access to all the snapshots simultaneously are in the present context of limited use. What is needed is a method that allows not only to compute approximation to SVD, but also to do it in a sequential manner. Suppose that there exists a snapshot matrix X with SVD eq. (2.24) that is being updated with new snapshots. Instead of computing SVD anew for the new X, one could attempt updating SVD that already exists. Combined with the considerations from previous paragraph this enables to compute a low-rank updated SVD. This allows to reduce computational cost as there is no need to upload all snapshots into operational memory. It also allows to construct reduced basis *online*, during FOM simulation.

The ground for this type of methods was formed by Brand in [8]. His algorithm leads to error accumulation, as described by Baker in [5], who in the same paper develops a better algorithm. Baker's low-rank single-pass incremental SVD is the algorithm that is applied in the present research. It will now be briefly described, in all aspects based solely on [5].

The purpose is to find dominant singular values and the corresponding dominant subspace. This needs to be done in a sequential manner, by updating SVD based on a part of data e.g. snapshot matrix:

$$X = \left[\underbrace{V_h(t_1), \ldots, V_h\left(t_{l_1}\right)}_{1^{st}\text{ increment}}, \ldots, \underbrace{V_h\left(t_{l_1+\ldots+l_{j-1}+1}\right), \ldots, V_h\left(t_{l_1+\ldots+l_j}\right)}_{j^{th}\text{ increment}}, \ldots, V_h\left(t_{N_t}\right) \right], \tag{2.26}$$

with a new set of columns at each step. Increment sizes $l_j, j = 1, \ldots p$ are such that $l_1 + l_2 + \ldots_l + p = N_t$. The updated decomposition is then truncated so that only dominant SVs and modes are kept. It is stressed, that it is the SVD that is being updated, no actual snapshots are reconstructed in the process. The procedure runs in loop until all the snapshots are processed. The subspaces that correspond to the dominant SVs are dominant subspaces. The subspaces corresponding to the remaining SVs are called subordinate.

A method will now be described, which must be applied at each step to separate dominant and subordinate subspaces. Let Y be an $N \times (k+l)$ matrix. Its QR decomposition may be written as:

$$Y = \begin{bmatrix} Q_1 & Q_2 \end{bmatrix} \begin{bmatrix} R \\ 0 \end{bmatrix} = Q_1 R, \tag{2.27}$$

where $Q_1 \in \mathbb{R}^{N\times(k+l)}$, $Q_2 \in \mathbb{R}^{N\times(N-k-l)}$ and $R \in \mathbb{R}^{(k+l)\times(k+l)}$. SVD of R itself may be written in a block form:

$$R = \Phi\Sigma\Psi^T = \begin{bmatrix} \Phi_1 & \Phi_2 \end{bmatrix} \begin{bmatrix} \Sigma_1 & 0 \\ 0 & \Sigma_2 \end{bmatrix} \begin{bmatrix} \Psi_1^T \\ \Psi_2^T \end{bmatrix}. \tag{2.28}$$

Here, $\Phi_1, \Phi_2, \Sigma_1, \Sigma_2, \Psi_1, \Psi_2$ denote generally *blocks* (matrices), instead of single columns, as in eq. (2.25). Entities with index 1 correspond to singular values above an arbitrarily set threshold, while those with index 2 are below that threshold. Orthogonal transformations G_Φ and G_Ψ may be defined, such that block-diagonalize left and right singular vectors of R:

$$G_\Phi^T \Phi = \begin{bmatrix} T_\Phi & 0 \\ 0 & S_\Phi \end{bmatrix} \quad \text{and} \quad G_\Psi^T \Psi = \begin{bmatrix} T_\Psi & 0 \\ 0 & S_\Psi \end{bmatrix}, \tag{2.29}$$

where T_Φ and T_Ψ are $k \times k$, whereas S_Φ and S_Ψ are $l \times l$. When these transformations are applied to R, a new matrix, with block-diagonal structure is obtained:

$$R_{new} = G_\Phi^T R G_\Psi = \begin{bmatrix} T_\Phi \Sigma_1 T_\Psi^T & 0 \\ 0 & S_\Phi \Sigma_2 S_\Psi^T \end{bmatrix}. \tag{2.30}$$

This leads to a new factorization of Y, because, owing to orthogonality of G_Φ and G_Ψ:

$$Y = Q_1 R = (Q_1 G_\Phi)\left(G_\Phi^T R G_\Psi\right) G_\Psi^T \overset{def}{=} Q_{new} R_{new} G_\Psi^T = Q_{new} \begin{bmatrix} T_\Phi \Sigma_1 T_\Psi^T & 0 \\ 0 & S_\Phi \Sigma_2 S_\Psi^T \end{bmatrix} G_\Psi^T. \tag{2.31}$$

After presenting this generic technique, proposed first by Brand in [8], Baker in [5] proceeds to the actual algorithm. In an extreme case, the separation could be performed on the full snapshot matrix X, however the purpose of memory saving would then be lost. Instead, X is divided into blocks X_j to be uploaded in each step. Each block contains l_j columns. The first step is to QR-decompose the first block of snapshots as $X_1 = Q_1 R_1$, while setting $\Psi_1 = \mathbb{I}_{l_1}$. A new group of columns of X is used in each step j to update the decomposition from previous step $Q_{j-1} R_{j-1} \Psi_{j-1}$. The new factorization is truncated, so that only dominant singular values and vectors, found with eq. (2.31), are kept. Note that in this context, lower indices j denote an incremental step number, not column number.

Algorithm 1: Incremental SVD

```
Input: $N \times N_t$ matrix $X = [X_1, X_2, ..., X_f]$, where $X_j \in \mathbb{R}^{N \times l_j}$ and $l_1 + l_2 + ... + l_f = N_t$
  1. $QR$ decomposition of the first block $X_1 = Q_1 R_1$;
     Set $\Psi_1 = \mathbb{I}_{l_1}$, rank $k_1 = l_1$, width $s_1 = l_1$;
for $j = 2, ..., f$ do
    2. Compute rank $(k_{j-1} + l_j)$ $QR$ decomposition of $\hat{Q}_j \hat{R}_j = [Q_{j-1} R_{j-1} | X_j]$;
    3. Block-reorthogonalize if needed ;
    4. Set $\hat{\Psi}_j = \begin{bmatrix} \Psi_{j-1} & 0 \\ 0 & \mathbb{I}_{l_j} \end{bmatrix}$;
    5. Set $s_j = s_{j-1} + l_j$;
    6. Choose $k_j \in (0, k_{j-1} + l_j]$, set $d_j = k_{j-1} + l_j - k_j$ ;
    7. Separate dominant and dominated subspaces in $\hat{R}_j$ by eq. (2.31) (construct $G_\Phi$ and $G_\Psi$);
    8. $\bar{R}_j = G_\Phi^T \hat{R}_j G_\Psi$;
    9. $\bar{Q}_j = \hat{Q}_j G_\Phi$;
    10. $\bar{\Psi}_j = \hat{\Psi}_j G_\Psi$;
    11. Truncate last $d_j$ columns of $\bar{Q}_j$, $\bar{\Psi}_j$ to obtain $\Phi_j$ and $\Psi_j$. Truncate last $d_j$ rows and columns of $\bar{R}_j$ to
        obtain $\Sigma_j$;
end
Output: Rank $k_f$ matrix decomposition as $\Phi_f \Sigma_f \Psi_f^T$, approximating SVD of $X$
```

The algorithm was cited as found in [5] by Baker, but in the present research the parametric settings have been simplified. The increment size l_j, which normally varies within $l_{min} \leq l_j \leq l_{max}$ remains fixed, $l_{min} = l_{max} = l_j := k_{add}$ for each increment[3] j.

The parameter d_j in the above algorithm is related to maximum dimension of dominant singular subspace/number of singular values sought, M_{dom}. The latter does not appear directly in the algorithm, but is one of the basic input arguments of the implementation. Essentially this is the rank to which the SVD approximation is truncated after each increment, see points 6 and 11 in the algorithm. In this context setting M_{dom} is regarded as enforcing a maximum value of the rank $k_j = M_{dom}$ at each step j. If other criteria do not truncate the current matrix to lower rank, then this is the imposed rank.

Step 6 is where dimension of the identified dominant singular subspace is chosen (a priori). The choice is affected by both M_{dom} and threshold. M_{dom} sets an upper bound on the number computed singular values (and corresponding singular vectors). When the threshold is set very low, all SVs up to M_{dom} are computed. With high threshold, that might not be the case, because the limit set by threshold is reached earlier and decision at step 6 is then made based on that.

As will be shown, iSVD accuracy relies greatly on parameters: k_{add}, M_{dom} and threshold. The basis produced is different than that of cSVD, typically in that orthogonality of modes is violated and errors between respective modes increase with mode index. The latter is expected, since iSVD is a low-rank method. There also appear errors in divergence of modes and in SV decay w.r. to cSVD, which also affect lower-index SVs and modes.

Since orthogonality and zero-divergence are important properties of RB in the present research, some of the iSVD bases investigated in chapter 5 will also undergo Gram-Schmidt orthogonalization and Helmholtz decomposition (to extract divergence-free parts of basis vetors). Effects of this treatment will also be exam-

---

[3] With the exception of the last increment, see section 4.4.2

ined. The procedures are well known and grounded in literature, therefore their details will not be discussed.

2.5. Closure in ROM context

EC-ROM relies on high-fidelity data insofar as most ROMs do: to construct POD basis, the FOM snapshots are used. The closure problem in [31] is not addressed though. This section gives a brief review of approaches to closure modeling related to the present research. Particular model that is applied is described in section 2.5.1. Two alternative approaches, which are not pursued in this thesis, are presented in section 2.5.2.

Typical Galerkin-ROM (see eq. (2.8)):

$$\dot{a} = Aa + a^T Ba, \tag{2.32}$$

tends to be inaccurate and unstable. Hence frequently a closure (or correction) term dependent on ROM variables a is simply added, so that:

$$\dot{a} = Aa + a^T Ba + \tau(a). \tag{2.33}$$

An extensive review of ROM closure modeling techniques, with an outlook to applications of machine learning, may be found in [2] by various authors.

2.5.1. Eddy viscosity ROM

A brief overview of eddy viscosity type closure modeling is considered of interest now. General features of this paradigm of modeling were described in section 2.3. The model discussed in this section is chosen specifically due to its simplicity.

The concept of EV hinges on *Boussinesq hypothesis*. All textbooks ([25],[37],[33] to mention the most notable) on turbulence modeling contain description of this most popular type of approach. Perhaps the most descriptive and intuitive is laid out by Leschziner in [18].

A review of closure models for POD-projection-ROMs is presented in the paper [35] by Wang et al., including a mixing-length POD-ROM among others. This model is the least complex of all discussed models and it is of interest in the present thesis. A variant of this model will be the object of examination in the a priori analysis of turbulence modeling, see section 3.2 and chapter 7. The idea is to introduce additional dissipation, that is supposed to fulfill the role of finest scales, which are not represented in ROM. In FOM dissipation of kinetic energy into heat happens on those scales. The dissipation is introduced via modification of (symmetricized) diffusion term $\nu\nabla\cdot\left(\nabla\boldsymbol{u}+(\nabla\boldsymbol{u})^T\right) = \nabla\cdot\nu\left(\nabla\boldsymbol{u}+(\nabla\boldsymbol{u})^T\right)$ by simply adding turbulent viscosity ν_t to the molecular viscosity ν. The modified diffusion term is $\nabla\cdot\left((\nu+\nu_t)\left(\nabla\boldsymbol{u}+(\nabla\boldsymbol{u})^T\right)\right)$.

Eddy viscosity ν_t is a constant in the mixing-length model. Wang et al. in [35] propose, following Aubry et al. [4] to compute it based on:

$$\nu_t := u_> l_> = \frac{\int_0^{X_2} \langle u_{i>} u_{i>} \rangle \, dx_2}{\left(X_2 \int_0^{X_2} \left\langle \frac{\partial u_{i>}}{\partial x_j} \frac{\partial u_{i>}}{\partial x_j} \right\rangle dx_2 \right)^{1/2}}, \tag{2.34}$$

where $\langle\cdot\rangle$ is averaging along x_1, x_3, the wall-normal direction is x_2 and $>$-sign denotes unresolved scales, $u_{i>} = u_i'$. This quantity has dimensions of viscosity so in terms of dimensional analysis it makes sense. The underlying assumptions in [4] (or rather experimental facts) were that the unresolved part of the flow $u_{i>}$ was "(...) approximately homogeneous in streamwise (x_1) and spanwise (x_3) directions, stationary in time, inhomogeneous and of integrable energy in wall-normal x_2 direction.". Note that this model is of little practical use, as it always requires FOM solution. As such it would have to be regressed s.t. $\nu_t = \nu_t(a)$, based on high fidelity data to be useful in ROM past FOM integration time. This is outside the scope of this thesis, limited to the solution reproduction problem. However, a priori analysis of a similar EV model is pursued in the present research, only, by definition it is confined to FOM integration period.

The EV resulting from eq. (2.34) is a spatially-invariant scalar. In the present research the flow is not stationary, so $\nu_t = \nu_t(t)$. Instead of averaging over all spatial directions, one could imagine leaving out one of them. This would be justified when there is a mean structure of the field expected in one particular direction, e.g. the cross-flow direction y in a periodic shear layer. Then EV would be a field, $\nu_t(y,t)$, the model could still be independent of $\boldsymbol{u}$ (except through eq. (2.34)). That is in contrast with e.g. Smagorinsky model, where $\nu_t = \nu_t(\boldsymbol{u}(\boldsymbol{x},t))$. It is worth mentioning, for reasons to be explained in the next chapter, that in case of $\nu_t = \nu_t(\boldsymbol{x},t)$ special treatment must be made to arrive at ROM operators. Simply projecting the FOM (time-varying) diffusion operator, is too costly. The authors of [35] propose a two-level scheme, described in [34], where EV interpolations on coarser mesh are applied to reduce the cost. An alternative would be to use discrete empirical interpolation method (DEIM) [9]. A variant of EV models is one described by Hijazi et al. [14]. Here the authors use RANS equations as FOM and thus EV-diffusion term arises naturally, being already present in the full model equations. What distinguishes this article from others, and also the idea drawn from it into the present research, is that proper orthogonal decomposition of eddy viscosity itself is performed: $\nu_t \approx \sum_{i=1}^{M} g_i\left(t\right) \boldsymbol{\eta}\left(\boldsymbol{x}\right)$. The authors further develop the model by finding the relation $g_i\left(a_i\right)$ between EV-POD coefficients and ROM variables, through the use of radial basis functions. The idea of eddy viscosity POD is drawn from this paper for the purpose of performing precomputation of turbulent diffusion operator (the closure term).

2.5.2. Examples of alternative approaches to closure modeling

In the article [20] by Mohebujjaman et al., *data-driven* is understood not in the sense that high-fidelity data is used to construct the reduced basis (which is the common feature of virtually all ROMs). Instead, FOM solution serves as reference to find an improved form of ROM operators via an error minimization process. The optimization here is additionally *constrained* according to the known physics of the particular flow reflected by the mathematical properties of the operators, such as those mentioned by Sanderse in [31]: skew-symmetry of convection operator, and negative semi-definiteness of the diffusion operator.

The authors of [20] postulate a particular form (ansatz) of the correction term: $\tau = \widetilde{A}a + a^T \widetilde{B}a$. This way, the data-driven correction ROM (DDC-ROM) takes on the form:

$$\dot{a} = \left(A + \widetilde{A}\right) a + a^T \left(B + \widetilde{B}\right) a. \tag{2.35}$$

It is important, that in the *constrained* CDDC-ROM, only the correction *to the operators* A and B, and not the whole ROM equation, is a solution of an optimization problem. This problem is stated in [20] as:

$$\min_{\substack{\widetilde{A}\in\mathbb{R}^{M\times M}\\ \widetilde{B}\in\mathbb{R}^{M\times M\times M}\\ a^T\widetilde{A}a\leq 0\\ a^T\left(a^T\widetilde{B}a\right)=0}} \sum_{i=1}^{N_t} \left\|\tau^{true}\left(t_i\right) - \tau^{ansatz}\left(t_i\right)\right\|, \tag{2.36}$$

where the constraints on $\widetilde{A}, \widetilde{B}$ stem from negative semi-definiteness of diffusion operator and skew-symmetry of convective operator.

CDDC-ROM is a major improvement w.r. to DDC-ROM [20]. The authors of [20] provide evidence that their physics-informed modeling is able to maintain energy error of the flow around a circular cylinder for $Re = 1000$ in reasonable bounds, whereas DDC-ROM energy deviates much faster. The downside of CDDC (and DDC as well), apart from complexity, is that there is an optimization problem involved, with equality and inequality constraints, which is increasingly more expensive to solve with increasing M.

A different approach, drawing analogies from LES is presented by Xie et al. in [38]. Filtering NS equations with a differential filter and using solutions to these spatially filtered equations, they construct a POD basis as a preliminary step. They argue that, given a coarse mesh, this basis would be more accurate than a basis obtained from the full NS equations.

The idea that is proposed is the following. Filtered velocity solution of continuous equation is $\overline{\boldsymbol{u}}$. Discretization must also include translating filtering (bar operator) to discrete setting, so that $\overline{\boldsymbol{u}} \approx \overline{V_h}^h$. Then, considering ROM approximation $\overline{V_r}^r$ of the filtered discretized field $\overline{V_h}^h$, on finds approximation of the original, non-filtered discretized field V_h by approximate deconvolution. Deconvolution is attempted, since filtering is defined via convolution of the filtering operator $\boldsymbol{G}$ with $\boldsymbol{u}$. However the exact procedure is ill conditioned, and additional treatment is needed, such that instead of computing $\boldsymbol{u}^{AD} = \boldsymbol{G}^{-1}\overline{\boldsymbol{u}}$, the inversion of $\boldsymbol{G}$ with regularization term is performed:

$$\boldsymbol{u}^{AD} = \left(G + \mu \boldsymbol{I}\right)^{-1} \overline{\boldsymbol{u}}. \tag{2.37}$$

$\boldsymbol{u}^{AD}$ is needed precisely to model the closure term that arises while spatially filtering the NS equations: $\overline{\boldsymbol{u} \cdot \nabla \boldsymbol{u}}$. Both $\boldsymbol{u}$ and the filtering operation with kernel $\boldsymbol{G}$ denoted by the overbar, must be translated to discrete setting. There are two possible choices of filter: ROM-filter and FE-filter. They result in two different AD-ROMs. This modeling is promising, as it provides more accurate results (similar to EV-ROM) than standard Galerkin-ROM with comparable computational cost, all of this without explicit numerical dissipation mechanisms [38]. However, AD-ROMs are more complex, requiring regularization due to ill-conditioning of deconvolution. Moreover they are not yet thoroughly investigated for higher Reynolds number flows and multiple test cases, and there are some issues known from LES that pertain in ROM setting.

3

Methodology

This chapter is organized into the following sections. Key aspects of EC-ROM are discussed in (section 3.1). Description of methodology used to assess EV model is given in section 3.2. Error estimators are defined in section 3.3 and definitions of additional investigated quantities may be found in section 3.4

3.1. Energy-Conserving ROM

The ROM used throughout the thesis is a non-linearly stable ROM based on an energy-conserving FOM with FV numerical scheme, by Sanderse [31]: EC-ROM. As the author mentions, the stability here is understood as boundedness of a norm of solution (here: global kinetic energy). It is instructive to refer to a flowchart from [31], which indicates the possible sequence of operations on the way to obtain ROM.

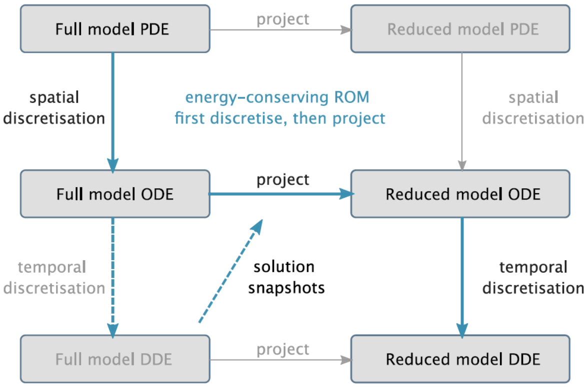

Figure 3.1: Possible ways of obtaining projection-ROM [31]. PDE, ODE, DDE - partial/ordinary/discretized differential equation.

Because spatial discretization and projection are operations that generally do not commute, it is important to maintain the correct sequence, otherwise some FOM properties will not be inherited by ROM. The energy conservation is one such property. It appears already on the continuous level, due to some operator symmetry considerations, to be explained in the following section (see also appendix of [31]).

Although, FOM temporal discretization must be set in order to obtain snapshots for reduced basis construction, it is the FOM semi-discrete equations that are to be projected in order for the energy-conservation property to be inherited by ROM. One may also project fully discrete FOM equations and still maintain the energy-conserving feature. In this case however, the choice of ROM time stepping scheme is limited by the choice made for FOM.

Time marching will not be discussed in detail, however it is worth mentioning that (see section 6.2.1) FOM and ROM temporal discretization schemes may be chosen independently. In the present project both FOM and ROM are integrated in time using 4^{th} order explicit Runge-Kutta method.

3.1.1. Continuous domain

The Navier-Stokes equations on a periodic domain Ω are given in the form:

$$\nabla \cdot \boldsymbol{u} = 0 \quad \text{in } \Omega, \tag{3.1}$$

$$\frac{\partial \boldsymbol{u}}{\partial t} + \nabla \cdot (\boldsymbol{u} \otimes \boldsymbol{u}) = -\nabla p + \nu \nabla \cdot \left(\nabla \boldsymbol{u} + (\nabla \boldsymbol{u})^T \right) \quad \text{in } \Omega, \tag{3.2}$$

with initial condition:

$$\boldsymbol{u}(\boldsymbol{x}, 0) = \boldsymbol{u}_0(\boldsymbol{x}). \tag{3.3}$$

Kinetic energy serves as the norm of solution and is defined via L^2 inner product

$$K := \frac{1}{2} \|\boldsymbol{u}\|^2 = \frac{1}{2} (\boldsymbol{u}, \boldsymbol{u})_\Omega = \frac{1}{2} \int_\Omega \boldsymbol{u} \cdot \boldsymbol{u} d\Omega. \tag{3.4}$$

In [31] the convective operator $\nabla \cdot (\boldsymbol{u} \otimes \boldsymbol{u}) = C(\boldsymbol{u}, \boldsymbol{u})$ is always skew-symmetric:

$$(C(\boldsymbol{u}, \boldsymbol{v}), \boldsymbol{w})_\Omega = -(\boldsymbol{v}, C(\boldsymbol{u}, \boldsymbol{w}))_\Omega. \tag{3.5}$$

Diffusion operator D in $\nu \nabla \cdot \left(\nabla \boldsymbol{u} + (\nabla \boldsymbol{u})^T \right) = \nu D \boldsymbol{u}$ is symmetric, hence through integration by parts:

$$(D\boldsymbol{u}, \boldsymbol{u})_\Omega = -\nu (\nabla \boldsymbol{u}, \nabla \boldsymbol{u})_\Omega. \tag{3.6}$$

Furthermore, again integration by parts and mass conservation dictate that pressure gradient field is orthogonal to velocity field, $\left(\nabla p, \boldsymbol{u}\right)_\Omega = \left(p, \nabla \cdot \boldsymbol{u}\right)_\Omega = 0$. Therefore, energy evolves according to:

$$2\frac{dK}{dt} = \frac{d}{dt} (\boldsymbol{u}, \boldsymbol{u})_\Omega = 2\left(\frac{d\boldsymbol{u}}{dt}, \boldsymbol{u} \right)_\Omega = \underbrace{\cancelto{0}{-2(C(\boldsymbol{u}, \boldsymbol{u}), \boldsymbol{u})_\Omega}}_{\text{skew symmetry}} \cancelto{0}{-2\left(\nabla p, \boldsymbol{u}\right)_\Omega} + 2\nu (D\boldsymbol{u}, \boldsymbol{u})_\Omega = -2\nu (\nabla \boldsymbol{u}, \nabla \boldsymbol{u})_\Omega, \tag{3.7}$$

or simply:

$$\frac{dK}{dt} = -\nu \|\nabla \boldsymbol{u}\|^2, \tag{3.8}$$

i.e. energy may only decrease and does so solely due to the action of diffusion operator, while in the inviscid limit $\nu \to 0$ it is constant. It is reiterated that this property holds for periodic and no-slip boundary conditions. With different types of BCs, integration by parts will result in additional terms that will affect energy evolution.

3.1.2. Discrete domain

The discretization chosen is such that follows the attractive property of the continuous equations, expressed by eq. (3.8). Periodic box is divided into $N_x \times N_y \times N_z = N_p$ cells, succinctly called pressure grid. Staggered grid technique is used in which separate grids are constructed for each of the velocity components, with total no. of DoFs $N_V = N_u + N_v + N_w = 3N_p$.

A 2^{nd} order accurate finite volume (FV) scheme is used. FV means, that the equations (3.1)-(3.2) are to be integrated upon discretization. The resulting (semi-discrete) FOM is:

$$M_h V_h = 0, \tag{3.9}$$

$$\Omega_h \frac{dV_h}{dt} = -G_h p_h - C_h(V_h) V_h + \nu D_h V_h, \tag{3.10}$$

where M_h is discrete divergence operator, Ω_h is a diagonal matrix with volumes of FV-cells surrounding appropriate variable location in the domain, and $C_h(V_h)$ is the skew-symmetric convective operator and D_h is discrete diffusion operator. The equation is similar to the general ROM equation eq. (2.6), only Ω_h matrix is new. In fact however the differences lie also in the operators G_h, C_h, D_h. In eq. (2.6) discussion is disconnected from numerical method used, whereas in the present chapter FV method is applied, whereby variables are computed in integrated form. The FV matrix Ω_h is already encoded in each of the operators in eq. (3.10).

Staggered grid setting, makes the property $G_h = -M_h^T$ easy to achieve. It also allows to avoid the checkerboard problem, as described by e.g. Patankar in [22].

Now, after Sanderse [31] it is adequate here to define a discrete inner product, as it will serve to construct discrete version of eq. (3.8), one particularly useful in the context of FV method. The definition, already stated in eq. (2.15) reads:

$$(V_h, W_h)_{\Omega_h} := V_h^T \Omega_h W_h, \tag{3.11}$$

for $V_h, W_h \in \mathbb{R}^{N_V}$. The definition will be used throughout the thesis to compute various errors and other integral quantities as well as to define orthogonality condition for the reduced basis.

The energy equation again amounts to:

$$\frac{dK_h}{dt} = -\nu \left\| Q_h V_h \right\|^2, \tag{3.12}$$

where $-Q_h^T Q_h = D_h$, as D_h is a symmetric negative definite matrix. Convective term vanishes by skew-symmetry of C_h and pressure term is canceled due to continuity equation 3.1.

Sanderse discusses in [31] that a careful choice of time discretization must be made, for the discrete model to retain the above property.

To obtain snapshots, time marching scheme is applied and thus fully discrete FOM emerges. However, it is the semi-discrete (only spatially discretized) FOM equations that will be projected to obtain ROM operators. This allows to omit some difficulties with boundary conditions and eliminates pressure from ROM equations, making ROM velocity-only. It also allows to select a separate time marching for ROM and FOM.

3.1.3. Projected domain

The framework used in this section is Bubnov-Galerkin projection. The space onto which the terms of semi-discrete FOM eq. (3.9)-(3.10) are projected is generated via proper orthogonal decomposition of the snapshot matrix X :

$$X = \left[V_h\left(t^1\right), V_h\left(t^2\right), \ldots, V_h\left(t^{N_t}\right) \right], \tag{3.13}$$

containing the fully discrete FOM solution at N_t time instants t^i (see section 2.4.2). Before projection though, FOM variables are expanded into POD-series:

$$V_h(t) \approx \Phi a(t), \tag{3.14}$$

where columns of $\Phi \in \mathbb{R}^{N_V \times M}$ are POD truncated basis vectors. For reasons explained in section 2.4.2, there is no need to project eq. (3.9), because columns Φ_i are linear combinations of snapshots. Hence eq. (3.9) is identically satisfied when eq. (3.14) is inserted and no information regarding $a(t)$ may be inferred.

When eq. (3.14) and the property $G_h = -M_h^T$ are inserted into momentum equation eq. (3.10), the equation becomes

$$\Omega_h \frac{d\Phi a(t)}{dt} = M_h^T p_h - C_h(\Phi a(t)) \Phi a(t) + \nu D_h \Phi a(t). \tag{3.15}$$

Projection with $\mathscr{P} = \Phi^T$ results in:

$$\underbrace{\Phi^T \Omega_h \Phi}_{\mathbb{I}} \frac{da(t)}{dt} = \Phi^T M_h^T p_h - \Phi^T C_h(\Phi a(t)) \Phi a(t) + \nu \Phi^T D_h \Phi a(t), \tag{3.16}$$

which, dropping explicit time-dependence, amounts to:

$$\dot{a} = a^T B a + A a, \tag{3.17}$$

where A and B are diffusive and convective ROM operators respectively. It is important to notice here, that the pressure term in eq. (3.16) vanishes, because $\Phi^T M_h^T p_h = (M_h \Phi)^T p_h = 0$ and Φ_i are all discretely divergence-free. Gradient-divergence compatibility $G_h = -M_h^T$ enables this but only for Φ_i satisfying zero-divergence property. Clearly therefore it is a crucial feature of the basis for the equations to hold. Also in eq. (3.16), orthogonality of Φ plays an important role. On the left-hand side it allows reduction of the matrix $\Phi^T \Omega_h \Phi$ to an identity.

Equation (3.17) is an ODE system for truncated POD coefficients a.The reconstructed field $V_r = \Phi a$ approximates FOM solution $V_h \approx V_r$. Denote a^{FOM} the POD coefficients that result from projecting FOM solution V_h onto full POD basis (with $\dim(\Phi) = N_t$):

$$(\Phi, V_h)_{\Omega_h} = \Phi^T \Omega_h V_h =: a^{FOM}. \tag{3.18}$$

In this case $V_h = \Phi a^{FOM}$ is an exact relation. Energy is given by:

$$K = \frac{1}{2}\left(V_h, V_h\right)_{\Omega_h} = \frac{1}{2}\left(\Phi a^{FOM}, \Phi a^{FOM}\right)_{\Omega_h} = \frac{1}{2}\left(a^{FOM}\right)^T \Phi^T \Omega_h \Phi a^{FOM} = \frac{1}{2}\left(a^{FOM}\right)^T a^{FOM}. \tag{3.19}$$

Similar to [10] by Couplet et al., snapshot-averaged energy of the i-th mode is related to i-th eigenvalue of the matrix $X^T X$ (or singular value σ_i of the SVD $X = \Phi\Sigma\Psi^T$) through:

$$\underline{2K_i} = \underline{\left(a_i^{FOM}\right)^2} = \lambda_i = \sigma_i^2, \quad i = 1, ..., N_t, \tag{3.20}$$

where orthogonality of snapshot-averaged coefficients a is used, $\underline{a_i a_j} = \lambda_i \delta_{i,j}$. So the mean energy of the i-th mode is simply half the square of the corresponding singular value. In section 5.3 wavenumber spectra of individual modes will be plotted to exemplify that indeed higher-index modes carry more energy in high wavenumbers.

3.1.4. Enforced momentum conservation

This section is only a brief description of how conservation of momentum is enforced in [31] by Sanderse. The method will be tested in combination with iSVD to check whether the two are compatible. In section 6.2.2 ROM simulation results with enforced momentum conservation are presented.

In NS equations on periodic domains global momentum is conserved, $\frac{d}{dt}\int_\Omega \boldsymbol{u} d\Omega = 0$. Presently used FOM with FV spatial discretization also has this property, e.g. for u-component:

$$e_u^T \Omega_h \frac{dV_h(t)}{dt} = e_u^T F_h(V_h, p_h) = 0, \tag{3.21}$$

where $e_u = [1, ...1, 0, ..., 0]^T$ vector of zeroes and ones, with ones corresponding to u-cells. When POD-expansion and projection is applied, and the resulting ROM terms are reconstructed in FOM space, ROM momentum evolution is:

$$e_u^T \Omega_h \Phi \frac{da(t)}{dt} = e_u^T \Omega_h \Phi \Phi^T F_h\left(\Phi a(t), p_h\right). \tag{3.22}$$

As proven by Sanderse in [31], his EC-ROM conserves global momentum in periodic domains, when basis vectors are enforced to satisfy $e_u^T = \Omega_h \Phi \Phi^T = e_u^T$, and similar for e_v, e_w. To describe how this is achieved, denote $E = [\frac{e_u}{\|e_u\|}, \frac{e_v}{\|e_v\|}, \frac{e_w}{\|e_w\|}]$, i.e. a matrix consisting of columns of the three normalized vectors e. The steps are now the following ([31]):

1. "Form adapted snapshot matrix $\tilde{X} = X - EE^T \Omega_h X$,
2. Transform to include weighted norm: $\hat{X} = \Omega_h^{\frac{1}{2}} \tilde{X}$,
3. Perform SVD of $\hat{X}$: $\hat{X} = \hat{\Phi}\Sigma\Psi^T$,
4. Transform back to include weighted norm $\tilde{\Phi} = \Omega_h^{-\frac{1}{2}} \hat{\Phi}$,
5. Append E and truncate: $\Phi = \left[E\tilde{\Phi}\right]_M$".

3.2. Closure modeling

The concept and application of EV-type modeling are described in section 2.3 and section 2.5.1. In the present chapter the shape of exact closure terms will be derived. This will be done with the aid of division of solution space into resolved and unresolved parts (similar to [3] by Akkerman et al.): $\text{span}(\Phi) = \text{span}\left(\overline{\Phi}\right) \oplus \text{span}\left(\Phi'\right)$, where $\oplus$ denotes direct sum of spaces. Next, a methodology of assessing validity of EV modeling will be presented.

In the present section the number of resolved modes, i.e. the dimension of reduced basis, is M and total number of modes obtained is N_t (or close enough s.t. SV with higher indices are negligible). It must be stressed that the symbols $\overline{\Phi}, \Phi'$ are only used in this section and in chapter 7, everywhere else the resolved modes are denoted Φ.

3.2.1. Exact closure term

What is meant here by *closure term* is not strictly what is missing in ROM w.r.t. FOM. Instead, the part that is disregarded due to using non-maximal dimension of RB is sought. This will become clear once matters are put into symbols. The FOM solution $V_h(t)$ evolves in the space $\mathbb{R}^{N_V}$. MOR attempts to approximate this, $V_r(t) \approx V_h(t)$, by constructing a low-dimensional subspace $\text{span}\left(\overline{\Phi}\right) \subset R^{N_V}$ where $V_r(t)$ evolves. Note that in the present notation time integration method has not yet been invoked. Therefore the discussion is about two separate ODE systems, of different dimensions. The high-dimensional system (FOM) is solved by a time-stepping scheme and the solution is given in snapshots, serving to construct RB. Low-dimensional system (ROM) may be solved by a different scheme, with a different time step. Hence it may deviate from FOM trajectory because it evolves autonomously starting from IC projected onto RB space. This evolution is governed by ROM equations eq. (3.16). If the ROM solution is spanned by all N_t modes, then this is a full-rank approximation. It is still only an approximation, because:

- time is limited to FOM integration time
- time is not discretized yet in ROM so continuous time between snapshots is not well defined
- ROM solutions $a_i(t)$ are results of solving an ODE system, not projection of FOM

Recall eq. (3.16), with some terms already simplified:

$$\frac{da(t)}{dt} = -\Phi^T C_h(\Phi a(t))\Phi a(t) + \nu\Phi^T D_h \Phi a(t), \tag{3.23}$$

and FOM solution is given as N_t snapshots, ordered in the $N_V \times N_t$ snasphot matrix eq. (3.13), where typically $N_V \gg N_t$. Acquisition of those requires selection of a time-marching scheme. As mentioned, different scheme might be used for ROM solution, but the present research uses the same time march as in FOM.

Eq.(3.23) does not state the dimension of RB explicitly. Let $\Phi = \left[\overline{\Phi}\middle|\Phi'\right]$ be an $N_V \times N_t$ matrix containing all left-singular vectors of the full-rank SVD of the snapshot matrix X. $\overline{\Phi}$ contains the first M left-singular vectors of this decomposition, while Φ' the remaining $N_t - M$ vectors. $\text{span}\left(\overline{\Phi}_i\right)$ and $\text{span}\left(\Phi'_i\right)$ are orthogonal subspaces of Φ. By construction all columns of Φ are orthogonal. POD approximation is the best approximation *within the set of snapshots*. When continuous time is considered, and all N_t modes are taken as basis, then:

$$V_h(t) \approx \sum_{i=1}^{N_t} \Phi_i a_i(t). \tag{3.24}$$

The relation is exact when the following conditions are met

1. The time discretization is performed so that FOM solution is $V_h\left(t_j\right)$
2. N_t-dimensional reduced basis is constructed, and the ROM coefficients are found by projecting $V_h\left(t_j\right)$ onto this RB, $a\left(t_j\right) = a^{FOM}\left(t_j\right) = \Phi^T \Omega_h V_h\left(t_j\right)$
3. The relation is confined to $t \in [0, t_{end}]$.

The above explanation was made to stress that the present considerations concern only FOM integration period at time instants dictated by FOM temporal discretization (except when downsampled set is considered in one example) and that ROM variables are now in fact projected FOM variables. Then the relation may be expressed:

$$V_h\left(t_j\right) = \sum_{i=1}^{N_t} \Phi_i a_i\left(t_j\right), \quad t_j \in [0, t_{end}],\ j = 1, 2, ..., N_t. \tag{3.25}$$

In the further part of this section the ROM coefficients will denote $a = a^{FOM}\left(t_j\right)$, i.e. the coefficients of FOM projected solution in the ROM basis. Denote parts of the POD expansion eq. (3.25) in matrix notation as:

$$V_h = \underbrace{\overline{\Phi}\overline{a}}_{\text{resolved part}} + \underbrace{\Phi' a'}_{\text{unresoved part}} = \left[\overline{\Phi}\middle|\Phi'\right]_{N_V \times (M+M')} \begin{bmatrix} \overline{a} \\ a' \end{bmatrix}_{(M+M')\times 1}, \tag{3.26}$$

where $M' = N_t - M$. For the sake of discussion ROM equations for maximum possible dimension of basis Φ will be written out. Explicit expansion of convection *operator* $C_h(V_h)$ (see appendix of [31] by Sanderse) is:

$C_h(V_h)(\cdot) = K_h \mathrm{diag}(I_h(V_h))\, A_h(\cdot)$ where K_h, I_h, A_h are well defined, grid-dependent: differencing, interpolation and averaging matrix operators, respectively, V_h is the convecting velocity and $\mathrm{diag}(\cdot)$ accepts a vector as an argument and outputs a diagonal matrix, with the vector components ordered on the diagonal. Using the block notation as in eq. (3.26), allows to write the ROM equation eq. (3.16) in a "scale-separated"[1] form:

$$\begin{bmatrix} \overline{\Phi}^T \\ \Phi'^T \end{bmatrix} \Omega_h \left[\overline{\Phi} \middle| \Phi'\right] \begin{bmatrix} \dot{\overline{a}} \\ \dot{a}' \end{bmatrix} + \begin{bmatrix} \overline{\Phi}^T \\ \Phi'^T \end{bmatrix} C_h\left(\overline{\Phi}\overline{a} + \Phi' a'\right) \left[\overline{\Phi} \middle| \Phi'\right] \begin{bmatrix} \overline{a} \\ a' \end{bmatrix} = \nu \begin{bmatrix} \overline{\Phi}^T \\ \Phi'^T \end{bmatrix} D_h \left[\overline{\Phi} \middle| \Phi'\right] \begin{bmatrix} \overline{a} \\ a' \end{bmatrix}. \tag{3.27}$$

Orthogonality condition $\Phi^T \Omega_h \Phi = \mathbb{I}$ implies that e.g. $\Phi'^T \Omega_h \overline{\Phi} = [\boldsymbol{O}]_{(N_t - M)\times M}$, i.e. $\overline{\Phi}$ and Φ' span mutually orthogonal subspaces. Convective operator $C_h(\cdot)(\cdot)$ is actually linear in each of its arguments, meaning, that for a fixed $W_h \in \mathbb{R}^{N_V}$, $C_h(W_h)\, V_h$ is linear in V_h and conversely. When the first argument is fixed, $C_h(V_h)(\cdot)$ is represented as a matrix. Using linearity in the first argument, eq. (3.27) may be rewritten, keeping the previous form of convective operator:

$$\begin{aligned} \begin{bmatrix} \dot{\overline{a}} \\ \dot{a}' \end{bmatrix} = -&\begin{bmatrix} \overline{\Phi}^T C_h\left(\overline{\Phi}\overline{a}\right)\overline{\Phi} + \overline{\Phi}^T C_h\left(\Phi' a'\right)\overline{\Phi} & \overline{\Phi}^T C_h\left(\overline{\Phi}\overline{a}\right)\Phi' + \overline{\Phi}^T C_h\left(\Phi' a'\right)\Phi' \\ \Phi'^T C_h\left(\overline{\Phi}\overline{a}\right)\overline{\Phi} + \Phi'^T C_h\left(\Phi' a'\right)\overline{\Phi} & \Phi'^T C_h\left(\overline{\Phi}\overline{a}\right)\Phi' + \Phi'^T C_h\left(\Phi' a'\right)\Phi' \end{bmatrix} \begin{bmatrix} \overline{a} \\ a' \end{bmatrix} \\ &+ \nu \begin{bmatrix} \overline{\Phi}^T D_h \overline{\Phi} & \overline{\Phi}^T D_h \Phi' \\ \Phi'^T D_h \overline{\Phi} & \Phi'^T D_h \Phi' \end{bmatrix} \begin{bmatrix} \overline{a} \\ a' \end{bmatrix} \end{aligned}. \tag{3.28}$$

Considering only equations originating from projection of FOM equations onto span$\{\overline{\Phi}\}$, is the same as considering equations corresponding to the first row (upper blocks) of the matrices in eq. (3.28). The system reads:

$$\begin{aligned} \dot{\overline{a}} = \underbrace{-\overline{\Phi}^T C_h\left(\overline{\Phi}\overline{a}\right)\overline{\Phi}\overline{a}}_{\text{coarse scale convective term}} \underbrace{\cancel{-\overline{\Phi}^T C_h\left(\Phi' a'\right)\overline{\Phi}\overline{a}} \cancel{- \overline{\Phi}^T C_h\left(\overline{\Phi}\overline{a}\right)\Phi' a'}}_{\text{mixed convective terms}} \underbrace{\cancel{-\overline{\Phi}^T C_h\left(\Phi' a'\right)\Phi' a'}}_{\text{fine scale convective term}} \\ + \underbrace{\overline{\Phi}^T \nu D_h \overline{\Phi}\overline{a}}_{\text{coarse scale diffusive term}} + \underbrace{\cancel{\overline{\Phi}^T \nu D_h \Phi' a'}}_{\text{fine scale diffusive term}} \quad , \end{aligned} \tag{3.29}$$

where the crossed out terms are neglected in the Bubnov-Galerkin projection framework, and are the ones for which a closure model typically needs to be formulated.

These crossed-out terms involve unresolved scales $\Phi' a'$ and their relations to resolved scales $\overline{\Phi}\overline{a}$. The interactions between the two subspaces are confined to the two mixed convective terms. In one of those terms unresolved scale field is convecting the resolved scale field and in the other vice versa. The third (crossed-out) convective term describes convection of unresolved scales by unresolved scales. Lastly, the (crossed-out) remaining term describes diffusion of unresolved scales.

3.2.2. A priori turbulence modeling test

The present discussion is limited to the solution reproduction problem. The aim is to compensate for the absence of the crossed out terms of eq. (3.29). In the context of RANS-FOM with EV-type turbulence model (see section 2.3), the ν_t-appended diffusion term appears naturally in ROM as a projection of the FOM corresponding term. In the present context the term does not appear in FOM. Nevertheless, it is being postulated and its potential in ROM accuracy improvement investigated.

Using eddy viscosity ansatz to model the influence of the missing fine scales amounts to adding another diffusion term to eq. (3.29): $\overline{\Phi}^T L_h\left[\alpha \nu_h^t \odot \left(S_h\left(\overline{\Phi}\overline{a}\right)\right)\right]$. The term expresses the discretized and projected term $\nabla\cdot\left(\nu^t \nabla^s \overline{\boldsymbol{u}}\right)$. Here $L_h : \mathbb{R}^{3N_V} \to \mathbb{R}^{N_V}$ is a divergence operator (different than M_h), α is a constant, $\nu_h^t \in \mathbb{R}^{3N_V}$ is the discretized EV at points where $S_h(\cdot)$ returns values, $S_h(\cdot)$ is a symmetricized gradient (straining) operator $S_h : \mathbb{R}^{N_V} \to \mathbb{R}^{3N_V}$ and $\odot$ is elementwise product. Projection is performed via $\overline{\Phi}^T$ and the inner operator S_h acts on resolved scales.

For the turbulence model to be assessed properly, the question that should be answered is whether the

---

[1] "Mode separated" would be a more accurate term, although as mentioned in section 3.1.3 there is an equivalence (to a degree) between Fourier and POD modes. Also: the separation is only symbolic, so that there is a distinction between resolved ($\overline{\Phi}$) and unresolved (Φ') modes.

following holds:

$$\underbrace{-\overline{\Phi}^T C_h\left(\Phi' a'\right)\overline{\Phi}\overline{a} - \overline{\Phi}^T C_h\left(\overline{\Phi}\overline{a}\right)\Phi' a' - \overline{\Phi}^T C_h\left(\Phi' a'\right)\Phi' a' + \overline{\Phi}^T \nu D_h \Phi' a'}_{\overline{\Phi}^T R} \overset{?}{=} \underbrace{\overline{\Phi}^T L_h\left[\alpha_1 \nu_h^t \odot \left(S_h\left(\overline{\Phi}\overline{a}\right)\right)\right]}_{\alpha_1 \overline{\Phi}^T W_1} + \beta_1, \tag{3.30}$$

which has more physical meaning when no projection is applied[2]:

$$\underbrace{-C_h\left(\Phi' a'\right)\overline{\Phi}\overline{a} - C_h\left(\overline{\Phi}\overline{a}\right)\Phi' a' - C_h\left(\Phi' a'\right)\Phi' a' + \nu D_h \Phi' a'}_{R} \overset{?}{=} \underbrace{L_h\left[\alpha_1 \nu_h^t \odot \left(S_h\left(\overline{\Phi}\overline{a}\right)\right)\right]}_{\alpha_1 W_1} + \tilde{\beta}_1, \tag{3.31}$$

where α is the model constant and β is an offset parameter, expected to vanish with increasing M.

To avoid the question mark, eq. (3.30) will be put into a form with explicit closure modeling error $\epsilon_E V$:

$$\overline{\Phi}^T R = \overline{\Phi}^T L_h\left[\alpha_1 \nu_h^t \odot \left(S_h\left(\overline{\Phi}\overline{a}\right)\right)\right] + \epsilon_{\text{EV}} + \beta_1. \tag{3.32}$$

When POD expansion of EV is used (see section 2.5.1 and [14] by Hijazi et.al), $\nu_t^h \approx \eta g$, where $\eta \in \mathbb{R}^{3N_V \times M}$, $g \in \mathbb{R}^M$ the problem eq. (3.30) becomes:

$$\overline{\Phi}^T R = \overline{\Phi}^T L_h\left[\alpha_2 \left(\eta g\right) \odot \left(S_h\left(\overline{\Phi}\overline{a}\right)\right)\right] + \beta_2 + \epsilon_{\text{EVPOD}}, \tag{3.33}$$

now with a different error term. In either of equations eq. (3.32), eq. (3.33) α denotes a constant of the model, to be fit through least squares regression. In further discussion the dimensions of POD bases for velocity and eddy viscosity fields will be taken the same, i.e. M.

Consider just the projection onto k-th basis vector Φ_k, $k = 1, ..., M$. Consider i-th element of linear combination in POD expansion of FOM solution: $\Phi_i a_i(t)$ and only j-th element of POD expansion of EV field $\eta_j g_j(t)$, $i, j = 1, ...M$. Then the i-th component of turbulent ROM diffusion term in eq. (3.33) is:

$$\Phi_k^T L_h\left[\left(\eta_j g_j(t)\right) \odot \left(S_h \Phi_i\right) a_i(t)\right] = \underbrace{\Phi_k^T\left[\left(L_h \eta_j\right) \odot \left(S_h \Phi_i\right)\right]}_{H_{ijk}} a_i(t)\, g_j(t), \tag{3.34}$$

in which the time dependence has been made explicit for clarity. $H \in \mathbb{R}^{M \times M \times M}$ is a third order tensor. Precomputation of diffusion operator is achieved by reshaping H into $H^{mat} \in \mathbb{R}^{M \times M^2}$:

$$H^{mat} = \left[H_1, ..., H_M\right], \tag{3.35}$$

where each H_i is a $M \times M$ matrix with elements $[H_i]_{jk} = \Phi_k^T L_h\left(\eta_j \odot \Phi_i\right)$. This yields the following precomputed form:

$$\overline{\Phi}^T R = \alpha_2 \underbrace{H^{mat}\left[a(t) \otimes g(t)\right]}_{\overline{\Phi}^T W_2} + \beta_2 + \epsilon_{EVPOD}, \tag{3.36}$$

where $\otimes$ is the Kronecker product.

Precomputation involves H being 'matricized' (see analogous convection precomputed operator in [31] by Sanderse). Only right-hand side (RHS) of eq. (3.32) and eq. (3.33) contains ν_t. This eddy viscosity is based on eq. (2.34), with some alterations. Eddy viscosity eq. (2.34) was originally used by Aubry et al. [4], but for different type of flow: wall-bounded, where a special dependence was anticipated between of ν_t on wall-normal coordinate y. Here this model was only selected as it is a simple model. As the currently considered flow is not wall-bounded, for the purpose of the present research the integral along $x_2 = y$ in eq. (2.34) is omitted. Additionally filtering is applied with Gaussian filter kernel h, to aid in smoothing of the otherwise noisy field:

$$\nu_t\left(y, t\right) = h * \frac{\langle \boldsymbol{u}_> \cdot \boldsymbol{u}_> \rangle_{x,z}}{\sqrt{\left\langle \nabla \boldsymbol{u}_> : \nabla \boldsymbol{u}_> \right\rangle_{x,z}}}, \tag{3.37}$$

---

[2] Before projection the terms have a clear physical interpretation, e.g. $C_h\left(\overline{\Phi}\overline{a}\right)\Phi' a'$ is a term expressing convection of truncated scales by resolved scales, $\nu D_h \Phi' a'$ is diffusion of truncated scales and $L_h \nu_t S_h \overline{\Phi}\overline{a}$ is a term representing diffusion of resolved scales, with spatially varying (eddy) viscosity . After projection with $\overline{\Phi}^T$ some data is filtered out, since projection is filtering [39].

$$h(y,\xi) = \left(\frac{\gamma}{\pi\overline{\Delta}^2}\right)^{\frac{1}{2}} \exp\left(-\frac{\gamma|y-\xi|^2}{\overline{\Delta}^2}\right), \tag{3.38}$$

using always $\gamma = 6$, $\overline{\Delta} = \frac{8\pi}{\xi_{Nyq}}$. Symbols used above denote:

($*$) - convolution: $f(x) * g(x) := \int_{-\infty}^{+\infty} f(x-y)g(y)dy$,

(:) - double-dot product (for tensors): $\boldsymbol{T} : \boldsymbol{T} = \sum_i \sum_j T_{ij} T_{ij}$,

$\langle\cdot\rangle_{x,z}$ - x,z-averaging: $\langle\cdot\rangle_{x,z} := \frac{1}{L_x L_z}\int_0^{L_x}\int_0^{L_z}(\cdot)dxdz$.

Clearly therefore, what distinguishes EV used here, eq. (3.37) from eq. (2.34) is that the latter is constant, while the former varies in time and shear one coordinate direction. The discrete EV: v_h^t is arrived at by inserting discretized unresolved scale velocities $\left(V_h - \overline{\Phi}\overline{a}\right)$ for $\boldsymbol{u}_>$ and appropriate discrete operators for $< \cdot >_{x,z}$ and $\nabla(\cdot)$. The filtering is performed in wavenumber space, with FFT and FFT^{-1}. Since staggered grids are used, velocity components have separate locations in space (e.g.u-component is computed at different spatial points than v-component etc.). This necessitates interpolation to common grid. The pressure grid is chosen fo that, so that velocity is interpolated from cell walls onto cell centers. So computed EV has to be interpolated back to cell walls, so that it may be used in eq. (3.32) or eq. (3.33). So prepared eddy viscosity is ready for being tested in an 'a priori' analysis. The analysis will consist of plotting various terms of equations (3.30-3.31) separately and summed, as well as their magnitudes and also projections onto fine-scale subspace Φ'. In order to enable visualization, the terms will be averaged in xz plane (regardless of whether 1D or 3D EV was used).

3.2.3. LS regression

Least squares fit is performed of α, a multiplicative constant of ν_t, and an additive constant β . Regression is done on xz-averaged versions of eq. (3.30) and eq. (3.36). Such fit is done at each time step and resultant time-varying regression coefficients for various M are plotted.

The snapshots of discrete 1D eddy viscosity are given at each instant t_i, $i = 1,...,N_t$. The EV diffusion term in eq. (3.32), averaged over xz plane, is $\langle\overline{\Phi}\,\overline{\Phi}^T L_h \alpha_1 v_h^t S_h \overline{\Phi}\overline{a}\rangle_{xz} = \langle\overline{\Phi}\,\overline{\Phi} W_1\rangle_{xz} \in \mathbb{R}^{3N_y}$. The dimension is $3N_y$, because although the term had been averaged over two directions, it still has three components in each discrete point along y. Constants α_1, β_1 are regression coefficients and the functions $\langle\overline{\Phi}\,\overline{\Phi}^T W_1\rangle_{xz}$ and 1 (constant function) are the corresponding basis functions. Least squares fit is performed with target function being the entire averaged *reconstructed* LHS of eq. (3.30), $\langle\overline{\Phi}\,\overline{\Phi}^T R\rangle_{xz} \in \mathbb{R}^{3N_y}$. Since eq. (3.30) is in ROM space and the xy-averaging takes place in physical space, a left-multiplication by $\overline{\Phi}$ is needed to reconstruct the ROM projection in physical space. The least squares problem is posed:

$$\arg\min_{\alpha_1,\beta_1\in\mathbb{R}} \frac{1}{2}\left\|\langle\overline{\Phi}\,\overline{\Phi}^T R\rangle_{xz} - \alpha_1\langle\overline{\Phi}\,\overline{\Phi}^T W_1\rangle_{xz} - \beta_1\right\|^2. \tag{3.39}$$

At each time instant the coefficients are to be computed from (see appendix for detailed derivation):

$$\alpha_1 = \frac{\langle\overline{\Phi}\,\overline{\Phi}^T W_1\rangle_{xz}\cdot\langle\overline{\Phi}\,\overline{\Phi}^T R\rangle_{xz} - \frac{1}{3N_y}\left(\mathbf{1}_{3N_y}\cdot\langle\overline{\Phi}\,\overline{\Phi}^T R\rangle_{xz}\right)\left(\mathbf{1}_{3N_y}\cdot\langle\overline{\Phi}\,\overline{\Phi}^T W_1\rangle_{xz}\right)}{\left\|\langle\overline{\Phi}\,\overline{\Phi}^T W_1\rangle_{xz}\right\|^2 - \frac{1}{3N_y}\left(\mathbf{1}_{3N_y}\cdot\langle\overline{\Phi}\,\overline{\Phi}^T R\rangle_{xz}\right)^2}, \tag{3.40}$$

and

$$\beta_1 = \frac{1}{3N_y}\left(\mathbf{1}_{3N_y}\cdot\langle\overline{\Phi}\,\overline{\Phi}^T R\rangle_{xz} - \alpha_1\mathbf{1}_{3N_y}\cdot\langle\overline{\Phi}\,\overline{\Phi}^T W_1\rangle_{xz}\right), \tag{3.41}$$

where $\mathbf{1}_N$ is a vector of ones of length N, so that for any vector $V \in \mathbb{R}^N$, $V\cdot\mathbf{1} = \sum_i^N V_i$ i.e. scalar product of $\mathbf{1}$ and a vector yields sum of elements of this vector. With POD of EV the expressions (for α_2, β_2) are analogous. Since u-component is dominant in this flow, it is better to perform LS fit only on u-component of target function, i.e. $\langle\overline{\Phi}_u\overline{\Phi}_u^T R_u\rangle_{xz} = \left[\langle\overline{\Phi}\,\overline{\Phi}^T R\rangle_{xz}\right]_u \in \mathbb{R}^{N_y}$, because matching all three radically different and oscillating velocity components would result in unstable coefficient behaviour (concerning particularly β). This simplified problem is

$$\arg\min_{\alpha_1,\beta_1\in\mathbb{R}} \frac{1}{2}\left\| \langle \overline{\Phi}_u \overline{\Phi}_u^T R_u \rangle_{xz} - \alpha_1 \langle \overline{\Phi}_u \overline{\Phi}_u^T W_{1,u} \rangle_{xz} - \beta_1 \right\|^2. \tag{3.42}$$

In this case the constants for EV term are:

$$\alpha_1 = \frac{\langle \overline{\Phi}_u \overline{\Phi}_u^T W_{1,u} \rangle_{xz} \cdot \langle \overline{\Phi}_u \overline{\Phi}_u^T R_u \rangle_{xz} - \frac{1}{N_y}\left(\mathbf{1}_{N_y} \cdot \langle \overline{\Phi}_u \overline{\Phi}_u^T R_u \rangle_{xz}\right)\left(\mathbf{1}_{N_y} \cdot \langle \overline{\Phi}_u \overline{\Phi}_u^T W_{1,u} \rangle_{xz}\right)}{\left\| \langle \overline{\Phi}_u \overline{\Phi}_u^T W_{1,u} \rangle_{xz} \right\|^2 - \frac{1}{N_y}\left(\mathbf{1}_{N_y} \cdot \langle \overline{\Phi}_u \overline{\Phi}_u^T R_u \rangle_{xz}\right)^2}, \tag{3.43}$$

and

$$\beta_1 = \frac{1}{N_y}\left(\mathbf{1}_{N_y} \cdot \langle \overline{\Phi}_u \overline{\Phi}_u^T R_u \rangle_{xz} - \alpha_1 \mathbf{1}_{N_y} \cdot \langle \overline{\Phi}_u \overline{\Phi}_u^T W_{1,u} \rangle_{xz}\right), \tag{3.44}$$

and for α_2, β_2 in EV-POD analogously. This is the actual regression that is being performed in the course of a priori analysis, chapter 7. The above expressions may be found as solutions to a certain optimization problem, appendix A.8 in the appendix contains more details.

3.3. Error estimators

Here several measures of error are discussed. There are errors in the basis construction, but not in terms of how well the RB approximates the manifold of FOM, only how well cSVD is reproduced by iSVD. The ROM velocity error measure is the same as in [31] by Sanderse. There are some differences in energy error definition.

3.3.1. Errors in basis construction

Because ROM construction hinges on divergence-free property of each mode Φ_i, and (to a lesser extent) on orthogonality, these properties are in focus.

Firstly, orthogonality condition is $\Phi^T\Omega_h\Phi = \mathbb{I}_M$. Therefore, a reasonable orthogonality error L_2 measure would be $\epsilon^j_{ort} = \left\| \left(\Phi^T\Omega_h\Phi\right)_j - (\mathbb{I}_M)_j \right\|_{\Omega_h}, j = 1,...M$. Each column j contains the difference between scalar products of j-th vector with all others **and** a column of identity matrix with 1 in j-th row. It is therefore a pairwise quantity. It is somewhat problematic to interpret, however when vectors are exactly orthogonal, this quantity will be zero. Thus it may be treated as a sort of binary indicator.

Secondly, divergence error is defined:

$$\epsilon^i_{div} = \left\| M_h\Phi_i \right\|_{\Omega_h}, \tag{3.45}$$

here with simpler interpretation. Namely, it is an integral measure of divergence in each mode $i = 1,...M$.

Both of these errors will be tested against two iSVD parameters: k_{add} and M_{dom}, see algorithm 1 and section 4.4.2). To further reduce data, to make the measures even more concise, Frobenius weighted norm is applied:

$$\epsilon^F_{ort} = \| \underbrace{\Phi^T\Omega_h\Phi - \mathbb{I}_M}_{\epsilon} \|^F_{\Omega_h} = \sqrt{\sum_{i=1}^{M}\sum_{j=1}^{M}\left([\epsilon]_{ij}\right)^2}. \tag{3.46}$$

This is similar to ϵ_{ort}, only characterizes the orthogonality error over the whole set of vectors with a single number. The quantity will be computed for $\dim(\Phi) = M_{dom}$ and divided by no. of columns/modes, so that eventually $\frac{\epsilon^F_{ort}}{M_{dom}}$ will be plotted and compared with reference quantity of this error (for modes constructed via classical SVD (cSVD)). Similar error may be constructed for divergence in an analogous way, only $i = 1,...N$.

Finally, mode-to-mode point-wise L_2 error w.r. to cSVD is computed:

$$\epsilon^i_{modal} = \left\| \Phi^{iSVD}_i - \Phi^{cSVD}_i \right\|_{\Omega_h}. \tag{3.47}$$

Baker et al. in [5] use different criteria than eq. (3.47) to assess the fidelity of iSVD left-singular basis. Instead of looking at the differences between modes of the same index, they measure difference between two subspaces. This is performed through computation of canonical angles between spaces. The procedure was found too complex for the present research, hence mode-to-mode pointwise error is the basic tool to assess accuracy of iSVD basis w.r. to cSVD.

3.3.2. Errors in the solution

The main variable of interest is the field that is being approximated: velocity field. The approximation is $V_h \approx V_r = \Phi a$. Apart from direct examination of the difference between FOM and ROM-reconstructed solutions

$$\epsilon_{ROM}(t_i) = \frac{\left\| V_h(t_i) - V_r(t_i) \right\|_{\Omega_h}}{\left\| V_h(t_i) \right\|_{\Omega_h}} = \frac{\left\| V_h(t_i) - \Phi a(t_i) \right\|_{\Omega_h}}{\left\| V_h(t_i) \right\|_{\Omega_h}}, \tag{3.48}$$

the ROM is compared to the best possible ROM solution on that basis (V_{best}), i.e. FOM solution $V_h(t_i)$ projected at each time step onto M-dimensional reduced space span(Φ):

$$\epsilon_{best}(t_i) = \frac{\left\| V_h(t_i) - V_{best}(t_i) \right\|_{\Omega_h}}{\left\| V_h(t_i) \right\|_{\Omega_h}} = \frac{\left\| V_h(t_i) - \Phi\Phi^T \Omega_h V_h(t_i) \right\|_{\Omega_h}}{\left\| V_h(t_i) \right\|_{\Omega_h}}. \tag{3.49}$$

Both of these errors are normalized by the Ω_h-norm of the FOM solution.

Errors in integral quantities like global kinetic energy $k(t) = \frac{1}{2}(\boldsymbol{u}, \boldsymbol{u})_\Omega$ and momentum $P(t) = \int_\Omega \boldsymbol{u} d\Omega$ are also of interest. The following error measures are proposed:

$$\epsilon_K(t_i) = \frac{K^{ROM}(t_i) - K^{FOM}(t_i)}{K^{FOM}(t_i)}, \tag{3.50}$$

$$\epsilon_{P_u}(t_i) = \frac{P_u^{ROM}(t_i) - P_u^{FOM}(0)}{P_u^{FOM}(0)}. \tag{3.51}$$

Both of these error measures are allowed to change sign, so that relation to reference quantity is better visualized (whether it is under- or over-estimated). Reference for kinetic energy error is FOM solution at time t_i while for the u-momentum it is the FOM solution at initial instant. While the former is a reasonable choice for non-equilibrium systems the latter does not always make sense when no distinct mean flow exists (see TG vortex solutions).

Finally, an error that is particularly important in incompressible flows - divergence error - is being measured as simply $\epsilon_{div}(t_i) = \left\| M_h V_h(t_i) \right\|_\infty$, where $\|\cdot\|_\infty$ is maximum norm. It is not normalized, because $\nabla \cdot \boldsymbol{u}$ should be as small (or as close to 0) as possible.

3.4. Other investigated quantities

3.4.1. Energy spectrum

Instantaneous spectra of FOM and ROM solutions, V_h, V_r will be considered. These will be computed from snapshots. To simplify, an approach usually used in homogeneous isotropic turbulence (HIT) will be applied here. Namely, spectral energies corresponding to different wavenumbers but with magnitudes from the same discrete interval (discretized sphere) are summed.

$$\hat{K}(\xi_m, t) := \sum_{\xi_0\left(m-\frac{1}{2}\right) \le |\boldsymbol{\xi}| < \xi_0\left(m+\frac{1}{2}\right)} \frac{1}{2} \hat{\boldsymbol{u}}(\boldsymbol{\xi}, t) \cdot \hat{\boldsymbol{u}}^*(\boldsymbol{\xi}, t), \tag{3.52}$$

where $\hat{\boldsymbol{u}}$ is a spatial Fourier transform of the velocity field $\boldsymbol{u}$ and $\hat{\boldsymbol{u}}^*$ is its complex conjugate, $\xi_{0,x} = \frac{L}{2\pi}$ is the base wavenumber associated to x, $\xi_0 = \sqrt{\xi_{0,x}^2 + \xi_{0,y}^2 + \xi_{0,z}^2}$ - magnitude of base wavenumber vector and $\boldsymbol{\xi} \in \mathbb{R}^3$ is the wavenumber vector $\boldsymbol{\xi} := \xi_0 \boldsymbol{n} = (\boldsymbol{e}_1 n_1 + \boldsymbol{e}_2 n_2 + \boldsymbol{e}_3 n_3)$ with e_i - unit coordinate vectors, $\boldsymbol{n}$ - vector of wavenumber indices, m - index of the integer wavenumber $\xi_m = \xi_0 m$. With these symbols the relation between velocity field and its Fourier transform is

$$\boldsymbol{u} = \sum_{\boldsymbol{\xi}} e^{I \boldsymbol{\xi} \cdot \boldsymbol{x}} \hat{\boldsymbol{u}}, \tag{3.53}$$

where I-imaginary unit, $\boldsymbol{x}$ is the spatial coordinate and both $\boldsymbol{x}, \boldsymbol{\xi} \in \boldsymbol{R}^3$.

Those spectra are not full spectra of energy, but projections onto integer-wavenumber space. In vector-wavenumber space each wavenumber vector has its associated energy. The projection is performed, such that energy associated to all wavenumber vectors of a particular magnitude (i.e. lying on a sphere) is summed and assigned to an ’integer wavenumber’ corresponding to that magnitude.

On finite mesh, there exists maximum representable wavenumber: the Nyquist wavenumber. It is estimated as $\xi_{Nyquist} \approx \frac{\pi}{h_x}$ for domain length $L = 2\pi$. In actual numerical computations Fourier transform is performed via FFT and V_h, V_r snapshot vectors are considered instead of the continuous fields $\boldsymbol{u}$.

4

Setup of numerical experiments

This chapter is a description of numerical experiments performed in the study. Information on test cases, is found in section 4.1. Throughout this research explicit 4^{th} order Runge-Kutta time stepping scheme is used with $\Delta t = 0.01$. Consequences of this choice are briefly discussed in section 4.3. Key part with descriptions of experiments is contained in section 4.2. Section 4.4 summarizes the software packages and settings used in the research.

In all experiments equidistant uniform cartesian grids are used, i.e. all cells are identical. Spatial discretization is performed with FV second order scheme on staggered grids. ROMs are velocity-only, but it is more convenient to state mesh size using pressure nodes, which are centered at cells, whose walls correspond to velocity fluxes. For FOM total number of variables is $N_V + N_p$, but N_p cells constitute primordial mesh, out of which (by translations along x, y, z) three staggered grids (with a total of N_V cells) are derived. For simplicity, mesh size will be given using N_p, e.g. coarse grid is $N_p = 150^3$, but its total number of DoF is $N_p + N_V = 150^3 + 3 \cdot 150^3$.

4.1. Test cases

Two test cases are investigated: periodic shear layer (SL) and periodic Taylor-Green vortex (TG). In either case the domain is a periodic box $L \times L \times L$ with $L = 2\pi$ (SL) and $L = 2$ (TG). Reynolds number is $Re = 1000$.

Initial condition for shear layer is given by:

$$u_0 = 1 + \epsilon \sin z + \begin{cases} \tanh \frac{y - \frac{\pi}{2}}{\delta} & \text{if } y \leq \pi \\ \tanh \frac{\frac{3\pi}{2} - y}{\delta} & \text{if } y > \pi \end{cases}, \tag{4.1}$$

$$v_0 = w_0 = \epsilon \sin x, \tag{4.2}$$

with $\epsilon = 0.05$ and $\delta = \frac{\pi}{15}$.

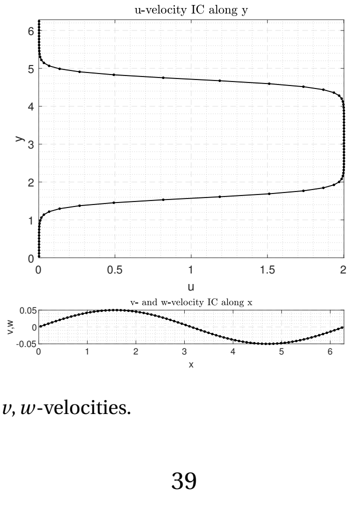

Figure 4.1: Shear layer: Initial conditions for u, v, w-velocities.

Initial velocity field has an additional small disturbance along x in v, w components, see fig. 4.1 and along z in u component.

Initial condition for Taylor-Green vortex is given by:

$$u_0 = -\sin(\pi x)\cos(\pi y)\cos(\pi z), \tag{4.3}$$

$$v_0 = 2\cos(\pi x)\sin(\pi y)\cos(\pi z), \tag{4.4}$$

$$w_0 = -\cos(\pi x)\cos(\pi y)\sin(\pi z). \tag{4.5}$$

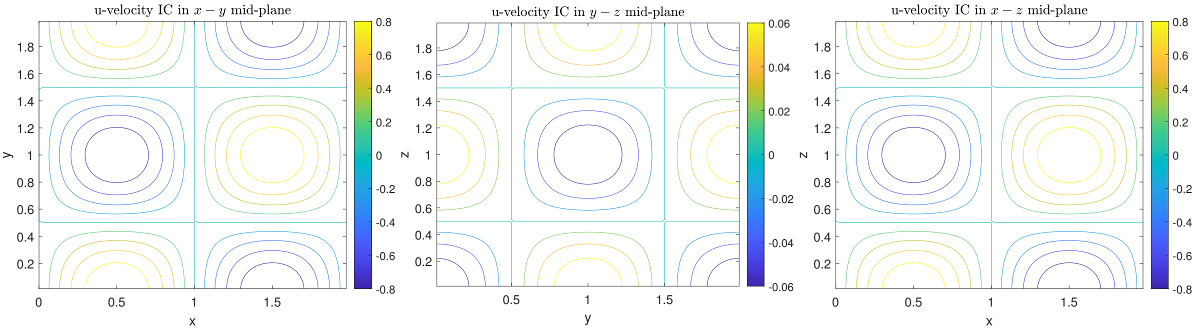

Figure 4.2: Taylor-Green Vortex: Initial condition for u-velocity, sections in 3 midplanes.

4.2. Experiments

This section provides an overview of numerical experiments performed during the research: reduced basis quality check (section 4.2.1), ROM simulations (section 4.2.2) and a priori analysis section 4.2.3.

4.2.1. RB quality tests

In this section plan of assessing the quality of iSVD basis is laid out.

Testing basis quality is performed on SL test case, using coarse-grid FOM, $N_p = 150^3$ with $t_{end} = 20$, $\Delta t = 0.01$ $N_t = 2001$. Three parameters considered crucial for iSVD are varied separately: increment size ($k_{add} = 1, 10, 100$), maximum number of singular values sought $M_{dom} = 50, 100, 200$, and threshold $= 10^{-10}, 10^{-8}, 10^{-6}$. The resultant bases are then either: left untreated, orthogonalized by Gram-Schmidt procedure or made divergence-free through Helmholtz decomposition or both. A separate case is also examined: using 50% downsampled snapshot set, i.e. every 2^{nd} snapshot is taken for SVD. These tests are aimed at measuring the influence of the three iSVD parameters: k_{add}, M_{dom} and threshold, on the two important properties of RB: orthogonality and solenoidity (zero-divergence) and on the fidelity to cSVD basis. Wavenumber and singular value spectra are also examined. In order to measure the combined influence of pairs of iSVD parameters on quality of the basis, Frobenius norm is applied to compute errors in orthogonality and divergence. This way no information on error distribution over modes is known, but it is possible to assess the combined influence of M_{dom}, k_{add} and threshold on the whole reduced basis quality.

An auxiliary experiment is planned, aimed at checking how robust ROM is w.r. to basis accuracy in general. The first step is to obtain a basis from cSVD, then modify it (description in the present section), and finally, test it in a ROM simulation (described in section 4.2.2). The two distinct modifications performed are the following.

- Distortion according to:

  $$\tilde{\Phi}_{ij} = \Phi_{ij} + c_i X, \tag{4.6}$$

  where $X \sim \mathcal{N}(0,1)$ is a random variable with standard normal distribution and $c_i = p \cdot \frac{1}{M}\sum_j |\Phi_{ij}|$ is an l_1 norm, with $p = 5\%, 10\%$ - percentage, multiplicative/scaling factor. This is simply white noise.

- Rotation in such way that each pair of *subsequent* modes ($\Phi_1 - \Phi_2, \Phi_2 - \Phi_3, \ldots$) is rotated about $(M-2)$-dimensional subspace of the reduced space $\text{span}(\Phi)$, spanned by the 'remaining' vectors (ones not rotated at a given rotation stage). All such rotations are comprised in an orthogonal full-rank transformation matrix $R_1 \cdot R_2 \ldots \cdot R_M = R \in \mathbb{R}^{M \times M}$, where rotation 2×2 'mini-matrix' at each stage is:

  $$r_i = \begin{bmatrix} \cos\alpha_i & -\sin\alpha_i \\ \sin\alpha_i & \cos\alpha_i \end{bmatrix}, \tag{4.7}$$

and is to be installed into an all-zeroes $M \times M$ matrix R_i on row positions $(i, i+1)$ and column positions $(i, i+1)$.

To obtain a rotated basis $\hat{\Phi}$ one must transform Φ according to $\hat{\Phi} = \Phi R$, where the multiplication with R is on the right side, because it is the *columns* of Φ that are being rotated. Angles of rotation are also random, between 0 and $\frac{\pi}{2}$, as in $\alpha_i = Y_i \cdot \frac{\pi}{2}$, where $Y_i \sim \mathscr{U}(0,1)$ is a random variable with uniform distribution. A simple explanation of why the rotated basis must provide the same ROM solution (down to roundoff errors) is the following. ROM is an approximation to FOM given by:

$$V_h \approx V_r = \Phi a. \tag{4.8}$$

Another approximation (with different basis and coefficient, but of the same dimension) is:

$$V_h \approx \hat{V}_r = \hat{\Phi}\hat{a}. \tag{4.9}$$

Given any orthogonal matrix R ($RR^T = R^T R = \mathbb{I}$), we may write:

$$V_r = \Phi a = \Phi \mathbb{I} a = \Phi R R^T a, \tag{4.10}$$

which shows that when the rotated ROM is defined via:

$$\hat{\Phi} = \Phi R, \tag{4.11}$$

and

$$\hat{a} = R^T a, \tag{4.12}$$

it holds that $V_r = \hat{V}_r$. It is therefore obvious that there is no sense in performing analysis of rotated-basis ROM simulations, because the results will be the same as in case of non-rotated basis. However, basis quality itself will be checked for rotated basis.

4.2.2. ROM simulations

Simulations are performed mainly on the grid, $N_p = 250^3$. An exception are simulations with distorted basis, which were run on coarse grid $N_p = 150^3$. FOM data is available up until $t_{end} = 20$ ($t_{end} = 10$ in TG). Time step is set to $\Delta t = 0.01$. Dimension of FOM snapshot matrix is $N_V \times N_t$, where N_t is the number of snapshots , including IC-snapshot. The following ROM simulations are performed:

1. SL with $t_{end} = 20$ (referred to as long period), on fine grid, using iSVD non-treated basis with $k_{add} = 100$, $M_{dom} = 100$, threshold 10^{-6}, $M = 8, 16, 32, 48$
2. SL exact as above, with 50% downsampling
3. SL exact as item 1. only with Helmholtz and Gram-Schmidt treatment
4. SL with $t_{end} = 10$ on coarse grid, using cSVD-basis with $5-10\%$ distortion $M = 8, 16$
5. SL with $t_{end} = 10$ on fine grid, with enfored momentum conservation, using iSVD-basis with $k_{add} = 100$, $M_{dom} = 100$, threshold 10^{-6}, $M = 11, 19, 35$
6. SL with extrapolation from FOM $t_{end} = 10$ to ROM $t_{end} = 15$ on fine grid, using iSVD-basis with $k_{add} = 100$, $M_{dom} = 100$, threshold 10^{-6}, $M = 8, 16, 32, 48$
7. TG with $t_{end} = 10$ on fine grid, using iSVD-basis with Helmholtz and GS treatment, with $k_{add} = 100$, $M_{dom} = 100$, threshold 10^{-6}, $M = 8, 16, 32, 48$

4.2.3. A priori test

A priori turbulence modeling test (results in chapter 7) is limited to the SL case. Basis used to simulate ROM (item 3 on the list in section 4.2.2)is selected for the investigation. Tests follow the exact methodology of section 3.2.

4.3. Estimation of some grid parameters

Let L be the length of a side of the discrete periodic domain Ω_h: a periodic box $L \times L \times L$. Let N_x, N_y, N_z be the numbers of pressure grid cells in x, y, z- directions, and $N_p = N_x \times N_y \times N_z$ total number of pressure cells. To capture a vortex in 3D, at least 3 nodes (cells) are needed in each direction, a total of 7 nodes (center node is shared). That is, assuming that the vortex is aligned with the grid, with axis along one of the coordinate directions. With a mesh uniform in all directions, of cell size $h_x = \frac{L}{N_x}$ this means that the smallest represented scales are of the size $\approx 2\frac{L}{N_x} = h$. Domain sizes differ for the investigated cases and also two grids are investigated (coarse and fine), thus different values are obtained for different scenarios. A 4^{th} order explicit Runge-Kutta time march (RK4) is used. In this case the scheme is stable for Courant number $c \le c_{max} = 2\sqrt{2} \approx 2.8$, following [15] by Hirsch. This dimensionless parameter reflects the fraction of a single cell that a disturbance travels within Δt interval (after LeVeque [19]). A rough estimate on Courant number in the present scenario (with nonlinear convective term) is made based on 2-norm and linear advection equation:

$$c = \sqrt{\left(\frac{u_0 \Delta t}{h_x}\right)^2 + \left(\frac{v_0 \Delta t}{h_y}\right)^2 + \left(\frac{w_0 \Delta t}{h_z}\right)^2} = \underbrace{\sqrt{u_0^2 + v_0^2 + w_0^2}}_{q} \frac{\Delta t}{h}. \tag{4.13}$$

Following Hirsch [15], when 2^{nd} order central scheme is applied to linear advection equation with periodic BCs and advection velocity q, the resulting system of ODEs has only imaginary eigenvalues:

$$\lambda \Delta t = -I \underbrace{\frac{q \Delta t}{h}}_{c} \sin\phi, \tag{4.14}$$

where I denotes the imaginary unit, $\lambda \in \mathbb{C}$ is a eigenvalue of the system of ODEs to be solved and $\phi \in (-\pi, \pi)$ is a so called phase angle. An estimate on magnitude of largest/smallest eigenvalues is:

$$|\lambda_{max}| \Delta t = \frac{q \Delta t}{h} = c. \tag{4.15}$$

RK4 method includes a part of imaginary axis as a border line of its stability region, however it is more prudent to remain further inside the region. This is aided by viscosity term, naturally present in the analyzed NS equation. Positive viscosity pulls the eigenvalue spectrum in negative real axis direction. On the other hand, when diffusion equation is considered, all eigenvalues lie on the negative real axis and CFL condition is then $\frac{4}{Re}\frac{\Delta t}{h^2} < c_{max}$. This condition for low Reynolds number can be difficult to satisfy by explicit schemes, requiring very small Δt. The region of stability of RK4 on purely real axis extends also to $\lambda_{min} \Delta t = -2\sqrt{2}$, which leads to $c_{max} \approx 2.8$. Using either SL or TG test case grid size and time step, this condition would be met.

The research did not concern stability of numerical schemes, it was assumed that, albeit non-optimally, the time step was selected such that guaranteed stability, $\Delta t = 0.01$. It was used on all simulations on all grids, but perhaps was excessively small for $N_p = 150^3$. For shear layer case, on the fine uniform grid with $N_p = 250^3$ pressure cells and domain length $L = 2\pi$, the length of cell is $h = \frac{2\pi}{250} \approx 0.025$. Based on initial condition, arguing that the velocity components will not substantially increase all at once in the investigated period (as they only evolve from IC and no energy is put into the system), the rough estimate of CFL may be stated $c \approx \sqrt{2^2 + 2 \cdot 0.05^2}\frac{0.01}{0.025} \approx 0.8 \le c_{max}$. This condition is thus met on the fine mesh, an even more so, on the coarse mesh, in shear layer case.

For the Taylor-Green case, the estimates are less optimistic. Domain length is $L = 2$, which gives $h = 0.008$, so smaller vortex size is achievable, but IC results in higher values of v, w velocity components, and such h means division by smaller number resulting in estimate $c \approx \sqrt{1^2 + 1^2 + 1^2}\frac{0.01}{0.008} \approx 2.17 < c_{max}$. The risk of instability at the present time step size is therefore higher here than in SL test case. Looking at stability regions of RK4 method (fig. 4.3), this sentence should be refined. The risk of instability due to excessive viscosity is higher than in S-L case, as the method is now operating on imaginary axis values varying in range ±2.17. On higher levels on imaginary axis, the stability region does not reach as far in negative real axis values as in SL case with $c \approx 0.8$. Hence there is a risk that for an excessively high viscosity some eigenvalues would be drawn to the left of RK4 stability region.

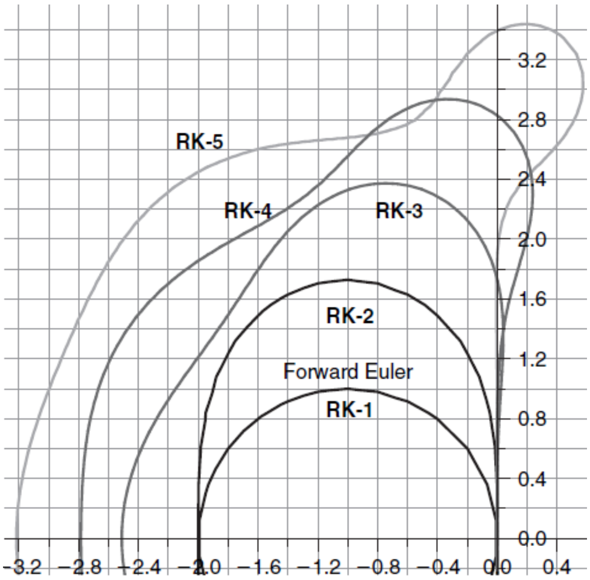

Figure 4.3: Stability regions of Runge-Kutta methods [15]. Here abscissa and ordinates are real and imaginary axes respectively, $Re(\lambda), Im(\lambda)$

.

Nevertheless, an educated guess is that for both test cases and on either mesh, given the spatial and temporal discretization, the CFL stability condition is met.

A sufficient (but not necessary) condition, for spatial stability, is the condition on mesh Peclet number:

$$Pe_x = \frac{u \cdot h_x}{1/Re} < 2. \tag{4.16}$$

It is more stringent than CFL condition in case of temporal stability analysis and actually is not met on either mesh. For example in SL case, fine mesh has $Pe \approx 50$, while the coarse mesh Peclet number is $Pe \approx 83$. Nevertheless, wiggles do not appear in the FOM solution until almost the end of simulation, thus this condition was ignored.

The research was focused on reproduction of FOM solution, which was assumed accurate enough to remain relevant for turbulent flow problems.

4.4. Software

4.4.1. FOM/ROM solver

The Matlab code INS3D (compare with [31] by Sanderse where INS2D was used) is used to perform all the computations. Essentially INS3D had been tested and verified as FOM solver (see [31] by Sanderse), but the ROM functionality was only available in 2D version. Some generalization was performed on the INS2D-ROM code in the preliminary stage of the present project. The process included adding additional code to precompute 3D-ROM operators.

4.4.2. iSVD package

Baker et al. in [5] use a software package of their invention, *IMTSL*. The package contains more than just the incremental SVD algorithm, but it is the implementation of this algorithm, contained within a subpackage *incPACK2* that is the focus of the present section.

The algorithm itself is described in the previous chapter, Algorithm 1. Although incPACK2 has multi-pass functionality (constructing basis incrementally by several passes through snapshot matrix), only single-pass method is used at present. The primary goal of iSVD in the present project is to save operational memory by performing SVD in sequence (or incremental fashion). The authors of [5] and incPACK2 made it possible (which is not the case for later versions of this software) to load snapshots from HDD in parts. After an update of SVD by each new group, the group is removed from operational memory, the decomposition is truncated and a new group is loaded. A single feature of the code allowed this: the main argument of iSVD main function *seqkl* - the snapshot matrix - may be defined as a *function handle*. The only arguments that this handle is 'interested in', are the initial column and the number of columns (starting from the initial) that will be taken as input.

$$X_j = @(start, num)\textbf{getFromHDD}\left(\Omega_h^{\frac{1}{2}}, path_{FOM}, start, num\right). \tag{4.17}$$

As seen from the above user-definition, calling X_j with two arguments results in uploading appropriate groups of columns into operational memory from the pre-defined path, with prescribed weights $\Omega_h^{\frac{1}{2}}$. Once the whole pass is complete, the resultant left-singular vectors Φ are transformed back by $\Omega_h^{-\frac{1}{2}}$ (see modified problem eq. (2.23)).

The number of dominant singular subspaces sought, M_{dom}, is set beforehand. It regulates the size of the final output dimension of RB and is related to the transformation matrices G in Algorithm 1 in section 2.4.4 pt.7. It may be influenced by threshold, also set a priori. Threshold, treated as an absolute quantity after each increment eliminates all singular values (and their corresponding singular vectors) below its value, $\sigma_i < thr$. The relative threshold does essentially the same, only the value of cut-off may vary, depending on the maximum (in current incremental step) singular value, $\frac{\sigma_i}{\max \sigma_i} < thr$.

It is possible to set maximum and minimum increment size, as well as the size of first increment. For simplicity in this research the increment size in each incremental step is taken the same and denoted $k_{add} = l_{max} = l_{min} = l_1$ (see Algorithm 1 in section 2.4.4 and Baker's manual to iSVD [1]). An exception is found in the last increment (in present research) due to the fact, that the no. of snapshots N_t is generally not an integer multiple of k_{add}. For example when $t_{end} = 10$, $\Delta t = 0.01$, then $N_t = 1001$. Hence with $k_{add} = 10, 100$ the last increment is always a single snapshot.

5

Basis computation

In the present chapter, results of iSVD analysis are presented. FOM is obtained on coarse grid $N_p = 150$, $\Delta t = 0.01$ and $t_{end} = 20$. The data from FOM is contained in $N_t = 2001$ snapshots and serves to compute basis via either conventional or incremental SVD. Flow test case considered in section 5.1 is shear layer (SL). Three main types of basis are investigated: basis without treatment; basis with treatment and non-treated downsampled basis. The treatment is either Gram-Schmidt orthogonalization or extraction of divergence-free part via Helmholtz decomposition, or both of those. Additionally, distorted and rotated bases are checked. The results are described in section 5.1. In section 5.2 iso-surfaces of selected modes are displayed for both flow test cases (SL and TG). Comparison of spectra of selected modes is performed in section 5.3, while section 5.4 compares singular value decay of SL and TG cases. The brief section 5.5 explains applications of the findings to further analysis.

5.1. Basis quality

Only SL test case is considered in this section. Orthogonality, zero-divergence property and deviation from reference (cSVD) shapes of modes are examined by measures explained in section 3.3.

Bases in the present section are constructed from FOM with grid size $N_p = 150^3$ and $t_{end} = 20$. The following bases are constructed with iSVD:

- Full set of snapshots, no additional treatment of the basis,
- Full set of snapshots, Gram-Schmidt orthogonalization applied to the basis,
- Full set of snapshots, Helmholtz decomposition applied to the basis,
- 50% downsampled set of snapshots, no additional treatment of basis.

The analysis is primarily done on the basis constructed with full set of snapshots and no additional treatment. The aim is to identify iSVD settings that provide satisfactory basis quality. The influence of three iSVD parameters is investigated: size of a single increment (k_{add}), maximum number of singular values sought (M_{dom}) and threshold, see section 2.4.4. The various types of treatments from the above list are compared in each subsection as well, for selected fixed iSVD parameters. Typically three values are used for each of those parameters, which will be sometimes referred to as *low, middle* and *high*.

Frobenius norm is used to compare orthogonality (section 5.1.1) and divergence (section 5.1.2) errors for varying two iSVD parameters with the third one fixed. In the latter section, divergence error is plotted also per-mode. Section 5.1.3 contains plots of errors between modes of the same indices of iSVD and cSVD, for various settings of iSVD parameters. Singular value decay is presented in section 5.1.4 for selected cases. Finally, cSVD (reference) basis (with $N_p = 150^3$) is randomly distorted or rotated. The resultant basis is also checked for orthogonality and zero-divergence and compared with reference basis (section 5.1.5).

5.1.1. Orthogonality

In this section various settings iSVD are presented with their influence on the orthogonality of the basis. Frobenius norm is used as a tool to enable overall comparison of all basis approximations obtained with various k_{add}, M_{dom} and threshold. The value of the Frobenius-norm error is divided by the number of modes in the analyzed set, to obtain a per-mode value. The effect of downsampling is also included. Furthermore, the influence of treatment (Helmholtz and GS) is analyzed.

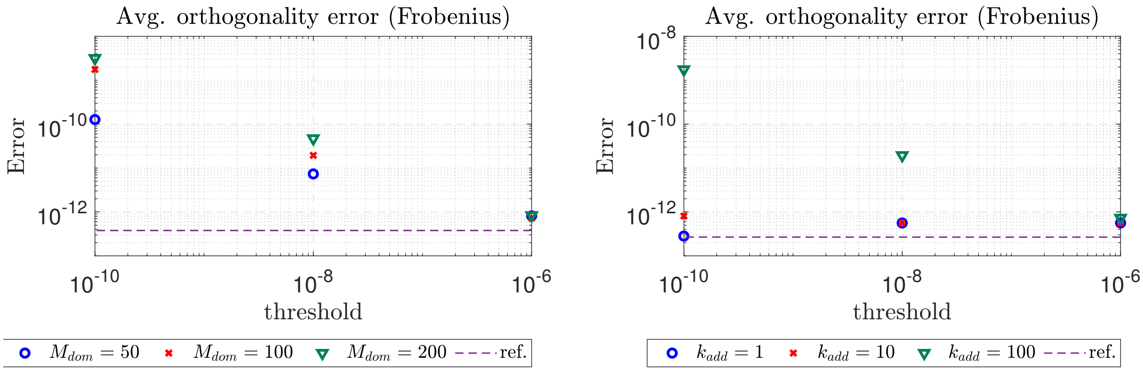

(a) With varying M_{dom}

(b) With varying k_{add}

Figure 5.1: Frobenius L_2 orthogonality error, $\|\mathbb{I} - \Phi^T \Omega_h \Phi\|^F_{\Omega_h}$. Influence of threshold, k_{add} and M_{dom}

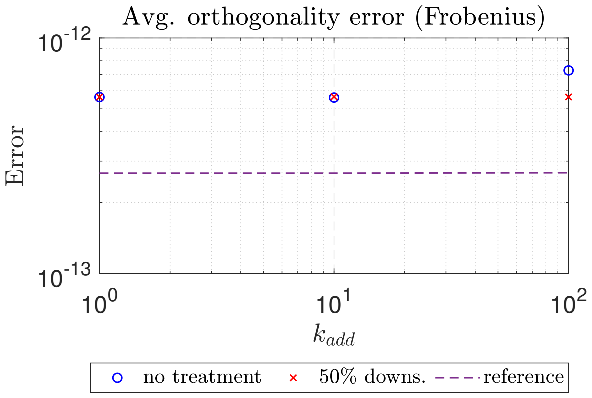

Figure 5.2: Frobenius L_2 orthogonality error, $\|\mathbb{I} - \Phi^T \Omega_h \Phi\|^F_{\Omega_h}$. Influence of k_{add} and downsampling.

The test, whose results are displayed in fig. 5.1a, is performed with $k_{add} = 100$. The figure indicates, that threshold has detrimental influence on orthogonality error, namely the error decreases with rising threshold. Moreover, with high threshold, M_{dom} does not influence the error. This may be explained by the following reasoning. In SL case there is a slow development of flow in the beginning phase, hence the snapshots are highly correlated in that period which makes them close linear dependent. The increment size is fixed. With a low threshold and high M_{dom} many singular values vectors must be computed in an incremental step. Since in any added block during the first phase, $t \in [0, 5]$, the snapshots are correlated, the intermediate Gram-Schmidt orthogonalization (see section 2.4.4) does not output a well orthogonalized set of vectors. Also, at one such incremental step, errors in computation of small singular values appear, which are transferred to the next incremental step. Those errors appear because there is only a limited number of large singular values of a matrix with highly correlated columns. The decay is rapid and thus most of the singular values that are computed during a step are prone to numerical (iSVD) and roundoff errors.

The next test, fig. 5.1b, is performed at $M_{dom} = 100$. It appears that the increment size k_{add} influences orthogonality error, in such way that at low threshold lower error is produced with smaller increments than with larger. At higher threshold the differences between errors for different k_{add} are smaller. For single-snapshot incrementation and for $k_{add} = 10$ the error is maintained low and is rather insensitive to threshold. With $k_{add} = 100$ the strong influence of threshold is observable. The explanation is similar as before, low threshold and still fairly high $M_{dom} = 100$ necessitate error-generating computation of small singular values in the initial increments. For low k_{add} this is avoided in the presented threshold range.

Influence of k_{add} and temporal downsampling of snapshot set is presented in fig. 5.2, where $M_{dom} = 100$ and threshold 10^{-6} were applied. Every 2^{nd} snapshot was skipped in construction of basis. Influence of downsampling seems insignificant.

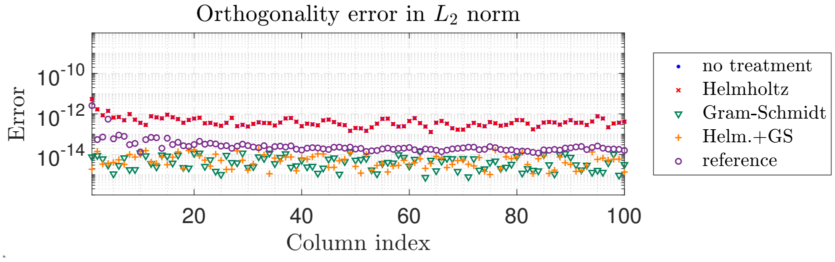

(a) High threshold

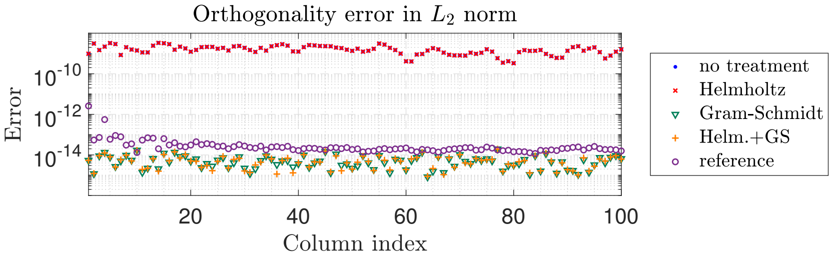

(b) Low threshold

Figure 5.3: L_2 orthogonality error, $\|\mathbb{I} - \Phi^T \Omega_h \Phi\|_{\Omega_h}$. Influence of Gram-Schmidt and Helmholtz procedures.

As depicted in fig. 5.3, there is practically no influence of Helmholtz deomposition on basis orthogonality, that is if only this treatment is applied. The data points coincide with those of non-treated basis for both thresholds. GS process essentially performs as desired. Interestingly, after orthogonalization, Helmholtz procedure does change the orthogonality error. It occurs possibly because Helmholtz procedure makes alterations of the order $\sim 10^{-14}$ to the modes. It cannot be therefore ruled out that if stronger violation of zero-divergence condition had occured the treated modes would have been affected in terms of their orthogonality.

5.1.2. Zero-Divergence

This section is focused on divergence error and uses similar tools as the previous section, i.e. Frobenius norm. However, the error in divergence is differently defined, $\epsilon^i_{div} := \|M_h \Phi_i\|_{L_2}$, i.e. it is not pairwise as the error in orthogonality. Therefore it is easier to draw conclusions regarding error in particular modes separately.

From fig. 5.4 it seems that threshold does not affect the error in divergence. The influence of M_{dom}, as will become clear from the more detailed plots, is due to larger divergence error in higher index modes, which increases the Frobenius error also in cSVD. This error is averaged (divided by given M_{dom}, see section 3.3), therefore any effect of cumulation of error due to larger number of modes is already ruled out. Increment size k_{add} is more decisive. It is noted, that for single snapshot incrementation, error in divergence is lower than for reference cSVD. In fact the error for $k_{add} = 10$ is two orders of magnitude larger. Further increase of increment size yields only minor increase in error.

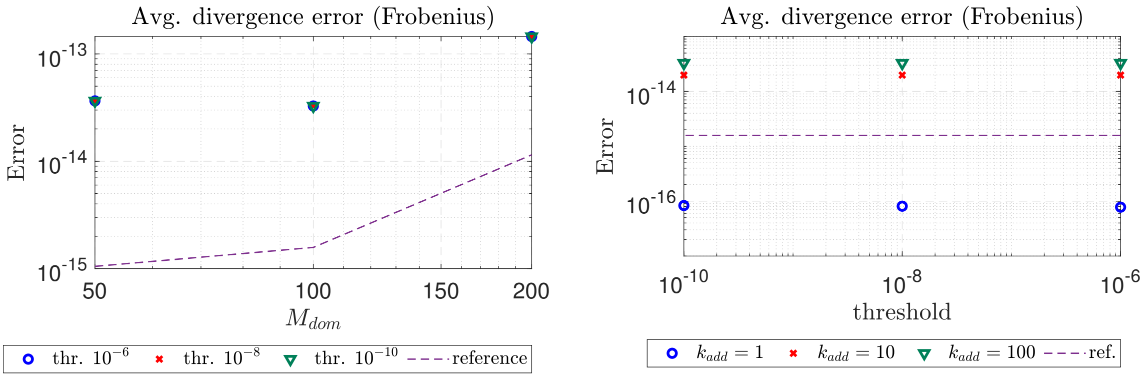

Figure 5.4: Frobenius L_2 divergence error, $\|M_h \Phi\|^F_{\Omega_h}$.

As observed in fig. 5.5, downsampling has little to no effect on the error in divergence, at $M_{dom} = 100$ and threshold 10^{-6}. It should be noted that the downsampled snapshot set is processed in half the number of incremental steps needed for the full set. This means that if an incremental block of the full set ends with the snapshot $V_h(t)$ then the incremental block of downsampled set ends with the snapshot $V_h(2t)$. This allows to suspect that divergence error generated by iSVD does not depend much on particular relations between snapshots (e.g. how correlated they are).

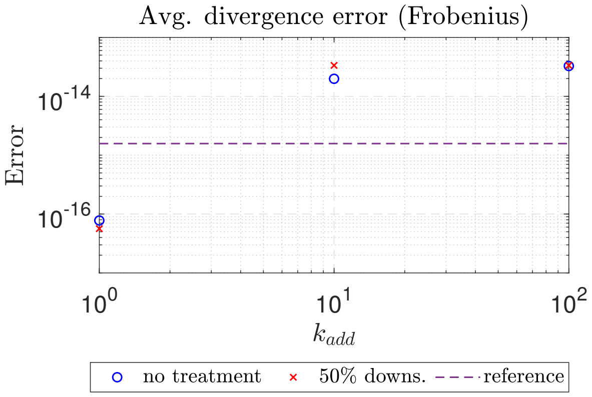

Figure 5.5: Frobenius L_2 divergence error, $\|M_h \Phi\|^F_{\Omega_h}$. Influence of downsampling.

M_{dom} seems to be having only marginal influence on divergence error. Threshold also has little effect. Plots fig. 5.6 and fig. 5.7 display a more detailed information about the errors, in particular that there is a tendency that only low-index modes are satisfactorily divergence-free. Thus the increment size dictates the quality of the basis in this aspect.

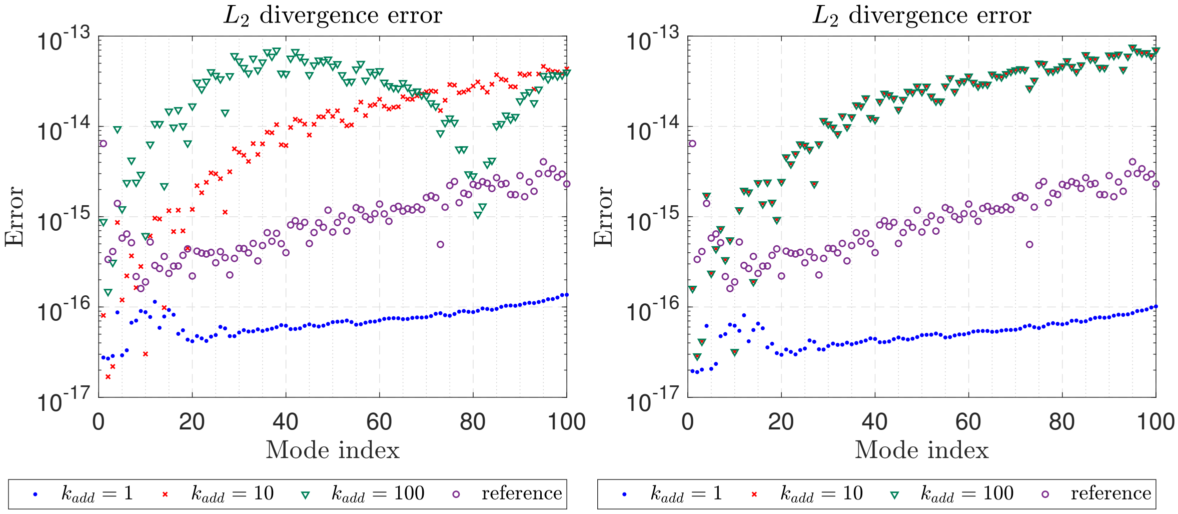

(a) full set

(b) downsampled set

Figure 5.6: L_2 Divergence error $\|M_h\Phi_i\|_{\Omega_h}$ of individual modes. Full and downsampled sets, threshold 10^{-6} $M_{dom} = 100$, varying k_{add}

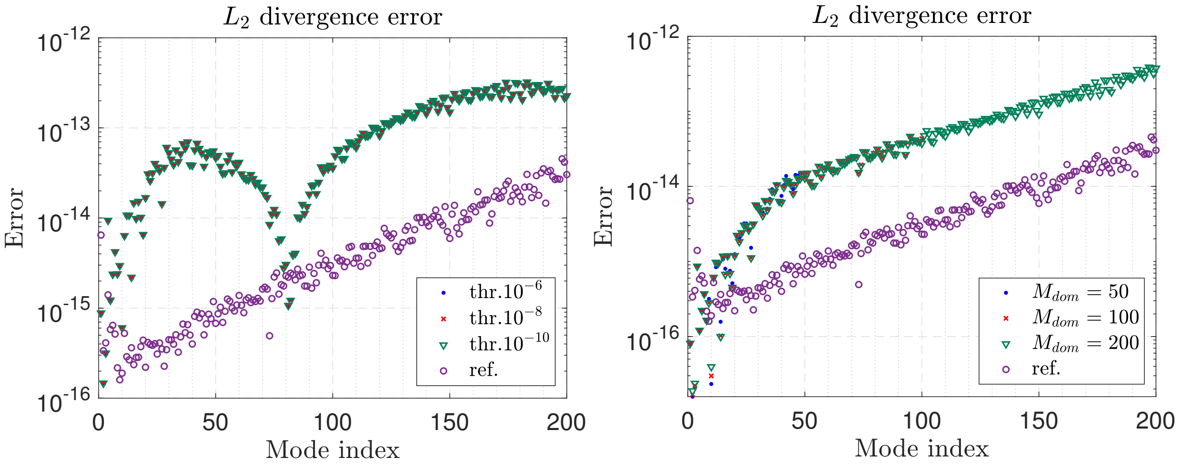

(a) $M_{dom} = 200$, $k_{add} = 100$, varying threshold

(b) $k_{add} = 10$, threshold 10^{-8}, varying M_{dom}

Figure 5.7: L_2 Divergence error $\|M_h\Phi_i\|_{\Omega_h}$ of individual modes.

As the threshold affects divergence of the modes in no visible way, only the plot at high threshold is presented in the comparison of treatments (GS, Helmholtz), fig. 5.3. Gram-Schmidt orthogonalization has practically no effect on diveregence error, while Helmholtz decomposition yields the expected divergence-free basis.

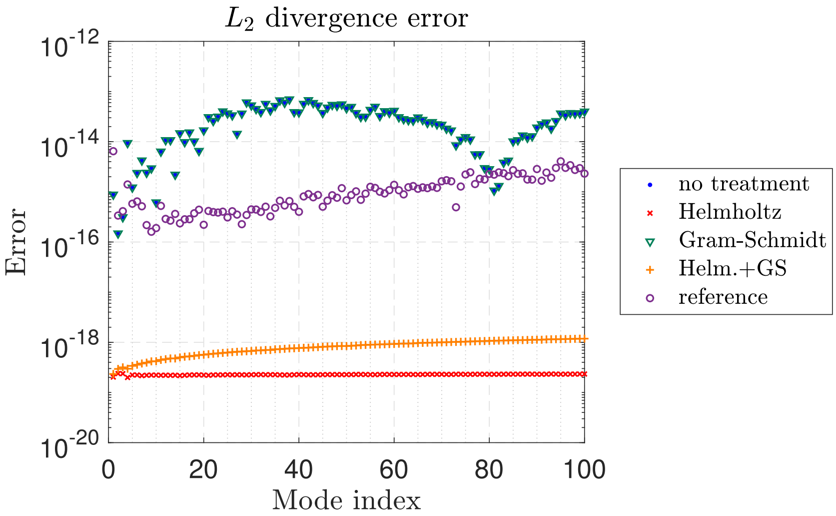

Figure 5.8: L_2 Divergence error $\|M_h\Phi_i\|_{\Omega_h}$ of individual modes. Influence of Gram-Schmidt and Helmholtz procedures. Threshold 10^{-6}, $k_{add} = 100$, $M_{dom} = 100$

5.1.3. Quality of approximation to cSVD basis

In this section, mode-to-mode error between modes from iSVD and cSVD is examined. Errors are presented for the same iSVD settings as in previous section.

Figure 5.9 - 5.10 contain plots for non-treated bases; fig. 5.11 gives a comparison of treatment effects. On all the plots there appear data points with high error values $> 10^0$, some of which are indeed showing actual error. Most of those however correspond to modes with reverse-sign w.r. to the modes of the same index from cSVD. Incremental algorithm tends to return modes with opposite sign for high indices of modes. Therefore, for pure consistency, such modes should to be accordingly modified prior to comparing them with reference modes. One way to do that would be to use the fact, that all modes are normalized so $\|\Phi_i^{cSVD} - \Phi_i^{iSVD}\| \leq 2$. One could then make the conditional statement, that if for a given mode the mode-to-mode error $\|\Phi_i^{cSVD} - \Phi_i^{iSVD}\|$ exceeds a pre-set value $\epsilon_{switch} \in (\sqrt{2}, 2)$ then it is to be re-computed on the same mode only with the opposite sign. This is a simple workaround, but it is not universal, e.g. a hypothetical mode Φ_i^{iSVD} that is so distorted that it is almost orthogonal to the reference mode Φ^{cSVD} will produce an error around $\sqrt{2}$. Then it could be problematic to distinguish the error caused by different sign from numerical error introduced by iSVD. This is actually the case at low k_{add} in this section. The proposed workaround was not applied, because the discussed effect, obscures the interpretation of results to a lesser extent than the workaround itself would have.

Figure 5.9 shows how bases constructed with iSVD operating on full set of snapshots compare to cSVD. Increment size is varied. For all investigated k_{add} there is a tendency of rapid error increase in the first ~ 20 modes. Clearly, lowest k_{add} results in Φ with lowest degree of resemblance to reference basis. There is only small difference for lower indices between $k_{add} = 10$ and 100, but it is increasing with index. Additionally, there appear 'oscillations' in error at $k_{add} = 100$. It is observed, that the number of reverse-sign modes decreases with increasing k_{add}.

Next, fig. 5.9b indicates that the basis obtained from downsampled set has on average much worse fidelity w.r. to cSVD basis (based on full set). Furthermore, the degree of accuracy starts depending on k_{add} at mode index $i = 25$, where single-snapshot incrementation generally becomes unreliable faster than $k_{add} = 10, 100$.

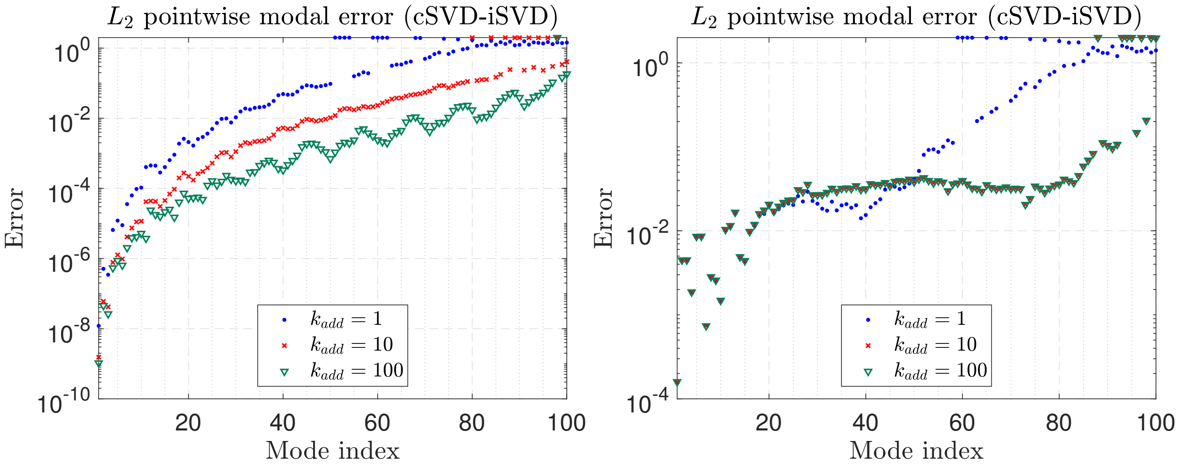

(a) $M_{dom} = 100$, threshold 10^{-6}, full set.

(b) $M_{dom} = 100$, threshold 10^{-6}, downsampled set.

Figure 5.9: L_2 mode-to-mode error $\|\Phi_{i,\text{cSVD}} - \Phi_{i,\text{iSVD}}\|_{\Omega_h}$.

Influence of the threshold at fixed $M_{dom} = 200$, $k_{add} = 100$ is shown in fig. 5.10a, where differences appear mostly for modes with $i < 15$. In that range lowest threshold results in highest error. The difference between errors for thresholds $10^{-6}, 10^{-8}$ is very small. In fig. 5.10b the error is ploted for varying M_{dom}. Clearly, high M_{dom} is desirable for higher fidelity of the basis. At the particular settings of k_{add} and threshold used here, it is observed that the rate of increase of error with mode index is more diverse for varying M_{dom} than it was for varying k_{add} (with other parameters fixed), fig. 5.9a. I.e. $M_{dom} = 200$ has a much slower growing error than $M_{dom} = 50$.

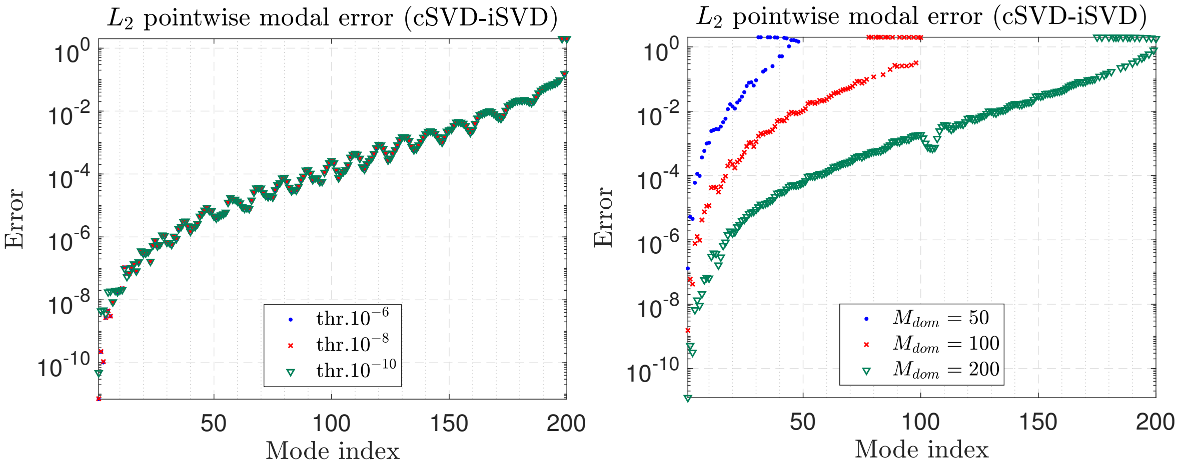

(a) $M_{dom} = 200$, $k_{add} = 100$.

(b) $k_{add} = 10$, threshold 10^{-8}

Figure 5.10: L_2 mode-to-mode error $\|\Phi_{i,\text{cSVD}} - \Phi_{i,\text{iSVD}}\|_{\Omega_h}$.

An important observation concerning M_{dom} is the following. Although for higher fidelity w.r.t. cSVD basis high M_{dom} is preferable (see fig. 5.10b), there is a conflict with k_{add}. The latter parameter should be set low in order to obtain good orthogonal quality and zero-divergence of modes, as figures fig. 5.1 and 5.4 suggest. There are other reasons why low k_{add} is preferable, e.g. online computation of basis. However with low k_{add} a high total number of increments is performed. In each update, the approximate SVD must be computed, with number of SV bounded by (high) M_{dom}. If the smallest singular value in a particular update is well above the threshold (i.e. the threshold does not truncate any information at that incremental update), then all SVs up to M_{dom} are computed and this is costly. It also generates errors when SV are very small.

One should keep in mind, comparing the data sets in fig. 5.10b, that there is an underlying reason for such results. M_{dom} is only the upper bound for the number of SVs. It is not necessary that at every incremental step all SVs up to M_{dom} are computed. This is decided at step 6 of the algorithm in section 2.4.4. If snapshots in a particular block are strongly correlated, then there exist many very small singular values. Those are clipped by the threshold. In a block where larger SVs start to dominate the spectrum, so that more SVs are above the threshold, the limit is set by M_{dom}. Hence increasing this parameter in combination with properly selected threshold may only improve the quality. It would not be so if the the threshold was very low. Then it would also be only M_{dom} limiting the number of singular values sought. Only this time it would be desirable to have this limit set lower, so that the blocks with more correlated snapshots are processed accurately.

The treatment by Helmholtz and GS process does not affect mode to mode-error, regardless of the threshold set. Hence plots for different thresholds are omitted. The error to cSVD is plotted in fig. 5.11. This is a useful piece of information. Combined with the plots from two previous sections, it allows to conclude that the significant differences between bases (iSVD and cSVD) do not lie in the lack of orthogonality or zero-divergence property.

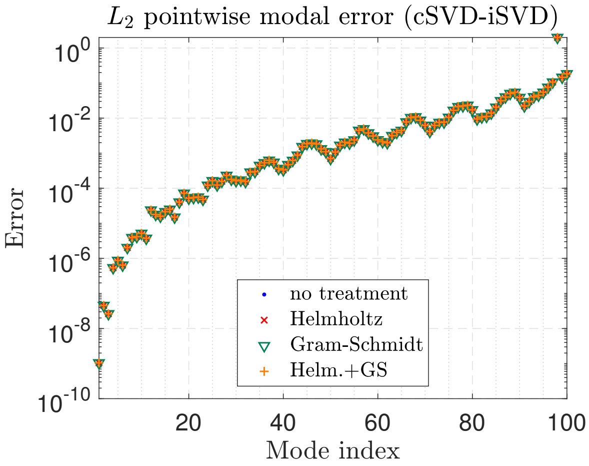

Figure 5.11: L_2 mode-to-mode error $\|\Phi_{i,\text{cSVD}} - \Phi_{i,\text{iSVD}}\|_{\Omega_h}$ with $M_{dom} = 100$, $k_{add} = 100$, threshold 10^{-6}. Influence of GS and Helmholtz procedures.

5.1.4. Singular value decay

In this section singular value spectra will be compared for the same settings as in previous sections. The treatment by GS and Helmholtz procedures are not considered, as those only concern correction to singular vectors, not values.

Comparing SV decay for bases from full and downsampled snapshot sets, fig. 5.12, that at $M_{dom} = 100$ and threshold 10^{-6} the data is most accurate for highest k_{add}. Single-snapshot incrementation results in underestimation of higher-index singular values. Although SVs are not used directly, their over or under-estimation could mean that there is already an inaccurate energy relation captured in the modes. Furthermore, on the scale of the plots it cannot be noticed, if the deficit in higher-indexed SVs had not moved as an energy surplus on some higher SVs. The effect occurs in singular values from both full and downsampled sets. Interestingly, downsampling itself did not cause any further errors in SV computation w.r.t. to cSVD, see fig. 5.12b.

The SV spectra remain unaffected by threshold at either $M_{dom} = 50, 100, 200$ and at either $k_{add} = 1, 10, 100$, hence only selected data is presented, fig. 5.12-5.13. For $k_{add} = 100$, neither threshold nor M_{dom} affect SV decay, where only the latter is shown, fig. 5.13a. At lower k_{add} (= 10) the effect of M_{dom} is more pronounced, fig. 5.13b, which possibly also depends on threshold. When the bound on total number of singular values computed in a step is low, the ones with the highest indices are underestimated by iSVD. Data for lower threshold and k_{add} was not acquired, because the elapsed computation time exceeded the hardware limitations.

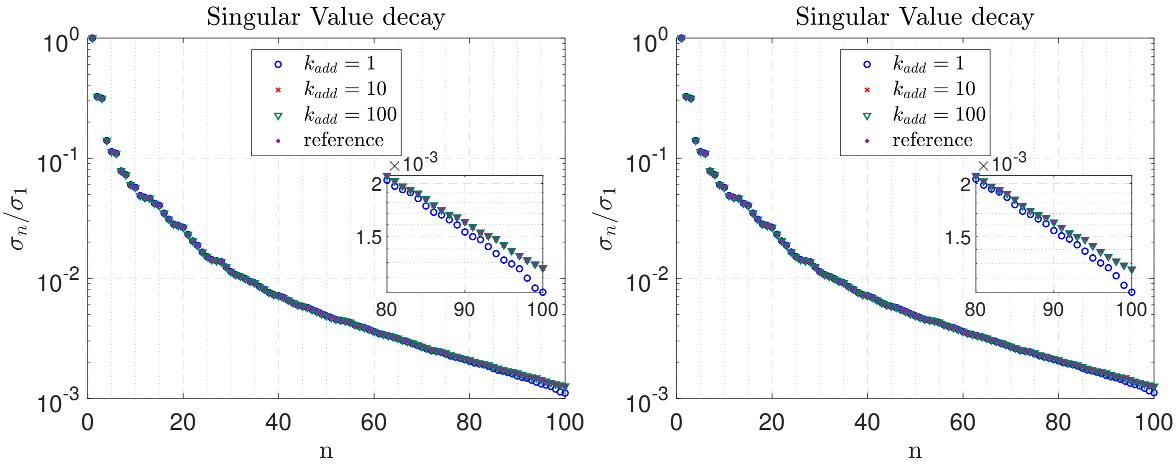

(a) full set

(b) downsampled set.

Figure 5.12: Singular value decay, $M_{dom} = 100$, threshold 10^{-6}.

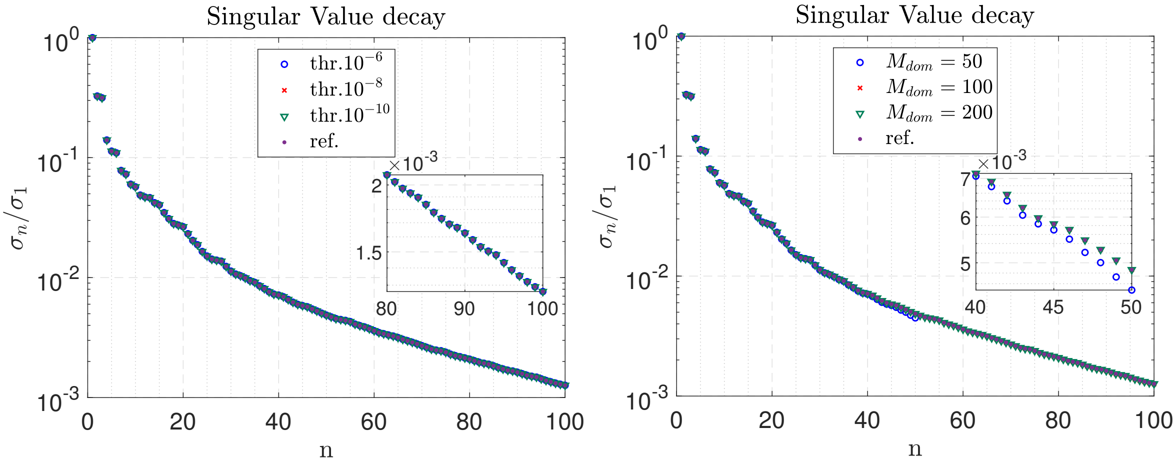

(a) $M_{dom} = 200$, $k_{add} = 100$.

(b) $k_{add} = 10$, threshold 10^{-8}

Figure 5.13: Singular value decay

Accuracy of SV computation is important for accuracy of basis vectors, because at j-th update, the matrices $\Phi j - 1$, Σ_{j-1} are re-multiplied to reconstruct the QR-decomposition from previous update and append to it the j-th block. Therefore errrors in singular values propagate eventually to singular vectors.

5.1.5. Distorted bases

As a reminder (see section 4.2.1), in this section all modes are being either randomly distorted or rotated. These will be used to build a ROM, whose accuracy will be assessed in section 6.2.1. Distortion is according to:

$$\tilde{\Phi}_{ij} = \Phi_{ij} + c_i X, \tag{5.1}$$

where $X \sim \mathcal{N}(0,1)$ is a random variable with standard normal distribution and $c_i = p \cdot \frac{1}{M} \sum_j |\Phi_{ij}|$ is an l_1 norm, with $p = 5\%, 10\%$ - percentage.

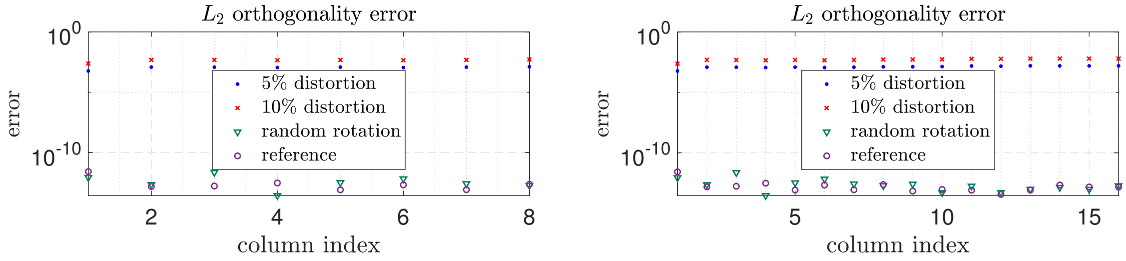

(a) Error within modes 1-8

(b) Error within modes 1-16

Figure 5.14: L_2 orthogonality error, $\|\mathbb{I} - \Phi^T \Omega_h \Phi\|_{\Omega_h}$, for various distortions of the reference basis.

Clearly the random distortions greatly deteriorated orthogonal quality. Rotation on the other hand, as an orthogonal transformation, maintained the proper quality.

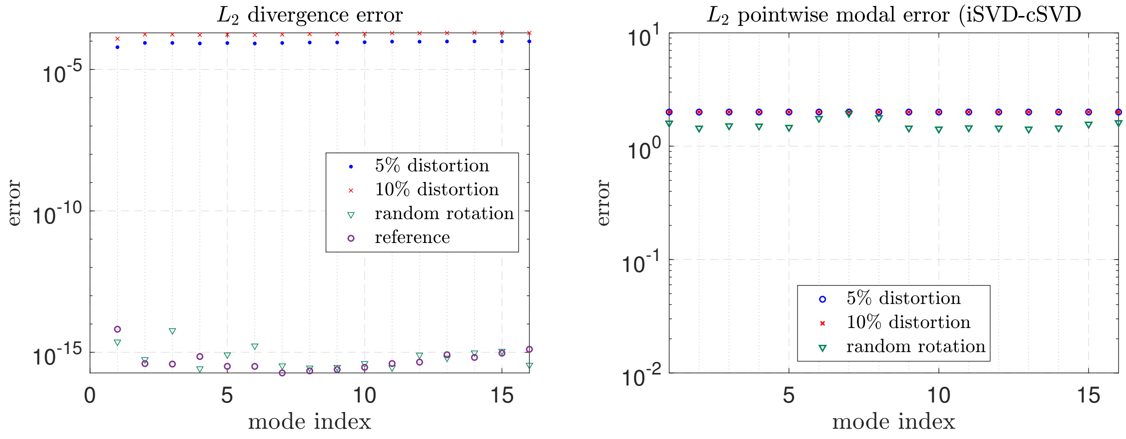

(a) Divergence error

(b) Mode-to-mode error

Figure 5.15: L_2 divergence and mode-to-mode errors , for various distortions of the reference basis.

After distortion the modes suffer also from divergence issues, fig. 5.15. As in the case of orthogonality error, random rotations do not affect divergence error. As mentioned, rotation is an orthogonal transformation and as such does not change the relations between components of a vector. It may change the change components themselves however, which is why the rotations also produced high mode-to-mode error. The distorted bases constructed here will be used in the next chapter to perform simulations.

5.2. Comparison of modes: shapes

In this section iso-surface plots of selected modes Φ_i and selected components will be presented. The cascade hypothesis is the foundation of EV modeling, so it is prudent to visually inspect the shapes of modes, in order to find out whether indeed fine scales are confined to high-index modes. This is to check whether the modes are segregated according to structure sizes (POD segregates w.r. to energy which is claimed to be similar e.g. by Couplet et al. in [10]). Furthermore, visual inspection allows a rough assessment of quality, scale sizes captured by various modes or dominating directions of flow, etc. This section contains plots for both shear layer and Taylor-Green vortex, with more focus still on the former.

5.2.1. Shear layer

Modes 1, 2 and 8 are presented in the first part, also with modifications applied: distortion and rotation. Here the treatment (Helmholtz or GS procedures) is not discussed, as it makes changes that are not visible on the scale of the presently discussed iso-surfaces. The mesh size used is $N_p = 150^3$, $t_{end} = 10$. In the second part, the same index modes are presented but three FOM snapshot set sizes used to obtain the basis are compared. Here the mesh size is $N_V = 250^3$, because the results were available for the fine grid only.

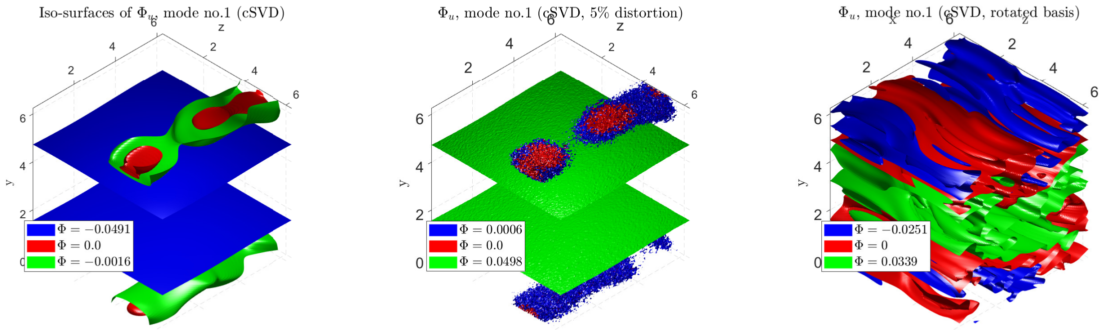

(a) Reference (cSVD)

(b) 5% distorted

(c) Random rotation

Figure 5.16: Isosurfaces of Φ_1^u, $N_p = 150^3$ for various settings

Mode 1, fig. 5.16 according to theory represents the highest-energy structures, containing highest or one of the highest amounts of kinetic energy in the whole POD set. The figure also show the distorted mode (here with opposite sign). The rotated mode does not look similar, it rather represents some higher-frequency content of the spectrum. Thus after rotation the ordering of modes from lowest to highest, which supposedly reflects the lowest and highest wavenumbers, is generally lost. However, it may still be the case that the mode carries the most energy.

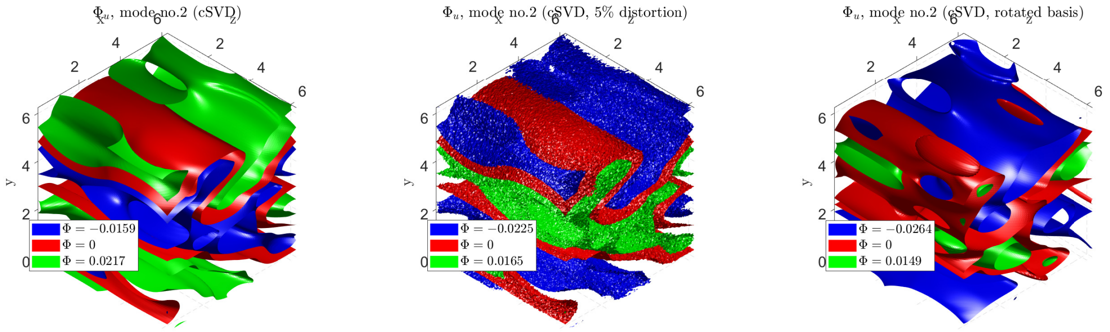

(a) Reference (cSVD)

(b) 5% distorted

(c) Random rotation

Figure 5.17: Isosurfaces of Φ_2^u, $N_p = 150^3$ for various settings

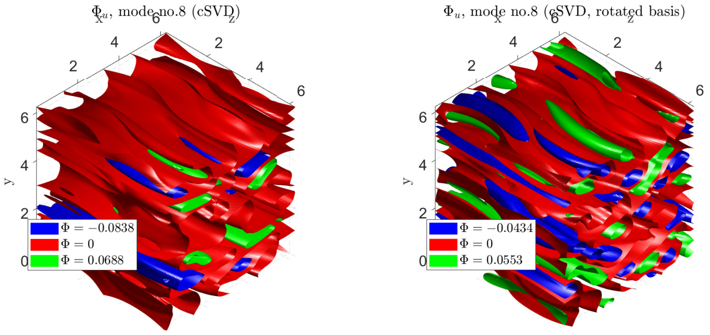

(a) Reference (cSVD)

(b) Random rotation

Figure 5.18: Isosurfaces of Φ_8^u, $N_p = 150^3$ for various settings

As i increases, higher wavenumbers start appearing, fig. 5.17. On fig. 5.18 even more high wavenumber structures appear. Iso-surfaces form noticeable tubes of moderate diameter. These are clearly aligned with

z-axis. The rotated basis does not lose this alignment.

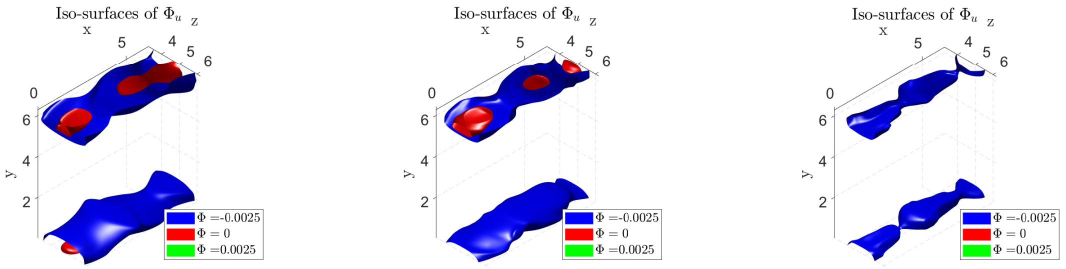

(a) $t_{end} = 10$ (b) $t_{end} = 15$ (c) $t_{end} = 20$

Figure 5.19: Isosurfaces of Φ_1^u, $N_p = 250^3$ for FOMs with various end times, $t_{end} = 10, 15, 20$

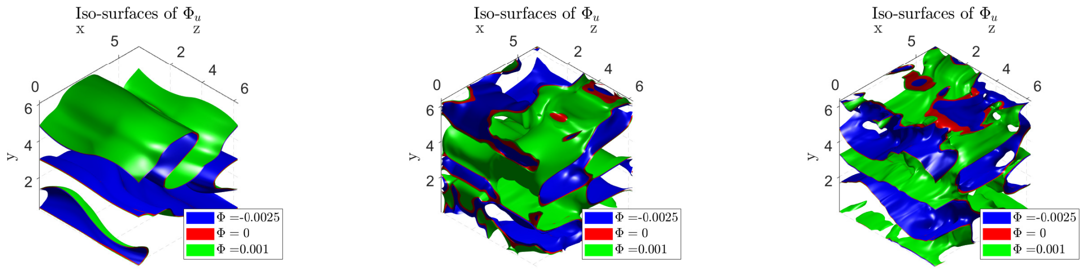

(a) $t_{end} = 10$ (b) $t_{end} = 15$ (c) $t_{end} = 20$

Figure 5.20: Isosurfaces of Φ_2^u, $N_p = 250^3$ for FOMs with various end times, $t_{end} = 10, 15, 20$

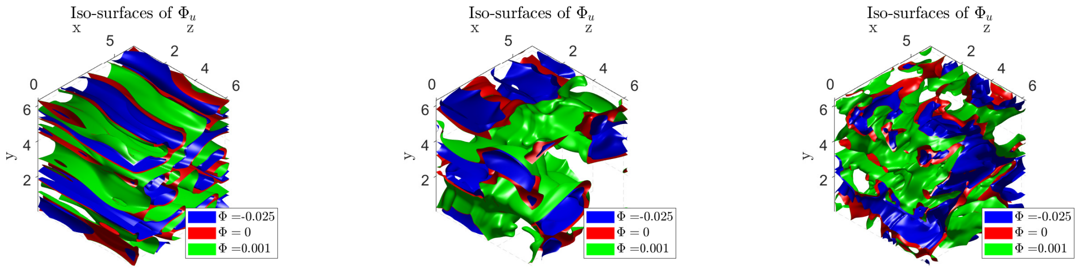

(a) $t_{end} = 10$ (b) $t_{end} = 15$ (c) $t_{end} = 20$

Figure 5.21: Isosurfaces of Φ_8^u, $N_p = 250^3$ for FOMs with various end times, $t_{end} = 10, 15, 20$

With increasing t_{end}, lower modes of the same index capture progressively more three-dimensional structure, which is apparent from examining fig. 5.19-5.21. The fine scale content there could also partially contain numerical noise (from iSVD) but most likely the appearance of small 3D structures is dictated by the POD ordering: high-energy structures first. I probably so turns out that those motions, which are fare from coarse-scale, indeed contain a significant portion or energy. This undermines the concept of equivalence/similarity between fine-scale and low-energy scale.

5.2.2. Taylor-Green vortex

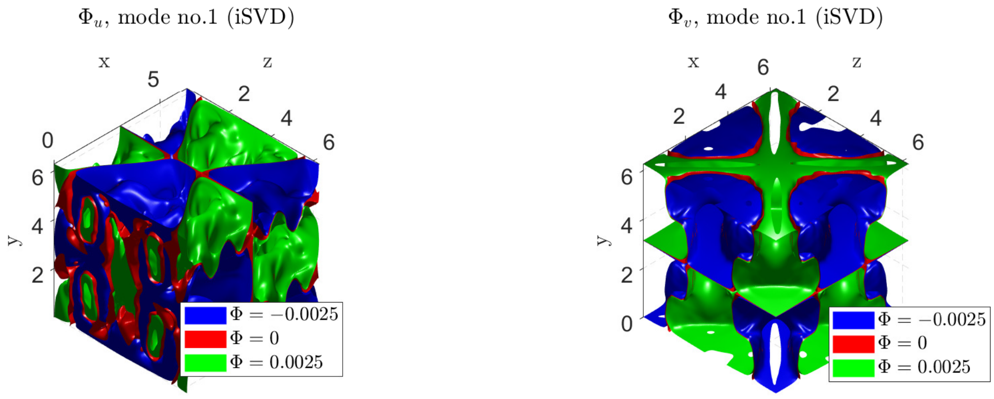

(a) Φ_u

(b) Φ_v

Figure 5.22: Isosurfaces of Φ^u_1,Φ^v_1 on grid $N_p = 250^3$

The lower modes in this test case, fig. 5.22 are already strongly 3D, since the FOM is 3D from the initial instant. There is no quantitative difference between u and v components for higher modes, hence only u-component is shown in fig. 5.23. Here, as in SL case, higher-index modes, as expected, carry higher-wavenumber structures, than the low-index modes.

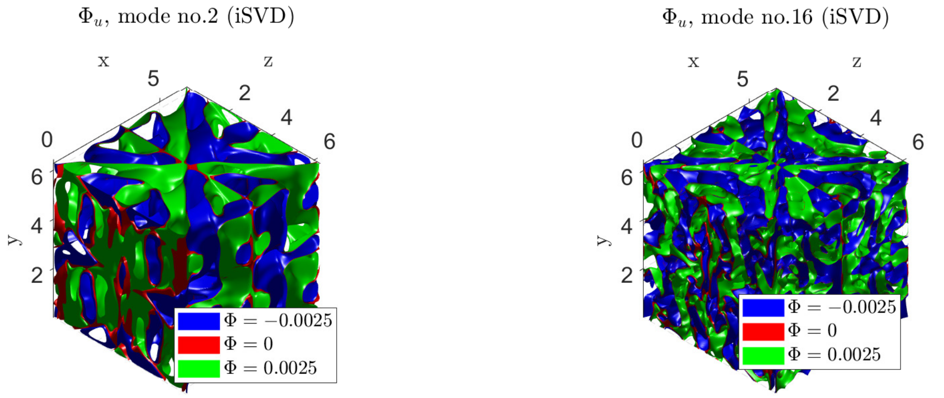

(a) Φ_u

(b) Φ_u

Figure 5.23: Isosurfaces of Φ^u_2,Φ^u_{16} on grid $N_p = 250^3$

5.3. Comparison of modes: spectra

In this section wavenumber spectra of selected modes are analyzed. Influence of iSVD parameters and treatment is examined.

5.3.1. Non-modified modes

In this section integer wavenumber spectra of modes are compared. Visual differences start appearing at higher indices, therefore the mode index selected for this analysis is $i = 100$. Spectra of modes with indices ~ 50 and lower seem unaffected by GS or Helmholtz treatment. They are also not sensitive to iSVD settings. The higher modes display more dependence on iSVD parameters, but still very little response to treatment.

As a rule, iSVD overestimates energy at low wavenumbers and underestimates that of high wavenumbers, see fig. 5.24-5.26. The effect is stronger with lower k_{add}, fig. 5.24 and more so, when downsampling is applied, fig. 5.24b.

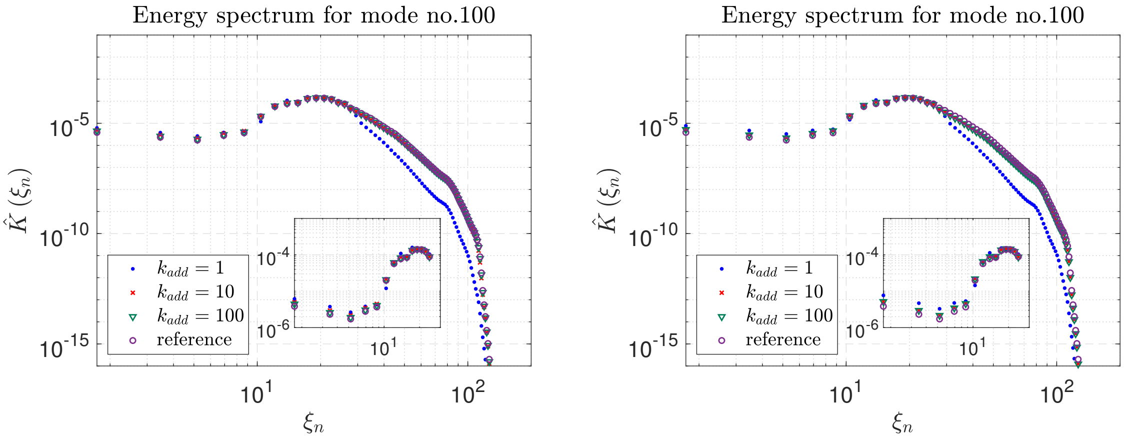

(a) full set

(b) downsampled set

Figure 5.24: Energy spectra of **mode 100**, threshold 10^{-6}, $M_{dom} = 100$, varying k_{add}. Full and 50% downsampled set of snasphots used.

At $k_{add} = 100$ threshold does not affect the spectrum at $M_{dom} = 100$: there is a mismatch between iSVD and reference increases but it is independent of threshold fig. 5.25a. For $M_{dom} = 200$ the spectrum is well aligned with reference. fig. 5.25b.

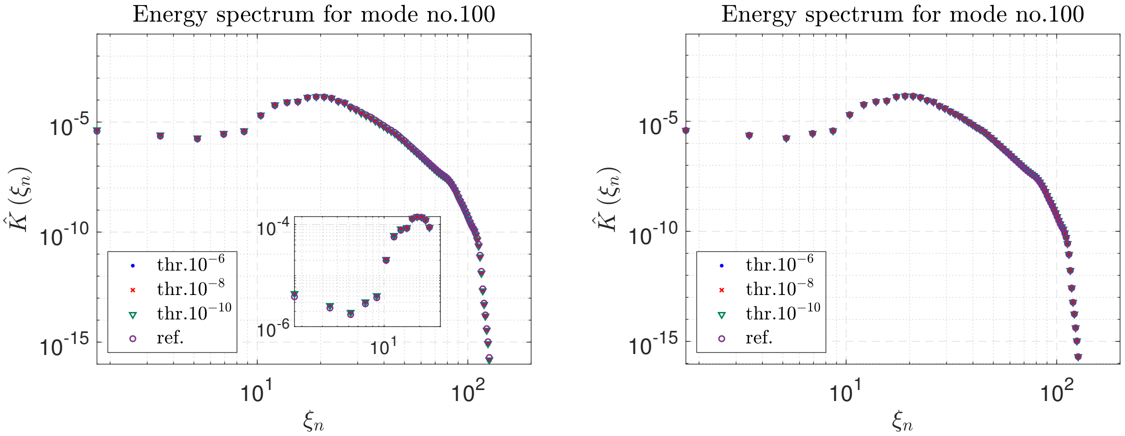

(a) $M_{dom} = 100$

(b) $M_{dom} = 200$

Figure 5.25: Energy spectra of **mode 100** varying threshold, $k_{add} = 100$. Full set of snasphots used.

Finally, it is found that the treatment by Helmholtz and GS procedures does not alter the spectrum, which is another useful piece of information enabling safe recommendation for such treatment.

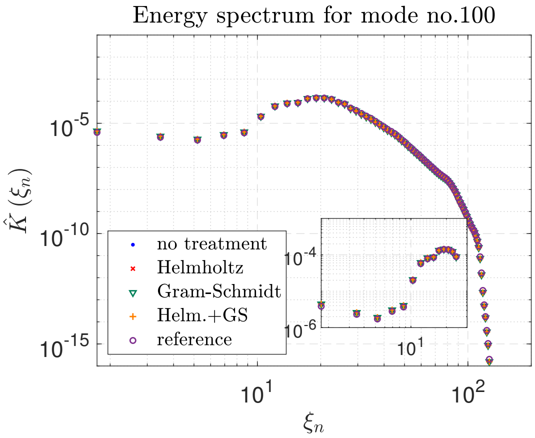

Figure 5.26: Energy spectra of **mode 100** threshold 10^{-6} , k_{add} = 100. GS and Helmholtz procedures applied.

5.3.2. Random distortions and rotations

In this section effects of distortion on modes spectra are compared for selected modes.

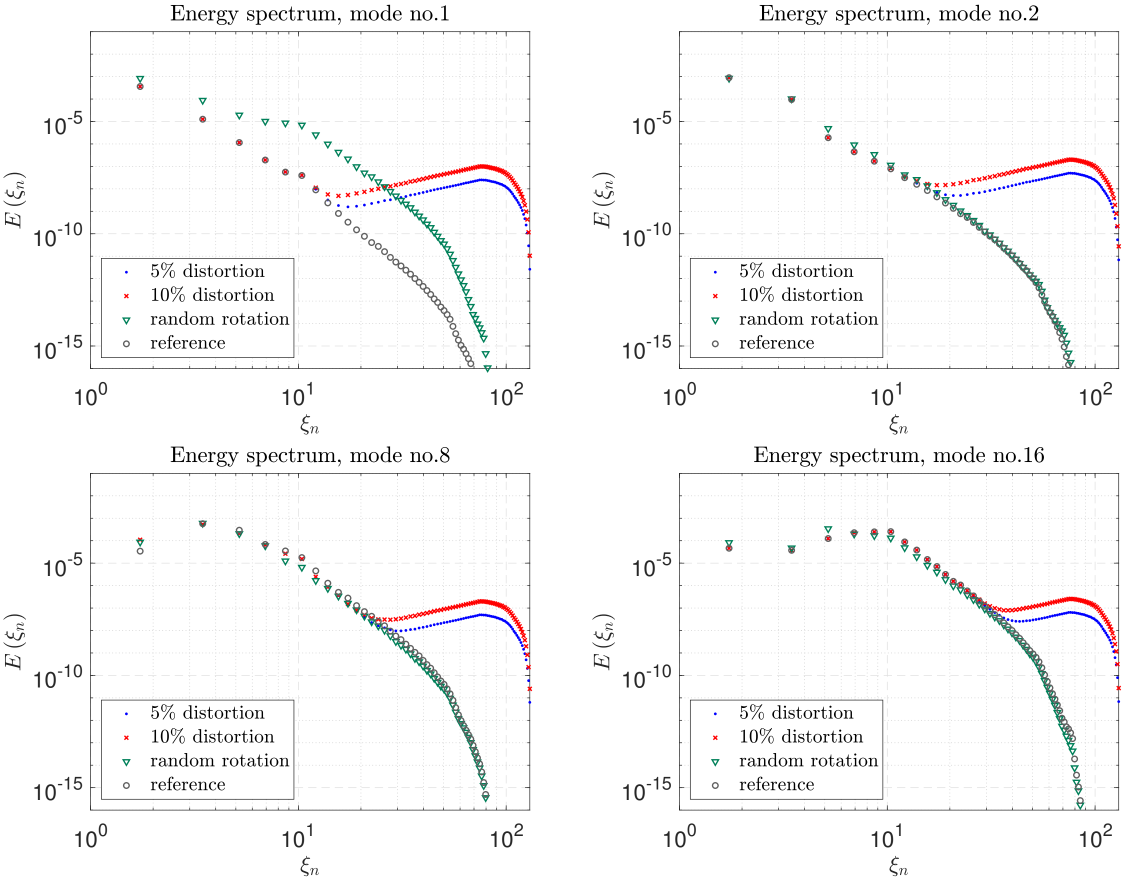

Figure 5.27: Energy spectra of randomly distorted/rotated basis

Random distortion, as is clear from the plots above, affects only higher wavenumbers. Spectra of the rotated modes in general case vary from reference (depending on the angle of rotation). However, in this case, the sum of spectral energies of all modes $\hat{\Phi}$ must essentially be the same as for modes Φ. This is because energy[1] defines a norm in Hilbert space and orthogonal transformations (such as rotation, eq. (4.11)) do not alter the norm.

---

[1] Total (kinetic) energy of the system is the same regardless of whether it is computed in spectral or physical space (Parseval's Theorem).

5.4. Comparison of bases: singular values

In this section a comparison of SV decays is made. It is analogous to the one made in section 5.1.4, only there it was aimed only at measuring the influence of iSVD parameters. Presently, bases obtained using fixed iSVD settings but varying input data, are compared. SV decay allows to estimate the magnitude of best attainable ROM error. The comparison is made between SL and TG test cases for fine and coarse grid snapshots but also for various t_{end} of SL. Shear layer cases have mostly $t_{end} = 20$ (except where various t_{end} are compared) while the Taylor-Green vortex cases run with $t_{end} = 10$. Different $M_{dom} \leq 200$ were applied, resulting in varying number of available SVs. The basis constructed with cSVD (SL with $N_p = 150^3$) has $n = 2001$ singular values, which are not all plotted here (full plot may be found in the appendix appendix A.1).

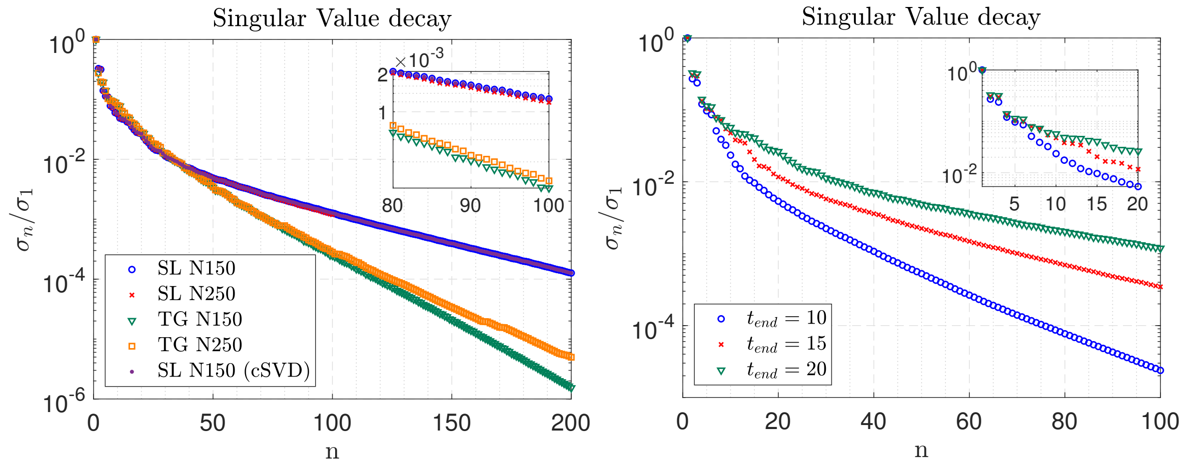

(a) TG and SL on coarse and fine grids.

(b) SL with $N_p = 250^3$, $t_{end} = 10, 15, 20$.

Figure 5.28: Comparison of singular value decay.

TG vortex has a faster SV decay than shear layer, fig. 5.28a. This is reasonable, since the case runs with $t_{end} = 10$ while in SL the simulation time is 20. In fact however, when SL case with $t_{end} = 10$ fig. 5.28b is compared with this TG singular value spectrum, it becomes apparent that TG decays slower. This is caused by there being more complex and three-dimensional fields involved, requiring more modes to describe. For example, to reach $\frac{\sigma_n}{\sigma_1} = 10^{-4}$, shear layer requires ~ 70 singular values, while TG vortex ~ 120. As observed in fig. 5.28a, TG on fine grid corresponds to more rapid decay than that of coarse grid. In case of SL the situation is opposite. Based on section 5.1.4, it is suspected that this is the effect of lower M_{dom} applied. Figure 5.28b presents SV spectra corresponding to FOM with various simulation lengths. As expected in a transient case, longer simulation time yields slower decay of singular values.

It was mentioned that SV decay might be used to estimate the error of ROM. For example for $M = 48$ shear layer case best error should lie at best somewhere below ~ 10^{-2}, whereas $M = 8$ it will not get much better than 10^{-1}. As will be revealed by comparing with fig. 6.1 in the next chapter, these rough estimates are surprisingly accurate.

5.5. Summary

The interplay between the three investigated iSVD parameters: k_{add}, M_{dom} and threshold, is an essential element to consider while constructing a basis that approximates the cSVD basis. The approximate basis should not only have a degree of fidelity to cSVD, but also retain the important properties: orthogonality and zero-divergence.

It is obvious that the increment size k_{add} affects orthogonality strongly (negatively) for low values of threshold and less so for high values. To a lesser extent the same is also true for relation of M_{dom} with the threshold. From this viewpoint it would be beneficial to apply high values of k_{add} and M_{dom} and threshold.

Divergence of the modes is on average not affected by the threshold and only mildly influenced by M_{dom} - the error increases with increasing M_{dom}. Threshold does not alter the error on average, but it can change distribution of error over the modes. Lastly, low k_{add} results in low divergence error, iSVD with single-snapshot increments performs better than cSVD in this regard.

Fidelity to reference basis depends most strongly on M_{dom}, as assessed from the gathered data. However, as mentioned in section 5.1.4, this also depends on threshold. Increment size also influences the fidelity, which is also mentioned by Baker et al. in [5], where it is claimed that as $k_{add} \to N_t$, iSVD → cSVD. As also mentioned there, this is supported by intuition: with large increment size, the algorithm has access to a larger part of the matrix, whose SVD is being approximated. This feature of k_{add} is independent of the threshold.

Neither of the discussed properties of the approximate basis is affected negatively by the treatment with Gram-Schmidt and Helmholtz decomposition.

Singular values are most accurately computed at high k_{add} and high M_{dom}, see section 5.1.4. Threshold has little significance.

It is concluded that for high quality basis one should pursue computation with highest possible k_{add} and M_{dom} and set the threshold only as low as the desired accuracy of ROM solution (dictated by the ratio of smallest and largest singular value). Treatment by Helmholtz and GS procedures should be applied in all cases, because it does not harm and improves zero-diveregence and orthogonality of the modes. These preferences must now be properly matched with other constraints. This is not pursued in this thesis, but online basis computation (during FOM) would require low k_{add}. This lowers the quality of basis and increases the time requirements. On the other hand, too high value of that parameter poses infeasible requirements on the operational memory (too large block updates). With such limitations it is decided that the standard used parameters for the computation of the full-scale basis (i.e. based on FOM $N_p = 250^3$) will be $M_{dom} = 100$, $k_{add} = 100$ and threshold 10^{-6}.

Observations from the present chapter also help in the a priori analysis (chapter 7) in the following way. Because of large errors in higher modes $i > M$, in the a priori tests the unresolved part is simply taken as the difference between FOM solution and resolved part:

$$\underbrace{\Phi' a'}_{\text{unresoved part}} = V_h - \underbrace{\overline{\Phi}\overline{a}}_{\text{resolved part}} \quad . \tag{5.2}$$

That applies also to computation of eddy viscosity, for which unresolved scales are required.

6

ROM simulation

In this chapter the results of actual ROM simulations are presented. No closure model is applied in this chapter. Mostly iSVD bases are used, with some exceptions, all briefly discussed at the beginning of each section. Shear layer is the primary flow test case that is investigated. Taylor-Green vortex is only presented to document that 3D ROM is working and is compatible with iSVD. The chapter is organized into three sections. Section 6.1 contains the results of two simulations of SL case on fine grid, with long and short integration period. Section 6.2 presents additional simulation result data for: distorted bases; bases enforcing momentum conservation; comparison of three bases with three different FOM and ROM integration periods; and time extrapolation. The first item in that section is obtained on coarse grid, and the rest on fine grid. Finally, TG results are discussed in section 6.3, where simulations were done on fine grid and in short integration time.

The most important types of results include (see also section 3.3):

- errors of ROM Φa and projected FOM solution w.r. to FOM: ϵ_{ROM} and ϵ_{best}
- error in ROM kinetic energy w.r. to FOM: ϵ_K
- error of ROM u-momentum w.r. to FOM IC: ϵ_{P_u}
- kinetic energy spectrum in integer wavenumber space: $E(\xi_n)$
- error in divergence: ϵ_{div}

6.1. Shear layer: main results

This section contains results of three (sets of) simulations:

- SL with basis without treatment, section 6.1.1
- SL with basis from downsampled snapshots, section 6.1.2
- SL with basis orthogonalized and made divergence-free through Gram-Schmidt and Helmholtz processes, section 6.1.3,

all of which where run with bases of dimensions $M = 8, 16, 32, 48$. Spectra and contours are presented in section 6.1.3 only, as those are the most accurate. Since most errors remain unaffected on the (scale of the plots) by the GS-Helmholtz treatment, they are skipped, as they would duplicate of those in section 6.1.1.

6.1.1. Non-treated basis

In this section results of simulation using basis without GS/Helmholtz treatment are discussed.

Error in velocity for bases $M = 8, 16, 32, 48$ is presented in fig. 6.1. ROM simulation accuracy (errors with solid lines) is progressively improving with increasing M. The difference between $M = 8$ and $M = 16$ is small. $M = 32$ behaves slightly better, but in the end error of all three is ~ 1. $M = 48$ is much more accurate and able to retain that feature until t_{end}, where the error is 10^{-1}. The gap between $M = 48$ and the lower-dimension models increases, especially in the second half of the simulation. The flow develops into a more turbulent state, and during that development some lower-energy information is missing in the model $M = 32$, because the difference to $M = 48$ is much larger than in case of ϵ^{best}. So the basis $M = 32$ is theoretically capable of attaining error $< 10^{-1}$ but the low-order dynamical system (ROM) does not naturally evolve in such direction. It seems that there is crucial physics information in modes 33 – 48, since appending those modes to the basis enabled lowering the ROM error by an order of magnitude. In comparison doubling the number of modes from $M = 8$ to 16 and then again to 32 in the end resulted in a rather small improvement at the end frame. Furthermore, there is a clear oscillatory tendency of ϵ^{best}, particularly visible for higher M. The frequency of error oscillations increases and their amplitude decreases with increasing M. The amplitude effect is universal and connected to POD basis property, that bases with increasing dimension span increasingly (or at least non-decreasingly) more accurate approximation of the true solution space. Moreover, a rapid change in ϵ^{best} appears near the beginning and end of simulation. Currently the origin is not clear, but the phenomenon was observed before, e.g. in [31] by Sanderse. Finally, the link should be recalled to SV decay, fig. 5.28. Value of the ratio $\frac{\sigma_n}{\sigma_0}$ for $i = 48$ in the fine-grid shear layer case lies somewhere below 10^{-2}. In fig. 6.1 ϵ^{best} is at best slightly below 10^{-2}. Similar estimates remain fairly accurate for lower M as well.

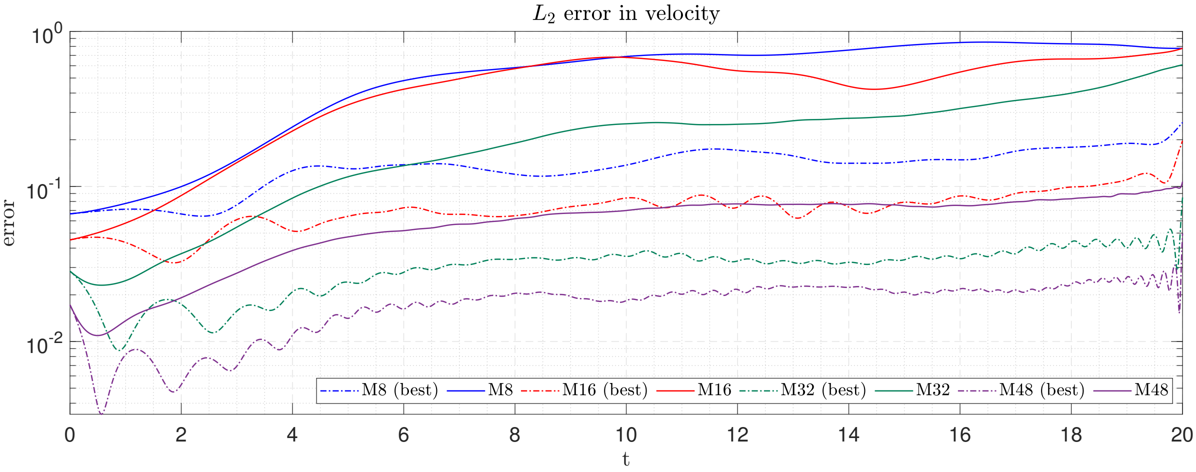

Figure 6.1: L_2 velocity error: basis w/o treatment.

Plots fig. 6.2a express evolution of kinetic energy in time. With increasing M, the estimate is increasingly more accurate. An exception is the lowest $M = 8$ case, which incidentally follows the end decay of FOM energy better than $M = 16, 32$. This is attributed to there being insufficient part of dissipation range resolved by ROM with such low dimension basis. Certainly it is not byproduct of an accurate solution, compare with fig. 6.1. Similar remarks apply to fig. 6.2b, which depicts evolution of u-component of global momentum in time.

Figure 6.3 presents the same data differently: in the form of error w.r. to FOM. Figure 6.3a shows error w.r. to FOM at current time, which is mostly a deficit of energy. From fig. 6.3b it appears that, especially for $t \in [10, 20]$, there appears a deficit in momentum. In the worst case $M = 16$ at the end of simulation there is a loss of almost ~ 25% of momentum, while the loss of energy is roughly an order of magnitude smaller.

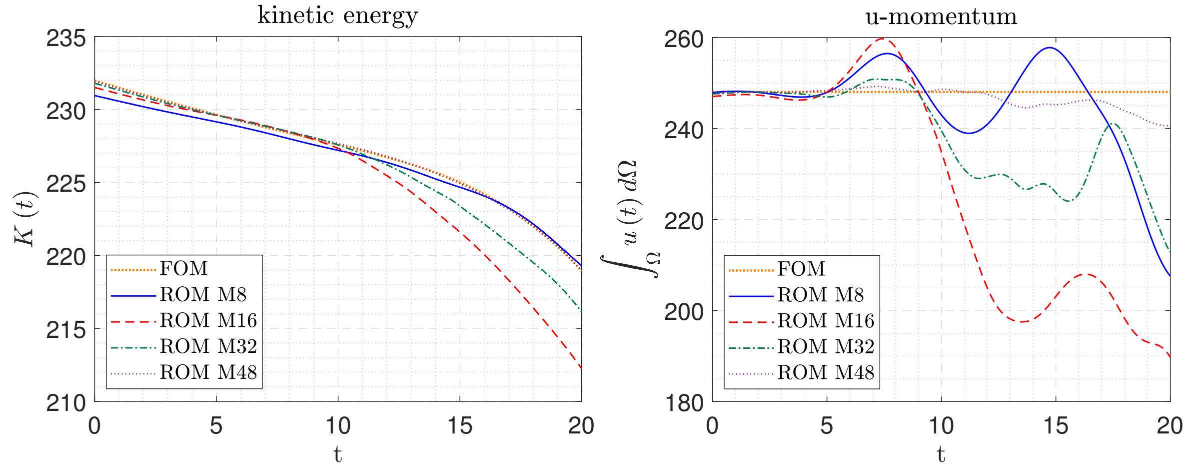

(a) kinetic energy (b) u-momentum

Figure 6.2: Total kinetic energy K and u-momentum temporal evolution, basis w/o treatment.

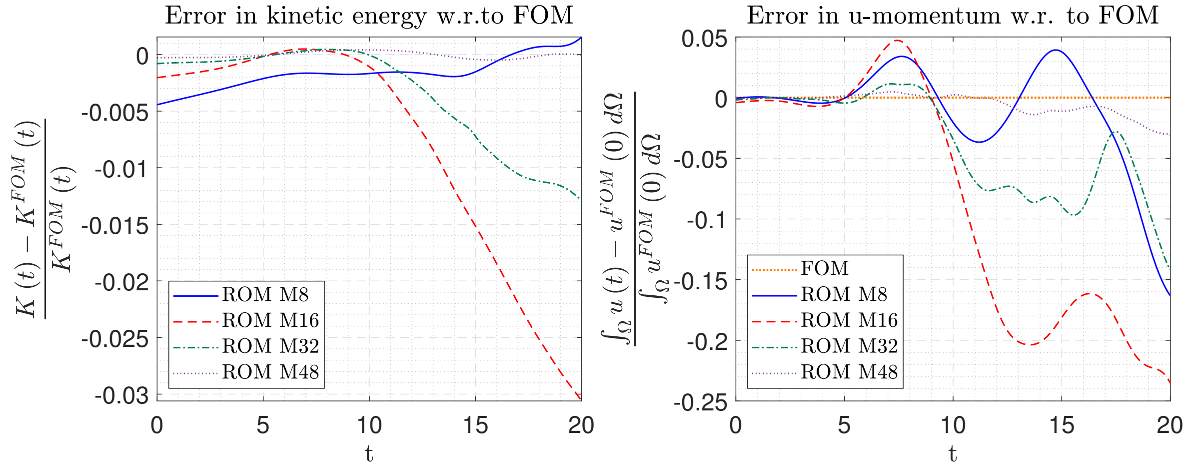

(a) kinetic energy (b) u-momentum

Figure 6.3: Error in total kinetic energy K and u-momentum, basis w/o treatment.

Error in divergence is plotted in fig. 6.4. For ROM it is significantly higher than for FOM. On average it is the same for all M, only the frequency increases with RB dimension.

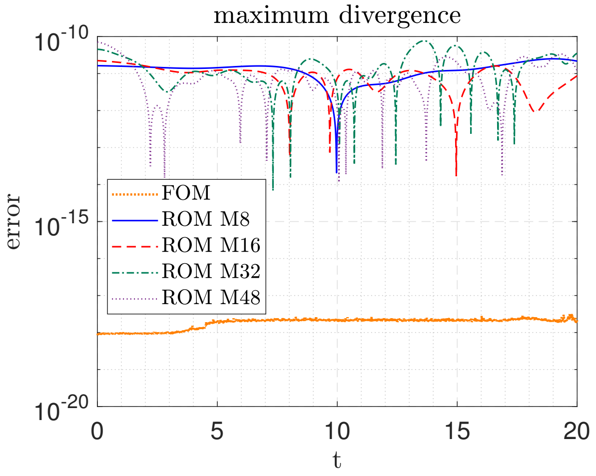

Figure 6.4: Divergence error $\|\nabla \cdot \boldsymbol{u}(t)\| \approx \|M_h V_h(t)\|_\infty$ in maximum norm.

6.1.2. Basis obtained from downsampled snapshots

In this section influence of downsampling on errors of solution and derived quantities is investigated. Snapshots are downsampled by 50%, i.e. every 2^{nd} snapshot is used in computing iSVD (see section 5.1.3 for the effect of downsampling on quality of approximation to cSVD). Rather than plotting the same results as in previous section, which are similar, the new results are now compared with those from the previous section for $M = 32, 48$. For lower M there are no noticeable differences.

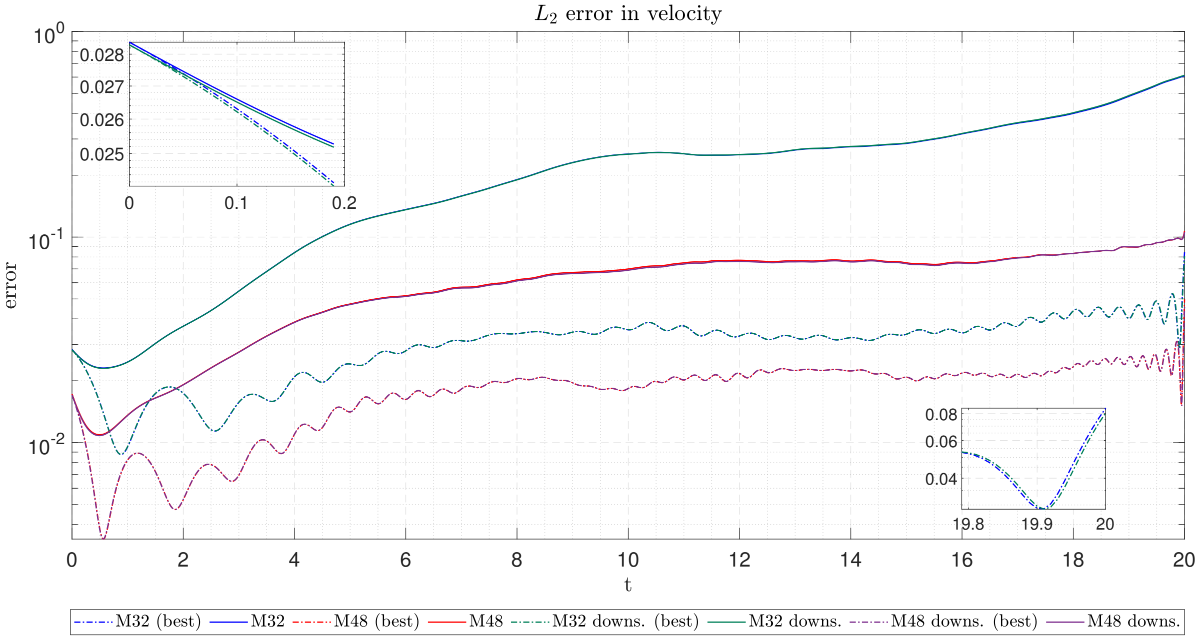

Figure 6.5: L_2 velocity error. Full and downsampled snapshot sets used to obtain basis - comparison.

Differences between errors for bases with and without downsampling are very small on the scale of the plots, fig. 6.5. At initial instant, downsampled-set errors in accordance with inutition are higher than those corresponding to full set. However, near t_{end} the downsampled-set yields a slightly lower error ϵ_{best} than the full set. This draws suspicion, because POD yields a basis that is supposed to be the best possible approximation within a given set. Here yet a different basis performes better (albeit for a brief instant). This could be due to error in orthogonality and/or divergence of the modes (see section 5.1.1 and section 5.1.2). For example, when per-mode error in divergence for full and downsampled sets is compared (see fig. 5.6) one observes that for downsampled set at indices ~ 32, error in divergence differs by an order of magnitude w.r.t. to full set.

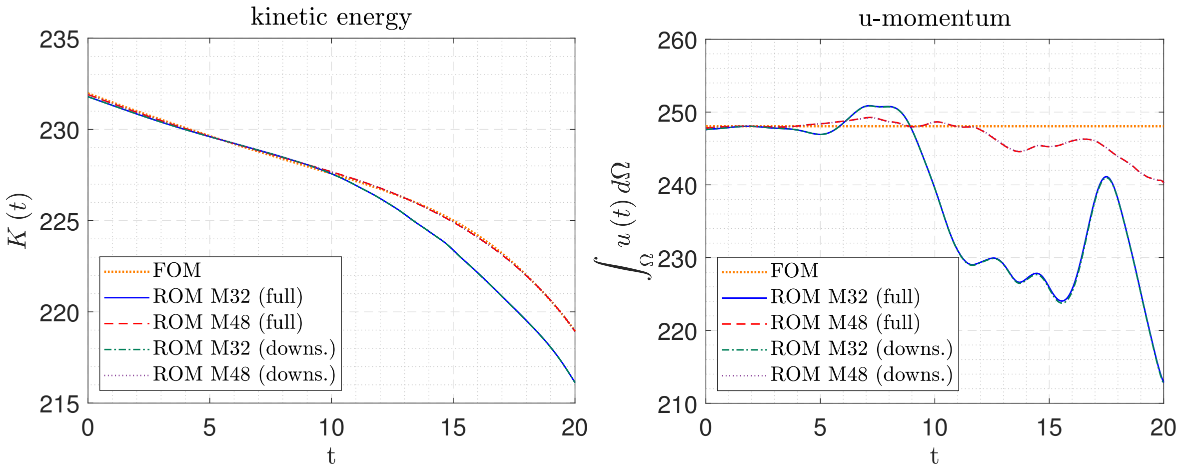

(a) kinetic energy

(b) u-momentum

Figure 6.6: Total kinetic energy K and u-momentum. Full and downsampled snapshot sets used to obtain basis - comparison.

Figure 6.6 shows, that downsampling of snapshots performed in basis construction had very little effect on ROM energy and momentum estimates.

Divergence error, fig. 6.7, appears similar in each case. It is measured in maximum norm, therefore this result does not rule out the possible influence of L_2 divergence error in modes on the final errors (ϵ^{best}) in fig. 6.1.

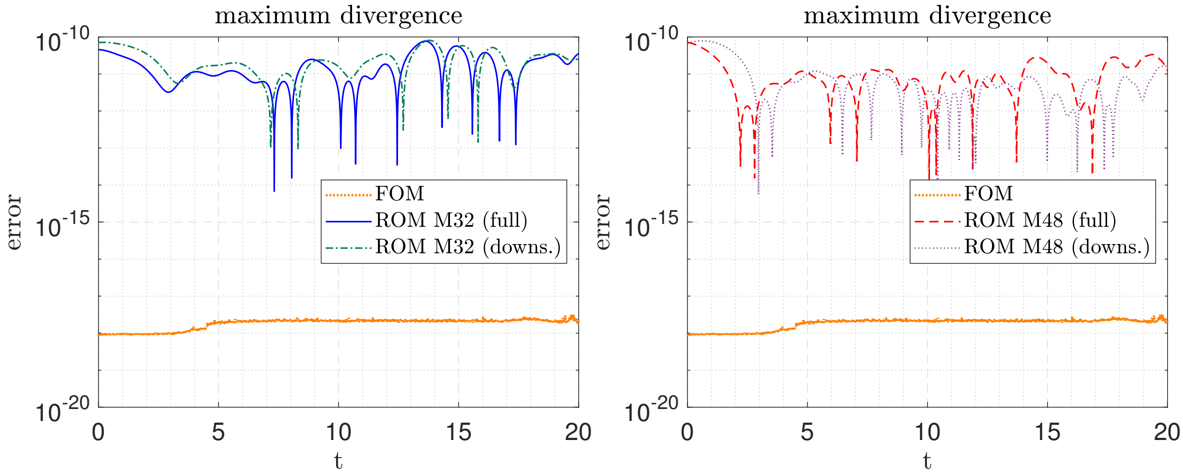

(a) $M = 32$

(b) $M = 48$

Figure 6.7: Divergence error $\|\nabla\cdot\boldsymbol{u}(t)\| \approx \|M_h V_h(t)\|_\infty$ in maximum norm.

6.1.3. Basis with Helmholtz and Gram-Schmidt treatment

This section discusses the results of simulations in which modified bases were used. It is found that all the quantities of interest except divergence error remain almost unchanged w.r. to the cases using non-treated basis. Hence, only divergence error is plotted, fig. 6.8, with other errors and quantities (velocity, energy, momentum) omitted. Next, flow spectra and 2D contours of solutions are presented at selected time instants for FOM and investigated ROMs. Those are displayed exclusively in this section, as the present group of results is considered the most accurate.

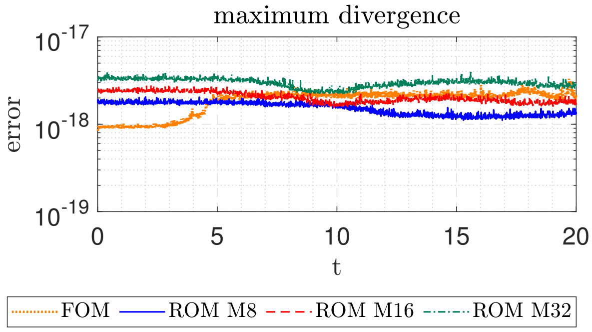

Figure 6.8: Divergence error $\|\nabla\cdot\boldsymbol{u}(t)\| \approx \|M_h V_h(t)\|_\infty$ in maximum norm.

Energy and momentum errors are very similar to those of non-treated-basis case. Error in divergence is lower by 8 – 10 orders of magnitude, see fig. 6.4. On the other hand, ROM errors themselves (see fig. 6.1) are at best ~ $10^{-2} - 10^{-3}$. It is possible that, with longer integration time, differences would start appearing in solution errors between the treated and non-treated case due to incomplete elimination of pressure from equations (as mentioned in section 3.1.2). Here it is not the case, even though the model with non-treated basis does not fully respect mass conservation, see fig. 6.4.

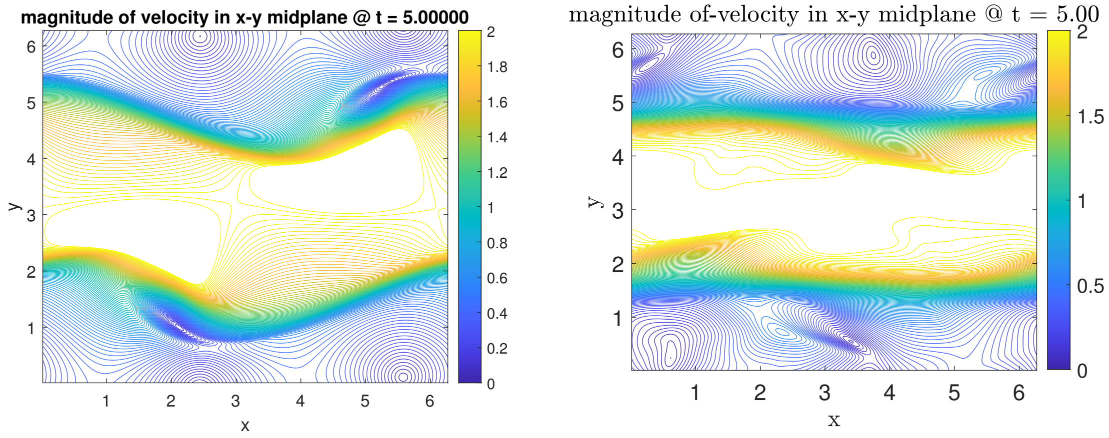

(a) FOM

(b) ROM $M = 16$

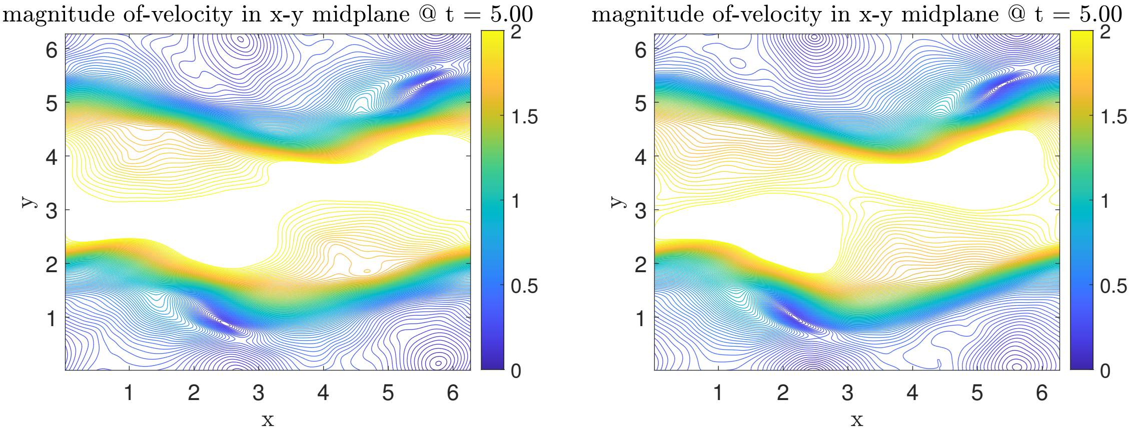

(c) ROM $M = 32$

(d) ROM $M = 48$

Figure 6.9: Velocity magnitude at $t = 5$: FOM and ROMs. Contours in xy plane.

Figure 6.9 and fig. A.3 show contours of velocity magnitude $\sqrt{u^2 + v^2 + w^2}$. At $t = 5$ it is observed that ROM with $M = 16$ struggles to capture the roll-up of shear layer. With increasing M the contours become more similar to FOM contours. In the present case, the highest M ($= 48$) still displays visually traceable distortions, e.g. see vicinity of the saddle point, fig. 6.9 near $x = 4$. This may be caused by distortions in the iSVD basis (increasing with mode index, see fig. 5.11). As the flow develops, there appear more fine-scale structures, as shown by contours, fig. A.3. It is observed that only ROM $M = 48$ resembles FOM, in that most small vortices are captured, however distortions persist.

Kinetic energy spectra are presented in fig. 6.11. Those are in the form per integer wavenumber (based on wavenumber magnitude). This 'contraction' makes most sense for homogeneous isotropic turbulence, where no mean flow is present. This somewhat obscures the interpretation in the present (shear layer) case, which must be kept in mind. Certainly, for $t \in [15, 20]$ the flow has a more turbulent character, which makes the analysis concerning that period more credible.

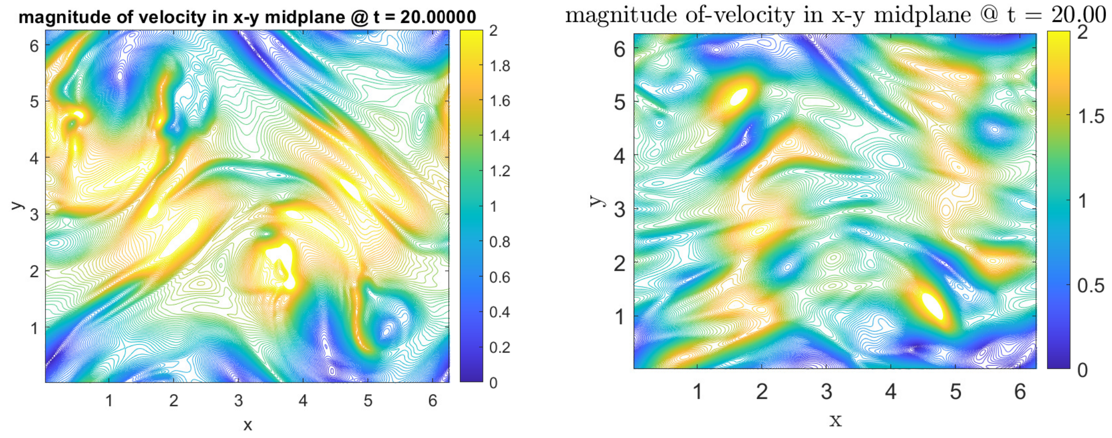

(a) FOM

(b) ROM $M = 16$

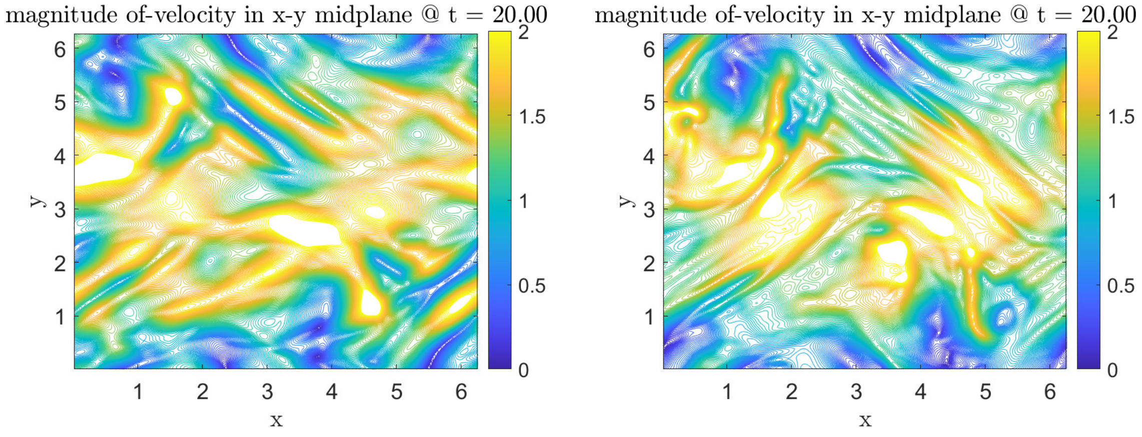

(c) ROM $M = 32$

(d) ROM $M = 48$

Figure 6.10: Velocity magnitude at $t = 20$: FOM and ROMs. Contours in xy plane.

It may be said that at $t = 5, 10$ (fig. 6.11a-6.11b)only the energy at lowest wavenumber is captured correctly by ROMs. $M = 8$ struggles with low wavenumbers $\xi_n \in [0, 6]$, but strangely, $M = 16$ underestimates even more. There could be several reasons behind this: distortions in modes increasing with mode index, inaccuracy of the hypothesis of equivalence between Fourier and POD modes, the fact that POD modes capture high-energy structures on the mean and not instantaneously.

At $t = 15$, fig. 6.11c, intertial range starts to appear, observed as three nodes parallel to reference $-5/3$ spectrum, approximately in the range $\xi_n \in [6, 10]$ and develops to four nodes at $t = 20$, fig. 6.11d. Is is only predicted by ROM with $M = 48$. In all figures ROM with $M = 48$ follows FOM the most closely and it departs from FOM spectrum as the last, i.e. at higher wavenumber than for lower basis dimension. ROMs with lower M behave in a less straightforward manner. Again, this could be caused by distortions in basis or lack of full equivalence between high-energy and large-scale structures.

ROM performance in terms of spectrum, is increasingly better with increasing M. The fact that $M = 8$ at times seems to be more accurate than $M = 16, 32$ is regarded as a coincidence in integral quantities, similarly to energy error considerations, fig. 6.6a. Intuitively, following the hypothesis of equivalence of Fourier and POD modes, good agreement between spectra at low wavenumbers for $M = 8$ would be expected. Figure 6.11 show that it is not always the case. Recalling that POD modes are energy-optimal in time-averaged sense, perhaps it would have been more prudent to investigate time-averaged spectra. However in the present research, where periodic BCs are considered, with no energy inflow, the underlying process is not stationary. Statistics then depend on time, which makes it difficult to draw conclusions.

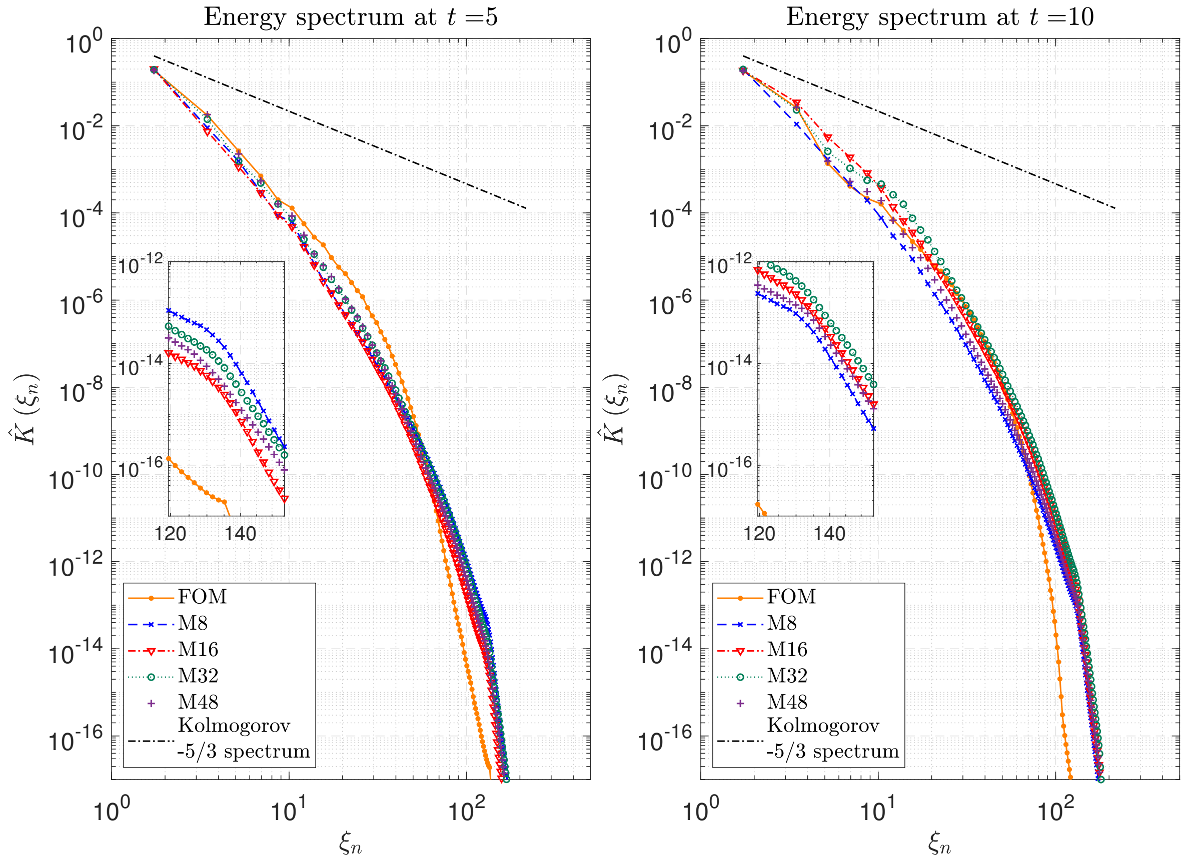

(a) $t = 5$

(b) $t = 10$

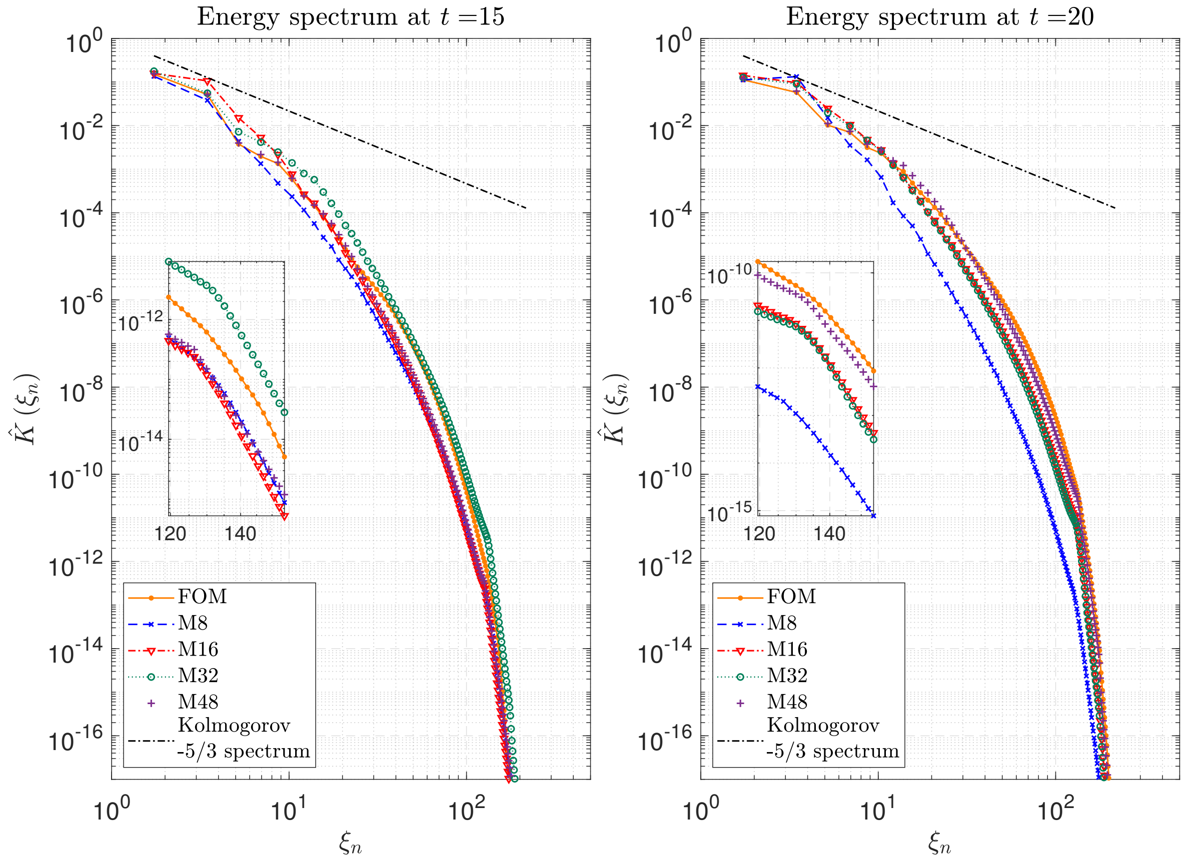

(c) $t = 15$

(d) $t = 20$

Figure 6.11: Instantaneous energy spectra of FOM and ROMs with $M = 8, 16, 32, 48$.

At all times there is a knee-effect present in all ROMs: at a specific wavenumber the rate of decay of energy plummets. In FOM it is rather soft. This phenomenon is likely associated with grid resolution. Base wavenumber[1] is $\xi_0 = \frac{2\pi}{L} = 1$, number of cells in x-direction (or any other) $N_x = 250$, hence maximum wavenumber index is $n_{max} = 125$ and maximum describable wavenumber is $\xi_{n_{max}} = \xi_0 n_{max} \approx 125$. The knee occurs close to that number.

Of course, the spectral measure of energy that is used, defined on *integer* wavenumber space, is meant for homogeneous isotropic turbulence. However such simplification was here necessary to make observations regarding comparisons of different M ROM. It is also somewhat justified in the second half of simulation, where 3D effects and vortex breakdown start to take place.

6.2. Shear layer: additional results

In this section additional analyses are performed based on shear layer test case. Section 6.2.1 is focused on distorted bases. Section 6.2.2 contains results of simulations with enforced momentum conservation. In section 6.2.3 FOM integration periods with $t_{end} = 10, 15, 20$ serve to construct three bases of the same dimension and results of corresponding ROM simulations are compared. Section 6.2.4 discusses time-extrapolation results: with $t_{end}^{FOM} < t_{end}^{ROM}$.

6.2.1. Randomly distorted/rotated bases

In this section ROM simulation is performed with the same basis as examined in section 5.1.5. Influence of white-noise distortion basis (see section 4.2.1) will be investigated. This it to check how EC-ROM operates with corrupt input data.

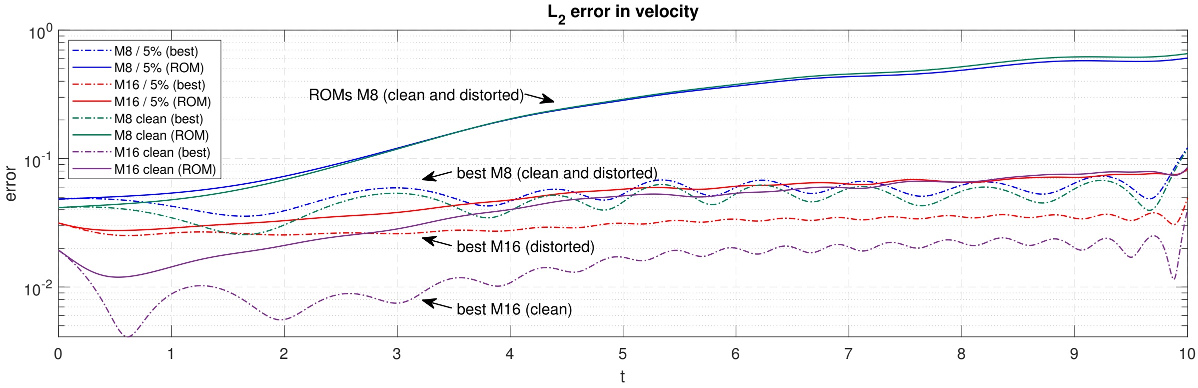

Figure 6.12: L_2 velocity error, cSVD-basis with 5% distortion

For 5% distortion (see eq. (4.6)) fig. 6.12 shows how ROMs with distorted and clean bases evolve in time in terms of errors. This distortion mildly affected ϵ_{ROM}. The log scale obscures this, but the distance between clean and distorted ROMs best errors, for either M is roughly the same, i.e. ~ 0.01. In either case clean and distorted results are increasingly closer together as time evolves. For $M = 8$ best achievable error at t_{end} is almost identical in the clean and distorted case. For $M = 16$ there is a gap.

---

[1] In section 3.4.1 ξ_0 is taken based on diagonal of the periodic cube, hence it is $\sqrt{3}$. Energy spectrum plotted in the present section is based on $\xi_0 = \sqrt{3}$, but it behaves practically the same as with $\xi_0 = 1$, because the energy is simply being integrated within different intervals (bounded by spheres in wavenumber space). Still, the correct highest representable wavenumber (Nyquist) is based on $\xi_0 = 1$

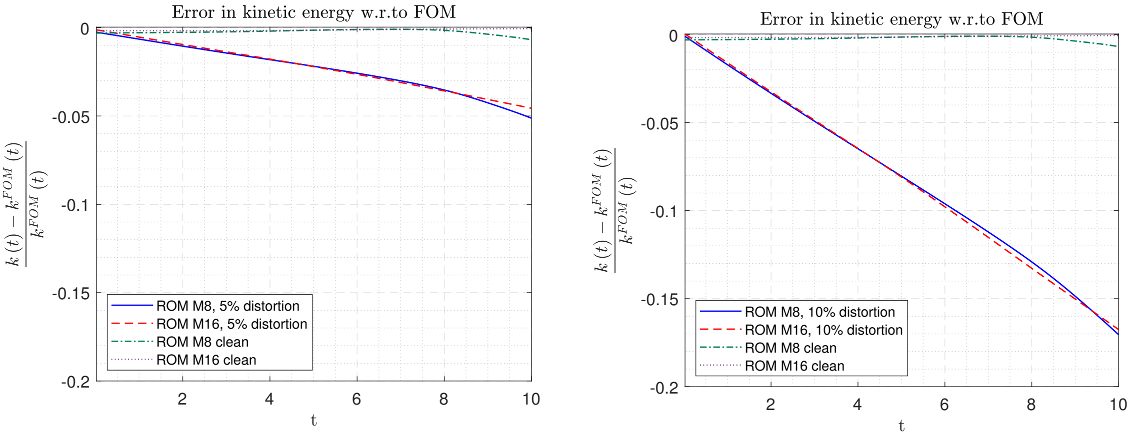

(a) error in energy

(b) 10% distortion

Figure 6.13: Error in kinetic energy (to FOM at time t): cSVD basis with 5,10% distortion

The discrepancy in global energy of clean $M8$, $M16$-ROM w.r. to FOM is < 1%, fig. 6.13. With 5% distortion the model loses 4.5 ∼ 5% of energy w.r. to FOM at t_{end}. When 10% distortion is applied to basis, the energy loss rises to 17% at the end of simulation.

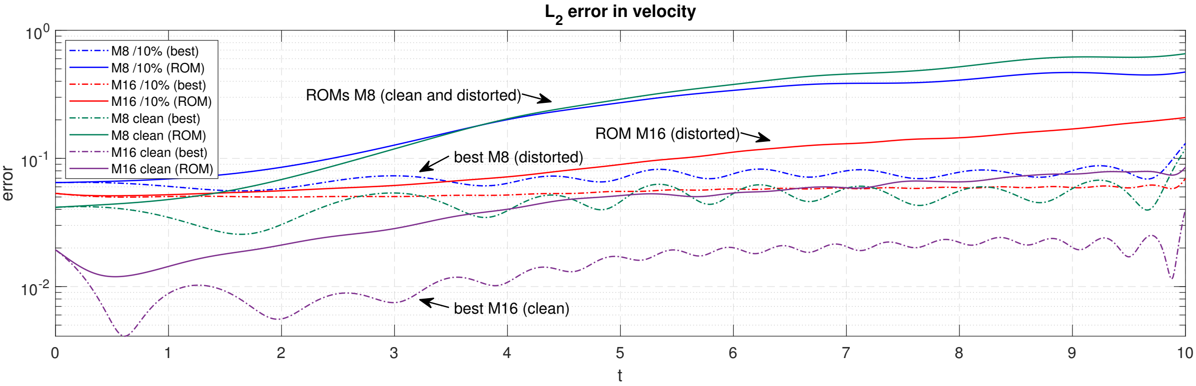

Figure 6.14: L_2 velocity error, cSVD-basis with 10% distortion

On fig. 6.14 $M16$ distorted starts off at higher error than $M8$. For best achievable error it matters more when $M = 16$ is used, as at the and frame, difference $\epsilon^{M16}_{best} - \epsilon^{M16dist.}_{best} \approx 0.03$ and $\epsilon^{M8}_{best} - \epsilon^{M8dist.}_{best} < 0.01$. When $M = 16$ distortion by 10% almost eliminates ϵ_{best} oscillations (raising the error as well).

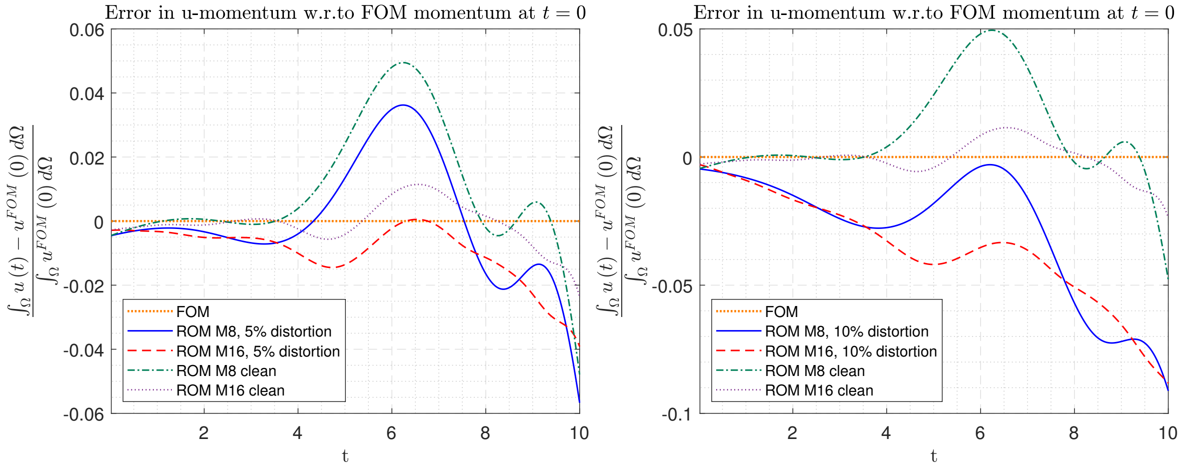

(a) 5% distortion (b) 10% distortion

Figure 6.15: Error in u-momentum (to FOM IC) : cSVD basis with distortion.

It is observed on fig. 6.15 that stronger distortion causes faster and eventually larger momentum loss. At t_{end} $M8$ with 5% distortion loses ~ 5% momentum. With 10% distortion, 9% of momentum is lost.

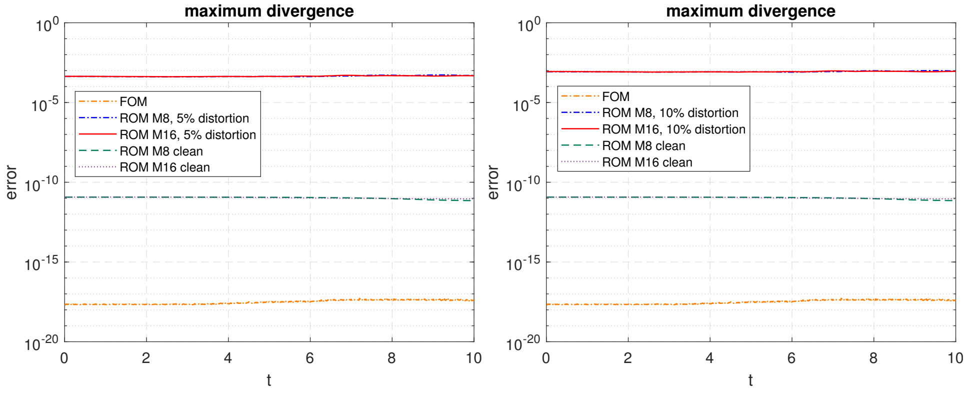

(a) 5% distortion (b) 10% distortion

Figure 6.16: Max divergence error $\|M_h V_h(t)\|_\infty$ temporal evolution: cSVD basis with 5- and 10% distortion

Both 5 and 10% distortions raise the error to ~ 10^{-3}. No significant difference between divergence errors of either distorted bases was observed. Original clean ROMs had errors of the order ~ 10^{-11} so it had risen 8 orders of magnitude due to distortion.

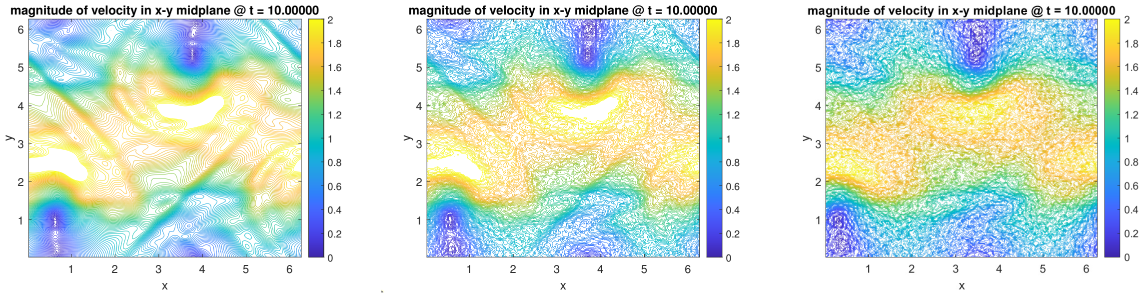

(a) ROM $M16$ cSVD (b) ROM $M16$ cSVD with 5% distortion (c) ROM $M16$ cSVD with 10% distortion

Figure 6.17: Velocity magnitude at $t = 10$: ROM $M = 16$, $t_{end} = 10$, cSVD reference basis and distorted bases. Contours in xy-plane.

10% distortion of RB obscures the formation of oblique structures oriented at ~ 45° angle to x, see fig. 6.17. This could be the action of diffusion operator which smooths steep gradients and dissipates energy on high wavenumbers.

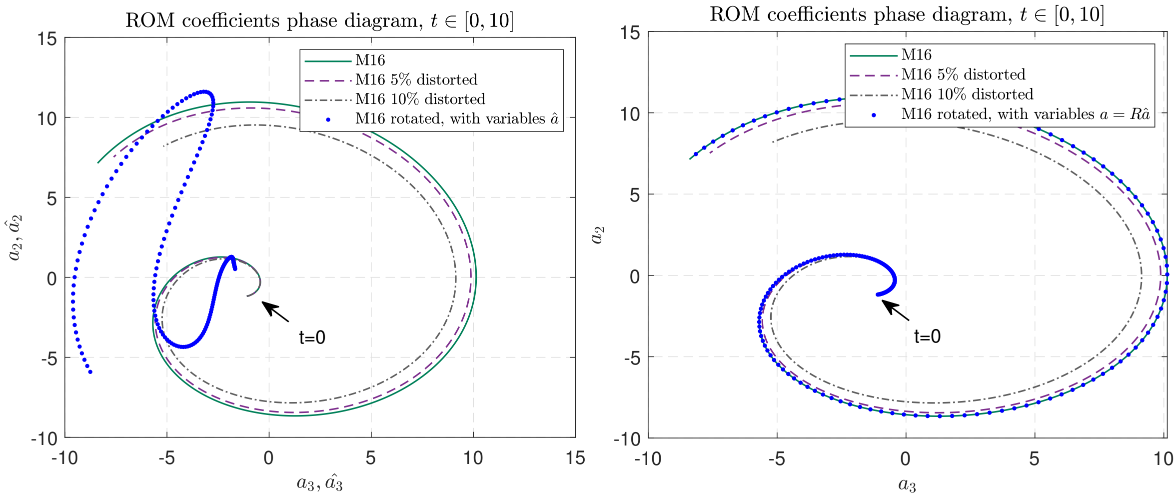

Figure 6.18: ROM trajectories for clean, distorted and rotated ROM. Variables in primary and rotated space.

From fig. 6.18 it may be observed that using distorted bases results in correspondingly distorted trajectory (here of coefficients a_1, a_2) in the phase plane. As expected, the higher the distortion, the further away the trajectory if ROM from reference ROM trajectory. When rotated basis is applied, relations between the respectable rotated ROM space coefficients are different than in the primary example. However, when the variables are transformed back, the identity relation (see section 4.2.1) with primary ROM variables becomes clear.

6.2.2. Enforced momentum conservation

In this section constrained SVD will be used to enforce momentum conservation in ROM (see section 3.1.4). The experiment is aimed at examining the compatibility of this technique with iSVD and comparing the results with ROM in which momentum conservation was not enforced.

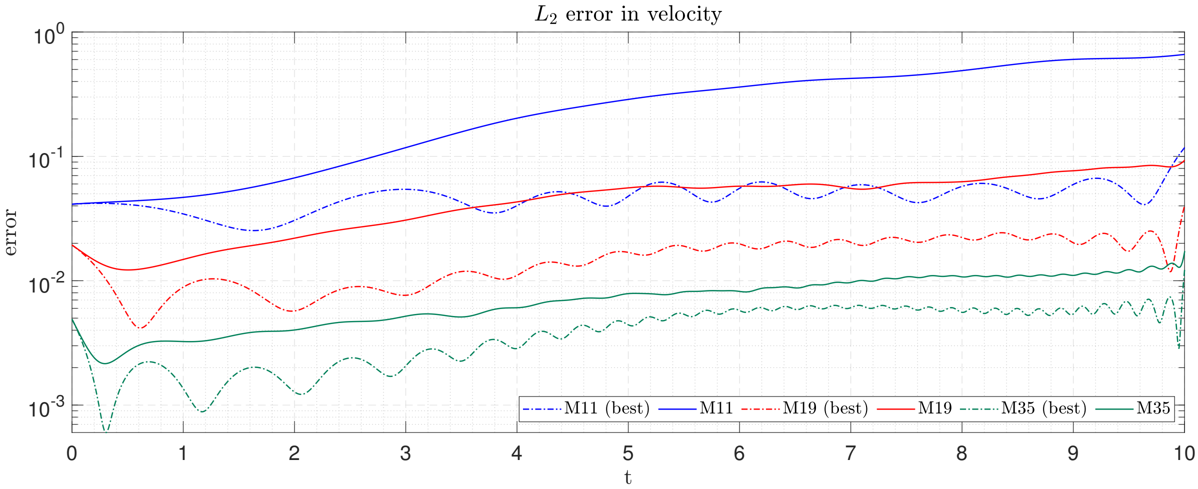

Figure 6.19: L_2 velocity error, enforced momentum conservation.

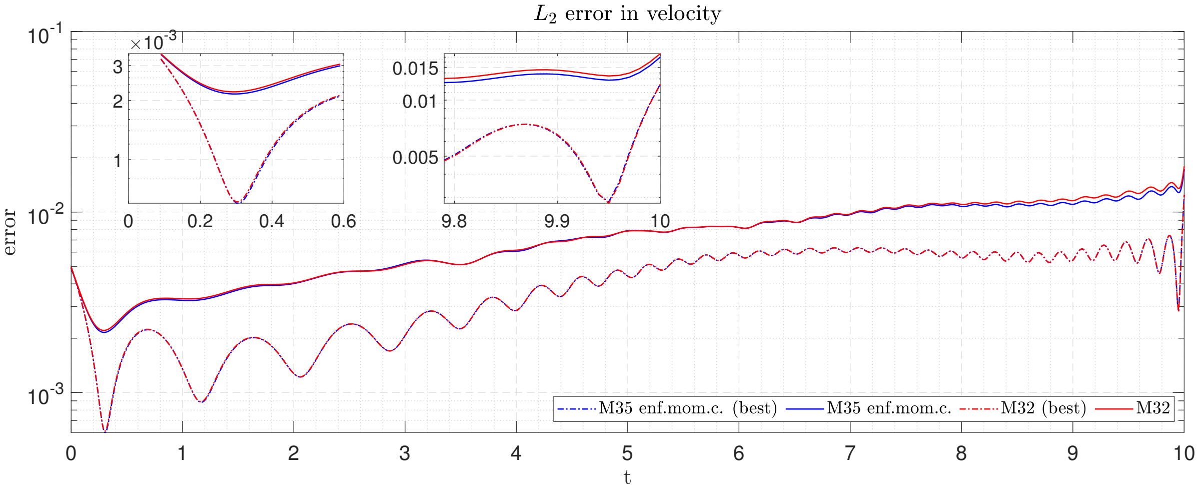

Figure 6.20: L_2 velocity error, enforced momentum conservation and iSVD reference simulation.

$M = 35$ basis is able to maintain at most 2% error in velocity, fig. 6.19. A comparison is made for the same FOM and ROMs with and without enforced momentum conservation in fig. 6.20.

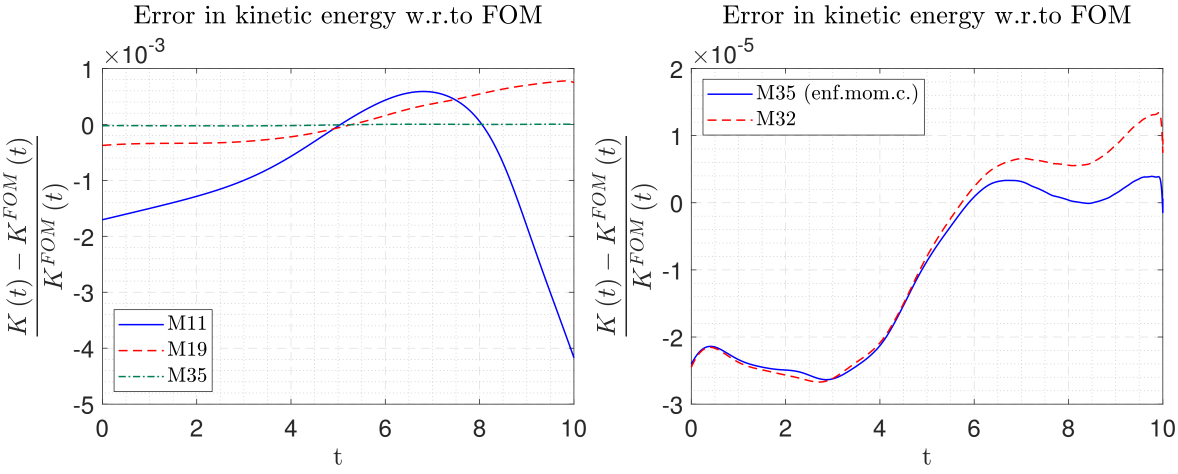

(a) Enforced momentum conservation

(b) Comparison with reference cSVD case

Figure 6.21: Error in kinetic energy (to FOM at time t) temporal evolution, with and w/o enforced momentum conservation.

Energy behaviour is similar to the case where momentum conservation is not enforced, yet slightly improved. ROM with $M = 35$ with enforced momentum conservation is mostly closer to FOM than $M = 32$ without the modification applied, as may be seen in fig. 6.21.

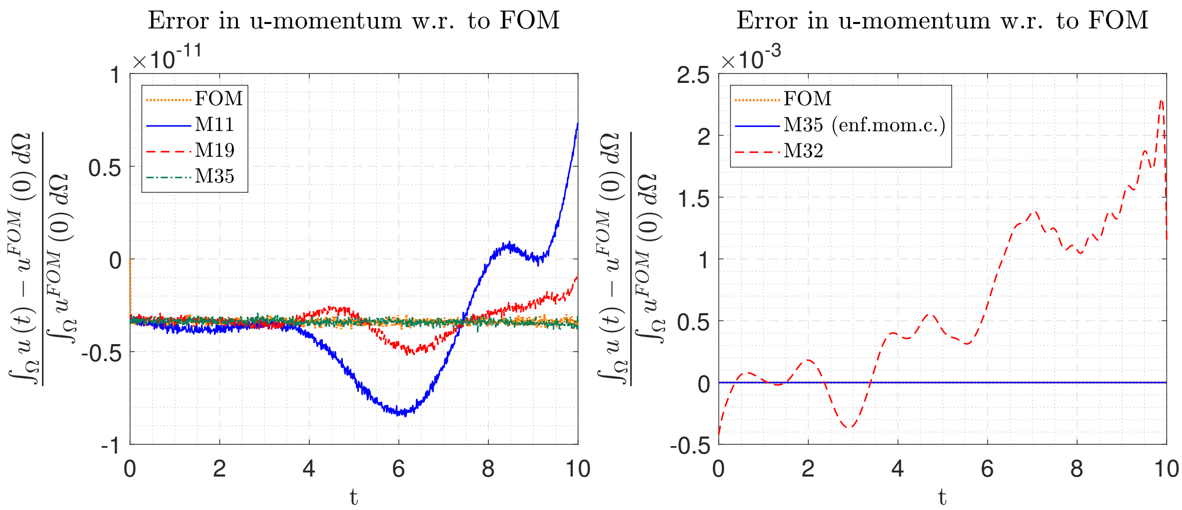

Figure 6.22: Error in u-momentum (to FOM IC) temporal evolution, with and w/o enforced momentum conservation.

The conservation of momentum holds in all ROMs to within 10^{-11} w.r. to FOM, fig. 6.22. Comparison with reference shows, that enforced momentum conservation works well with iSVD.

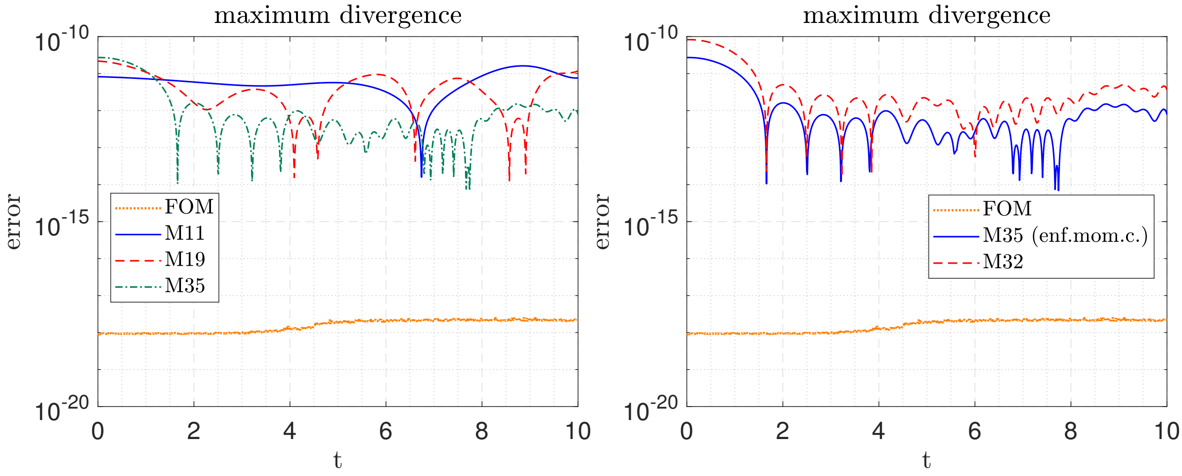

Figure 6.23: Divergence error $\|M_h V_h(t)\|_\infty$ in maximum norm.

As depicted on fig. 6.23, the order of error in divergence $\sim 10^{-10}$, which is more, compared to the case without enforcing momentum conservation, with cSVD, fig. 6.16. On average divergence maximum error is of the order $\sim 10^{-11}$ with $M = 16, 32$. Compared to clean cSVD fig. 6.16, the errors in divergence for $M = 16$ bases on either figure are roughly the same ($\sim 10^{-11}$).

Compared the primordial and modified bases: enforced momentum conservation slightly improves L_2 velocity error w.r. to ROM w/o this treatment and to a lesser degree ϵ_{best}. At t_{end} the errors become approximately equal (for the same M).

6.2.3. Varying integration period

In this section ROM SL solutions are compared. Three separate sets of snapshots $\{V_h(t_i)\}_{t10} \subset \{V_h(t_i)\}_{t15} \subset \{V_h(t_i)\}_{t20}$ are considered in basis construction. These sets are FOM SL solutions with $t_{end} = 10, 15, 20$. In all cases $M = 32$ was used. Standard iSVD settings were set: $k_{add} = 100$, $M_{dom} = 100$ and threshold 10^{-6}.

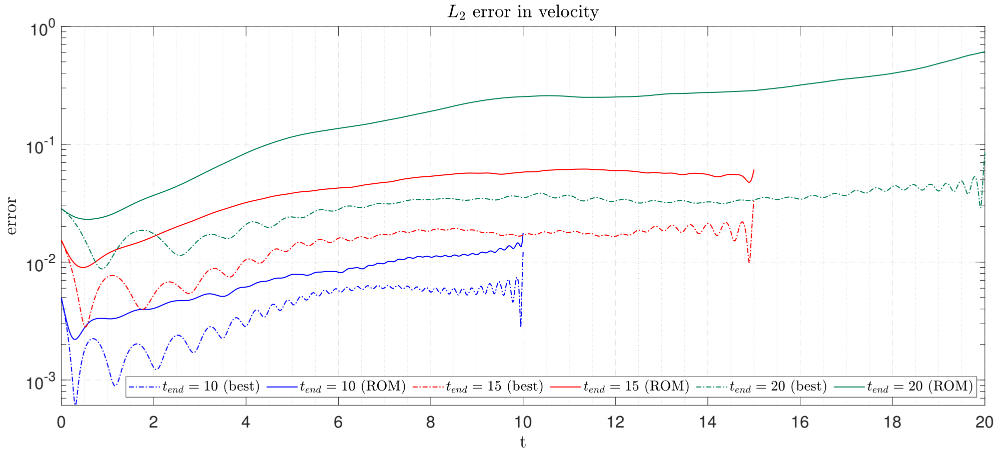

Figure 6.24: L_2 velocity error for $t_{end} = 10, 15, 20$ and fixed $M = 32$.

As anticipated, with increasing t_{end} the ROM solution accuracy deteriorates. That is as more distinct and complex structures appear in FOM as time passes, they influence POD outcome and with the same dimension of RB, when t_{end} rises, the basis becomes increasingly inaccurate. This is because for as t_{end} increases, singular values decay less rapidly. Complexity of solution space increases, more energy-carrying structures become relevant. It is worth recalling that turbulent flow, which develops during $t \in [15, 20]$ is typically characterized by slowly-decaying Kolmogorov n-width (see section 2.2.1). It seems though in the present comparison, fig. 6.24, that when $t_{end} = 20$, the quality of approximation ϵ_{best} does not deteriorate w.r. to $t_{end} = 15$ more than when $t_{end} = 15$ is compared to $t_{end} = 10$. It is also not apparent that frequency of error oscillations should decrease for longer integration period. It happens when $t_{end} = 10$ and 15 are compared but differences between $t_{end} = 15$ and 20 are not that clear, possibly due to flow specifics. In all cases there appears the typically observable jump of error near t_{end}, sharpest for the shortest period. What clearly distinguishes the case with $t_{end} = 20$ from the other two is much larger difference between ϵ_{best} and ϵ_{ROM} at end frame.

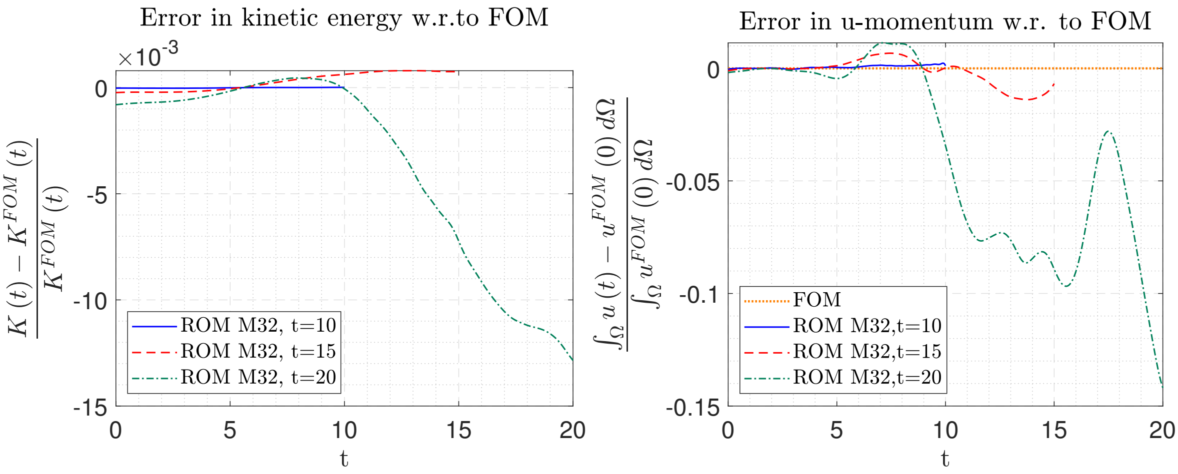

Figure 6.25: Error in total kinetic energy and momentum with $M = 32$ and $t_{end} = 10, 15, 20$.

In fig. 6.25 it is observed that errors in momentum and kinetic energy at $t = t_{end}$ differ by roughly an order of magnitude between each of $t_{end} = 10, 15, 20$.

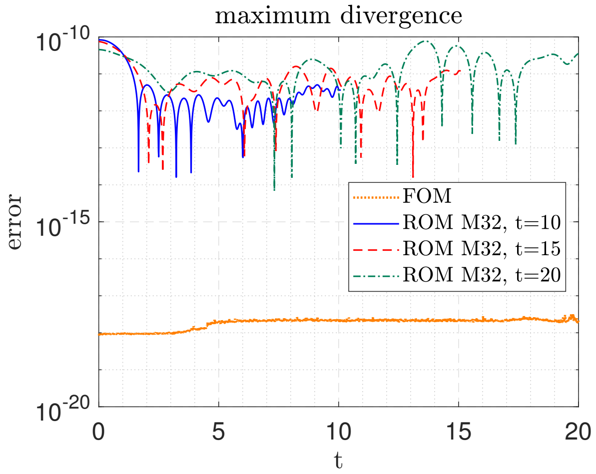

Figure 6.26: Divergence error $\|M_h V_h(t)\|_\infty$. Comparison of $t_{end} = 10, 15, 20$ cases.

Divergence error gradually increases on the mean with t_{end} for the same M, fig. 6.26. This could be a manifestation of iSVD errors. For longer t_{end} there are more snapshots to process. More incremental steps means that SVD must be reproduced more times, leading to a mild but apparent error accumulation. Incidentally, more complex fields appear in the snasphots with higher N_t, which also may have influenced basis computation in the aspect of zero-divergence property.

6.2.4. Time extrapolation

This section presents results of ROM simulations with bases constructed from FOM with $t_{end} = 10$, but ROMs are integrated to $t_{end} = 15$.

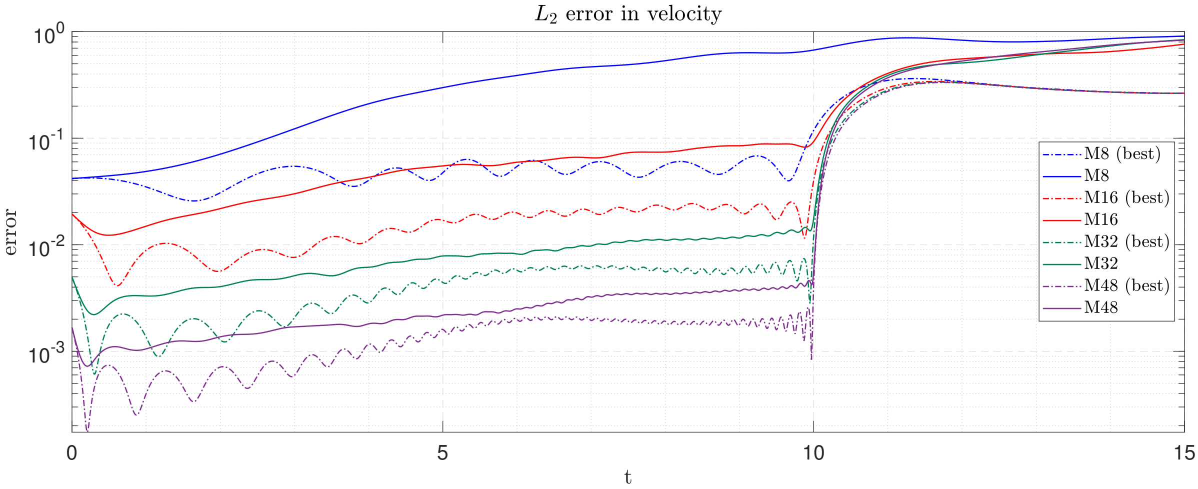

Figure 6.27: L_2 velocity error, time-extrapolated case.

Clearly, past t_{end} of FOM, error grows rapidly, fig. 6.27, except in the case where it was already high to begin with ($M = 8$). By $t = 15$ the dimension of RB ceases to matter, as all ϵ_{best} fall into single value ~ 0.27. If ϵ_{best} of all bases drops to the same order (or even number), and the bases with highest M are the most accurate, then it follows that steeper increase of error is expected for higher M near t_{end}.

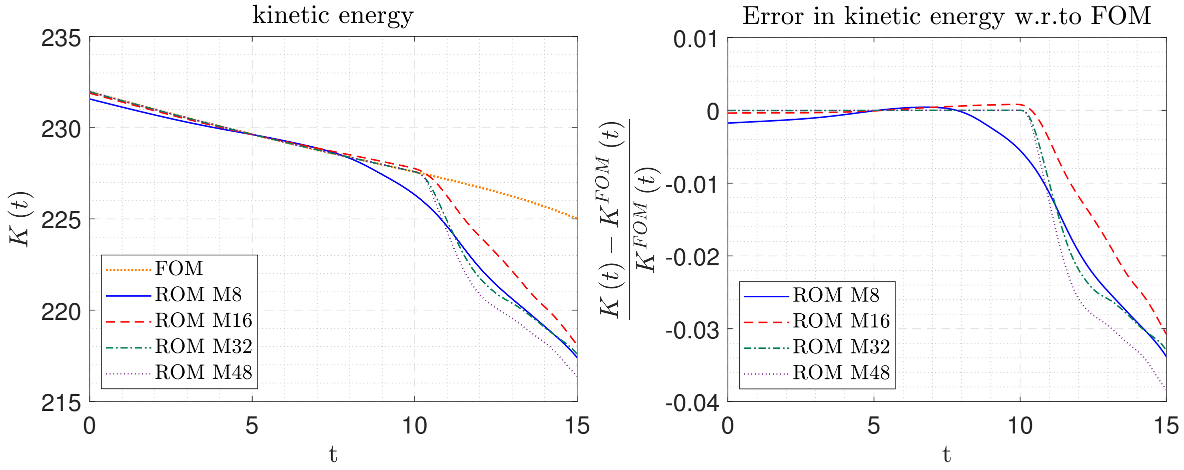

(a) kinetic energy

(b) error in kinetic energy

Figure 6.28: Energy and error (to FOM at time t). Time-extrapolated cases.

Energy is noticed to drop rapidly past FOM integration time, fig. 6.28. The drop is the more abrupt, the higher M is used. In the end total energy loss is $\sim 3-3.5\%$ for all ROMs. In fig. 6.29, momentum error is presented, indicating that momentum loss progresses at the same rate for all M. Eventually all ROMs lose $\sim 30\%$ of momentum.

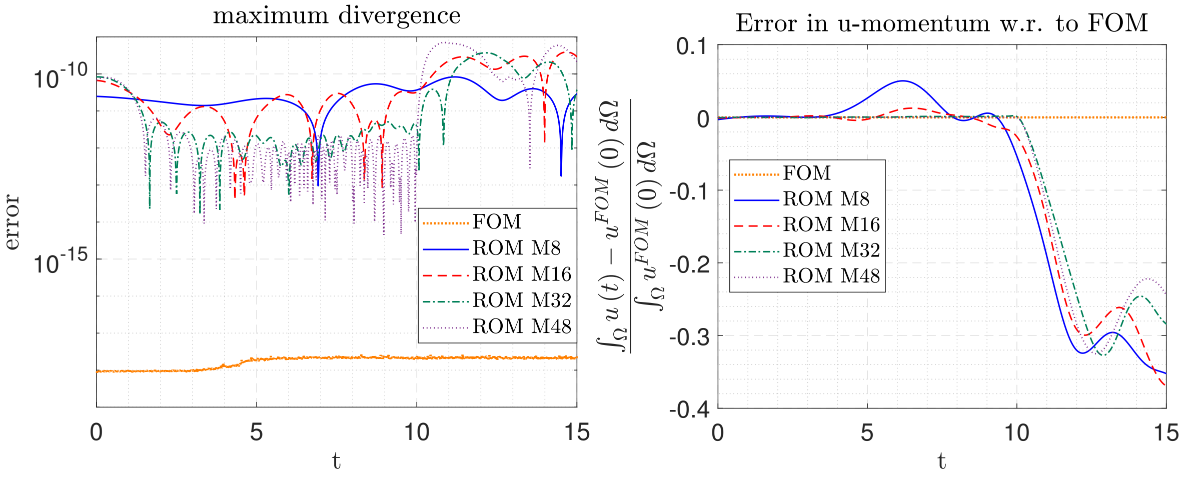

Figure 6.29: Divergence error $\|M_h V_h(t)\|_\infty$ and u-momentum error (to FOM IC). Time-extrapolated cases.

There is an observable increase in mean (time-wise) divergence error past t_{end}^{FOM} for $M = 16, 32$ fig. 6.29. For $M = 8$ the effect is not articulated. For $M = 32$ oscillations in error, prevailing almost throughout $t \in [0, 10]$, become less regular and somewhat damped. At t_{end} divergence maximum error is of the order $\sim 10^{-10}$. So the ROM struggles not only with keeping FOM trajectory, but also the feature of the solution which is zero-divergence. For $t \in [0, 10]$ the relations between ROM variables a_i are expected to be such that a_i decreases on average with increasing i. Past FOM integration time, those relations could be disturbed due to lack of information, resulting in higher values of ROM coefficients for higher i. Those coefficients correspond to higher-index modes, which have typically higher divergence errors, fig. 5.6-5.7.

6.3. Taylor-Green vortex

In this brief section, results are also shown for TG case, to provide evidence that iSVD is also capable of producing reduced basis for this test case. Taylor-Green vortex FOM (fine grid) snapshots with $t_{end} = 10$ serve to build a basis with iSVD parameters $M_{dom} = 100$, $k_{add} = 100$, threshold 10^{-6}. The basis is not treated further. ROM simulation then follow, with $M = 8, 16, 32, 48$.

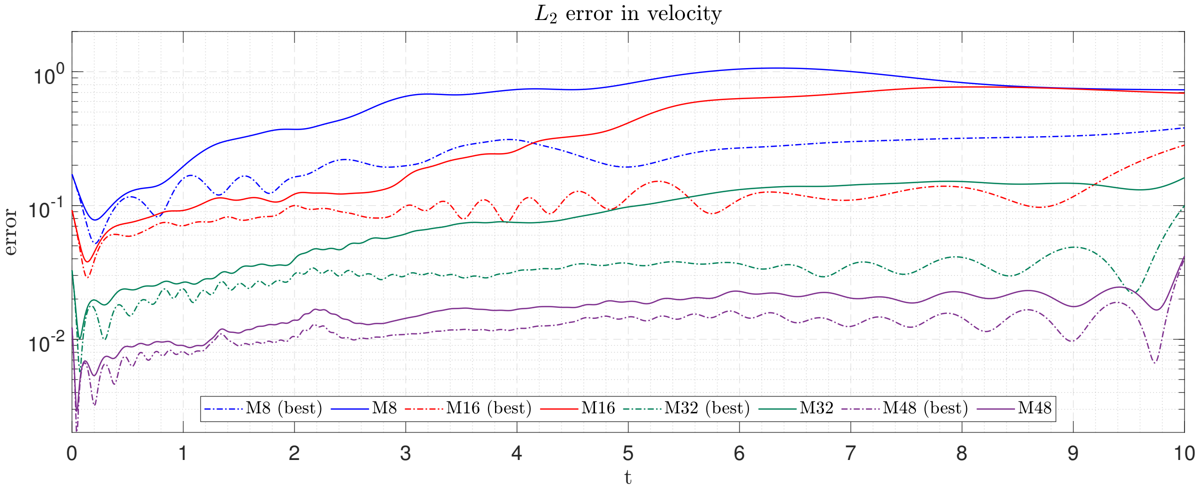

Figure 6.30: L_2 velocity error, $t_{end} = 10$.

Clearly with the same M, ϵ_{best} in TG case, fig. 6.30 is higher than in the shear layer case, fig. 6.27 with the same number of elements, time step and t_{end}. Even ROM with $M = 32$ struggles to reach $\epsilon_{ROM} \approx 10^{-1}$ at the end of the simulation, with ϵ_{best} only slightly below. The reason behind that is most likely that TG case is strongly 3D from the beginning, see eq. (4.5). More basis functions are needed to capture this complexity. Indeed, SV decay is slower in this case, see fig. 5.28 and compare TG with SL for $t_{end} = 10$.

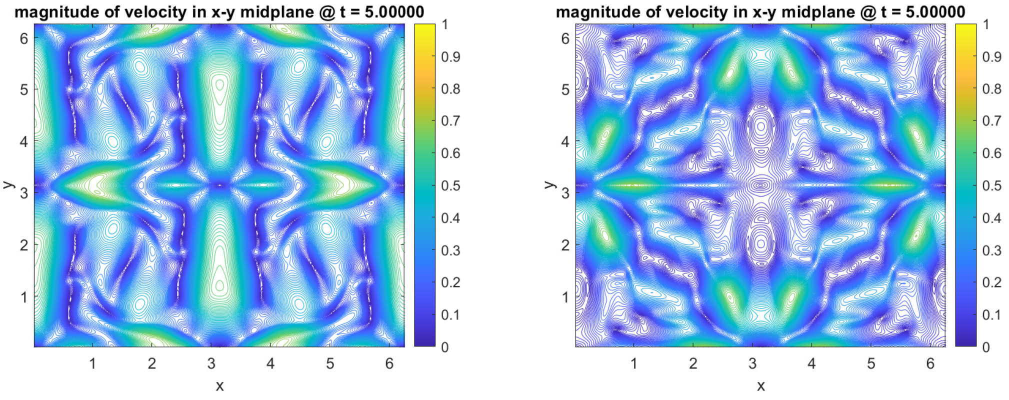

(a) FOM (b) ROM M8

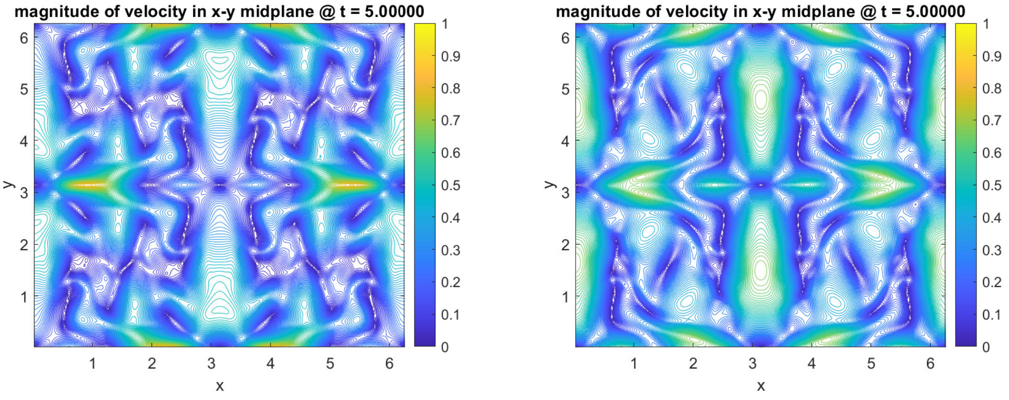

(c) ROM M16 (d) ROM M32

Figure 6.31: Velocity magnitude at $t = 5$: FOM and ROM with $M = 8, 16, 32$, $t_{end} = 10$, . Contours in xy-plane.

Case with $M = 48$ is by far the only one in this thesis where ϵ_{best} and ϵ_{ROM} are that close together, touching at t_{end}. It seems that even though TG is a more complex than SL in the beginning phase, this complexity does not further evolve. Diffusion appears quite quickly and it is possible that there are not very many modes needed to have a ROM solution that is best possible.

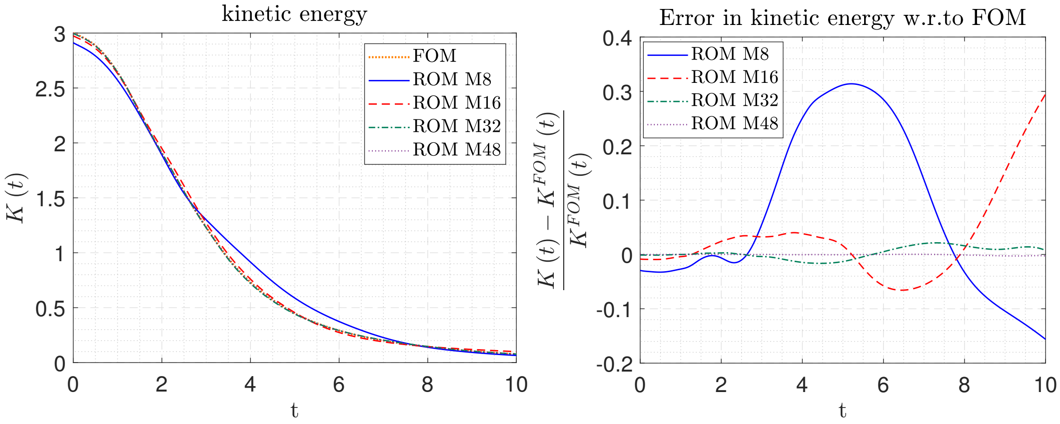

(a) energy (b) error in energy

Figure 6.32: Total kinetic energy k and error (to FOM at time t) temporal evolution: GS-orthogonalized and Helmholtz-decomposed basis.

As seen from fig. 6.32, energy drops fast in all ROMs and FOM. There are moments for $M = 8$ when energy overestimate w.r.to FOM is ~ 30%. Still energy is identically non-increasing, as dictated by EC-ROM framework.

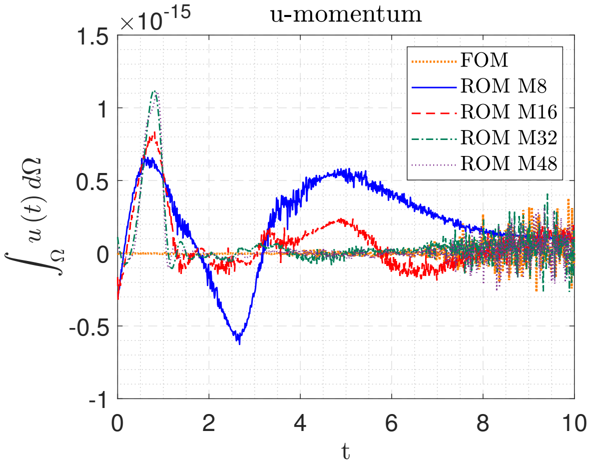

(a) u-momentum

Figure 6.33: u-momentum and error (to FOM IC) temporal evolution: GS orthogonalized and Helmholtz-decomposed basis.

Global momentum is nearly zero in the TG case, as there is no mean flow, fig. 6.33. This feature is well followed by FOM, whose u-momentum is never further away from FOM (or zero) than $5\epsilon_{machine}$. Interestingly, the first outburst of imbalance of u-momentum, near $t = 1$ is stronger with increasing M, which should not be the case. It is of little concern however, because values of the order ~ 10^{-15} are considered here, fig. 6.33, while ROM errors is still many orders of magnitude higher.

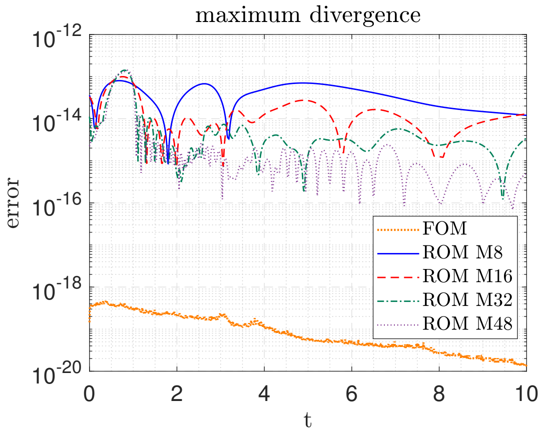

Figure 6.34: $\|M_h V_h(t)\|_\infty$ temporal evolution

Divergence error is kept fairly low, fig. 6.34, even though the basis was not treated with Helmholtz decomposition. A clearer tendency than in shear layer case (fig. 6.4) is noticeable: error in divergence considerably decreases when more modes are applied.

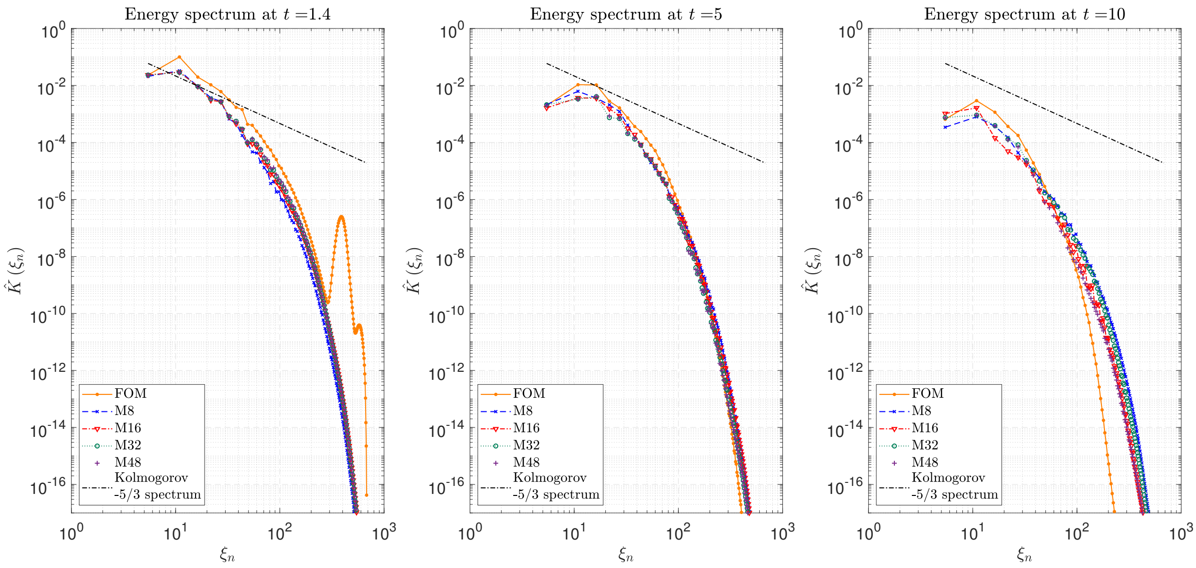

(a) $t = 1.4$

(b) $t = 5$

(c) $t = 10$

Figure 6.35: Spectra at three selected instants. On the first figure excessive accumulation of energy in FOM on highest resolved wave numbers is clearly noticable.

In the spectrum fig. 6.35 at $t = 1.4$ there is a clearly noticeable accumulation of energy on the highest grid-resolved ξ_n. This phenomenon does not lead to instability, as it quickly passes. It may be caused by high degree of symmetry in the initial condition, which is an unstable state, tending to change erratically into a more stable configuration. Due to symmetries there might appear doubling/quadrupling/ etc. of kinetic energy associated to a particular wavenumber, as many vortices are in coherent motions.

TG is a flow case that behaves differently that SL, in that there is no mean direction flow. Thus the investigation of integer wavenumber spectra makes more sense, as the flow evolves towards homogeneous isotropic turbulence. However intertial range has not been identified in FOM. Moreover, due to 3D complexity of TG flow case, eddy viscosity could not be conceived by averaging gradients in xz plane, rendering EV computation expensive. Hence TG is left out of a priori modeling.

7

A priori analysis

The present chapter discusses the results of a priori turbulence modeling analysis. Methodology of this test was presented in section 3.2. Considerations are limited to the SL case with $t_{end} = 20$ and grid $N_p = 250^3$. RB constructed from this FOM is conceived from $N_t = 2001$ snapshots, with iSVD increment size $k_{add} = 100$ and numbers of dominant singular values $M_{dom} = 100$. Helmholtz and Gram-Schmidt treatment is applied to the basis. It is reiterated, that in the whole a priori analysis the ROM equations are not solved. Instead, FOM solution projected onto span$\left\{\overline{\Phi}\right\}$ or appropriate subspaces is used, so in this chapter $a = a^{FOM}$ at all times. As a reminder, the least squares problem for α_1, β_1 eq. (3.42) was:

$$\min_{\alpha_1,\beta_1\in\mathbb{R}} \frac{1}{2}\left\| \langle \overline{\Phi}_u \overline{\Phi}_u^T R_u\rangle_{xz} - \alpha_1 \langle \overline{\Phi}_u \overline{\Phi}_u^T W_{1,u}\rangle_{xz} - \beta_1 \right\|^2, \tag{7.1}$$

for α_2, β_2 analogously.

The constant α_1 corresponds to projected diffusive term $\alpha_1\overline{\Phi}^T W_1 = \overline{\Phi}^T L_h \left[\alpha_1 \nu_h^t \odot \left(S_h\left(\overline{\Phi}\overline{a}\right)\right)\right]$. The constant α_2 is of the projected diffusive term with EV-POD $\alpha_2\overline{\Phi}^T W_2 = \overline{\Phi}^T L_h \left[\alpha_2 \left(\eta g\right) \odot \left(S_h\left(\overline{\Phi}\overline{a}\right)\right)\right]$. All functions are averaged in xz plane using $\langle\cdot\rangle_{xz}$ (first reconstructed via left multiplication of the projected terms by $\overline{\Phi}$). Relative error plots (normalized by norm of target function) are given, for $M = 8, 16, 32, 48$, along with plots of regression coefficients α, β for all M. The plots of actual target and regressor are presented for two time instants, $t = 5, 20$.

The closure model is deemed suitable when there is no need to adjust the closure term $\overline{\Phi}^T W$ (see eq. (3.30)) by either regulating the magnitude of diffusion term or by offset. This translates to regression coefficients taking on the values $\alpha = 1, \beta = 0$. In fig. 7.1 the coefficients are shown. Plots of each α and each β are scaled the same for on respective subfigures.

Upon comparison of different M it is clearly noticeable, that amplitudes of multiplicative constant α are rather steady, while that of additive constant β is diminishing with increasing basis dimension. The second observation states an obvious result: lower offset is required with increasing basis dimension because the magnitude of $\overline{\Phi}_u^T R_u$ becomes smaller. The first observation seemingly comes as a surprise for several reasons. Firstly it was expected, that ν_t would be vanishing with increasing M, since its computation (see eq. (3.37)) would be based upon low-energy motions. This is actually the case, see plots of EV in appendix A.3. There are always some finite gradients expected in very-low-energy motions, which means that the quotient of eq. (3.37) is likely to be vanishing for those $\boldsymbol{u}_>$ due to the square root in denominator. The EV (turbulent) diffusion operator acts on resolved field $\overline{\Phi}\overline{a}$, which has opposite tendency, i.e. its magnitude increases with increasing M. The latter effect is mild, as over 99% of energy (a squared norm of the solution) is contained in the first 8 modes already. Therefore the whole turbulent diffusive term is expected to vanish. But since $\overline{\Phi}_u^T R_u$ also decays with increasing M, α must adapt accordingly, to maintain optimum in the least squares sense. And since α oscillates with about the same amplitude for all M, it might be inferred that that the magnitudes of $\overline{\Phi}_u^T R_u$ and $\overline{\Phi}_u^T W_{1,u}$ (or $\overline{\Phi}_u^T W_{2,u}$) are decaying at the same rate (w.r. to M) as RB is appended with subsequent modes. It is still surprising that α is not decaying, because the closure term should be vanishing for a well-resolved flow. The reasons behind this should be sought in the way the error estimator is constructed (absolute error) and simply in that this EV model is not suitable for this particular problem.

Both regression coefficients at the same time increase in frequency with increasing M. For the first two bases, with dimensions $8, 16$ respectively, regression coefficients in $t \in [0, 2]$ are close to zero. This indicates that in the beginning phase of the flow there is no need for a closure model, as low-dimension bases describe dynamics accurately enough and very little fine-scale motions are present at that time. As will be revealed, this does not mean that the error is low in that period. It only means, that LS optimization yielded such values of regression coefficients, from which every deviation would result in a higher error. At that time, when mostly large scale structures are present, the quotient in EV, including velocities and their gradients (eq. (3.37)) likely does not properly reflect the action of truncated scales.

Another observation regarding regression coefficients is that (especially for $M = 8$), α and β seem to have a high degree of correlation throughout the integration period. This tendency is diminishing for higher M but it still may be said that high value of multiplicative constant frequently requires high value of additive correction. Furthermore, most of the time, signs of α and β are the same. This could be a response to temporal fluctuations of the target function. The matter will be further discussed at the end of this chapter.

Near $t = t_{end}$ there are noticeable oscillations of α in increased frequency for almost all M. This indicates onset of turbulence (compare with wavenumber spectra of ROM solutions fig. 6.11), whereby temporal fluctuations of target function (missing content based on FOM) become strong. Basis is also less accurate near t_{end}, as confirmed by almost all plots of solution error (see e.g. fig. 6.1), which could have also contributed to this effect.

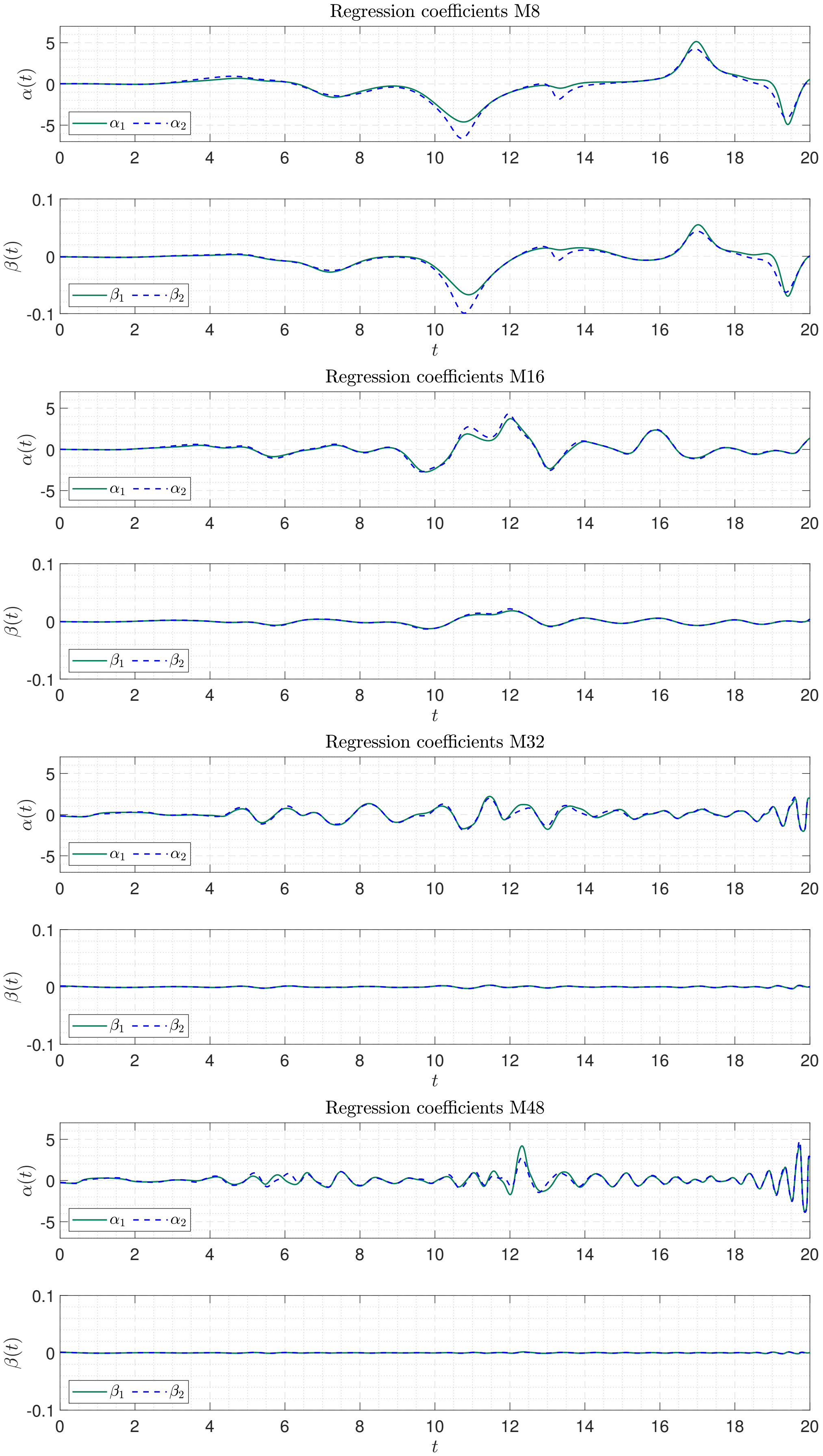

Regression coefficients M8

Regression coefficients M16

Regression coefficients M32

Regression coefficients M48

Figure 7.1: Coefficients of regression for $M = 8, 16, 32, 48$ and $t \in [0, 20]$

Relative errors are presented in fig. 7.2-7.3. Those measure how well does the EV-diffusive term along with an additive constant approximate the missing content. When the error is close to 1, it means that there is limited capability of the model to approximate unresolved content. It is clear from those plots, that the EV model does not work well for this particular problem. The lowest error overall is obtained for $M = 8$, fig. 7.2a. There are instants at which the error is satisfactory, even $< 10^{-1}$, but in general it is very high. What is more, this error is computed w.r.t. to the exact target function that was used in regression, i.e. xz-averaged unresolved terms R. However, EV diffusion term is supposed to model a missing term in discretized NS equations. Both terms are in non-averaged $3D$ setting. Errors are then of course even higher (see appendix A, appendix A.5). It is also observed, that, as in the case of regression coefficients, the frequency of error oscillations increases with M and for a fixed M near t_{end}. The reasons behind that are the same as in case of α, β and L_2 velocity errors in the previous chapter.

What is a significant finding is that POD-expansion of EV does follow the actual EV term well, as indicated by both errors and regression coefficients (blue curves in fig. 7.1 -7.3). This suggests, that precomputation with the use of EV-POD makes sense.

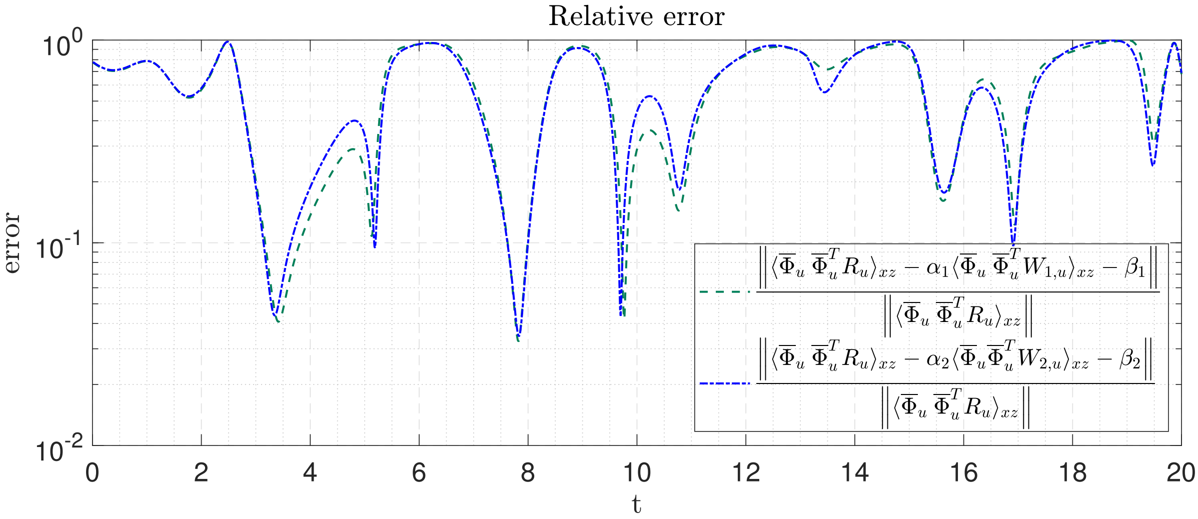

(a) $M = 8$

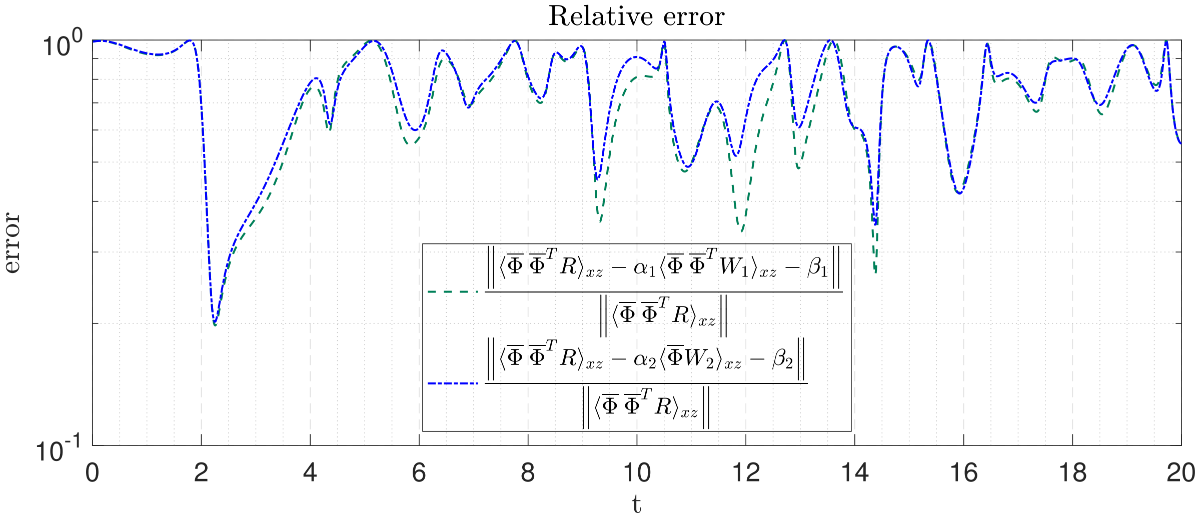

(b) $M = 16$

Figure 7.2: Relative error for $M = 8, 16$ and $t \in [0, 20]$ in averaged terms.

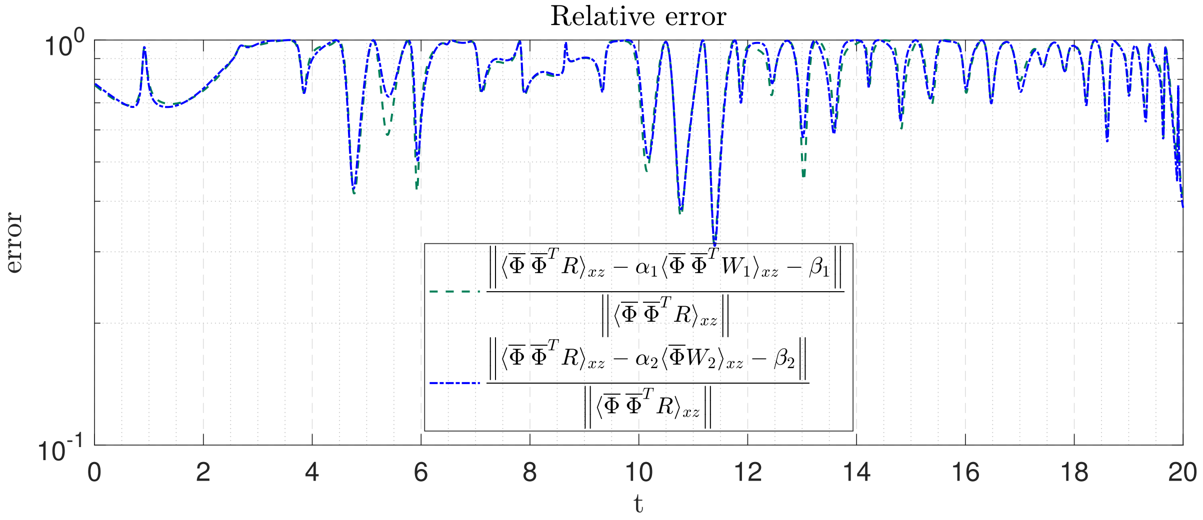

(a) $M = 32$

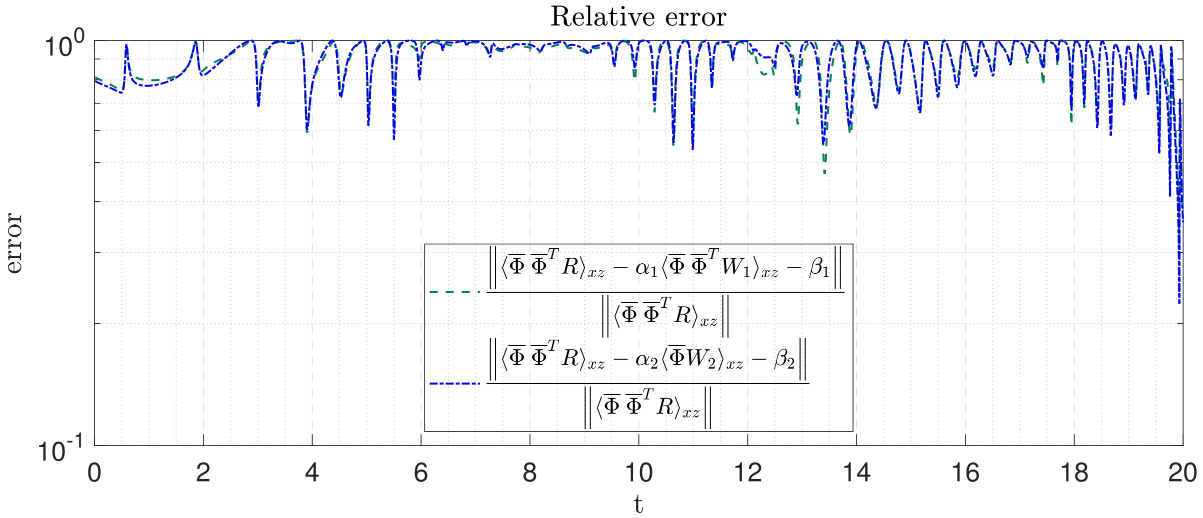

(b) $M = 48$

Figure 7.3: Relative error for $M = 32, 48$ and $t \in [0, 20]$ in averaged terms.

As described in section 3.2.3, eq. (3.43) - (3.44), LS fit may be achieved either for all components of the full target vector field $\langle\overline{\Phi\Phi}^T R\rangle_{xz}$, or only for u-component $\left[\langle\overline{\Phi\Phi}^T R\rangle_{xz}\right]_u$. Presently only the latter option is pursued. The errors that have been presented concern fitting xz-averaged regressors W_1, W_2. However initial considerations of the closure term in section 3.2.1 were focused on the non-averaged term. Such is also the role of eddy viscosity in a flow, where it acts on the whole 3D flow field. Errors of the present LS fit, but computed w.r.t. to 3D target function R are placed in the appendix, appendix A.5. The conclusion is that mixing-length EV model (eq. (3.32) with ν_t described by eq. (3.37)) is a completely inadequate model for unresolved scales.

Actual regressors and targets are plotted in fig. 7.4-7.5. Legend is common for all plots. It is observed that at times the approximation if fairly good, e.g. fig. 7.4 for $M = 8$, although it is too diffusive. From fig. 7.5 it seems that the regressor misses some high frequency content, which was probably truncated by filtering EV with Gaussian filter (see section 3.2.2). It appears that filtering could have been adapted better, i.e. by using lower filter width.

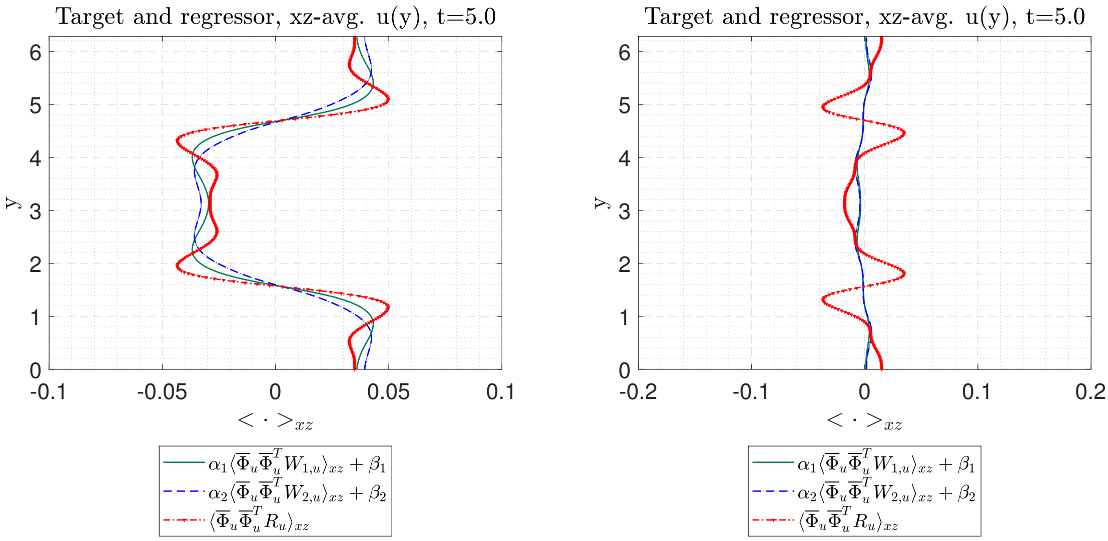

(a) $M = 8$

(b) $M = 16$

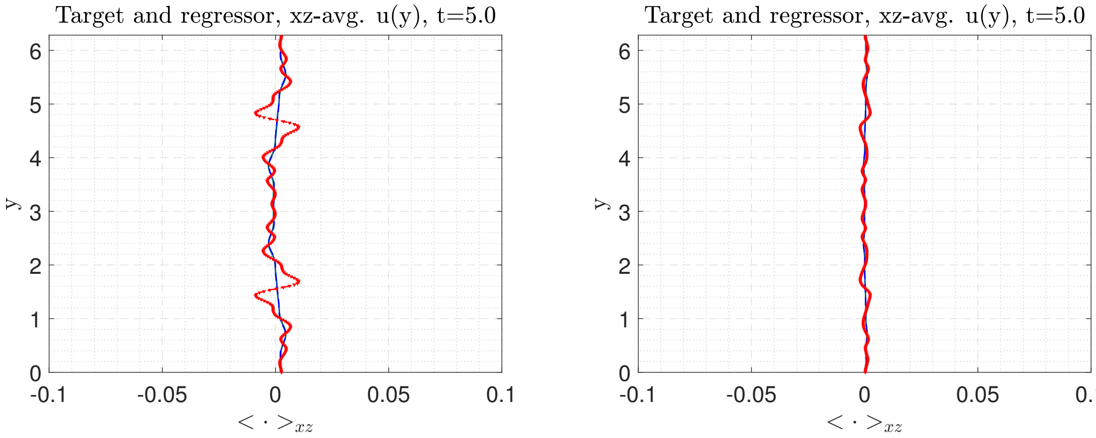

(c) $M = 32$

(d) $M = 48$

Figure 7.4: Regressor and target function for $M = 8, 16, 32, 48$ at $t = 5$, with and without EV-POD

As mentioned, there appears a correlation between regression coefficients α and β and they frequently have the same sign. Moreover, β is diminishing with increasing dimension of basis. Increasingly less high-energy content is included in the (projected) exact closure term $\overline{\Phi}^T R$ as M increases. Target function is derived from this term. On the other hand, there is increasingly more low-energy content in the regressor $\overline{\Phi}^T W_1$, because more modes are included in $\overline{\Phi}$. However, this tendency is further disrupted by $\nu_t(t, x)$, which, as M increases, is also built out of consequently lower-energy motions. It seems possible that β is compensating for a low-energy quasi-steady component of motion, that is not present in the EV diffusive term $\overline{\Phi}^T L_h \left[\alpha_1 \nu_h^t \odot \left(S_h\left(\overline{\Phi}\overline{a}\right)\right)\right]$ when M is low. This component could have arisen e.g. due to perturbations in IC, see section 4.1. If this was true, it would undermine the hypothesis of equivalence between Fourier and POD basis.

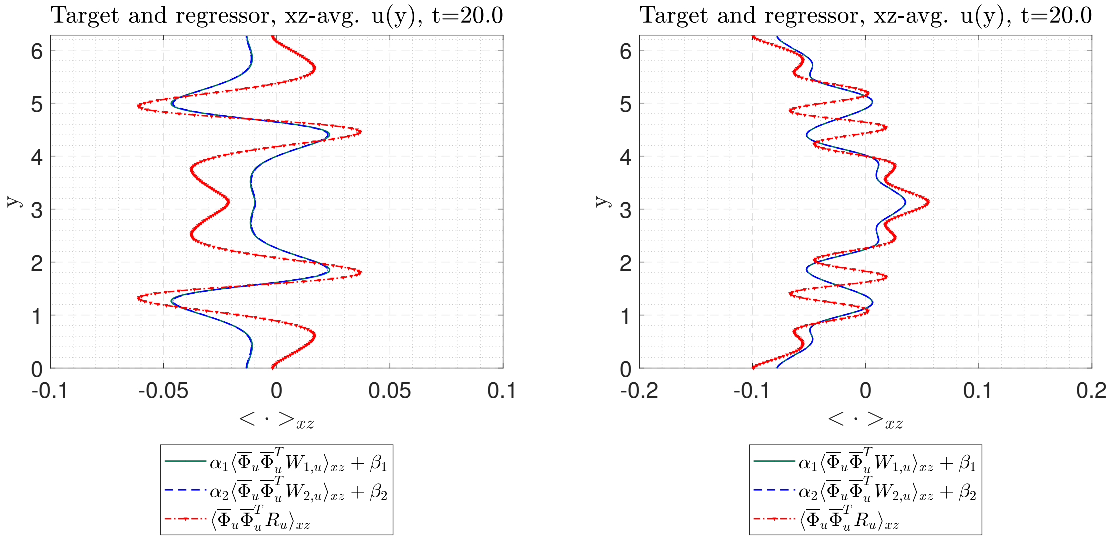

(a) $M = 8$

(b) $M = 16$

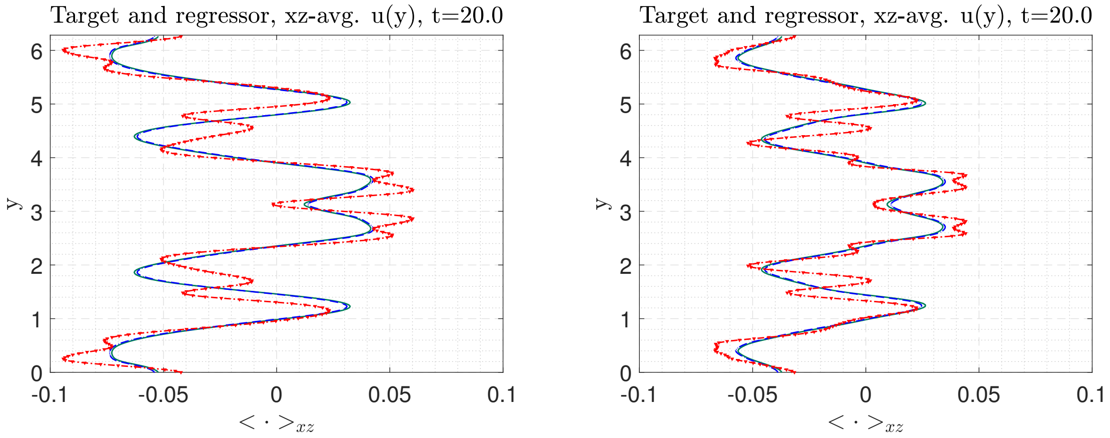

(c) $M = 32$

(d) $M = 48$

Figure 7.5: Regressor and target function for $M = 8, 16, 32, 48$ at $t = 20$, with and without EV-POD

One must keep in mind that POD was performed on the field of velocities V_h, not diffusive terms $D_h V_h$ or other, and that the regression is performed on xz-averaged terms. It is therefore difficult to argue that high dimension of basis really fixes the issue of regression additive term β. It is however evident, from the error plots, fig. 7.2-7.3, that the model simply does not accurately reflect the truncated content, and consequently more so, for higher-dimensional bases. It is likely that this failure is caused by xz-averaging or deviations from the original model by Aubry et. al [4], such as using filter on EV or computing EV as instantaneous. Using iSVD of course could have also added its share of distortion to the results, but it is not regarded as a key factor here.

8

Conclusion and recommendations

The subject matter of the research that has been carried out covers several topics of different fields: projection-ROM, closure modeling of eddy viscosity type, approximate SVD/POD. The first objective was to apply a particular algorithm, iSVD, to a particular ROM: EC-ROM. Then test the validity of produced basis against three key iSVD parameters by examining the quality of basis and ROM simulation errors, without unresolved modes modeling.

The second objective was an a priori turbulence modeling analysis, in which a mixing-length EV model had been implemented. The model coefficients have been regressed based on FOM data to fit to a target function: the derived exact closure term i.e. the sum of expressions that are missing in ROM equations after POD truncation. This was aimed at assessing the validity of this type of modeling for the investigated test cases.

Research questions are recalled with answers written below each question in section 8.1. General conclusion is presented in section 8.2. Recommendations for future research are listed in section 8.3.

8.1. Answers to research questions

In the light of the gathered results, the following answers to research questions from chapter 1 may now be formulated:

1. **Is it possible and to what extent, to use Baker's incremental SVD algorithm as an approximate memory-efficient method of computing ROM basis? (chapter 5)**

   It is possible, single-pass version of algorithm by Baker et al. [5] used in this research has provided bases resembling cSVD with mode-to-mode errors $< 10^{-4}$ in the first fifty modes for two different test cases.

   (a) **What influences the accuracy of basis computation and in what way?**

   The quality depends on an interplay between increment size k_{add}, maximum dimension of approximate basis M_{dom} and threshold. Preferably, these should be set as high as possible. For high fidelity w.r. to cSVD k_{add} is by far the most important. When $k_{add} = 1$ (single snapshot incrementation), setting the other parameters high does not compensate for low k_{add}. This is the price paid for limited access to snapshot matrix. Increment size affects orthogonality of basis when threshold is low. Zero-divergence property of the basis is affected by k_{add} but not by M_{dom} or threshold. Increment size also influences distribution of divergence error over modes. With low threshold more singular vectors are computed (limited only by M_{dom}). A low rank method, which iSVD is, is accurate only for modes with lowest indices. When M_{dom} is low, threshold does not affect the basis fidelity (w.r. to cSVD) significantly, otherwise it does, but only when it's set to below $\sim 10^{-12}$ with also low $k_{add} \in [1, 10]$. An imporant aspect related to effectiveness of iSVD is computational time. Although not documented, it is clear that with low k_{add} and threshold, and high M_{dom}, the algorithm becomes very slow. This is due to greater number of updates which must be performed at a cost per update similar as with higher k_{add}. SV decay is mostly affected by k_{add} (when $k_{add} < 10$) and M_{dom}, in that higher SVs, right below a given M_{dom}, are underestimated for low k_{add} and M_{dom}. Threshold affects SV in a similar way, but only when k_{add} is also low. All of those issues could have a different form when a different snapshot matrix is considered. However, snapshot matrix X used in this thesis contained blocks with highly correlated snapshots (rapid decay of singular values) and those with low degree of correlation (slow decay of SV), so it covered many scenarios.

All considerations may be summarized in the following way. Parameters k_{add}, M_{dom} and threshold should be set as high as possible without compromising: the advantage of limited access method (in order not to hit operational memory limits); and quality of basis (compute only as many SV as necessary for accuracy, based on anticipated SV decay). Additionally, when only low k_{add} is permitted, M_{dom} should not be too high and threshold too low, because computation time then increases.

(b) **How useful are Gram-Schmidt orthonormalization and Helmholtz decomposition as means of counteracting possible non-divergence-free or non-orthogonal output bases?**

There is evidence that they are useful and cause no harm to fidelity of iSVD basis w.r. to reference cSVD. Gram-Schmidt improves orthogonality, while not destroying zero-divergence property. Conversely, Helmholtz decomposition extracts non-divergent part of Φ at the same time not affecting orthogonality. The treatment has no effect on wavenumber spectra. However, care must be taken when corrections due to treatment are large, because then improvement in one property may result in deterioration of another.

(c) **What is the effect of downsampling on the basis accuracy?**

It does not strongly affect orthogonality or divergence errors. But it does influence fidelity (mode-to-mode errors to cSVD): only the first 10 modes have errors $< 10^{-2}$ when constructed from downsampled snapshot set, compared with 10^{-4} for full set. When k_{add} is low, this error further increases with mode index.

(d) **How susceptible is the 3D EC-ROM basis to distortions or rotations, in terms of basis quality?**

Both 5% and 10% distortions cause severe deterioration of orthogonality, zero-divergence property and fidelity to cSVD. Rotation does not affect orthogonality or zero-divergence, but it does alter the spectra and shapes of the modes. This confirms that rotation spoils the property of POD, which is that modes are ordered w.r. to energy. Since POD basis is unique, deviation from its original form generally results in loss of this property.

2. **How well does INS3D-EC-ROM code perform, in particular with iSVD-basis?** (chapter 6)

The code performs well, its behaviour is similar to the 2D-version in [31] by Sanderse in that energy is also non-increasing. An increase of accuracy is obtained by increasing basis dimension and there are also higher oscillations of solution errors near ends of the integration period. What is different w.r. to [31] is that here deviation between ϵ_{best} and ϵ_{ROM} is stronger. It is likely caused by the 3D character of the presently considered flow and the related forward energy cascade, not by iSVD.

(a) **What is the accuracy in terms of errors in velocity, energy, momentum and divergence?** (chapter 6 throughout)

As expected, with increasing M, solution accuracy increases. It is particularly observable in ϵ_{best}. ROM solution error, represented by ϵ_{ROM}, does not behave the same, which indicates that the full dimension system dynamics is complex. For highest investigated $M = 48$, $\epsilon_{ROM} \sim 10^{-1}$ and $\epsilon_{best} \sim 10^{-2}$. At lower M differences between ϵ_{ROM} for various M are very small. Global kinetic energy of FOM is followed more accurately by higher dimension ROMs with the exception of $M = 8$, which is regarded as incidental. At the end of simulation there is deficit in momentum $\sim 5-10\%$. In bases of low dimension considerable loss of global momentum was observed $(10-25\%)$. It would therefore be advisable to use constrained SVD (enforcing momentum conservation) in future research where periodic BCs are considered, since there is also evidence that that technique is compatible with iSVD. Divergence error in SL case behaves on the mean the same for all M, however its oscillations increase in frequency with M. Without treatment the mean divergence error is $\sim 10^{-11}$ in ROM (compared to $\sim 10^{-18}$ in FOM).

There is very little influence of either downsampling or GS/Helmholtz treatment on solution accuracy. Patterns of evolution of kinetic energy and momentum are unaffected. This is explained with the already high values of ROM solution errors $\sim 10^{-2}$ at best. The treatment or downsampling make changes to bases well below that value. Hence those changes do not emerge in the presence of high solution errors or perhaps do not have enough time to manifest themselves. There was one exception where supposedly 'better' full-set basis had higher ϵ_{best} than downsampled-set basis near t_{end}. This could be a manifestation of such inconsistencies e.g. in divergence (divergence error was lower for downsampled basis). Divergence error of ROM solution identically vanishes upon applying Helmholtz decomposition.

(b) **How do the ROM energy spectra compare to FOM?** (section 6.1.3)

FOM spectra are mostly underestimated in high range and overestimated in low range of wavenumbers. The knee-effect, which is very mild in FOM is exaggerated by ROMs. One could speculate that the 'knee' has something to do with energy buildup due to POD truncation, drawing an analogy to the well-known phenomenon caused by filtering in LES. Since EC-ROM framework is used, no indefinite buildup of global energy is possible, i.e. build-up in a range of spectrum would require compensation (deficit) in a different range. This would partially explain the over- and underestimation of energy in respectively low- and high-wavenumber range. What speaks against the 'knee' being a manifestation of energy buildup is that it occurs at the same wavenumber for all M. It is therefore more likely that the 'knee' is associated to grid cut-off wavenumber in FOM ($\xi_{Nyquist} = 125$), only exaggerated through effects of EC-ROM and iSVD.

Even though with low dimension of basis one would expect low wavenumber energies to be accurately reflected by ROM, the spectra do not always confirm that. However, since this is not a stationary process, only instantaneous spectra are available. Because POD modes are energy-optimal in a time-averaged sense, perhaps in a stationary process the lower-index modes would more accurately reflect low wavenumber energies.

(c) **How susceptible is 3D EC-ROM solution to distortions or rotations of basis in terms of the mentioned errors?** (section 6.2.1)

Distortion causes larger ϵ_{best}. When high enough, they also result in increasingly larger gap between ϵ_{ROM} and ϵ_{best}. There arise no indefinitely increasing instabilities (owing to EC-ROM framework). Energy errors increase considerably when comparing 5% to 10% distortions. This is explained by the presence of more fine scale content in the lower, high-energy modes due to distortion. Since those modes have usually high corresponding values of a_i, the diffusion dissipates energy faster. Rotations of basis do not affect ROM solution at all, because they are orthogonal transformations.

(d) **Is enforced momentum conservation compatible with incremental algorithm?** (section 6.2.2)

Constrained SVD has been documented as applicable with iSVD. Momentum is confined to $\sim 10^{-12}$, but the error in energy w.r. to FOM is not always better when enforced conservation is applied and gain in accuracy is marginal. Divergence error has been clearly lowered by almost an order of magnitude on the mean. This could suggest that the problems with zero-divergence are somehow connected to issues with momentum-conservation of ROM, but the differences in errors are very small.

(e) **How does the model behave when different FOM integration times are applied to construct basis of the same dimension?** (section 6.2.3)

As expected, comparing with the same M, the largest set of snapshots, corresponding to the longest FOM integration period, yielded the least accurate basis. With increasing t_{end} there appears increasingly more fine-scale energetic structures in the reduced basis. Dynamics of those evolves very differently than that of FOM, hence the increasing gap between ϵ_{best} and ϵ_{ROM} for the longest period. For shorter periods there exist correlations between these two errors (oscillations), for the longest period there are no such correlations observed. Energy and momentum are lost much faster for ROM with $t_{end} = 20$ than the shorter ROMs with the same M.

(f) **How does the model behave when computed past FOM integration time?** (section 6.2.4)

The well known issue with time extrapolation regretfully pertains in EC-ROM, because it is a feature of POD basis. It seems that there is a regularity in ϵ_{best} for all M. Shortly after t_{end}^{FOM} all ϵ_{best} fall into a single value.

3. **Is EV modeling of mixing length type an appropriate technique to model unresolved scale terms in the EC-ROM setting?** (section 3.2, chapter 7)

In the particular test case (periodic SL) and with a special variant of EV model, i.e. with filtered $\nu_t\left(t,y\right)$ it may be concluded that the closure model does not provide satisfactory approximation of truncated modes.

(a) **What is the exact form of the discrete closure term, i.e. what exactly is missing in ROM?** (section 3.2.1)

The term was derived in section 3.2.1. It comprises a sum of mixed convective terms $-\overline{\Phi}^T C_h\left(\Phi' a'\right)\overline{\Phi}\overline{a}$, $-\overline{\Phi}^T C_h\left(\overline{\Phi}\overline{a}\right)\Phi' a'$, a fine-scale convective term $-\overline{\Phi}^T C_h\left(\Phi' a'\right)\Phi' a'$, and a fine scale diffusive term $\overline{\Phi}^T \nu D_h \Phi' a'$. This is the exact closure term in the sense that it represents what is missing from ROM (within FOM integration time) after POD expansion, truncation and projection are applied to operators.

(b) **What are the errors of EV closure term w.r. to the exact closure term?**

The answer to that is simple: they are overall high, and more so, when basis dimension is high. Then they also oscillate more frequently. It seems that for high M the modeling is more frequently inadequate, i.e. when the error would have reached values exceeding 1 and it is better to switch off the EV term by setting α and β to zero. It is stressed however, that the magnitude of the exact closure term also decays with M, which has its role in increasing the relative error, because it is the normalizing factor in relative error computation.

(c) **What is the behavior of regression coefficients for various dimensions of RB?**

Just as L_2 error of solution oscillates more frequently as M increases, so do the regression coefficients α, β. The former does not lose its amplitude with increasing M, but the latter diminishes. This means that no additive compensation is necessary for higher dimension of basis, which is speculated to result from there being a low-energy quasi-steady motion encoded in the higher modes. Steady amplitude of α indicates not only that the EV model is not suitable, but also that the target and regressor terms decay at a similar rate with M.

(d) **Is POD a viable choice for EV field approximation in this type of modeling?**

Judging from all the plots in chapter 7, there are only rare and brief moments when EV and EV-POD terms are misaligned. Therefore the answer is: yes, EV may be approximated by its truncated POD. The same restrictions apply as when any other quantity is approximated by such decomposition, e.g. truncated POD is a form of filtering. Here, the effect of POD filtering is not as much visible, because ν_t is already conceived as filtered (by Gaussian filter), Therefore POD rarely introduces change to filtered EV field, provided enough modes are used.

(e) **Is precomputation of the EV diffusion operator in closure term possible?**

It is certainly possible, and also a recommended step. Estimates on cost savings are not available, but it is enough to mention that in 3D-EV case the time of computation of turbulent diffusion operator exceeds 72 hours when no precomputation of EV is performed. The proposed solution gives an alternative to the one presented by Wang et al. in [34], who propose a two-level scheme of projection; or to using discrete empirical interpolation (DEIM).

8.2. Conclusion

A priori analysis has revealed, that the proposed EV mixing-length model, inspired by Aubry et al. [4] and Wang et al. [35], is inadequate in the presently considered test case (SL). Of potential reasons behind this, using iSVD instead of cSVD seems of marginal significance. The more likely reasons are: the use of xz-averaging of terms in regression, xz-averaging and Gauss-filtering of ν_t, computing EV as unsteady ($\nu_t = \nu_t\left(y,t\right)$), and the sheer simplicity of expression for EV, which was primordially aimed at modeling turbulence in a near-wall region of a wall-bounded stationary flow [4]. Especially the last observation makes it understandable that such model could be inaccurate in an unsteady shear layer flow where no boundaries are present. Furthermore filtering made EV less noisy but also removed some high-wavenumber content, which is observed in the plots, see appendix A.3. Finally, EV term is simply imposed, artificially added to the ROM equations, while usually, e.g. in RANS-based ROMs (see [14]), it appears naturally, as one of the RANS-FOM terms, projected.

Summarizing, iSVD and similar algorithms are a promising direction of research withing MOR, because savings in computational time and resources are always desired. Even though online-computation (during

FOM) with single-snapshot increments is at present not recommended, auxiliary methods exist that aid this process and/or Baker's algorithm may also be applied to stored data, where also operational memory limitations apply. EV turbulence modeling in POD context is a more complicated matter. Primitive types of modeling like mixing-length EV mostly fail in ROM just as they fail in RANS/LES. As means of improving ROM stability, those are unnecessary, because EC-ROM is already stable in a non-linear sense. Energy is non-increasing, hence an imbalance (such as additional dissipation introduced by closure term) in a range of wavenumbers requires a compensation in a different range, thereby reducing accuracy. Therefore perhaps it is more reasonable to seek improvement e.g. in modifications of the SVD basis instead of in artificial dissipation. After all POD basis is optimal only in a single sense: capturing energetic structures within a set of snapshots in average sense. When truncated POD basis is used and/or when time extrapolation is applied reduced order modeling is still a challenge.

8.3. Recommendations

This section contains recommendations for future research. Those are grouped into several categories, corresponding to important aspects of this thesis.

8.3.1. Regarding iSVD

Future research using iSVD could benefit from combining it with algorithm of optimal snapshot selection by Oxberry et al. [21], see appendix A.7. This has a potential of reducing RB construction time.

Convergence properties of iSVD have been empirically investigated by Baker et al.([5]) only in case of multi-pass algorithm. No theoretical proof was provided for a general case of matrix A in the single-pass algorithm. Theoretical research should focus on providing error bounds for single-pass algorithm, as this version of iSVD is useful for online basis computation. The present research uses single-pass algorithm, whose performance is verified in [5] only on compression of photographs. Multi-pass algorithm is said to be more accurate, but requires access to all of A. For offline basis computation it is recommended to apply multi-pass version of iSVD for higher accuracy.

Due to higher divergence errors in higher-index modes and orthogonality errors which might also appear in iSVD, treatment of basis is should be considered. When the main iSVD parameters k_{add}, M_{dom} and threshold are maintained in a 'safe' range, Helmholtz decomposition and Gram-Schmidt orthogonalization is recommended. The 'safe' range is such that the resultant orthogonality and divergence errors are maintained well below basis fidelity errors. This range is case-dependent, but it is advised to keep all three parameters as high as possible while achieving the purpose of iSVD: accurate low-rank approximation SVD.

8.3.2. Regarding reduced basis

As already stated, SVD provides an optimal basis only in a sense - within a given set of snapshots. Therefore it is perhaps a convenient starting point, but for problem of time extrapolation it fails. In this case the basis should be further enhanced, possibly with the use of FOM data from further integration period.

It is difficult to assess what constitutes a good basis, but as a rule it holds that intermodal energy transfer must be the same as in the full-order basis. This is easier to imagine in solution reproduction problem, but in time-extrapolation not so much, full-order basis then is still equally inaccurate. Since the mechanism of energy transfer between modes is not yet well understood, further research in this topic in the spirit of [10] by Couplet et al. is recommended.

While investigating the ROM vulnerability to RB distortions, the bases should be modified with a distortion that is divergence-free. This would allow to isolate the effect of distortion from the effect of non-vanishing pressure which appears when the modes are not divergence-free.

8.3.3. Regarding mixing-length EV model in EC-ROM

EV was (in the primordial plan for this research) supposed to be *trained* on a neural network or otherwise regressed, based on high-fidelity data (FOM) to achieve $\nu_t = \nu_t(a)$. Regression is currently not pursued, but recommended in the future research. In the context of fitting the constant α in the presently used EV model, sophisticated LS regression could be attempted, such as proposed in appendix A.9 or [14] by Hijazi et al. POD basis for ν_t is not a necessary choice. Fourier basis could prove just as good, or better, due to lower computational effort, as Fourier modes are constructed independently of FOM snapshots. The advantage of using any series expansion of EV function is that the EV diffusion term can be pre-computed in this case, without the necessity to project this term at high cost. POD is recommended in case of 3D eddy viscosity,

$\nu_t = \nu_t\left(x, y, z, t\right)$, i.e. when storing snapshots is costly and when EV field cold be complex.

It is recommended to apply a more sophisticated EV model e.g. Smagorinsky and compare computation times of turbulent diffusion operator using EV-POD, 2-step scheme by Wang et. al [34] and discrete empirical interpolation method (DEIM). Perhaps the present EV model inspired by [4] would perform better for stationary test case, where $\nu_t = \nu_t\left(y\right)$ only. Other expression for ν_t could also be investigated.

8.3.4. Regarding INS3D

Performance of the code is limited to small-scale simulations. While INS2D is fit for $2D$ cases, its $3D$ counterpart requires major changes, particularly in how results data is stored inside and saved. Matrix operators, which are all fully assembled take considerable amount of memory. Speed is also limited due no multi-core capabilities. Restart options should also be re-invented.

A

Appendix

A.1. SV decay comparison

Singular value decay of TG and SL cases on fine and small grid are compared in this section. The reference cSVD full range is plotted (for SL case) and it is shown on scale how small is the fraction of total SV spectrum, that is the target of iSVD (compare with fig. 5.28)

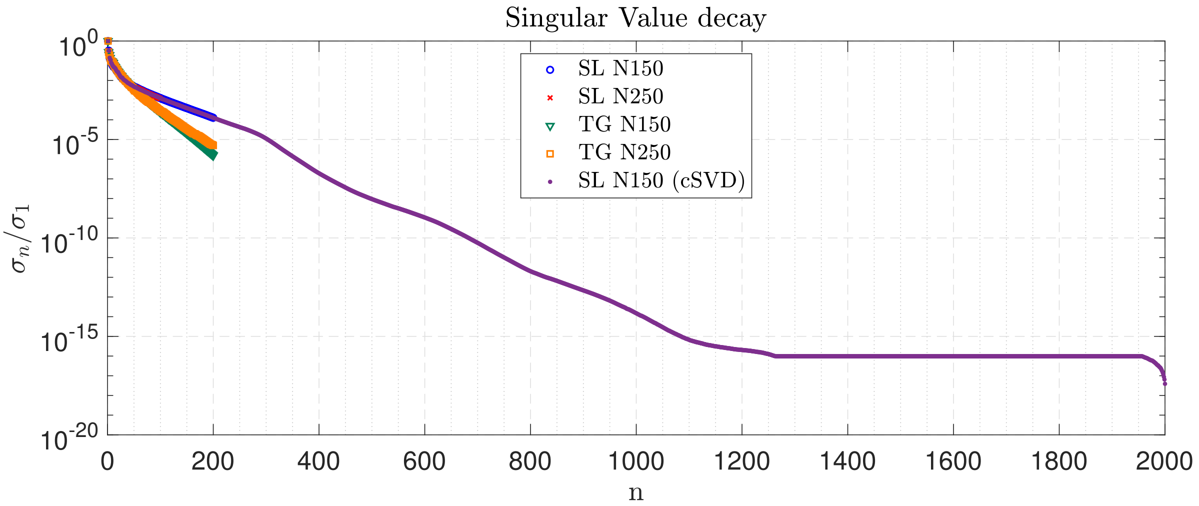

Figure A.1: Comparison of singular value decay for all tested cases: full range.

A.2. Selected fields

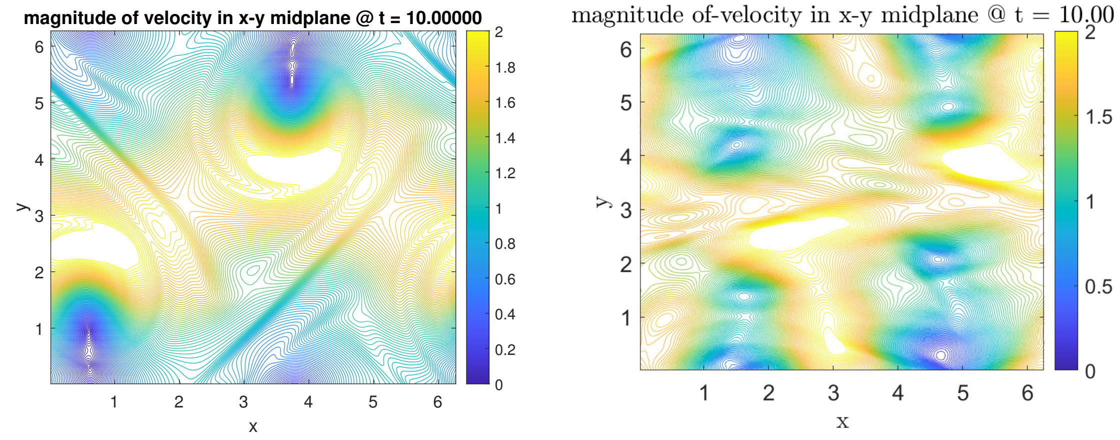

(a) FOM

(b) ROM $M = 16$

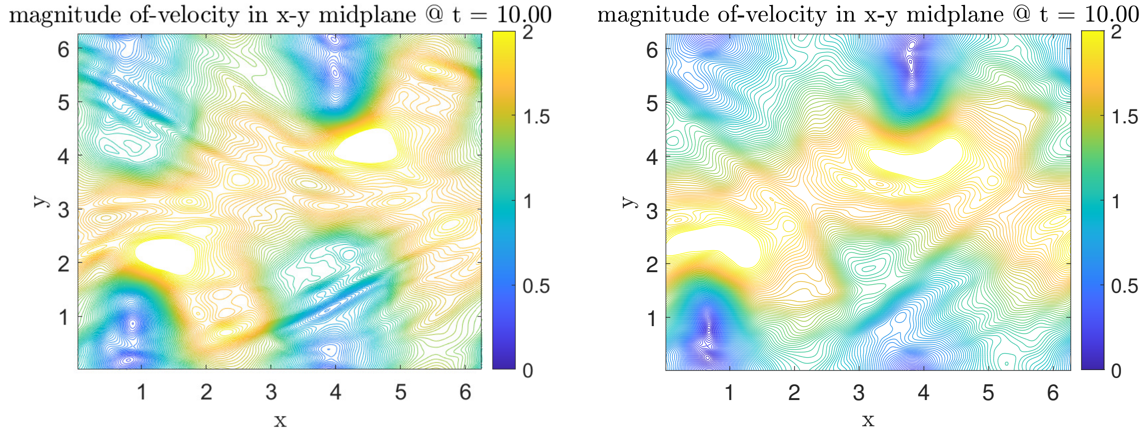

(c) ROM $M = 32$

(d) ROM $M = 48$

Figure A.2: Shear layer. Fine grid. Velocity magnitude at $t = 10$: FOM and ROMs. Contours in xy plane.

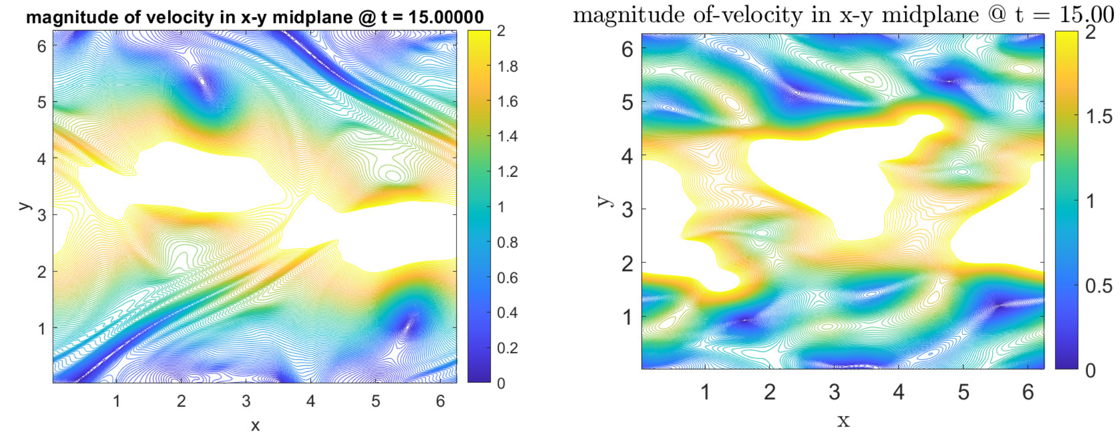

(a) FOM

(b) ROM $M = 16$

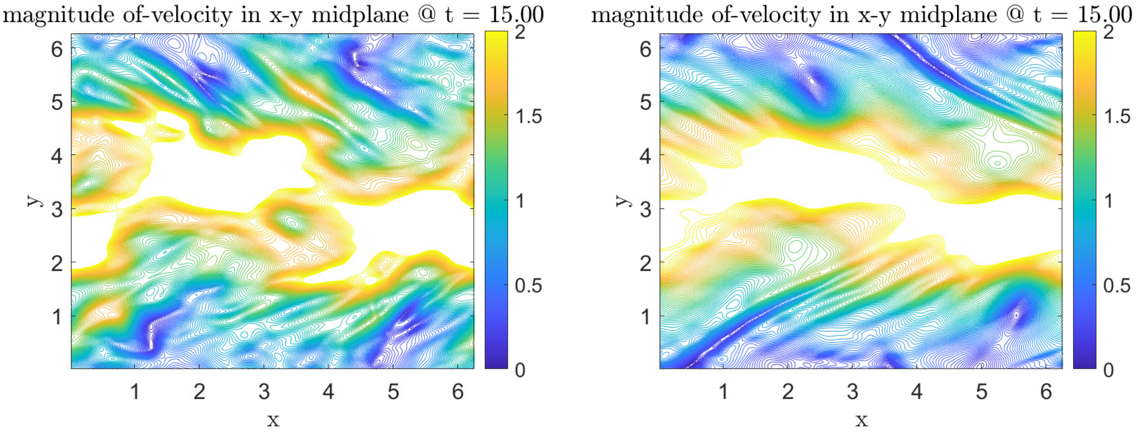

(c) ROM $M = 32$

(d) ROM $M = 48$

Figure A.3: Shear Layer. Fine grid. Velocity magnitude at $t = 15$: FOM and ROMs. Contours in xy plane.

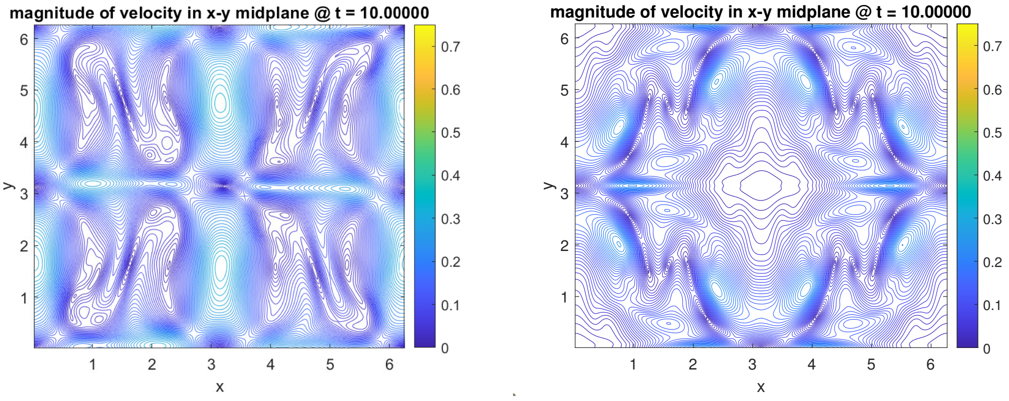

(a) FOM (b) ROM M8

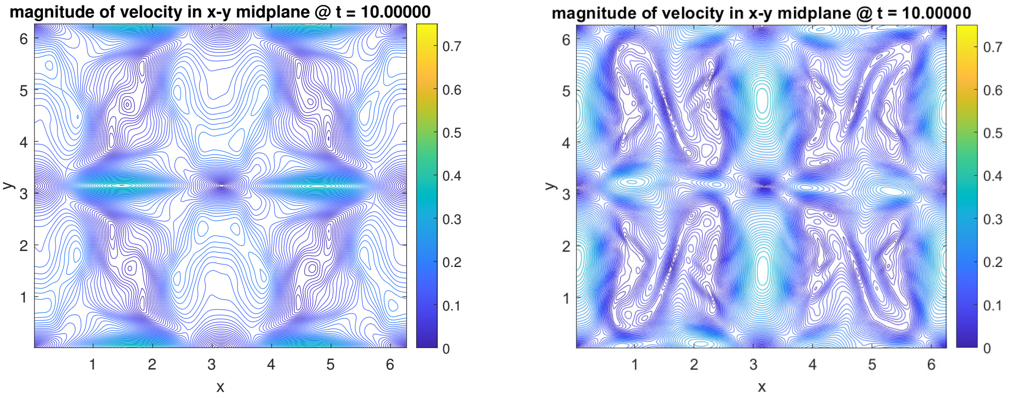

(c) ROM M16 (d) ROM M32

Figure A.4: Talor-Green vortex. Fine grid. Velocity magnitude at $t = 10$: FOM and ROM with $M = 8, 16, 32$, $t_{end} = 10$, . Contours in xy-plane.

A.3. A priori eddy viscosity plots

Here xz-averaged EV is plotted in three variants: raw as obtained from original expression based on [4]: $\nu_t(y,t) = \frac{\langle \boldsymbol{u}_> \cdot \boldsymbol{u}_> \rangle_{x,z}}{\sqrt{\left\langle \nabla \boldsymbol{u}_> : \nabla \boldsymbol{u}_> \right\rangle_{x,z}}}$; filtered with filter kernel h, see eq. (3.37); and POD of this filtered EV. The number of modes used in this POD is the as respective basis dimension (i.e. when EV is computed for basis $M = 16$, then the POD of EV also engages 16 modes).

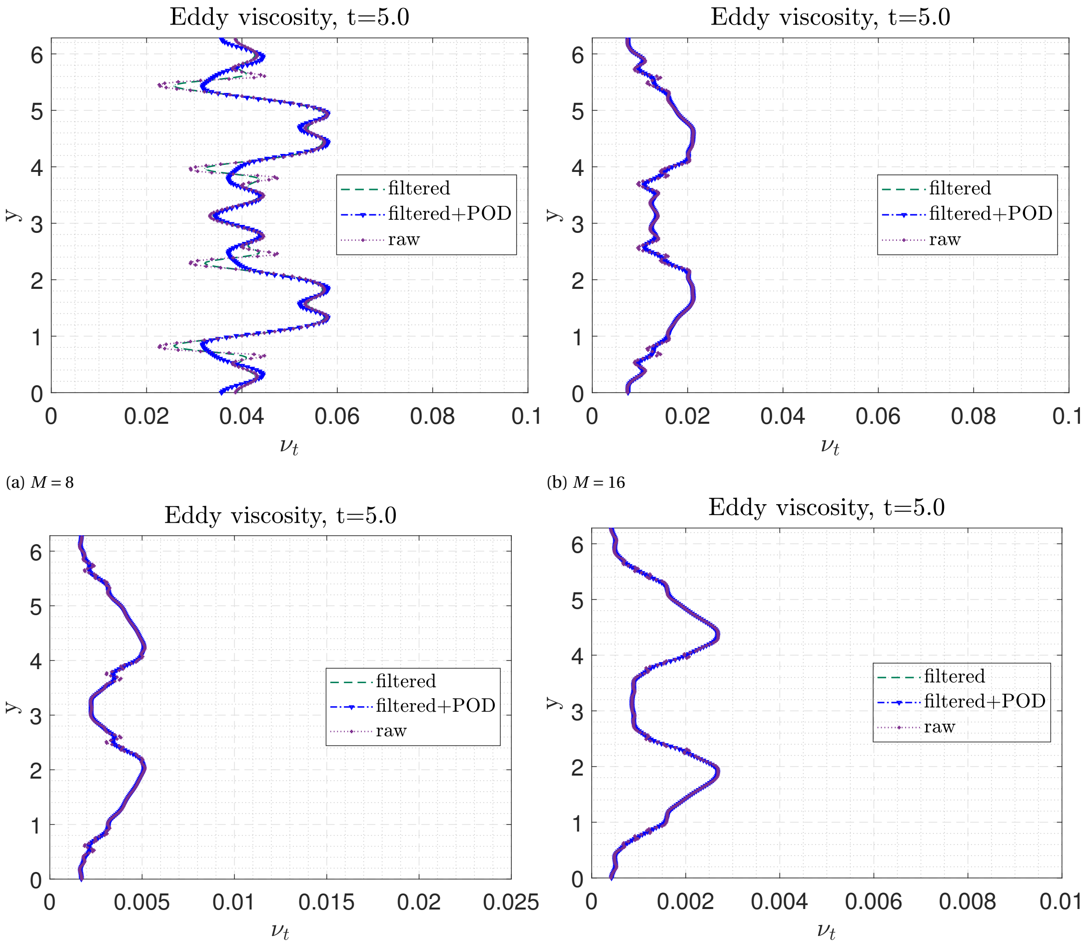

(a) $M = 8$

(b) $M = 16$

(c) $M = 32$

(d) $M = 48$

Figure A.5: Eddy viscosity at $t = 5$

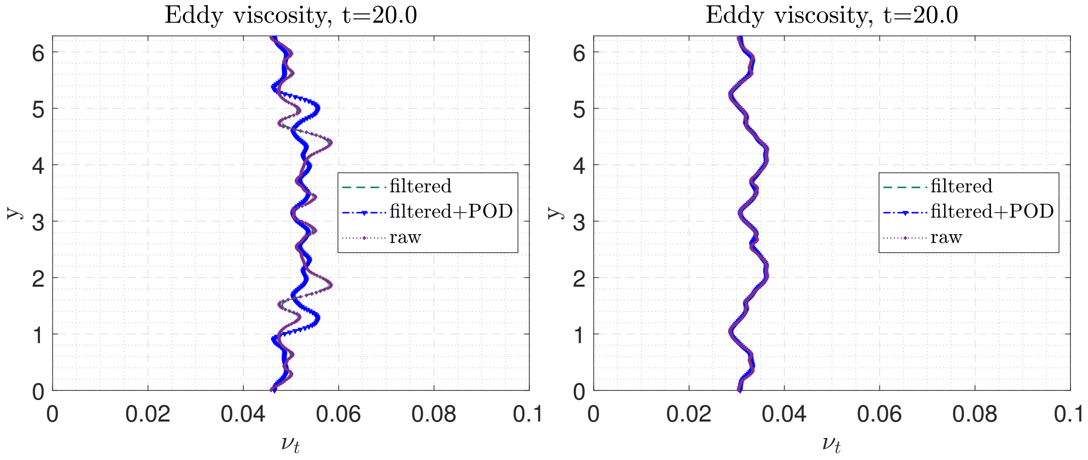

(a) $M = 8$

(b) $M = 16$

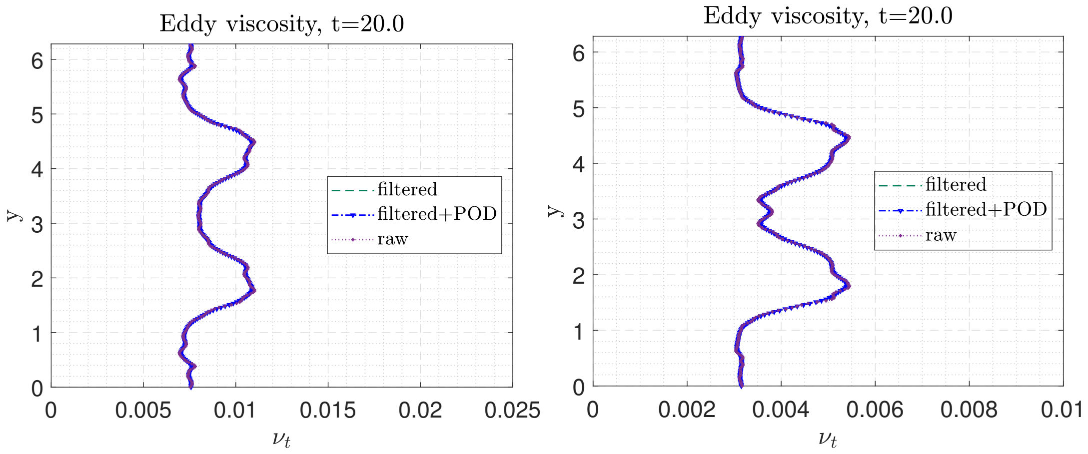

(c) $M = 32$

(d) $M = 48$

Figure A.6: Eddy viscosity at $t = 20$

A.4. A priori absolute errors

In this section absolute errors in averaged terms are presented.

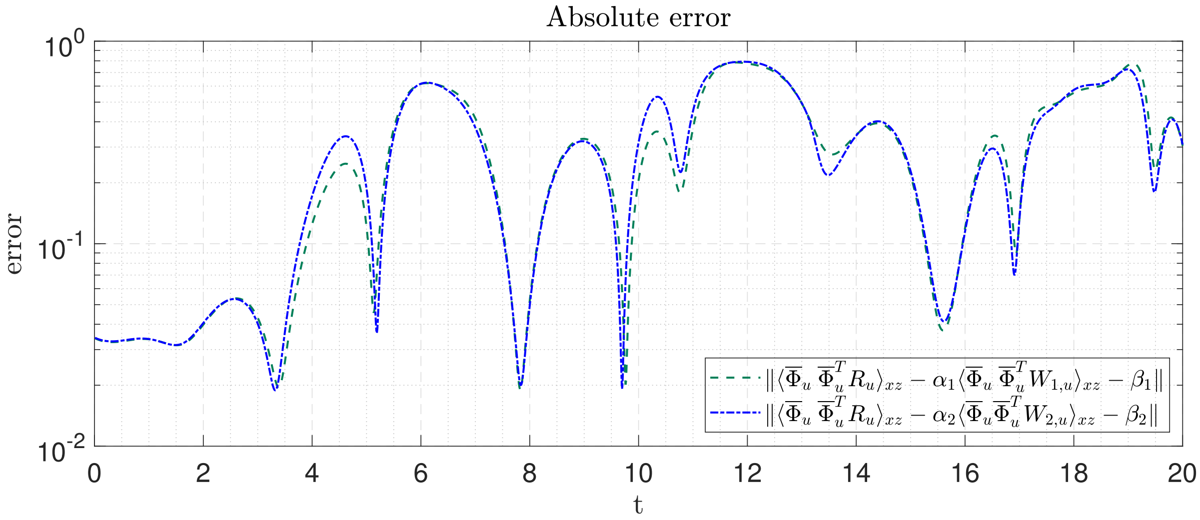

(a) $M = 8$

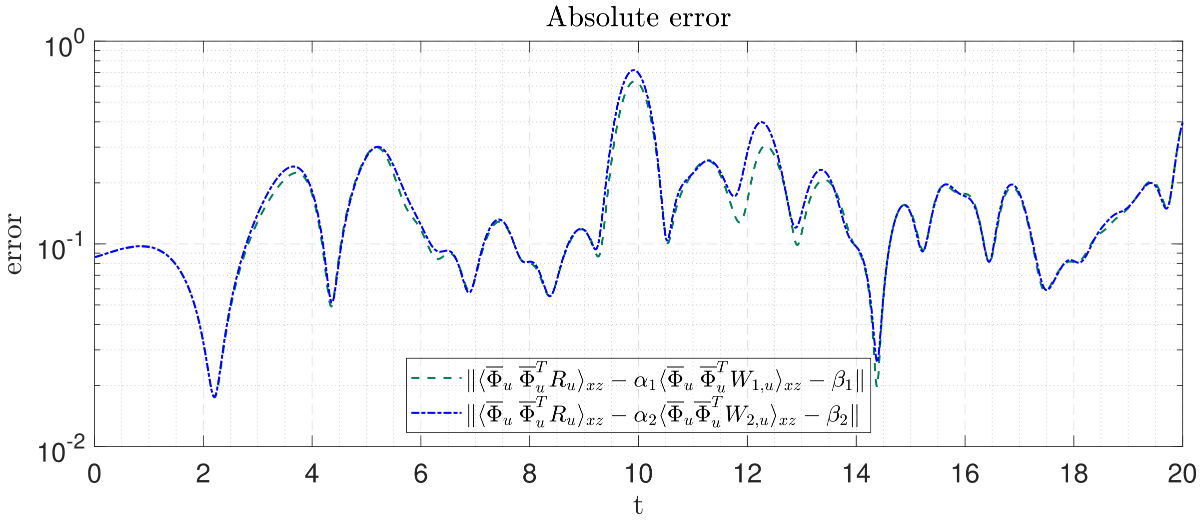

(b) $M = 16$

Figure A.7: Absolute error for $M = 8, 16$ and $t \in [0, 20]$ in averaged terms.

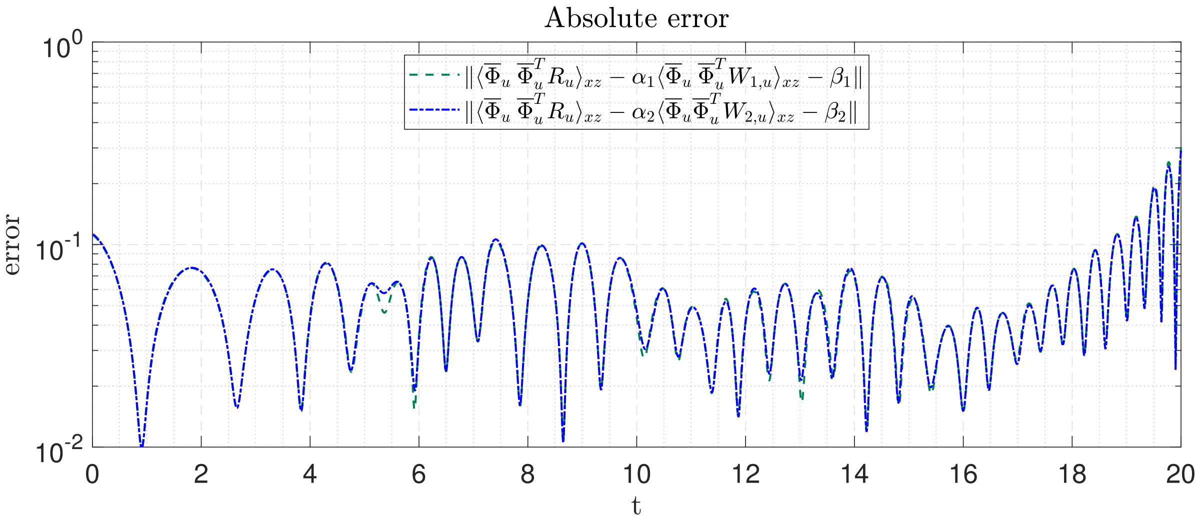

(a) $M = 32$

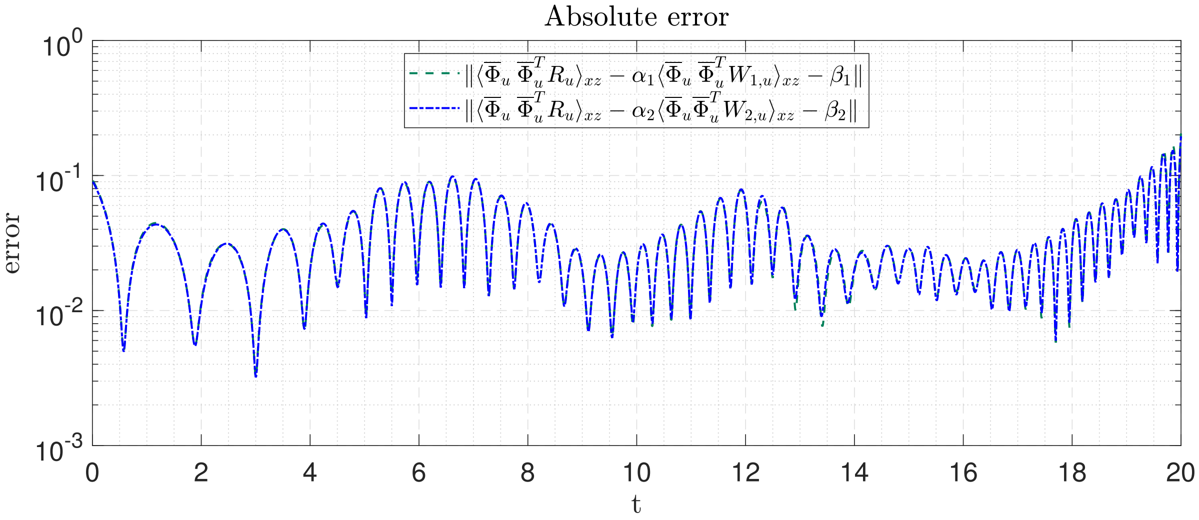

(b) $M = 48$

Figure A.8: Absolute error for $M = 32, 48$ and $t \in [0, 20]$ in averaged terms.

A.5. A priori relative errors

In this section relative errors in global terms are presented.

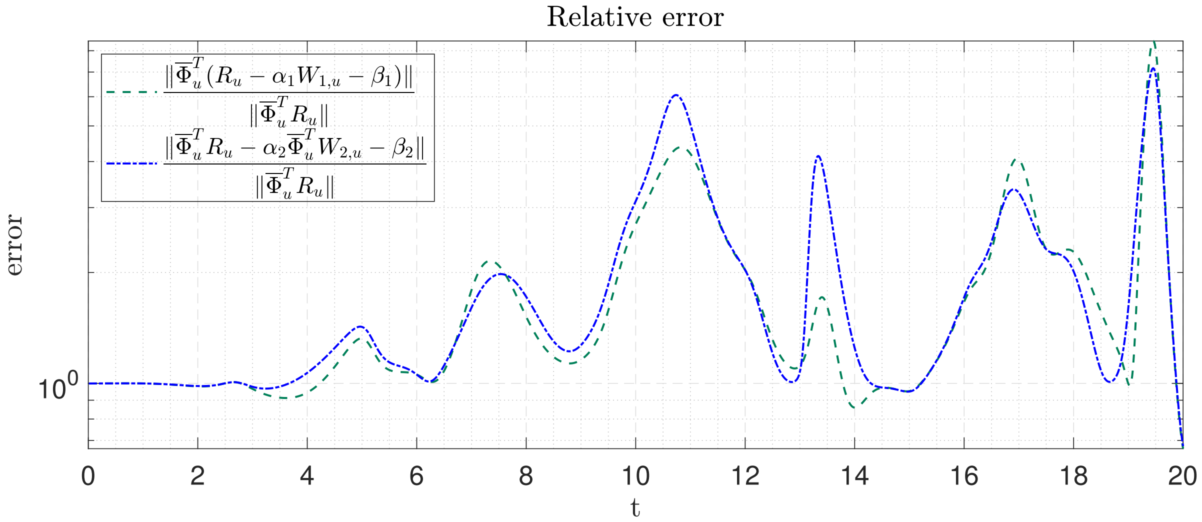

(a) $M = 8$

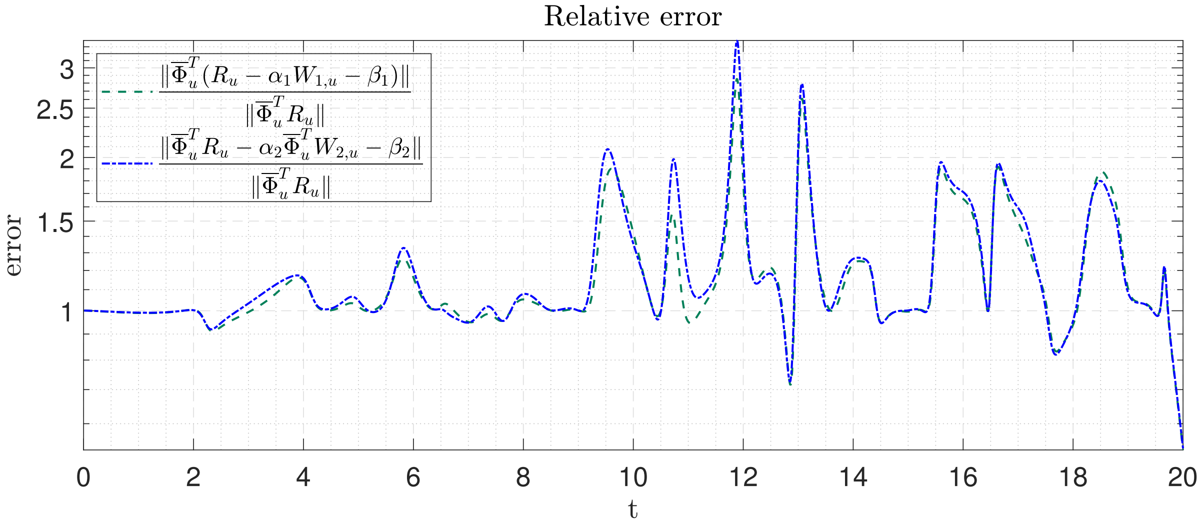

(b) $M = 16$

Figure A.9: Relative error for $M = 8, 16$ and $t \in [0, 20]$ in global terms.

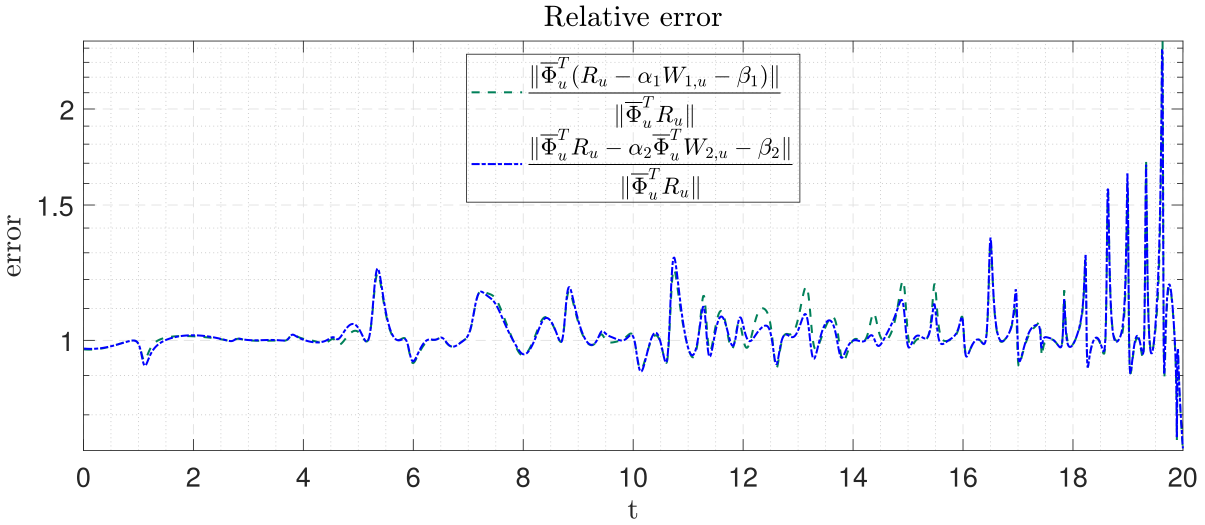

(a) $M = 32$

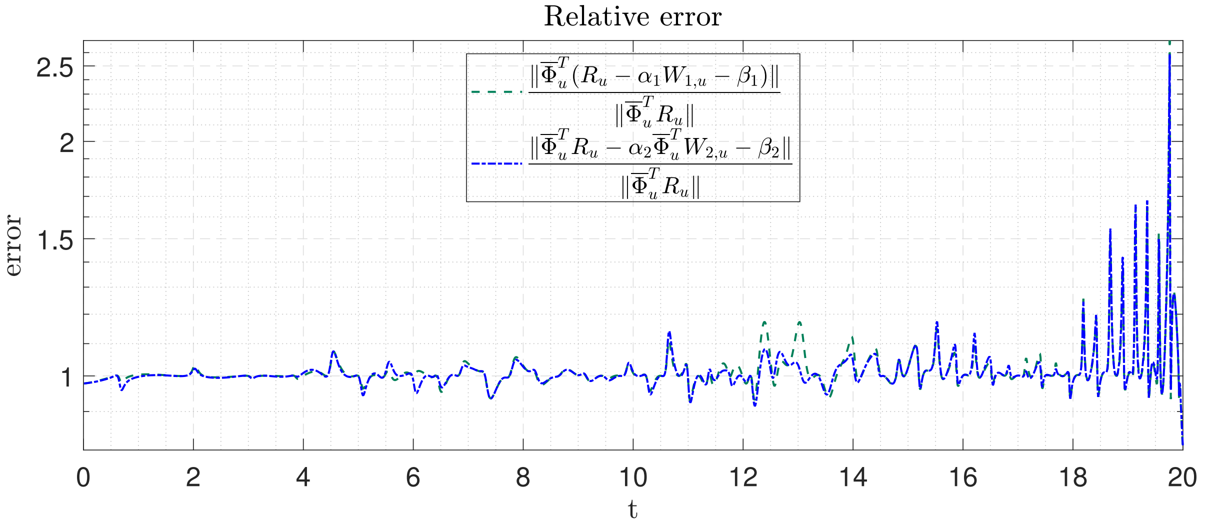

(b) $M = 48$

Figure A.10: Relative error for $M = 32, 48$ and $t \in [0, 20]$ in global terms.

A.6. Pressure Poisson equation

In incompressible flow, pressure is not a strictly independent variable and also needs to satisfy a certain Poisson equation, derived from eq. (3.9)-(3.10) by taking divergence of the latter equation (see [25] by Pope):

$$\frac{\partial}{\partial x_i}\frac{\partial u_i}{\partial t}+\frac{\partial}{\partial x_i}u_j\frac{\partial u_i}{\partial x_j}=-\frac{\partial}{\partial x_j \partial x_j}p+\nu\frac{\partial}{\partial x_i}\frac{\partial^2}{\partial x_j \partial x_j}u_i. \tag{A.1}$$

Periodic BCs, continuity and assumptions that divergence operator commutes with temporal and spatial derivatives in the terms, eliminate 3 terms from the above equation. The result is a Poisson equation with velocity-gradient-dependent RHS:

$$\frac{\partial}{\partial x_j \partial x_j}p=-\frac{\partial u_i}{\partial x_j}\frac{\partial u_j}{\partial x_i}. \tag{A.2}$$

In case of periodic BCs, a Fourier transform may serve to simplify the solution to this equation, now written using vector notation

$$\mathscr{F}\left(\nabla^2 p\right)=\mathscr{F}\left(f\right), \tag{A.3}$$

where f is a generic right-hand side in physical space. Then differentiation in spectral space simplifies, becoming multiplication by wavenumber vector:

$$\boldsymbol{\xi}^2\hat{p}=\hat{f}. \tag{A.4}$$

Therefore:

$$p=\mathscr{F}^{-1}\left(\hat{p}\right)=\mathscr{F}^{-1}\left(\frac{\hat{f}}{\boldsymbol{\xi}^2}\right), \tag{A.5}$$

retrieves the pressure in physical space.

Solving this Poisson equation (A.2) is equivalent to enforcing mass conservation, $\nabla\cdot\boldsymbol{u}=0$ (see [25]; in discrete domain a correction step must follow). Since periodic BCs are considered, fast Fourier transform (FFT) might be used, a brief explanation is as follows. Poisson equation in discretized form is:

$$A_h p_h=f_h. \tag{A.6}$$

Solving this system in general case requires LU decomposition of the pressure matrix, or other, iterative methods. However, as mentioned in the previous section, one might resort to Fourier transform to solve the equation much simpler, provided that BCs are periodic. Simply an FFT algoritm is used in the numerical domain:

$$\hat{A}_h\hat{p}_h=\hat{f}_h, \tag{A.7}$$

where $\hat{A}_h$ is a diagonal matrix with the following elements:

$$\hat{a}_i=2h_{x1}h_{y1}h_{z1}\left(\frac{2}{h_{x1}^2}\sin^2\left(\frac{(i-1)\pi}{N_x}\right)+\frac{2}{h_{y1}^2}\sin^2\left(\frac{(i-1)\pi}{N_y}\right)+\frac{2}{h_{z1}^2}\sin^2\left(\frac{(i-1)\pi}{N_z}\right)\right), \tag{A.8}$$

which correspond to the wave number product in eq. (A.5). The matrix is easily invertible, therefore discrete pressure is easy to recover from:

$$p_h=FFT^{-1}\left(\hat{A}_h^{-1}\hat{f}_h\right). \tag{A.9}$$

A.7. Optimal snapshot selection

Oxberry et al. in [21] demonstrate an algorithm of snapshot selection capable of deciding *online* (during FOM run) which snapshots should be selected to update the SVD of the current basis. The authors use Brand's iSVD, contrary to the present research, where Baker's iSVD is used. Although this approach had not been used in the present research, it is of interest to describe it, as potential savings in computational resources may be considerable and further recommendations include application of this algorithm.

Denote the right-hand side of FOM eq. (2.6) as $F_h\left(V_h(t)\right)$ and assume it is velocity-only. ROM equation is then

$$\dot{a}(t)=\Phi^T F_h\left(\Phi a(t)\right), \tag{A.10}$$

where Φ is the current ROM basis (not the one based on all snapshots, as these are not yet available).

Error is defined as the difference between current FOM solution and its projection onto the image of *current* basis:

$$\dot{e}(t) = F_h(V_h(t)) - \Phi\Phi^T F_h(\Phi a). \tag{A.11}$$

This may be rewritten as:

$$\dot{e}(t) = \underbrace{\left(\mathbb{I} - \Phi\Phi^T\right) F_h(V_h(t))}_{\text{out-of-subspace component}} + \underbrace{\Phi\Phi^T \left(F_h(V_h(t)) - F_h(\Phi a(t))\right)}_{\text{in-subspace component}}. \tag{A.12}$$

Error estimator is constructed by neglecting the in-subspace component:

$$\dot{\tilde{e}} = \left(\mathbb{I} - \Phi\Phi^T\right) F_h(V_h(t)), \tag{A.13}$$

which integrated w.r. to time yields:

$$\tilde{e} = \left(\mathbb{I} - \Phi\Phi^T\right) V_h(t)(t). \tag{A.14}$$

Current POD (SVD) is updated with a new snapshot at query time t_Q which is computed based on how fast the error estimator is *predicted* to grow, by forward Euler method (see equation (14) in [21]).

A.8. LS regression - derivation of formulas

The goal here is to find α, β in the relation between target and regressor, of the form $x = \alpha y + \beta$. Let $x, y \in \mathbb{R}^N$ be vectors containing discrete values of the target function f and regressor g at N 1D grid points, $x = \left[f_1, f_2, ..., f_N\right]$, $y = \left[g_1, g_2, ..., g_N\right]$. Let $\mathbf{1}_N = [1, 1, ..., 1]$ denote an N-component vector of ones. Define scalar product $\left(x, y\right) := x^T y = \sum_i f_i g_i$. Thus $(\mathbf{1}_N, x) = \sum_i f_i$ and $\left(\mathbf{1}_N, y\right) = \sum_i g_i$. Finally, let the objective function be defined as $J\left(\alpha, \beta\right) := \frac{1}{2}\left\|x - \alpha y - \beta \mathbf{1}_N\right\|^2$.

Necessary and sufficient condition for a minimum of the convex function $J\left(\alpha, \beta\right)$ is that partial derivatives of J vanish for minimizers $\alpha_{min}, \beta_{min}$:

$$\begin{cases} -\frac{\partial J}{\partial \alpha} = \left(y, x - \alpha y - \beta \mathbf{1}_N\right) = 0 \\ -\frac{\partial J}{\partial \beta} = \left(\mathbf{1}_N, x - \alpha y - \beta \mathbf{1}_N\right) = 0. \end{cases} \tag{A.15}$$

Further expansion of eq. (A.15) yields:

$$\begin{cases} \left(y, x\right) - \alpha \left\|y\right\|^2 - \beta \left(\mathbf{1}_N, y\right) = 0 \\ -N\beta + (\mathbf{1}_N, x) - \alpha \left(\mathbf{1}_N, y\right) = 0. \end{cases} \tag{A.16}$$

From the second equation in (A.16):

$$\beta = \frac{1}{N}\left((\mathbf{1}_N, x) - \alpha \left(\mathbf{1}_N, y\right)\right).$$

Inserting this into the first equation in (A.16) yields:

$$\left(y, x\right) - \alpha \left\|y\right\|^2 - \frac{1}{N}\left((\mathbf{1}_N, x) - \alpha \left(\mathbf{1}_N, y\right)\right)\left(\mathbf{1}_N, y\right) = 0. \tag{A.17}$$

The final formulas for the regression coefficients are then:

$$\begin{cases} \alpha = \frac{(y,x) - \frac{1}{N}(\mathbf{1}_N, x)(\mathbf{1}_N, y)}{\|y\|^2 - \frac{1}{N}(\mathbf{1}_N, y)^2} \\ \beta = \frac{1}{N}\left((\mathbf{1}_N, x) - \underbrace{\frac{\left(y, x\right) - \frac{1}{N}(\mathbf{1}_N, x)\left(\mathbf{1}_N, y\right)}{\left\|y\right\|^2 - \frac{1}{N}\left(\mathbf{1}_N, y\right)^2}}_{\alpha}\left(\mathbf{1}_N, y\right)\right). \end{cases} \tag{A.18}$$

The above derivation is equivalent to the following one, using Moore-Penrose inverse, found in many applied linear algebra textbooks e.g. [6] by Ben-Israel and Greville. Let $x = \left[f_1, ..., f_N\right]^T$ be the target, $c = \left[\alpha, \beta\right]^T$ regression coefficients and $A = \left[\left[g_1, ..., g_N\right]^T [1, ..., 1]^T\right]$ the regression basis functions. We seek the solution to an overdetermined system:

$$x = Ac,$$

which is given by $c = \left(A^T A\right)^{-1} A^T x$. If A has linearly independent columns (which it does here), the matrix $\left(A^T A\right)^{-1} A^T$ is the Moore-Penrose inverse (or pseudo-inverse), $\left(A^T A\right)^{-1} A^T =: A^\dagger$. Then the solution is simply $c = A^\dagger x$.

A.9. Proposition of LS regression (more sophisticated)

The following idea was not implemented, only mathematical derivation is performed. A more sophisticated regression may be built with coefficients g of EV-POD modes η. Let us invoke the term RHS_2 of investigated equation eq. (3.33). The regression will be performed on xz averaged terms as also EV is computed as an xz-averaged quantity, which is considered a fair approximation in the shear layer case. The regressor will also follow only u-component of the averaged LHS. Denote:

$$k(g) = \left\langle \underbrace{\overline{\Phi}^T L_h}_{\overline{L}_h} \operatorname{diag}(\eta g) \underbrace{S_h \overline{\Phi}\overline{a}}_{b} \right\rangle_{xz}, \tag{A.19}$$

where L_h is a $N_u \times N_u$ matrix, η is a $N_u \times M$ matrix and $b := S_h\overline{\Phi}\overline{a}$ is a $N_u \times 1$ vector. The regression problem is stated as: find a vector $g \in \mathbb{R}^M$, for which the function $f : \mathbb{R}^M \to \mathbb{R}$,

$$f(g) = \frac{1}{2}\left\| k(g) - h \right\|^2, \tag{A.20}$$

reaches its minimum. Vector h in this equation is simply $\overline{\Phi}^T R$. With the above symbolic k may be written:

$$k(g) = \left\langle \overline{L}_h \operatorname{diag}(\eta g)\, b \right\rangle_{xz}. \tag{A.21}$$

It is easily shown that $\operatorname{diag}(\eta g)\, b = \operatorname{diag}(b)\, \eta g$, therefore:

$$k(g) = \left\langle \overline{L}_h \operatorname{diag}(b)\, \eta g \right\rangle_{xz}. \tag{A.22}$$

Denoting $A := \overline{L}_h \operatorname{diag}(b)\, \eta$ allows to write:

$$k(g) = \left\langle Ag \right\rangle_{xz} = \left\langle A \right\rangle_{xz} g, \tag{A.23}$$

where the last equality hold because the averaging operation $\left\langle \cdot \right\rangle_{xz} := \frac{1}{L_x L_z}\Omega_h^{xz}$ is linear. Also because of this, it commutes with the gradient operation:

$$\nabla k(g) = \left\langle \nabla (Ag) \right\rangle_{xz} = \left\langle A^T \right\rangle_{xz}. \tag{A.24}$$

The objective function f is convex, hence a necessary and sufficient condition for a minimum is:

$$\nabla f(g) = 0. \tag{A.25}$$

The application of chain rule leads to:

$$\begin{gathered} \nabla f(g) = \nabla k(g)\left(k(g) - h\right) = \\ \left\langle A^T \right\rangle_{xz}\left(\left\langle Ag \right\rangle_{xz} - h\right) = \left\langle A^T \right\rangle_{xz}\left(\left\langle A \right\rangle_{xz} g - h\right). \end{gathered} \tag{A.26}$$

With the condition for minimum this yields (denoting $\left\langle A \right\rangle_{xz} := A_{avg}$):

$$A_{avg}^T A_{avg}\, g = A_{avg}^T h. \tag{A.27}$$

Provided an inverse of $A_{avg}^T A_{avg}$ exists, the solution to the regression problem i.e. minimizing eq. (A.20), is:

$$\hat{g} = \left(A_{avg}^T A_{avg}\right)^{-1} A_{avg} h. \tag{A.28}$$

A.10. Performed computations

The table below summarizes important settings in all performed computations, including tests of iSVD basis, ROM simulations with a variety of settings, and a priori analysis of turbulence modeling.

Type of computation	Snapshots	k_{add}	M_{dom}	threshold	treatment	t_{end}^{FOM}	t_{end}	M	N_p
Basis quality (SL)	full set	100	100	10^{-6}	-	20	-	-	150^3
		10	100	10^{-6}	-	20	-	-	
		1	100	10^{-6}	-	20	-	-	
		100	100	10^{-6}	Helmholtz	20	-	-	
		100	100	10^{-6}	GS	20	-	-	
		100	100	10^{-6}	Helmholtz +GS	20	-	-	
		100	100	10^{-10}	Helmholtz	20	-	-	
		100	100	10^{-10}	GS	20	-	-	
		100	100	10^{-10}	Helmholtz +GS	20	-	-	
		100	100	10^{-8}	-	20	-	-	
		10	100	10^{-8}	-	20	-	-	
		1	100	10^{-8}	-	20	-	-	
		100	100	10^{-10}	-	20	-	-	
		10	100	10^{-10}	-	20	-	-	
		1	100	10^{-10}	-	20	-	-	
		10	50	10^{-8}	-	20	-	-	
		10	100	10^{-8}	-	20	-	-	
		10	200	10^{-8}	-	20	-	-	
		100	200	10^{-6}	-	20	-	-	
		10	200	10^{-6}	-	20	-	-	
		100	50	10^{-6}	-	20	-	-	
		100	50	10^{-8}	-	20	-	-	
		100	50	10^{-10}	-	20	-	-	
		100	100	10^{-6}	-	20	-	-	
		100	100	10^{-8}	-	20	-	-	
		100	100	10^{-10}	-	20	-	-	
		100	200	10^{-6}	-	20	-	-	
		100	200	10^{-8}	-	20	-	-	
		100	200	10^{-10}	-	20	-	-	
	50% downsampled set	100	100	10^{-6}	-	20	-	-	
		10	100	10^{-6}	-	20	-	-	
		1	100	10^{-6}	-	20	-	-	
SL simulation (main)	full set	100	100	10^{-6}	-	20	20	8	
								16	
								32	
								48	

	50% downsampled set	100	100	10^{-6}	-	20	20	8 16 32 48	250^3
	full set	100	100	10^{-6}	Helmholtz + GS	20	20	8 16 32 48	
SL simulation (additional)									
5% distorted basis	full set	-	-	-	-	10	10	8 16	150^3
10% distorted basis	full set	-	-	-	-	10	10	8 16	
enforced momentum conservation	full set	100	100	10^{-6}	-	10	10	11 19 35	250^3
varying integration period	full set	100	100	10^{-6}	-	10	10	32	250^3
						15	15	32	
						20	20	32	
time extrapolation	full set	100	100	10^{-6}	-	10	15	8 16 32 48	250^3
TG simulation	full set	100	200	10^{-6}	-	10	10	8 16 32 48	250^3
SL a priori analysis	full set	100	100	10^{-6}	Helmholtz+GS	20	20	8 16 32 48	250^3

Table A.1: Summary of computations performed in the thesis

Bibliography

[1] Incremental svd package manual. URL `https://www.math.fsu.edu/~cbaker/IncPACK/docs/`.

[2] S.E. Ahmed, S. Pawar, O. San, A. Rasheed, T. Iliescu, and B.R. Noack. On closures for reduced order models – a spectrum of first-principle to machine-learned avenues. 2021. URL `https://arxiv.org/abs/2106.14954`.

[3] I. Akkerman, Y. Bazilevs, V.M. Calo, T.J.R. Hughes, and S. Hulshoff. The role of continuity in residual-based variational multiscale modeling of turbulence. *Computational Mechanics*, 41(3):371–378, 2008.

[4] N. Aubry and J.L. Lumley. The dynamics of coherent structures in the wall region of a turbulent boundary layer. *Journal of Fluid Mechanics*, 192:115–173, 1988.

[5] C.G. Baker, K.A. Gallivan, and P. Van Dooren. Low-rank incremental methods for computing dominant singular subspaces. *Linear Algebra and Its Applications*, 436(8):2866–2888, 2012.

[6] A. Ben-Israel and T. Greville. *Generalized Inverses: Theory and Applications*. Springer, 2003.

[7] P. Benner, S. Gugercin, and K. Willcox. A survey of projection-based model reduction methods for parametric dynamical systems. *SIAM Review*, 57(4):483–531, 2015.

[8] M. Brand. Incremental singular value decomposition of uncertain data with missing values. *Lecture Notes in Computer Science (including subseries Lecture Notes in Artificial Intelligence and Lecture Notes in Bioinformatics)*, 2350:707–720, 2002.

[9] S. Chaturantabut and D.C. Sorensen. Nonlinear model reduction via discrete empirical interpolation. *SIAM Journal on Scientific Computing*, 32(5):2737–2764, 2010.

[10] M. Couplet, P. Sagaut, and C. Basdevant. Intermodal energy transfers in a proper orthogonal decomposition - Galerkin representation of a turbulent separated flow. *Journal of Fluid Mechanics*, (491):275–284, 2003.

[11] L. Fick, Y. Maday, A.T. Patera, and T. Taddei. A stabilized POD model for turbulent flows over a range of Reynolds numbers: Optimal parameter sampling and constrained projection. *Journal of Computational Physics*, 371:214–243, 2018.

[12] Gene H. Golub and Charles F. van Loan. *Matrix Computations*. JHU Press, 2013.

[13] S. Grimberg, C. Farhat, and N. Youkilis. On the stability of projection-based model order reduction for convection-dominated laminar and turbulent flows. *Journal of Computational Physics*, 419, 2020.

[14] S. Hijazi, G. Stabile, A. Mola, and G. Rozza. Data-driven POD-Galerkin reduced order model for turbulent flows. *Journal of Computational Physics*, 416, 2020.

[15] C. Hirsch. *Numerical Computation of Internal and External Flows: The Fundamentals of Computational Fluid Dynamics*. Elsevier, 2007.

[16] Philip Holmes, John L. Lumley, and Gal Berkooz. *Turbulence, Coherent Structures, Dynamical Systems and Symmetry*. Cambridge Monographs on Mechanics. Cambridge University Press, 1996.

[17] A. N. Kolmogorov. The Local Structure of Turbulence in Incompressible Viscous Fluid for Very Large Reynolds' Numbers. In *Dokl. Akad. Nauk SSSR*, volume 30, pages 301–305, 1941.

[18] M. Leschziner. *Statistical Turbulence Modelling for Fluid Dynamics, Demystified: An Introductory Text for Graduate Engineering Students*. 2015. ISBN 9781783266623.

[19] R.J. LeVeque. *Finite-Volume Methods for Hyperbolic Problems*. Cambridge University Press, 2002.

[20] M. Mohebujjaman, L.G. Rebholz, and T. Iliescu. Physically constrained iven correction for reduced-order modeling of fluid flows. *International Journal for Numerical Methods in Fluids*, 89(3):103–122, 2019.

[21] G.M. Oxberry, T. Kostova-Vassilevska, W. Arrighi, and K. Chand. Limited-memory adaptive snapshot selection for proper orthogonal decomposition. *International Journal for Numerical Methods in Engineering*, 109(2):198–217, 2017.

[22] S. V. Patankar. *Numerical Heat Transfer and Fluid Flow.* Series on Computational Methods in Mechanics and Thermal Science. Hemisphere Publishing Corporation (CRC Press, Taylor & Francis Group), 1980.

[23] Janet S. Peterson. The reduced basis method for incompressible viscous flow calculations. *SIAM Journal on Scientific and Statistical Computing*, 10(4):777–786, 1989.

[24] Sagaut Pierre. *Multiscale and Multiresolution Approaches in Turbulence.* Imperial College Press, 2006.

[25] S.B. Pope. *Turbulent Flows.* Cambridge Univ. Press, 2011.

[26] A. Quarteroni and G. Rozza. *Reduced Order Methods for Modeling and Computational Reduction.* Springer Publishing Company, Incorporated, 2013.

[27] A. Quarteroni, A. Manzoni, and F. Negri. *Reduced Basis Methods for Partial Differential Equations: An Introduction.* Springer International Publishing, 2015.

[28] L.F. Richardson. *Weather prediction by numerical process, second edition*, volume 9780521680448. 2007.

[29] P. Sagaut. *Large Eddy Simulation for Incrompressible Flows, an Introduction.* Springer Verlag, Berlin Heidelberg, 2006.

[30] O. San and R. Maulik. Neural network closures for nonlinear model order reduction. *Advances in Computational Mathematics*, 44(6):1717–1750, 2018.

[31] B. Sanderse. Non-linearly stable reduced-order models for incompressible flow with energy-conserving finite volume methods. *Journal of Computational Physics*, 421, 2020.

[32] L. Sirovich. Turbulence and the dynamics of coherent structures part iii: Dynamics and scaling. *Quarterly of Applied Mathematics*, 45(3):583–590, 1987.

[33] E. Stein, R. Borst, de, and T.J.R. Hughes. *Encyclopedia of Computational Mechanics.* Wiley, United States, 2004. ISBN 0-470-84699-2. Volume 1: Fundamentals ; volume 2: Solids and Structures ; volume 3: Fluids.

[34] Z. Wang, I. Akhtar, J. Borggaard, and T. Iliescu. Two-level discretizations of nonlinear closure models for proper orthogonal decomposition. *Journal of Computational Physics*, 230(1):126–146, 2011.

[35] Z. Wang, I. Akhtar, J. Borggaard, and T. Iliescu. Proper orthogonal decomposition closure models for turbulent flows: A numerical comparison. *Computer Methods in Applied Mechanics and Engineering*, 237-240:10–26, 2012.

[36] D. Wells, Z. Wang, X. Xie, and T. Iliescu. An evolve-then-filter regularized reduced order model for convection-dominated flows. *International Journal for Numerical Methods in Fluids*, 84(10):598–615, 2017.

[37] D. C. Wilcox. *Turbulence Modelling for CFD.* DCW Industries, La Cañada, 1993.

[38] X. Xie, D. Wells, Z. Wang, and T. Iliescu. Approximate deconvolution reduced order modeling. *Computer Methods in Applied Mechanics and Engineering*, 313:512–534, 2017.

[39] X. Xie, M. Mohebujjaman, L.G. Rebholz, and T. Iliescu. Data-driven filtered reduced order modeling of fluid flows. *SIAM Journal on Scientific Computing*, 40(3):B834–B857, 2018.